PREDICTION OF STEADY SURFACE-LAYER FLOWS

by

Ayodeji Olukunle Demuren B.Sc.(Eng), A.C.G.I.

Thesis submitted for the degree of
Doctor of Philosophy
in the Faculty of Engineering,
University of London,
and
for the Diploma of Membership
of Imperial College.

Mechanical Engineering Department,
Imperial College of Science and Technology,
London SW7, England.

January, 1979

To

My parents, brothers and sisters, who continued to show more than a passive interest in my studies.

ABSTRACT

Three finite-difference calculation procedures are presented for solving the steady, two-dimensional, partial-differential equations governing the flow and heat transfer of surface layers. In the prediction of a surface-layer flow, one of the three procedures is employed, the choice depending on the relative importance of the gravitational or buoyancy forces. Both floating and full-depth layers are considered. Vertical variations of fluid properties within the layer are neglected. In the prediction of floating-layer flows, the effects of turbulence are modelled through entrainment relations derived from experimental data.

The present model predictions are compared with analytical solutions to three flow problems. Very good agreement is obtained in each case. The predictions are also compared extensively with laboratory experimental data on the discharges of warm water on to stagnant or crossflowing cold ambient water. Fairly good agreement is obtained in the cases of discharges into stagnant ambients. The predictions of the discharges into crossflowing ambients are only fair. The present predictions compare favourably with those made with some of the most popular models available. The predictions of field data on heated surface discharges into natural waters are not so good. Local conditions such as bottom topography and changing environmental conditions, on which adequate information is not presently available, may be important. The effects of these would have to be incorporated in the numerical models for good comparisons to be obtained.

Some experimental measurements are made of the supercritical flow of water in open channels of varying cross-sections. The predictions of these measurements are mostly fair. Some predictions of supercritical flows in open channels are also compared with measurements by other authors and solutions obtained with the method of characteristics. The agreement with the experimental data is fair, and the present predictions compare favourably with the method of characteristics. Some subcritical flow predictions are also presented.

PREFACE

The work reported in this thesis is the result of my research activities, from October 1975 to November 1978, at the Department of Mechanical Engineering of Imperial College, London. The work was carried out under a research contract with the Science Research Council, and was supervised by Professor D.B. Spalding.

The main objectives of the work were to develop and test numerical procedures for the prediction of surface-layer flows. The main emphasis was on the prediction of the thermal plumes resulting from heated surface discharges from power stations, but the prediction of non-buoyant flow in open channels could also be of practical importance in designing these channels.

I spent the first two years in developing the parabolic, hyperbolic and partially-parabolic surface-layer models, and in validating them with the prediction of some problems with analytical solution and some experimental data on heated surface discharges. In the third year, I extended these models, by the incorporation of a "rotating-grid" procedure for computing flows with strong curvature effects. I then proceeded to test the models by predicting some flows in open channels of varying cross-sections, and some heated surface discharges into cross-flowing ambient fluid. To supplement the available experimental data on open channel flows, for validating the numerical models, I performed some experiments of supercritical flow of water in channels of varying cross-section. These activities are described, in detail, in this thesis.

I must now express my gratitude to all those who have helped me in various ways during my research. First of all, I wish to thank my supervisor, Professor Spalding for his guidance and encouragement throughout the period of my research. Most of the achievements of the present study are largely due to his suggestions and inspiration.

I am also grateful to Dr. A.S.C. Ma, who encouraged me to undertake research in Heat Transfer, Dr. W.M. Pun, with whom I had some illuminating discussions, Dr. A.J. Policastro and Dr. J.J. McGuirk, both of whom provided me with many useful references on heated surface discharges.

My stay in Imperial College was enriched by the many discussions on social and scientific matters with my collegues, Alaa Awn, Denis Skiaderesis, Vinoth Ramachandra, Ian Jennions. Ahmed Abdelmeguid, Amin Bagdadi, Andrew Polard, Mohammed Elhadidi, George Carrol, S. Parameswaran, S. Al Sanea and the many others I may have forgotten to mention.

I am indebted to Professor J.R.D. Francis of the Civil Engineering Department for many suggestions on how to carry out my experimental investigation, and for allowing me the unlimited use of the facilities in the Hydraulics laboratory. I am also grateful to the many technicians in the laboratory who provided much needed assistance.

I wish also to thank: Bob King, who gave me invaluable help in designing, building and assembling my experimental rig, and also took and printed the photographs, Miss E.M. Archer and Mrs S. Boot, who provided excellent library services,

Sue Farmiloe, Colleen King, Maggie Dean and Marguerite Farrell, who were always very helpful on administrative matters, and Peter Dale, who helped to solve many computing problems. I am also very grateful to Mrs Sue Botter for the excellent typing of this thesis.

Finally, I wish to acknowledge the financial assistance provided by CHAM Limited, during the early period of my research.

London,

January, 1979 A.O. Demuren

LIST OF CONTENTS

		Page No.
ABSTRACT		(i)
PREFACE		(iii)
LIST OF CONTENTS		(vi)
LIST OF TABLES		(x)
LIST OF SYMBOLS		(xii)
1.	INTRODUCTION	1
1.1	The Problem Considered	1
1.2	Practical Relevance	2
1.3	Present Methods of Calculation	4
1.4	Main Results	7
1.5	Outline of the Thesis	10
2.	PAST WORK	11
2.1	Introduction	11
2.2	Buoyant Surface Discharges	11
2.2.1	Theoretical work	11
2.2.2	Experimental investigations	19
2.3	Full-Depth Flows	24
2.3.1	Theoretical work	24
2.3.2	Experimental studies	27
2.4	Status of Existing Information	28
2.5	Concluding Remarks	30
3.	MATHEMATICAL FORMULATION	31
3.1	Introduction	31
3.2	Main Features of the Procedures	31
3.2.1	Statement of the basic assumptions	31
3.2.2	Coordinate system	34
3.2.3	Dependent variable	35
3.2.4	Finite-difference grid	37
3.2.5	Auxiliary information	40
3.3	Governing Equations	41
3.3.1	The partial-differential equations	41
3.3.2	Finite-difference equations	49
3.3.3	Auxiliary information	51

3.4	Solution Procedures	53
3.4.1	Classification of flow types	53
3.4.2	The parabolic case	54
3.4.3	The hyperbolic case	56
3.4.4	The partially-parabolic case	58
3.4.5	Summary	62
3.5	Calculation of Flows with Curvature	62
3.5.1	Rotating-grid system	63
3.5.2	Relevant partial-differential equations	65
3.5.3	Calculation of jet trajectory	67
3.6	Concluding Remarks	69
4.	PREDICTION OF FLOWS WITH ANALYTICAL SOLUTION	70
4.1	Introduction	70
4.2	Uniform Flow in Curved Domains	70
4.2.1	Problem specification	70
4.2.2	Computational details	71
4.2.3	Results and discussion	73
4.3	The Radial Pool Problem	81
4.3.1	Problem specification	81
4.3.2	Computational details	81
4.3.3	Results and discussion	85
4.4	Subcritical Laminar Channel Flow	88
4.4.1	Problem specification	88
4.4.2	Computational details	88
4.4.3	Results and discussion	90
4.5	Concluding Remarks	90
5.	PREDICTION OF HEATED SURFACE DISCHARGES	92
5.1	Introduction	92
5.2	Treatment of Relevant Physical Phenomena	92
5.3	Computational Details	97
5.4	Prediction of Laboratory Discharges into Stagnant Surrouding	99
5.5	Prediction of Laboratory Dishcarges into Moving Ambient Fluid	121
5.5.1	Discharges into coflowing ambients	125
5.5.2	Discharges into crossflowing ambients	130

		Page No.
5.6	Comparison of the Present Predictions with Other Model Predictions	143
5.7	Prediction of Heated Surface Discharges into Natural Waters	149
5.8	Concluding Remarks	153
6.	PREDICTION OF FULL-DEPTH FLOWS	155
6.1	Introduction	155
6.2	Computational Details	155
6.3	Prediction of Supercritical Flows	157
6.3.1	Flows in channel contractions	157
6.3.2	Flow in curved channels	165
6.4	Prediction of Subcritical Flows	168
6.5	Concluding Remarks	172
7.	EXPERIMENTAL INVESTIGATION	174
7.1	Introduction	174
7.2	Experimental Apparatus	175
7.3	Experimental Procedure	180
7.4	Experimental Results	182
7.5	Comparison of Experimental Results with Numerical Predictions	183
7.5.1	Boundary conditions	189
7.5.2	Computational details	193
7.5.3	Results and discussion	194
7.6	Concluding Remarks	206
8.	CONCLUSIONS	209
8.1	Achievements of Present Work	209
8.2	Suggestions for Future Work	210
LIST OF REFERENCES		211
APPENDICES		225
A.	Derivation of the pressure-gradient terms for the momentum equations	225
B.	Derivation of the equations for the local correction of pressure or layer depth	231
C.	Derivation of the equations for the block correction of pressure or layer depth	238

		Page No.
D.	Exact solution of the angle of inclination in the computations of uniform flow in curved domains	240
E.	Analytical solution for the steady flow of a radial pool of warm water above a cold water mass	243
F.	Tabulated experimental data	247

LIST OF TABLES

Table No.	TITLE	Page No.
1.	Comparison of the features of heated surface discharges to open channel flows.	2
2.1	Summary of the parameters investigated in laboratory experimental studies of warm surface jets.	22
2.2	Statement of the analogy between free surface water flow and a compressible gas flow.	25
3.1	Source terms for floating-layer flows.	52
3.2	Source terms for full-depth flows.	52
3.3	Source terms for surface-layer flows with curvature.	66
4.1	Computational details for the uniform-flow calculations.	71
4.2	Computational details for the radial pool problem.	83
4.3	Computational details for subcritical laminar channel flow.	89
5.1	Computational details for the prediction of heated surface discharges.	97
5.2	Discharge parameters for the main comparisons.	99
5.3	Discharge parameters for the other comparisons.	117
5.4	Flow parameters employed in coflow predictions.	125
5.5	Discharge parameters for crossflow experiments.	131
6.1	Computational details for predicting supercritical and subcritical water flows in a contracting channel.	156
6.2	Prediction of wave height and wave angle in a 6^{o} channel contraction.	163
6.3	Prediction of wave height and wave angle in contracting channels at Froude number = 3.86.	165

Table No.	TITLE	Page No.
7.1	Test conditions for experiments.	182
7.2	Computational detals for predicting the experiments.	193

LIST OF SYMBOLS

Symbols	Meaning	Location of first appearance
A	$\equiv zx$.	Appendix E
A,B,C,D	Coefficients of genralised finite-difference equation.	Eqn. (3.3.12)
a	Distance between the centres of the circles forming the boundaries of the flow domain in uniform-flow computations.	Section (4.2.1)
a,b,c,d	Coefficients of generalisted partial-differential equation.	Eqn. (3.3.11)
B	Full width of orifice in the experiment.	Eqn. (7.5.3)
b	Half-width of the layer, at inlet.	Table (4.2)
C	Specific heat capacity of water	Eqn. (3.3.5)
C_f	Shear stress coefficient	Eqn. (5.2.8)
C_P, C_V	Specific heat capacity at constant pressure, and at constant volume, respectively.	Table (2.2)
c	Velocity of sound.	Table (2.2)
D	$\equiv \sqrt{2bz_{IN}}$ characteristic jet diameter.	Eqn. (5.4.3)
δx	Forward step size employed in marching integration.	Table (4.1)
F	Driving force on layer fluid	Table (2.2)
FR,Fr	$\equiv \frac{U}{((\frac{\Delta\rho}{\rho_o})gz^{\frac{1}{2}}}$, the densimetric Froude number.	Table (2.1)
g	Acceleration due to gravity.	Table (2.2)
h	Layer thickness.	Appendix A
K	Empirical constant employed in mixing length formula.	Eqn. (6.4.2)
ℓm	Turbulent mixing length.	Eqn. (6.4.1)
$\dot{m}''_h$	Lateral entrainment across grid lines, per unit area.	Eqn. (3.2.2)
$\dot{m}''_V$	Vertical entrainment of ambient fluid, per unit area.	Eqn. (3.2.2)

Symbols	Meaning	Location of first appearance
N	Number of cross-stream grid points.	Table (4.1)
P	Pressure.	Table (2.2)
Q	Heat transfer rate.	Eqn. (5.2.7)
R	Radial distance from grid node to a specified origin, or radius of curvature of grid line.	Eqn. (3.5.1)
Re	Reynolds number.	Table (2.1)
Ri	$\equiv \frac{1}{Fr^2}$, the overall Richardson number.	Eqn. (2.1)
s∿n	Natural or rotating-grid.	
S_ϕ	Source term in transport equation for ϕ.	Eqn. (3.3.11)
T	Temperature.	Table (2.2)
U,V	Longitudinal and lateral velocities.	Eqn. (2.1)
x,y	Cartesian coordinates.	Section (3.2.1)
z	Depth or thickness of the layer.	Table (2.2)

Greek Symbols	Meaning	Location of first appearance
α	Surface heat transfer coefficient.	Eqn. (3.3.5)
α	Angle between ω-grid line and the main flow direction.	Eqn. (3.4.9)
β	Volumetric expansion coefficient.	Eqn. (5.2.9)
Γ_ϕ	Transport property for ϕ.	Eqn. (3.3.5)
γ	C_P/C_V.	Table (2.2)
ε_P	Kinematic compatibility error.	Appendix B
θ	Angle of inclination of the ω-grid lines.	Eqn. (3.5.6)
λ	$\equiv \frac{\Delta\rho}{\rho_o} g$.	Eqn. (4.3.1)
μ	Viscosity.	Eqn. (3.3.2)
ρ	Density.	Table (2.2)
σ	Root mean square deviation.	Eqn. (7.5.5)
τ	Shear stress.	Eqn. (5.2.8)
ϕ	Generalised fluid property.	Eqn. (3.3.11)

Greek Symbols	Meaning	Location of first appearance
ψ	Stream function.	Eqn. (3.2.1)
ω	$\equiv \frac{\psi - \psi_I}{\psi_E - \psi_I}$, the normalised stream function.	Section (3.2.2)

Subscripts	Meaning	Location of first appearance
C_L	Centre-line condition.	Eqn. (3.3.16)
E	Condition along the E (external) boundary.	Fig. (3.2)
eq	Equilibrium condition.	Eqn. (3.3.5)
I	Condition along the I (internal) boundary.	Fig. (3.2)
IN	Initial condition.	Table (2.2)
i	Property value of the i^{th} control volume.	Fig. (3.2)
m	Vertical-average value.	Eqn. (2.1)
o	Supporting mass property.	Eqn. (3.3.5)
P	Condition at current plane, used in linearised source term.	Eqn. (3.3.16)
u,d	Upstream, downstream conditions.	Eqn. (3.2.3)

Superscripts	Meaning	Location of first appearance
*	Guess property value.	Eqn. (3.4.6)
'	Correction to guess value.	Eqn. (3.4.11)
''	Per unit area.	Table (2.2)
'''	Per unit volume.	Appendix A
—	Average value.	Eqn. (3.4.14)
U,V,T	Denotes coefficient of finite-difference equations for the respective variable.	Eqns. (3.4.1) - (3.4.3)

CHAPTER 1

INTRODUCTION

1.1 The Problem Considered

The advent of fast and large digital computers has led in the last decade to the development of many numerical methods for solving various engineering problems, which could only be investigated analytically or experimentally, in the past. In Europe and America, concern for environmental pollution due to thermal effluents from power stations has led to the introduction of stringent conditions for thermal discharges into natural waters. The discharge may be through a single-port or multi-port, submerged or surface outlet, depending on the receiving water body, local conditions and regulations. In the present study, only single-port, surface discharges are considered. A similarity exists between this flow and that of a shallow layer of uniform density liquid with a free surface. While the former is characterised by the densimetric Froude number, which is the ratio of the inertia to the buoyancy forces, the latter is characterised by the Froude number, which is the ratio of the inertia to the gravitational forces.

The basic similarities and differences of these two flow situations are summarised in Table 1 below:

Table 1: Comparison of the features of heated surface discharges to open channel flows.

Heated Surface Discharge	"Open-Channel" Flow
• Characterised by densimetric Froude number $\equiv \frac{\text{Inertial Force}}{\text{Buoyancy Force}}$.	• Characterised by Froude number $\equiv \frac{\text{Inertial Force}}{\text{Gravitational Force}}$.
• Supported by heavier liquid mass.	• Supported by solid mass.
• Vertical and horizontal mixing usually present.	• No mixing present.
• Interfacial friction may be important.	• Bottom friction important.
• Flow curvature is produced by cross-flowing ambient fluid or wind.	• Flow curvature is produced by curved channel walls.

The present study describes the application of a finite-difference solution procedure to the partial-differential equations governing the steady, two-dimensional flow and heat transfer of surface layers having a predominant flow direction along which there is no flow reversal.

1.2 Practical Relevance

The efficiency of most thermal power stations is between 30-40%, hence, about two-thirds of the energy in the fuel

is lost as waste heat, which must be disposed of. Water is the most commonly used cooling medium. The discharged cooling water is, in turn, cooled by mixing with the ambient fluid and by heat transfer to the atmosphere through the processes of evaporation, conduction and radiation. Submerged discharges undergo rapid mixing with ambient fluid, so that when the plume water finally rises to the water surface through the action of buoyancy forces, its temperature is very close to ambient and very little heat transfer to the atmosphere takes place. Surface discharges, on the other hand, undergo less mixing with the ambient fluid; with buoyancy forces limiting vertical mixing and increasing lateral spreading of the plume water. The much larger surface area and the higher relative temperatures of the plume result in a higher rate of heat transfer to the atmosphere. For discharges into a stagnant ambient reservoir, cooling ultimately takes place only through the water surface, hence, surface discharges would be prefered to submerged ones, unless local regulations dictated otherwise. Knowledge of the thermal impact of the discharged cooling water on the receiving water body is sought not only for ecological reasons or in compliance with local regulations but also to enable the correct siting of the cooling-water intake port, so that the discharged warm water is not being recirculated through the plant.

The use of hydraulic models is tedious and expensive. There is also the disadvantage that in order to satisfy the requirements of the relevant dimensionless parameters such as Reynolds and Froude numbers, in the laboratory, it is

often necessary to use distorted scales. The development of numerical models which are computationally cheap and easy to use is therefore useful for the design of cooling-water systems for power stations.

"Open-channel" flows occur in many man-made canals and channels, and in shallow rivers. The development of numerical models for computing these flows would help the design of the former. Such models could also be used to predict the dispersion of heated discharges into shallow fast-flowing rivers: on the discharge side of the river, the water is fully mixed and remains attached to the river bank and bottom a long way downstream.

1.3 Present Methods of Calculation

The present methods of calculation are developed for the prediction of steady, two-dimensional surface-layer flows with a predominant flow direction in which recirculation zones are absent. The two dimensions in which variations of flow variables are considered are the two horizontal directions; vertical variations within the layer being neglected. Figure 1 illustrates a typical flow situation of a warm surface layer discharged into a cold stagnant ambient fluid. However, the depth of the layer could vary in both horizontal directions. The non-linear partial-differential equations governing the transport of mass, momentum and heat within the surface layer are solved by finite-difference calculation procedures. The same set of equations is solved by three slightly different solution schemes, depending on the relative importance of the gravitational or buoyancy terms.

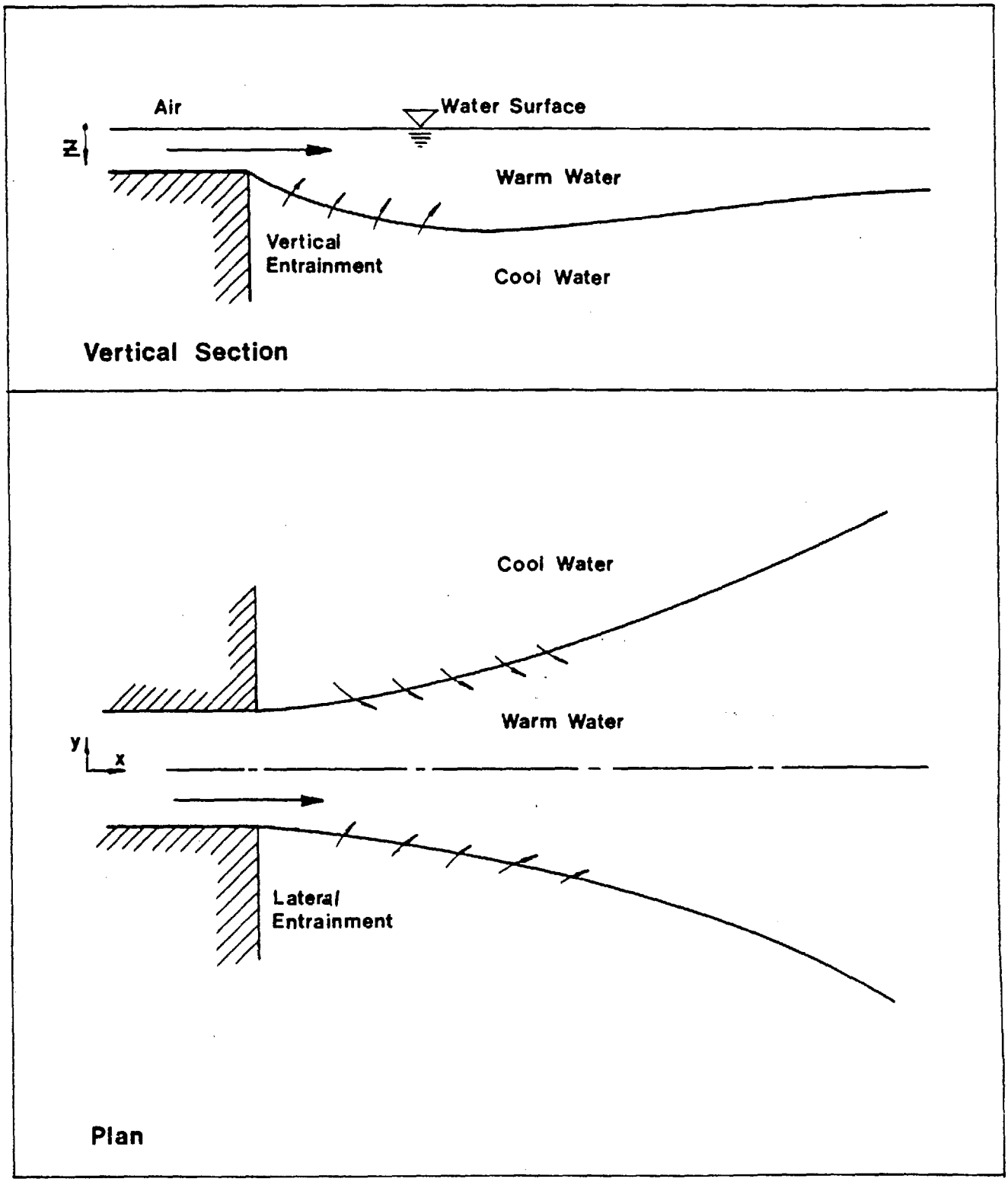


Fig.1: Warm Surface Layer Flowing Above Stagnant Ambient Fluid

When the gravitational terms are absent or negligible, the pressure is uniform everywhere and a "parabolic" solution procedure is used. All influences travel downstream in the main flow direction, and the equations of momentum and heat are solved in a downstreamwise marching-integration manner. This occurs mainly in uniform-flow situations. When the gravitational effects are less in magnitude than the inertia effects, the equations form a hyperbolic set, and a "hyperbolic" solution procedure is employed. In this case, the pressure terms are important and an extra equation needs to be solved to obtain them. However, the pressure influences can travel only downstream, hence, the"downstreamwise" marching-integration process is still used. This case applies to supercritical flow situations. When the gravitational terms are greater than the inertial terms, the equations form an elliptic set, and a "partially-parabolic" solution procedure is used to solve them. In this case, influences from downstream are transmitted upstream solely through the pressures. To allow these pressure influences to propagate upstream, a repeated "downstreamwise" marching-integration process is employed. This applies to subcritical flow situations.

The calculations are performed with computer codes based on GENMIX (A General Computer Program for Two-Dimensional Parabolic Phenomena), by Spalding (1978). The "parabolic" code is obtained by adapting GENMIX for layer flow computations. On the incorporation of a two-dimensional version of the SIMPLE (Semi Implicit Method for Pressure-Linked Equations) algorithm, by Patankar and Spalding (1972), in the

"parabolic" code, the "hyperbolic" code is obtained. In these two codes, all the flow variables are stored at two cross-sections only (the upstream and downstream sections), and a single sweep, in the main flow direction, of a marching-integration procedure is employed. The "partially-parabolic" code is obtained by extending the "hyperbolic" code to enable the whole two-dimensional pressure field to be stored, and several sweeps of the marching-integration process to be made in arriving at the solution.

For the calculation of flows with strong curvature, the non-linear partial-differential equations, containing curvature terms, are employed with a "rotating-grid" system. These are simply incorporated into the relevant computer code.

1.4 Main Results

The main objective of the present study is to develop fairly general numerical procedures for predicting surface-layer flows. The main requirement is that the procedures should be accurate, simple to use and computationally cheap. An experimental investigation was carried out to supplement the data, available in the literature, on supercritical open-channel flows suitable for validating the hyperbolic procedure.

The theoretical investigation comprised of:

(a) The prediction of three types of flow problems with analytical solutions.

(b) Comparison of present numerical predictions with experimental results of laboratory discharges of warm water into both stagnant and moving ambient fluid.

(c) A parametric study to show effects of:- discharge-to-ambient fluid-velocity ratio, Froude number and aspect ratio, on:- the temperature, velocity and depth of a heated surface layer discharged into a coflowing stream.

(d) Comparison of present numerical predictions with field measurements of heated surface discharges into natural waters.

(e) Comparison of present predictions with theoretical predictions by other authors.

(f) Comparison of present predictions with experimental results, and in some cases, predictions using the method of characteristics, for various prismatic open channel flows.

(g) Comparison of the present predictions with measurements from the present experiments.

The main achievements of the present study, and the conclusions thereof, are:

(i) All the comparisons of the present predictions with analytical solutions are very good. These show that the numerical procedures are mathematically accurate.

(ii) Comparison of the present predictions with experimental results of laboratory discharges into stagnant surroundings shows fairly good agreement. The numerical

method can therefore be used with some confidence in predicting heated surface discharges into stagnant ambients.

(iii) Comparison of the present predictions with experimental results of laboratory discharges into cross-flowing ambient fluid shows satisfactory agreement.

(iv) The parametric study of heated surface discharges into coflowing ambient fluid shows that the discharge-to-ambient fluid-velocity ratio has the most prominent effect on the layer-fluid properties, the aspect ratio having the least effect. Faster temperature decays are predicted, the further the value of the velocity ratio is from unity and the lower the Froude number is.

(v) The comparisons of the present predictions with field measurements of heated surface discharges into natural waters show that too rapid temperature decays are predicted. The empirical relations, derived from laboratory data, with which the ambient fluid entrainment and layer spreading are modelled may not be applicable to the prediction of the field data.

(vi) Comparison of the present predictions with predictions by other authors, of some laboratory data on heated surface discharges, shows that the present predictions are at least as good as the others.

(vii) The present model predicted the experimental data by other authors of supercritical flows in open channels fairly well, the predictions being comparable to those with the method of characteristics.

(viii) The present experimental data are fairly well predicted. The present numerical model may therefore be used confidently in predicting supercritical flows in open channels, so long as vertical accelerations are negligible.

1.5 Outline of the Thesis

The thesis so far contains the introductory material. The rest of the thesis is laid out as follows. Chapter 2 contains a review of the past work. The mathematical basis of the present work and the solution procedures are described in Chapter 3. Three types of flows with analytical solutions are predicted in Chapter 4. Chapter 5 contains the predictions of various heated surface discharges. The predictions of open channel flows are presented in Chapter 6. The experimental investigation is reported in Chapter 7. Concluding remarks are made in Chapter 8; the achievements of the present study are stated, and some suggestions for future work are made. This concludes the main part of the thesis.

A list of references and the appendices form the last part of the thesis.

CHAPTER 2

PAST WORK

2.1 Introduction

In this chapter, previous works on surface-layer flows are briefly reviewed. Floating-layer flow studies are first reviewed. These are mostly of surface thermal discharges, though there are one or two of fresh water flows above heavier saline water. The second part of the chapter contains a review of investigations of full-depth flows. To conclude the chapter, comments are made on the status of the existing information.

2.2 Buoyant Surface Discharges

So many theoretical and experimental investigations of surface thermal discharges have been carried out in the last decade that it is not intended to review them all here. Many of these are extensively reviewed by Parker and Knenkel (1970), Jirka, Abraham and Harleman (1975), and Dunn, Policastro and Paddock (1975). The last contains quite detailed information on many of the major studies. In the present review, the effort will be concentrated on the studies that are representative of the various approaches, and on the most recent works.

2.2.1 Theoretical work

Theoretical work on buoyant surface flows can be broadly divided into four categories.

(i) Dimensional Analysis

In the first category are those methods of analysis which use dimensional arguments coupled with order-of-magnitude force balances to determine the behaviour of the surface layer.

Fay (1969) deduced order-of-magnitude estimates of the rates of spread of oil, issuing from a finite source, on still water, and of oil, issuing from a steady source onto a moving stream. In both cases, three spreading regimes were recognised, depending on the following force-balances: gravity∿inertia, gravity∿viscous, surface-tension∿viscous. Hoult (1972) discussed Fay's results and showed how they could be obtained from similarity solutions of the equations of motion. He also compared the results with experimental data, showing fair agreement. Kao (1977) obtained similar results for the first spreading regime, but suggested that the appropriate balance of forces was buoyancy∿form-drag. Sharp (1969) and Anwar (1970) investigated the surface spreading of a jet of fresh water discharged horizontally, at depth, into saline water. Chen and List (1976) considered the surface spreading of a buoyant fluid discharged vertically into a stagnant ambient fluid. They showed that the first regime of surface spreading is dominated by a buoyancy∿inertia force balance, and the second by a buoyancy∿friction force-balance. They predicted rates of spread of the surface layer which agreed well with experimental data.

(ii) Semi-empirical Correlation Methods

The second method of analysis of surface-layer flows depends largely on the correlation of experimental and field data. Jet characteristics, such as temperature decay, surface isotherm area, vertical and lateral spread rates, and centre-line trajectory are correlated with flow parameters, such as initial densimetric Froude number, discharge aspect ratio, and discharge to ambient velocity ratio.

Relying heavily on data from various hydraulic and field studies, Pritchard (1971) developed a solution scheme for surface thermal discharges. The model makes the following assumptions: linear lateral spread, linear vertical spread up to a given depth after which the depth remained constant, temperature decay proportional to the inverse square root of the distance from outfall, and bullet-shaped isotherms. The model is simple to use, and its application by Dunn et al (1975) to some field data showed that correct trends were predicted.* With the aid of more hydraulic data by Carter et al (1973), (1974), Pritchard (1973) extended his first model to account for effects of crossflow and bottom interaction.

Shirazi (1973) performed a multiple regression analysis of eleven data sets from hydraulic and field studies to produce functional forms of the temperature decay, jet half-widths and jet half-depths. He assumed power-law expressions for the functional forms, and the data sets were divided into three categories: discharges into stagnant ambients with

*Note: Some of the field data was used in calibrating the model.

no bottom effects, discharges into stagnant ambients with bottom effects, discharges into moving ambients. The results were also presented in graphical form.

Pande and Rajaratnam (1977) studied surface thermal discharges of moderate to high Richardson numbers in the laboratory. They correlated the temperature and velocity decays, the temperature and velocity half-widths and half-depths, with the initial Richardson number and the longitudinal distance from the outfall. They showed that, for the range of Richardson numbers (0.15 - 1.14), the temperature field spread laterally about 1.9 times as rapidly as the velocity field, while the vertical spread of the temperature field was only 1.1 times that of the velocity field.

(iii) Integral Methods

Most of the mathematical models developed for predicting surface thermal discharges are of the integral type. Lateral and vertical profiles are assumed for the longitudinal velocity and the temperature, based on intuition or experimental data. The partial-differential equations of motion and heat are thus reduced to ordinary-differential ones, which are then solved analytically or numerically. Many physical phenomena, such as entrainment of ambient fluid, surface heat transfer, wind effects, crossflow interaction, and lateral spreading are simulated by the use of empirical relations.

Hayashi and Shuto (1967), in their analysis of warm surface jets, neglected all the terms of the momentum equations

except the diffusion and pressure terms. These equations were further simplified by the assumption of self-similar profiles for the temperature and velocities, and the neglect of vertical entrainment. The resulting equations were then solved analytically. Model predictions were compared with experimental data, but the agreement was poor. Motz and Benedict (1970) developed a two-dimensional steady-state model for a buoyant surface jet in crossflow. The partial-differential equations of mass, motion and heat were reduced to ordinary-differential ones, by the assumption of gaussian profiles for the horizontal variations of velocity and temperature, and by neglecting all vertical variations, vertical entrainment and buoyancy effects. The resulting equations were solved with a fourth-order Runge-Kutta scheme.

Koh (1971) analysed the two-dimensional (longitudinal and vertical directions) warm surface jet. He divided the jet into four zones: zone of flow establishment; supercritical jet-like zone; transition zone with an internal hydraulic jump; subcritical zone. He assumed, firstly that vertical entrainment was given by an empirical relation due to Ellison and Turner (1959), secondly that a similarity existed between the velocity and temperature profiles, and lastly that the jet was affected by a combination of surface heat loss and interfacial shear. By performing an order-of-magnitude analysis to determine the relative importance of the heat loss and interfacial-shear terms he obtained separate solutions for the supercritical and subcritical zones. He then proposed methods for determining which zones are present, in any flow, and for linking the solutions of the different zones.

Stolzenbach and Harleman (1971), Prych (1972), Stefan (1972), and Shirazi and Davis (1974) developed three-dimensional steady-state integral models for heated surface discharges. All these formulations used the assumption of self-similarity of temperature and velocity profiles in the main jet region, to reduce the equations of motion and heat to a set of coupled non-linear ordinary differential equations which were then solved numerically. Although, they considered that the jet was affected by more or less the same physical phenomena, there were variations in their treatments of these.

For example, Stefan, Prych, and Shirazi and Davis treated the jet in crossflow as a solid body with a drag force acting on it in a direction normal to its axis, while Stolzenbach and Harleman supposed that the effect of the crossflow was to produce an entrainment force which tended to turn the jet in the direction of the ambient flow. Stolzenbach and Harleman divided the jet into four regions, in the zone of flow establishment, providing a solution for each region which was then matched to the solutions of the other regions. Prych used information from non-buoyant jet analysis to determine the length of this zone, whilst Shirazi and Davis based their treatment on results from hydraulic studies. Stefan, on the other hand, did not treat this zone differently from the rest of the jet.

Pande and Rajaratnam (1975a) used an order of magnitude analysis of the equations of motion to divide surface buoyant flows into 3 classes: low, moderate and high Richardson numbers. For each class of flow, the equations

were reduced to their integral forms, and a similarity analysis was used to predict the manner of variations of the parameters characterising the temperature and velocity fields.

A notable criticism of integral models is the assumption of self-similar profiles for velocities and temperature in highly-buoyant jets, or jets in crossflow. Experimental data by Pande and Rajaratnam (1975b) and Carter (1969) suggest that this is inappropriate.

(iv) Numerical Models

The numerical methods of predicting surface thermal discharges are the most general ones. Suitably modified forms of the partial-differential equations governing the transport of mass, momentum and heat are solved by finite-difference or finite-element techniques. Turbulence models with varying levels of sophistication are required for the closure of the equation set. At the lower level, empirically determined constants are used, whilst the more sophisticated models require the solution of partial-differential equations. Many of these turbulence models are reviewed by Launder and Spalding (1972).

Brady and Geyer (1972) developed an unsteady three-dimensional numerical model for the prediction of buoyant surface discharges. The coupled non-linear partial-differential equations of mass, momentum and heat were solved with a finite-difference scheme. Prandtl's mixing-length model of turbulence was used. The model was applied to a river

discharge, but excessive computational-time requirement limited the computation to only 4 minutes of discharge time. England and Taft (1973) developed a similar model, but solved a further differential equation, for the turbulent kinetic energy, and calculated the length scale from mean turbulent flow characteristics. Calculation with this code for a 52 x 27 x 4 grid required 4 hours of central processor time on the Univac 1108 for a steady-state solution. Similar models were also developed by Waldrop and Farmer (1974), and Paul and Lick (1974).

Till (1974) developed a steady, parabolic, three-dimensional model for predicting heat dispersion in rivers. The whole flow domain was divided into rectangular subchannels laid out in the main flow direction. At each cross-section, the net flow of mass, momentum and heat into each subchannel was balanced against the rate of change of the corresponding property within the subchannel. An ordinary-differential equation was obtained for each variable in each subchannel, and the resulting set of coupled ordinary-differential equations was solved with an Euler predictor-corrector scheme. Comparison of model predictions with field data resulted in poor agreement.

Chien and Schetz (1975) developed a steady three-dimensional numerical model in which seven partial-differential equations, (three for vorticities, three for velocities and one for temperature) were solved using a finite-difference method. A constant eddy-viscosity turbulence model was used. Comparison of the prediction to some laboratory data showed fair agreement.

McGuirk and Spalding (1975) predicted the turbulent flow and heat transfer of buoyant jets in coflowing streams. In addition to the three equations of motion and the temperature equation, two partial-differential equations were solved for the turbulent kinetic energy and its dissipation rate. Six empirically determined constants were used to achieve closure, but these are fairly universal; having being successfully applied to many flow problems. The model was also applied to river flows with irregular boundaries. McGuirk and Rodi (1976) extended this model by including buoyancy terms in the turbulent kinetic energy equation. The turbulence model was also applied by Hossain and Rodi (1976) to predict the influence of buoyancy on turbulence intensities in two-dimensional surface jets.

2.2.2 Experimental investigations

Numerous experimental investigations of floating-layer flows have been carried out in the laboratory. There have also been quite a few field measurements of prototype flows, though the latter are quite difficult and expensive to make. The laboratory studies are reviewed in the first part of this section, and the field studies in the second part.

(i) Laboratory Studies

Ellison and Turner (1959) performed experiments with a two-dimensional surface layer of fresh water flowing above stagnant saline water. They measured the rate of entrainment of saline water into the fresh-water layer, and found that this entrainment rate was negligible if the overall

Richardson number, (Ri) was greater than about 0.85. However, Ellison and Turner had some difficulty in obtaining steady flow, with a well-defined layer existing only for a few minutes. This was probably due to their not replenishing the lower layer with saline water at the same rate as it was being entrained into the fresh-water layer.

Chu and Vanvari (1974), (1976) performed similar experiments, taking care to replenish the lower layer with saline water at the same rate as it was being entrained into the upper fresh-water layer. Their experimental conditions were such that the whole surface-layer flow was supercritical. According to their measurements, entrainment of saline water into the fresh-water layer was negligible above a Richardson number of about 0.15. An entrainment relation of the form:

$$\frac{V_e}{U_m} = 0.048e^{-12.5Ri} \qquad ,(2.1)$$

could be used to represent their data, whilst Ellison and Turner data could be represented by a relation of the form:

$$\frac{V_e}{U_m} = 0.075e^{-5Ri} \qquad ,(2.2)$$

where, V_e is the entrainment velocity,

U_m is the average velocity of the layer,

and, Ri is the overall Richardson number.

Hansen (1975) performed similar experiments at much higher Richardson numbers (1-4), and his finding, in contrast to that of the previous authors, was that there was still some entrainment of saline water, (though small in magnitude) into the surface layer at these high Richardson numbers.

Chu and Baddour (1975) investigated the transition from supercritical to subcritical layer flow by incorporating a sloping floor into the original apparatus of Chu and Vanvari. The position of the internal hydraulic jump was moved backwards and forwards by varying the slope of this floor. Wilkinson and Wood (1971) carried out similar experiments, but with warm water flowing above cold stagnant water. They showed the importance of the down-stream control in determining whether a supercritical, or subcritical layer flow, or a mixture of the two was obtained.

Laboratory studies of three-dimensional buoyant surface jets have been performed by Jen et al (1966), Hayashi and Shuto (1967), Tamai et al (1969), Stolzenbach and Harleman (1971), Carter (1969), Carter et al (1973), Carter et al (1974), Kuhlman and Prahl (1974), Stefan et al (1975), Koester (1974), Pande and Rajaratnam (1975b), and Wiuff (1978). These are mainly experiments of heated surface discharges into stagnant or crossflowing ambients.

Table 2.1 provides a summary of the range of parameters investigated in these experimental studies.

Table 2.1: Summary of the parameters investigated in laboratory experimental studies of warm surface jets.

NO	INITIAL FROUDE NUMBER (Fr)	INITIAL ASPECT RATIO (A.R.)	AMBIENT TO JET VELOCITY RATIO, $(\frac{U_o}{U_{IN}})$	INITIAL JET REYNOLDS NUMBER (Re)	AUTHORS
1	5.0∿ 50.0	4∿ 10	0	7×10^2∿ 9.3×10^4	JEN, MOBAREK AND WIEGEL (1966)
2	1.4∿ 16.1	1	0	3∿5.6 $\times10^3$	HAYASHI AND SHUTO (1967)
3	2.4∿ 11.3	1	0	5.6×10^3∿ 2.1×10^4	TAMAI AND WIEGEL (1969)
4	0.58∿ 11.6	0.35∿ 5.8	0∿ 0.40	7×10^3∿ 1.5×10^4	STOLZENBACH AND HARLEMAN (1971)
5	4.0∿ 25.2	.09∿ 2.08	.11∿ .86	2.5×10^3∿ 25.6×10^4	CARTER (1969) CARTER et al (1973), (1974)
6	0.17∿ 1.97	0.45∿ 3.75	0.2∿ 2.0	5×10^2∿ 2.5×10^3	KUHLMAN AND PRAHL (1974)
7	2∿ 15	1∿ 9.6	0∿ 0.41	6.5×10^3∿ 3.0×10^4	STEFAN, BERGSTEDT AND MROSLA (1975)
8	4.8∿ 15.7	1	0∿ 0.07	7.9×10^3∿ 1.2×10^4	KOESTER (1974)
9	0.94∿ 2.6	1.0∿ 3.06	0	7.0×10^3∿ 7.8×10^3	PANDE AND RAJARATNAM (1975b)
10	3.6	1.40	0	3.3×10^4	WIUFF (1978), (1977)

Comments:

(1) Stefan et al made detailed measurements of the velocity and temperature fields in the initial zone of the jet; the zone of flow establishment.

(2) Kuhlman and Prahl studied discharges with low densimetric Froude numbers. They observed an intrusion of cold water into the discharge channel, in discharges with densimetric Froude Numbers less than 1, such that the actual layer flow condition was critical (Froude number = 1) at exit. This agrees with the earlier observation of Harleman (1961). Instabilities of the Kelvin-Helmholtz type were also observed in discharges with densimetric Froude numbers less than about 0.56.

(3) Pande and Rajaratnam made detailed measurements of the velocity and temperature fields in both the horizontal and vertical directions.

(ii) Field Studies

Several field measurements of thermal plumes, resulting from cooling-water discharges from power stations into natural waters have been carried out in recent years. Frigo and Frye (1972) and Dunn et al (1975) reviewed many field studies of thermal plumes from five different power stations discharging into Lake Michigan, U.S.A. Dinelli (1975) presented results of infra-red surveys and in situ measurements of thermal discharges into the Vado Ligure Bay and the Torvaldaligo Coast in Italy. Fang et al (1975) and Rota et al (1973) have reported studies of thermal discharges into

the James River, U.S.A., and the Po River, Italy, respectively. Weil (1974) analysed the results of several field measurements of the thermal discharges of the Oskarshamnsverket Power plant, in Sweden, into the Baltic Sea.

Dunn et al (1975), observed that a feature common to most of these measurements was their doubtful level of reliability. This would limit their suitability to test the accuracy and predictive capabilities of theoretical models.

2.3 Full-Depth Flows

Theoretical and experimental studies of full-depth flows are discussed in this section. Specifically, works on the flow of water in open channels and of heated discharges into shallow rivers in which the river and plume waters are fully-mixed vertically, are reviewed.

2.3.1 Theoretical work

By applying the conservation of energy principle, Chow (1959) analysed various steady, one-dimensional open channel flows. He presented the various surface profiles obtainable in these flows. Water flows in channels with varying cross-sections or curvature would in general, require two- or three-dimensional analyses. These methods of analysis would depend on whether the flow is supercritical or subcritical.

Analysis of supercritical flows in open channels was first carried out in detail by Preiswerk (1940), using the method of characteristics developed by Busemann (1931) for

supersonic gas flow computations. The analogy between free surface water flows and compressible gas flows was pointed out by Prandtl (1931), Riabouchinsky (1932) and Von Karman (1938). The analogy may be described as shown in Table 2.2.

Table 2.2: Statement of the analogy between free surface water flow and a compressible gas flow.

	Two-dimensional compressible gas flow	Free-surface liquid flow
Medium	Gas with γ ($\equiv \frac{C_p}{C_v}$) = 2	Incompressible fluid like water
Equivalent quantities	Velocity ratio, $\frac{U}{U_{IN}}$	Velocity ratio, $\frac{U}{U_{IN}}$
	Temperature ratio, $\frac{T}{T_{IN}}$	Water depth ratio, $\frac{z}{z_{IN}}$
	Density ratio, $\frac{\rho}{\rho_{IN}}$	Water depth ratio, $\frac{z}{z_{IN}}$
	Pressure ratio, $\frac{P}{P_{IN}}$	Square of water depth ratio, $(\frac{z}{z_{IN}})^2$
	Pressure ratio, $\frac{P}{P_{IN}}$	Ratio of driving force per unit area $\frac{F''}{F''_{IN}}$
	Velocity of sound, C	Wave velocity, $\sqrt{gz}$
	Mach number, $\frac{U}{C}$	Froude number, $\frac{U}{\sqrt{gz}}$
	Supersonic flow	Supercritical flow
	Subsonic flow	Subcritical flow
	Shock waves	Hydraulic jumps

Busemann's method was applied by Ippen (1949), Rouse et al (1949), and Ippen and Dawson (1949) to calculate the hydraulic jumps produced in supercritical water flows in channels with varying cross-section.

In the presence of pressure forces due to surface elevation, or recirculation zones, subcritical flows in open channels are elliptic; otherwise they are parabolic. Some methods of analysing the two-dimensional flows are presented by Schlicting (1968). The 2/E/FIX computer code of Pun and Spalding has also been used. These methods neglect the effects of secondary velocities, which have been observed by Thompson (1876) and Nikuradse (1926) to be present in open-channel flows. These secondary velocities are especially strong in flows in curved channels, hence a complete analysis of such flows must be three dimensional. The secondary flows in closed, straight channels have been calculated by Tatchell (1975) and Ramachandra and Spalding (1976), employing three-dimensional numerical procedures, with the k and ε turbulence model. Mockmore (1943) and Shurky (1949) analysed open-channel flows in curved channels by assuming that the distributions of the secondary velocities were known, they then applied free-vortex theory to obtain the surface profiles and the primary velocities.

Thermal discharges into shallow rivers in which the heated water is attached to the river bottom may be regarded as open-channel flows with heat transfer. For river flows that are fully mixed laterally as well as vertically, one-dimensional analyses have been performed by Harleman (1972),

and Paily et al (1974). However, most rivers with heated discharges have been observed to be vertically fully-mixed but with lateral variations of temperature: a two-dimensional analysis is therefore essential. The integral approach of Abramovich (1963) was applied by Dunn et al (1975) in predicting such a river discharge. McGuirk and Rodi (1978), and Rastogi and Rodi (1978) applied, two-dimensional and three-dimensional numerical procedures to predict heated discharges into shallow channels. In the latter paper, the predictions with the two- and three-dimensional procedures coincided for discharges with Froude numbers greater than about 5, showing the absence of buoyancy forces which stratify the flow thereby making it three dimensional.

2.3.2 Experimental studies

Preiswerk (1940) carried out systematic measurements of surface profiles in supercritical water flow of varying flow rates through a Laval nozzle designed for a Froude number of 2.

Experimental measurements of surface profiles in both supercritical and subcritical water flows through channels with straight-wall and curved-wall contractions were carried out by Ippen and Dawson (1949). Rouse et al (1949) presented surface profiles of measurements in supercritical flows through channels with both gradual and abrupt expansions. Arumugam (1955) performed similar experiments in a channel with an abrupt expansion on one side and a wall of varying angle on the other. Measurements of supercritical flow in curved channels were made by Knapp (1949).

Mockmore (1943), Shurky (1949) and Choudhary (1977) all made measurements of the velocity distribution and surface elevation in subcritical water flows in strongly-curved open channels. Shurky's measurements show that, the strength of the secondary flow decreased with increase in the radius of curvature, the aspect ratio of the channel, and the Reynolds number of the flow.

2.4 Status of Existing Information

The status of the existing information on surface-layer flows resulting from theoretical and experimental investigations may be summarised as follows:

(1) There exist detailed and reliable laboratory experimental data, on the discharge of heated water at the surface of a deep stagnant pool, that could be used to validate mathematical models.

(2) Experimental studies of heated surface discharges into moving ambient fluid are not sufficiently detailed to allow adequate comparisons with mathematical models to be carried out.

(3) Field studies of discharges from power stations into natural waters, though numerous, are not as reliable as the laboratory experiments. This is due, in part, to the difficulty of monitoring changing environmental conditions and of taking detailed measurements over a wide area. While qualitative comparisons of model predictions with field data are desirable, no definite conclusions could be drawn from quantitative comparisons until more reliable data are available.

(4) Experimental studies of open channel flows are sufficiently detailed to give an insight into the behaviour of supercritical or subcritical flows in various types of channels. Only a few general mathematical methods of analysis exist.

(5) Semi-empirical correlation methods of analysing heated surface discharges are cheap and simple to use, providing general estimates of mean plume behaviour. They suffer from a lack of generality and the inability to provide much detail of plume characteristics. However, the advantage of their simplicity may be overriding.

(6) Most mathematical models developed for predicting the dispersion of heated surface discharges are of the integral type. They have fair realism, and have been used successfully to predict many laboratory discharges. Their main limitation is the need to assume self-similarity of lateral velocity and temperature profiles, which may not often exist in real discharges.

(7) Numerical models which solve the partial-differential equations of motion, mass and heat by finite-difference procedures have been successfully used to predict many surface-layer flows. Models of the steady two-dimensional, parabolic or elliptic types, and the three-dimensional parabolic types are the most adequately developed and tested. High computational costs have hindered the development and application of three-dimensional elliptic or three-dimensional unsteady models to surface-layer flows.

(8) In a course of lectures on the Transfer of Heat In Rivers, Bays, Lakes and Estuaries, (THIRBLE), Spalding (1975) discussed the various problems involved in assessing the environmental impact of energy production. Many physical phenomena of importance are considered and some methods of modelling these are proposed. The mathematical methods of analysis are classified as to their dimensionality and similarity of approach. In one such class are two-dimensional layer models to which the present study belongs. Spalding (1977) gave a detailed analysis of these models.

2.5 Concluding Remarks

In this chapter, theoretical and experimental studies of surface-layer flows were reviewed. Floating-layer flows were reviewed first; and then full-depth flows. Whilst numerous mathematical models exist for predicting surface-layer flows, the need is for computationally cheap and fairly general and accurate procedures that could be used for parametric studies and design.

The introductory part of this thesis is now complete.

CHAPTER 3

MATHEMATICAL FORMULATION

3.1 Introduction

This chapter contains information on the mathematical basis of the work reported in this thesis. The main features of the model are discussed in the first section. Then follows the description of the governing partial-differential equations and their discretization into finite-difference equations. The solution procedures are discussed in the context of the class of flow: whether parabolic, hyperbolic or partially-parabolic. Finally, extensions for dealing with flows with curvature are given.

3.2 Main Features of the Procedures

3.2.1 Statement of the basic assumptions

(1) It is supposed that the buoyant surface-layer flow is that of warm water discharged steadily at or near the surface of a stagnant or steadily-flowing stream.

(2) The warm water flow must have a predominant direction in which the velocity components are positive, and large in comparison to the velocity components in the transverse direction.

(3) It is assumed that the vertical profiles consist of a nearly uniform higher temperature region near the surface, a lower region in which the temperature is that of the

undisturbed stream, and a very thin intermediate region of steep temperature gradient. The first region is the so-called layer: the horizontal velocity components are supposed to have vertical profiles of corresponding shape. Figure 3.1 shows the assumed profiles.

(4) The layer conditions are thus characterised by the following two-dimensional variables:

$$T(x,y);\quad U(x,y);\quad V(x,y);\quad \text{and } z(x,y).$$

(5) In the floating-layer flow, the top surface is assumed flat, and any variations in the layer depth occur at the lower surface; i.e., the rigid-lid approximation is made. However, in the full-depth flow, both the levels of the top and lower surfaces can vary: the lower surface variation is due to the variation in the surface elevation of the supporting solid mass.

(6) The horizontal variations of the layer depth are assumed to be gradual so that vertical accelerations are absent.

(7) The flow properties in the surrounding fluid are assumed completely known, so that only property variations within the layer need be computed. Interactions between the layer and the surrounding fluid are prescribed by way of entrainment relations and boundary conditions.

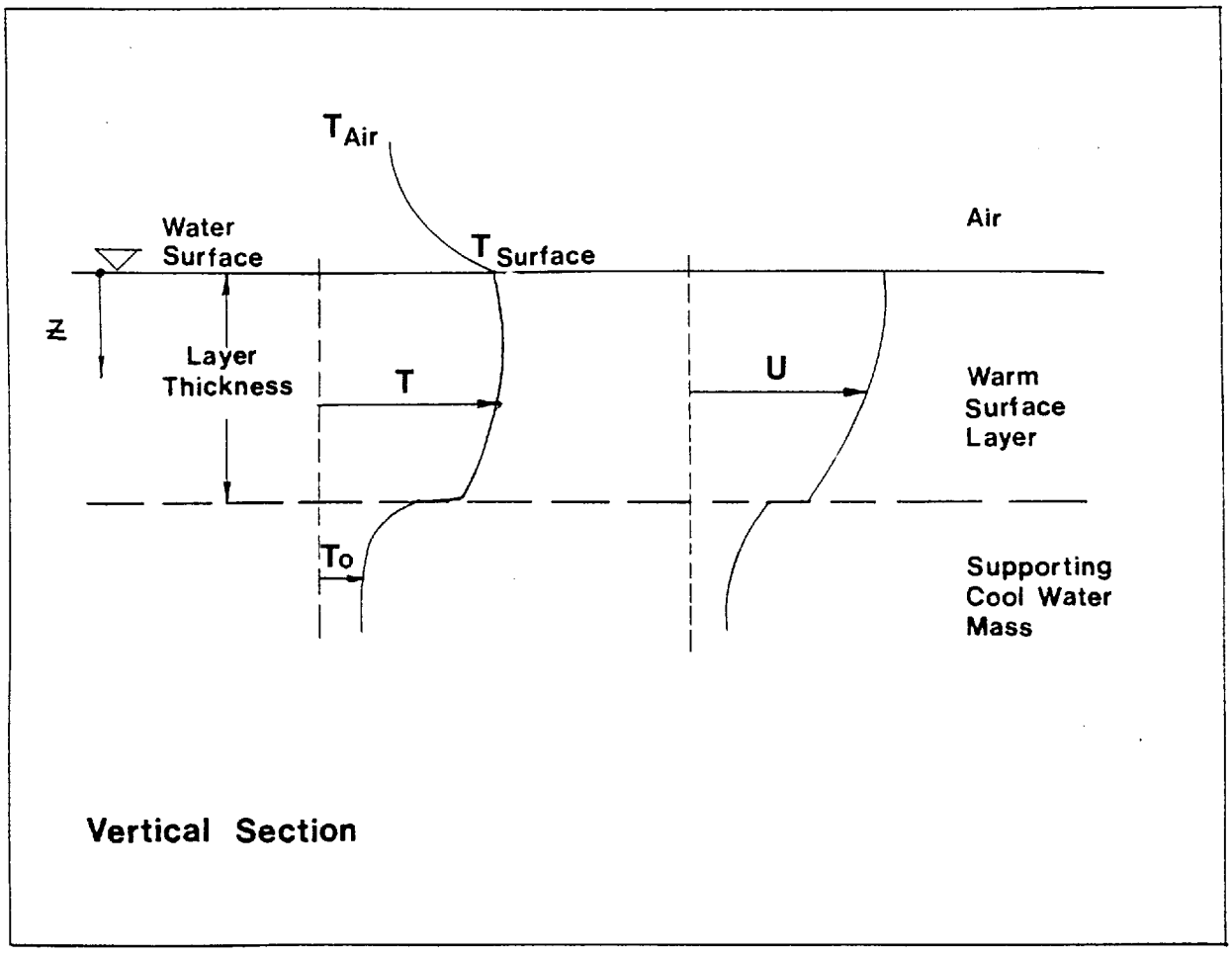


Fig. 3.1: Vertical Profiles of Temperature and Velocity

3.2.2 Coordinate system

The coordinate system by which the flow within the layer is described consists of:

(i) lines along which the dimensionless stream function, ω is constant; and

(ii) lines perpendicular to the main flow direction, x.

The dimensionless stream function, ω, at any point, is defined as the ratio of the mass flow rate between that point and the I-boundary to the total mass flow rate in the layer, at the cross-section. It is given by:

$$\omega \equiv \frac{\psi - \psi_I}{\psi_E - \psi_I} = \frac{\int_o^y z\rho U dy}{\int_o^{y_E} z\rho U dy} \qquad ,(3.2.1)$$

where ψ is the stream function.

This coordinate system is similar to the $x \sim \omega$ system of Patankar and Spalding employed in GENMIX by Spalding (1978). The main difference is that, in the present case, the lines of constant stream functions do not coincide with the stream-lines. This is a deviation from conventional practice, brought about by the vertical entrainment of lower layer fluid. The flow rate of fluid across the lines of constant stream functions is directly proportional to the rate of vertical entrainment of lower layer fluid. The mathematical implications of this are considered in a later section where the differential equations governing the layer flow are discussed. In all other ways the present coordinate system

is identical to that of Patankar and Spalding. The main advantage of these systems is that the grid is distributed only within the domain of interest. A typical grid is shown in Figure 3.2. The grid can be non-uniformly spaced in both x and ω. The physical locations of the constant ω-grid lines are not known "a priori" but must be calculated at each axial location. The method by which this is done is described in a later sub-section, after the dependent variables and the finite-difference grids have been discussed.

The coordinate system described above is that for the computation of straight surface-layer flows. When there is flow curvature certain modifications are necessary. These are described in Section 3.5.

3.2.3 Dependent variables

The dependent variables which characterise the layer flow and whose values are sought are:

(i) the longitudinal velocity, (U), which is in the x-direction;

(ii) the lateral velocity, (V), which is in the y-direction;

(iii) the temperature (T); and

(iv) the layer thickness, (z).

The U-velocities, at any axial plane, are parallel to each other but are, in general, not all in the same direction as the constant ω-grid lines. However, the V-velocities are always in the direction of the cross-stream grid lines: the constant x lines.

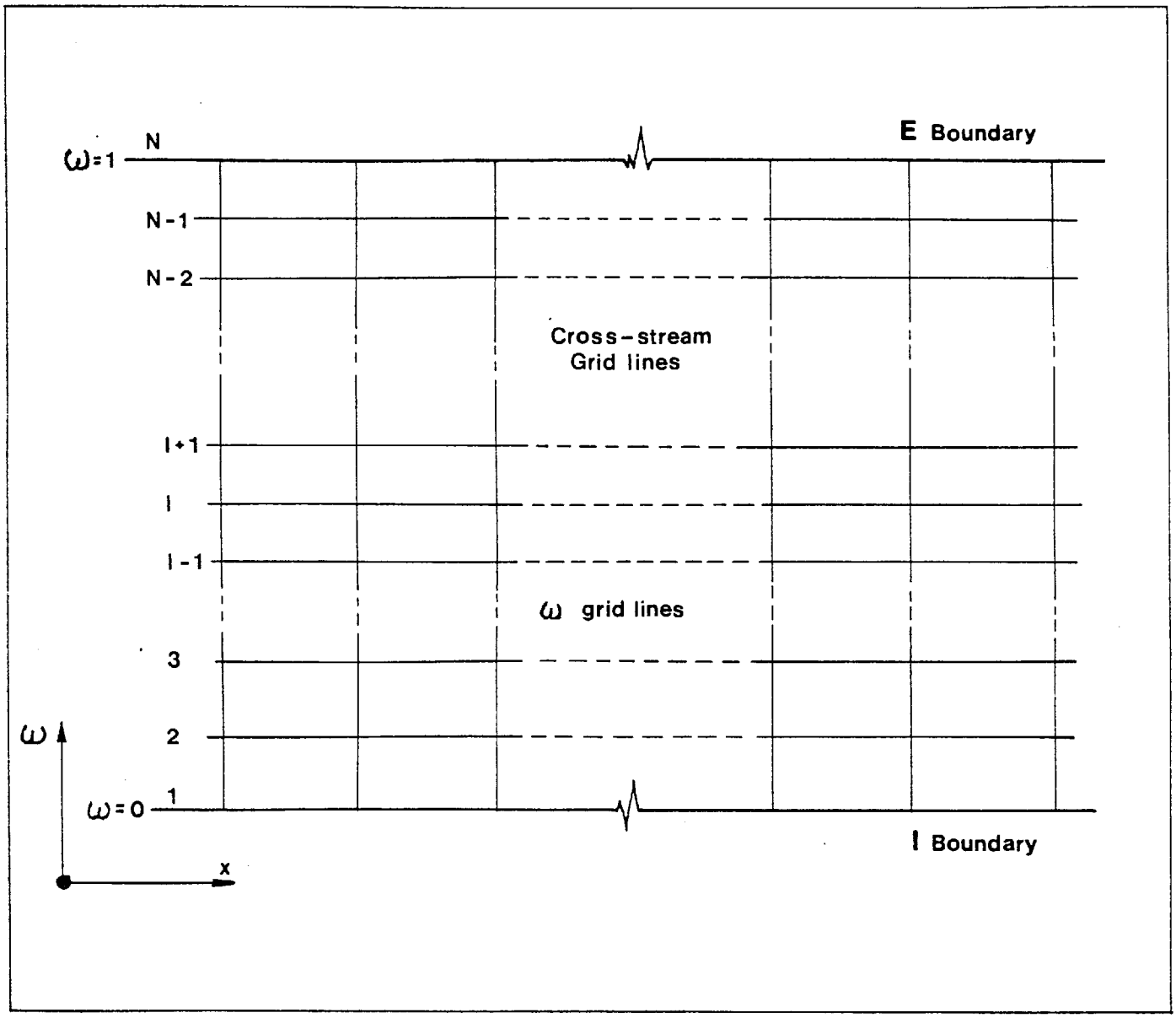


Fig.3.2: Typical Grid Distribution in the (x-ω) Co-ordinate System

This choice is dictated by the ease of calculating the inclination of the constant ω lines, when the mass flow rates across them are known. This is discussed in greater detail later. The implication of this is that, whilst V is affected by one pressure-gradient term, $\frac{\partial P}{\partial y}$, U is affected by two pressure-gradient terms: the extra term accounting for the difference in the angle between the directions of the longitudinal velocities and the ω-grid lines.

3.2.4 Finite-difference grid

The governing partial-differential equations must be discretized into finite-difference equations before they can be solved numerically. The finite-difference grid employed in the discretization is shown in Figure 3.3. The locations of the dependent variables on the grid are shown. The pressures, layer thicknesses, temperatures and U-velocities are located at the grid nodes, whilst the V-velocities are located between four grid nodes. The latter is done to ensure that the four neighbouring pressures can affect the V-velocities. The control volumes corresponding to each of these variable locations are shown in Figure 3.4. The control volumes at the near-boundary grid points are slightly different. This is illustrated in Figure 3.5. However, control volumes are not needed for the boundary points, since the values of the variables on the boundaries are either known or can be deduced from the values on the near-boundary points.

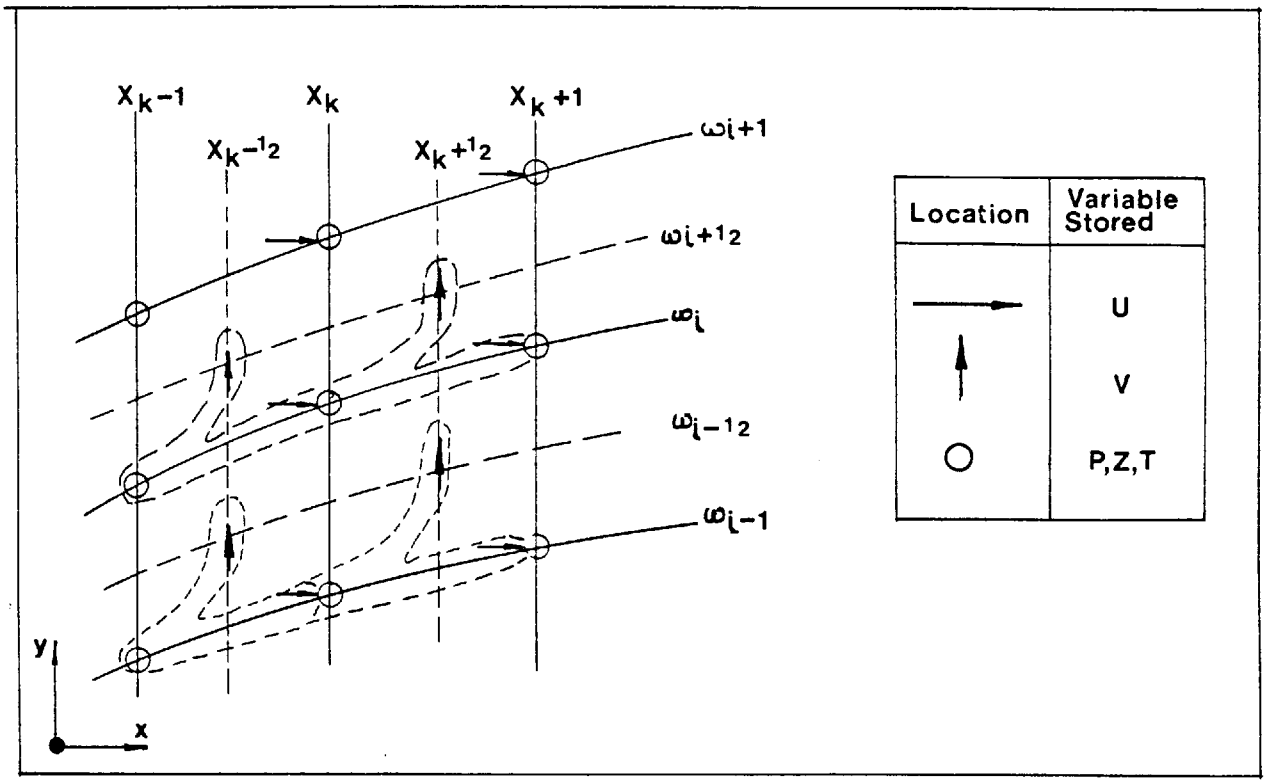


Fig.3.3: Location of Variables on the Finite-Difference Grid

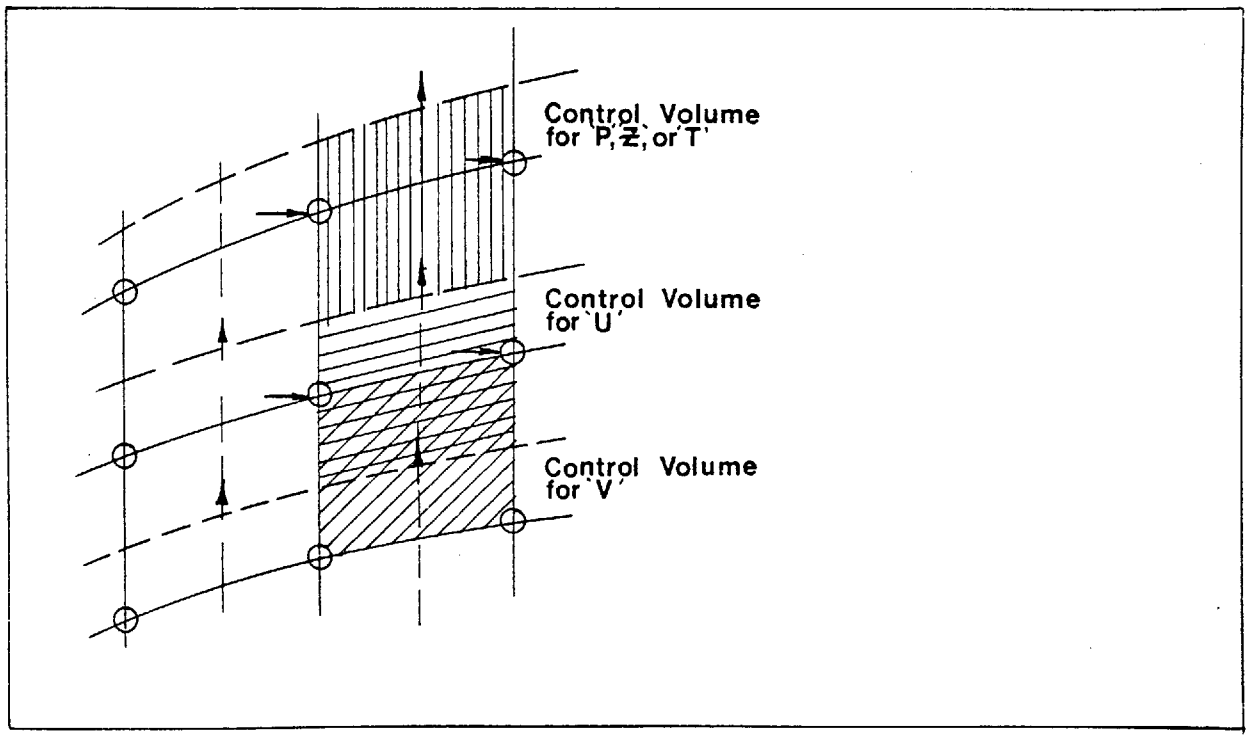


Fig.3.4: Control Volumes for the Variables

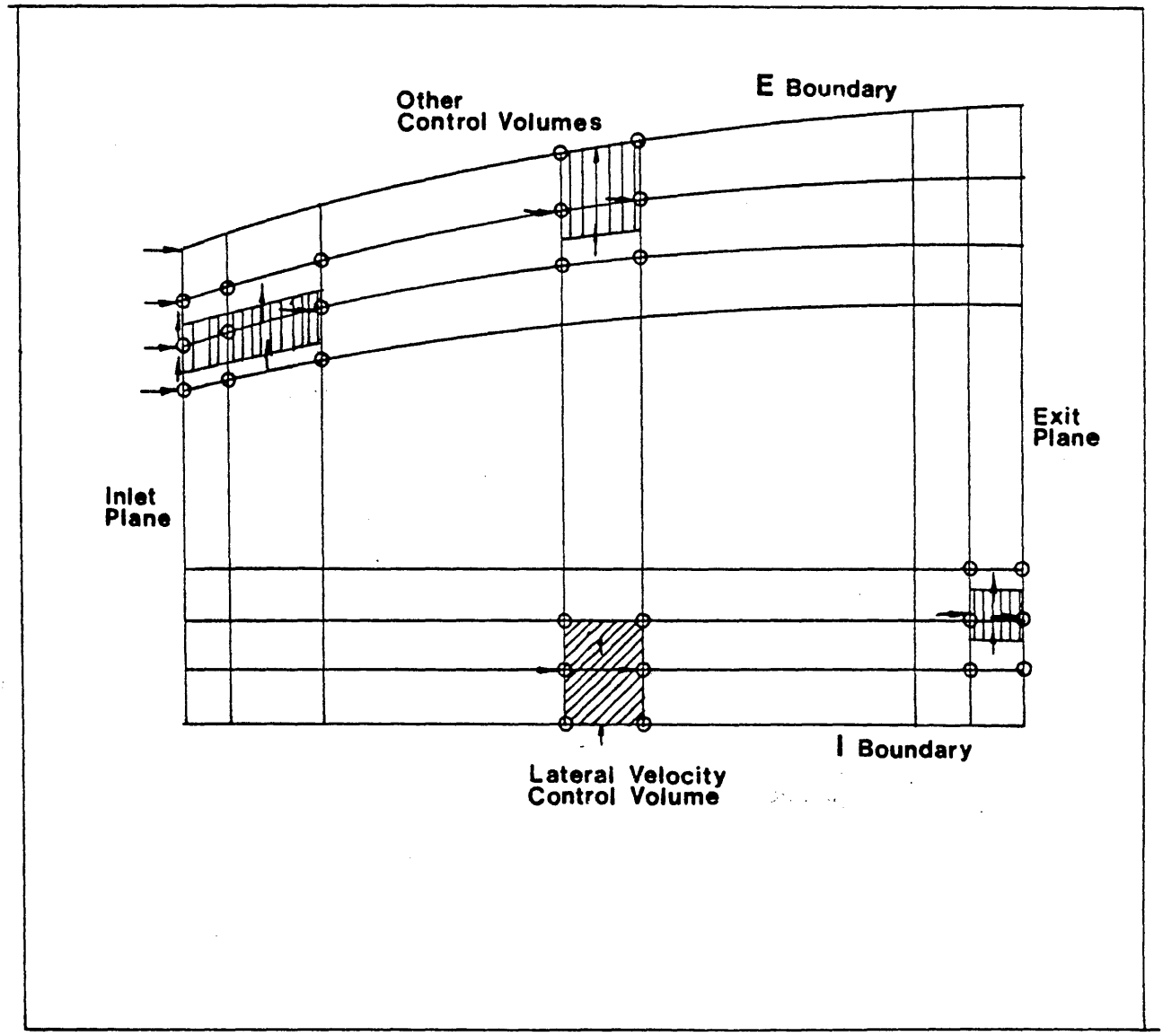


Fig.3.5: Variable Locations and Control Volumes Near the Boundaries

3.2.5 Auxiliary information

In the preceding three sections, the coordinate system, dependent variables and the finite-difference grids have been described. To conclude the description of the main features of the present procedures, the relationship between the $x\sim\omega$ coordinate system and the $x\sim y$ Cartesian coordinate system is given in this section.

x is the main flow direction, and is the same in both coordinate systems.

ω is the dimensionaless stream function, defined in subsection 3.2.2. It is related to y by equations (3.2.1), namely:

$$\omega \equiv \frac{\psi - \psi_I}{\psi_E - \psi_I} = \frac{\int_o^y z\rho U dy}{\int_o^{y_E} z\rho U dy} \qquad .(3.2.1)$$

In general, there may be fluid entrainment from the surroundings in both the lateral and the vertical directions. If these flow rates are denoted by $\dot{m}''_h$ and $\dot{m}''_v$, respectively, then the values of the stream functions, at the boundaries, may be calculated from the relations:

$$\psi_{I,d} = \psi_{I,u} - \delta x \, (z \, \dot{m}''_h)_I$$

and

$$\psi_{E,d} = \psi_{E,u} - \delta x \, (z \, \dot{m}''_h)_E + \delta x \int_o^{y_E} \dot{m}''_v \, dy \qquad ,(3.2.2)$$

where subscript u stands for upstream value, and subscript d stands for downstream value.

The value of the stream function along a constant ω-grid line, denoted by subscript S, may then be calculated at d, as:

$$\psi_{S,d} = \psi_{I,d} + \omega_S (\psi_{E,d} - \psi_{I,d}) \qquad .(3.2.3)$$

The lateral distance between the constant ω-grid line and the I-boundary, y_S, is then obtained from the relation:

$$\psi_{S,d} - \psi_{I,d} = \int_o^{y_S} z\rho U dy \qquad ;(3.2.4)$$

the integrand on the right-hand side being evaluated numerically.

3.3 Governing Equations

3.3.1 The partial-differential equations

The partial differential equations governing the flow and heat transfer of the surface layer are reduced forms of the Navier-Stokes equations. In the formulation of the surface-layer model, the following assumptions are made:

(1) The flow is steady and two-dimensional, vertical variations being negligible.

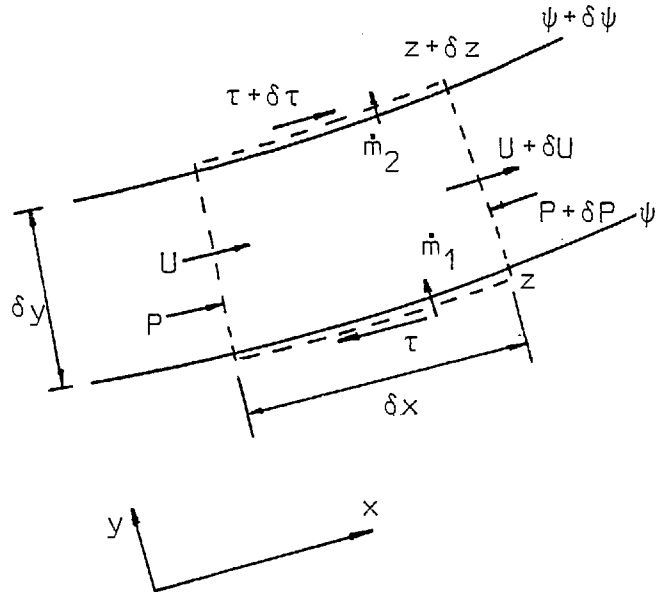
(2) There is a predominant flow direction in which flow reversal is absent and diffusion is negligible (the boundary-layer approximation).

(3) Change of layer depth is gradual, so that vertical veloctiy and acceleration may be neglected (the Hydrostatic approximation).

(4) The fluid is incompressible, and density variation is important only in its effect on buoyancy, inertial effects being neglected, (the Boussinesq approximation).

The differential equations are now derived, first, in the x∿ψ coordinate plane, and then, are transformed to the x∿ω coordinate system. These analyses follow closely those employed in GENMIX by Spalding (1978), except for the differences resulting from the fact that the lines of constant stream functions do not coincide with streamlines, as discussed in section 3.2.2.

First consider the conservation of the x-direction momentum, the control volume bounded by the lines (or more precisely, surfaces) of constant stream functions ψ and $\psi + \delta\psi$ is illustrated below:



Elementary control volume for the derivation of the differential equation

The rate of mass flow between the two lines is $\delta\psi$, where $\delta\psi$ is given by:

$$\delta\psi = z\rho U\delta y \qquad .(3.3.1)$$

The forces acting on the elemental control volume are now considered. Application of Newton's Second Law of Motion yields:

$$\{(U + \delta U) - U\}\,\delta\psi + (\dot{m}_2 - \dot{m}_1)\,U - \dot{m}_v\,U_o$$

$$- \{(\tau + \delta\tau)\,(z + \delta z) - \tau z\}\,\delta x$$

$$+ \{(P + \delta P) - P\}\,z\delta y = 0 \qquad ,(3.3.2)$$

where,

$\dot{m}_1$ is the mass flow rate across the constant ψ line,

$\dot{m}_2$ is the mass flow rate across the constant $\psi + \delta\psi$ line,

$\dot{m}_v$ is the rate of entrainment of fluid through the bottom of the layer, and

U_o is the x-direction velocity of the lower layer fluid.

Since the mass flow rate between the ψ and the $\psi + \delta\psi$ lines is constant, the rate of entrainment of lower layer fluid must be equal to the net rate at which the fluid mass is flowing out across the ψ and $\psi + \delta\psi$ lines, that is:

$$\dot{m}_v = \dot{m}_2 - \dot{m}_1 \qquad .(3.3.3)$$

When equations (3.3.1) and (3.3.3) are substituted in equation (3.3.2), and the secondary terms are neglected, the result may be expressed as a partial-differential equation of the form:

$$\frac{\partial U}{\partial x} = \frac{\partial}{\partial \psi}(\tau z) + \frac{1}{\rho U z}\left\{\frac{\dot{m}_v (U_o - U)}{\delta x\, \delta y} - z \frac{\partial P}{\partial x}\right\} \qquad .(3.3.4)$$

Define: $\dot{m}''_v \equiv \frac{\dot{m}_v}{\delta x \delta y}$.(3.3.5)

Equations (3.3.4) may then be expressed as:

$$\frac{\partial U}{\partial x} = \frac{\partial}{\partial \psi}(\tau z) + \frac{\dot{m}''_v}{\rho U z}(U_o - U) - \frac{1}{\rho U}\frac{\partial P}{\partial x} \qquad .(3.3.6)$$

It is now necessary to transform equation (3.3.6) into $x \sim \omega$ coordinates.

For the transformation it is necessary to express:

(i) $\left(\frac{\partial}{\partial x}\right)_\psi$ in terms of $\left(\frac{\partial}{\partial x}\right)_\omega$ and $\left(\frac{\partial}{\partial \omega}\right)_x$;

(ii) $\left(\frac{\partial}{\partial \psi}\right)_x$ in terms of $\left(\frac{\partial}{\partial x}\right)_\omega$ and $\left(\frac{\partial}{\partial \omega}\right)_x$.

Differentiation of equation (3.2.1) (i.e., the definition of ω) with respect to x, yields:

$$\left(\frac{\partial \omega}{\partial x}\right)_\psi = \frac{1}{\psi_E - \psi_I}\left\{\frac{d(\psi - \psi_I)}{dx} - \omega \frac{d(\psi_E - \psi_I)}{dx}\right\} \qquad .(3.3.9)$$

The vertical entrainment rates must be taken into consideration in evaluating the differentials, hence,

$$\left(\frac{\partial \omega}{\partial x}\right)_\psi = \frac{1}{\psi_E - \psi_I}\left\{\dot{m}'_v + (z\dot{m}''_h)_I + \omega\left((z\dot{m}''_h)_E - (z\dot{m}''_h)_I - (\dot{m}'_v)_E\right)\right\}$$

;(3.3.10)

where,

$\dot{m}'_v \equiv \int_o^y \dot{m}''_v \, dy$, the vertical entrainment rate, per unit length, between a constant ω line and the I-boundary,

$(\dot{m}'_v)_E \equiv \int_o^{y_E} \dot{m}''_v \, dy$, the vertical entrainment rate, per unit length, between the E-boundary and the I-boundary, and

$(\dot{m}''_h)_I$ and $(\dot{m}''_h)_E$ are the lateral mass flow rates, per unit area, across the I and E boundaries, respetively, and are positive in the positive y-direction.

It should be noted that $\dot{m}'_v$ is not necessarily equal to ω times $(\dot{m}'_v)_E$.

Equation (3.3.10) may be expressed as:*

$$\left(\frac{\partial \omega}{\partial x}\right)_\psi = a + b\omega \qquad ,(3.3.11)$$

where,

$$a \equiv \{\dot{m}'_v + (z\dot{m}''_h)_I\}/(\psi_E - \psi_I) \qquad ,(3.3.12)$$

and

$$b \equiv \{(z\dot{m}''_h)_E - (z\dot{m}''_h)_I - (\dot{m}'_v)_E\} / (\psi_E - \psi_I) \qquad .(3.3.13)$$

Similarly,

$$\left(\frac{\partial \omega}{\partial \psi}\right)_x = \frac{1}{\psi_E - \psi_I} \qquad .(3.3.14)$$

The equations (3.3.7) and (3.3.8) may now be expressed as:

$$\left(\frac{\partial}{\partial x}\right)_\psi = \left(\frac{\partial}{\partial x}\right)_\omega + (a + b\omega)\left(\frac{\partial}{\partial \omega}\right)_x \qquad ,(3.3.15)$$

---

*NOTE: This expression for $a + b\omega$ differs from the usual GENMIX one; however, it has the same meaning, i.e., it is a measure of the rate at which mass is crossing a given constant ω-grid line.

and

$$\left(\frac{\partial}{\partial\psi}\right)_x = \frac{1}{\psi_E-\psi_I}\left(\frac{\partial}{\partial\omega}\right)_x \qquad .(3.3.16)$$

The transformed version of equation (3.3.6) is therefore:

$$\frac{\partial U}{\partial x} + (a + b\omega)\frac{\partial U}{\partial \omega} = \frac{1}{(\psi_E-\psi_I)}\frac{\partial(\tau z)}{\partial\omega} + \frac{\dot{m}''_v}{\rho U z}(U_o - U) - \frac{1}{\rho U}\frac{\partial P}{\partial x} \qquad .(3.3.17)$$

The shear stress, τ is given by Newton's law of viscosity as:

$$\tau = \mu\frac{\partial U}{\partial y} \qquad ,(3.3.18)$$

where μ is the viscosity.

If the flow is turbulent, the effective viscosity, μ_{eff} is used rather than the laminar viscosity.

Equation (3.3.1) is used with equation (3.3.18) to obtain:

$$\tau = z\rho U\,\mu\frac{\partial U}{\partial\psi} \qquad .(3.3.19)$$

The final form of the x-momentum equation in the $x\sim\omega$ coordinate system is:

$$\frac{\partial U}{\partial x} + (a + b\omega)\frac{\partial U}{\partial\omega} = \frac{\partial}{\partial\omega}\left(c\frac{\partial U}{\partial\omega}\right) + d \qquad ,(3.3.20)$$

where,

$$c \equiv \frac{z^2\rho U\mu}{(\psi_E-\psi_I)^2} \quad ;$$

and

$$d \equiv \frac{1}{\rho U z}\{\dot{m}''_v(U_o - U) - z\frac{\partial P}{\partial x}\} \qquad .$$

The partial-differential equations for the lateral velocity, V and the temperature, T are derived in a similar manner. The results are:

Lateral momentum equation

$$\frac{\partial V}{\partial x} + (a + b\omega)\frac{\partial V}{\partial \omega} = \frac{\partial}{\partial \omega}\left(c\frac{\partial V}{\partial \omega}\right) + d \qquad ,(3.3.21)$$

where,

a, b, and c are as defined above, and

$$d \equiv \frac{1}{\rho U z}\left\{\dot{m}''_v (V_o - V) - z\frac{\partial P}{\partial y}\right\} \quad .$$

Temperature equation

$$\frac{\partial T}{\partial x} + (a + b\omega)\frac{\partial T}{\partial \omega} = \frac{\partial}{\partial \omega}\left(c\frac{\partial T}{\partial \omega}\right) + d \qquad ,(3.3.22)$$

where

a and b are as defined above;

$$c \equiv \frac{z^2 \rho U \Gamma_T}{(\psi_E - \psi_I)^2} \; ;$$

$$d \equiv \frac{1}{\rho U z}\left\{\dot{m}''_v (T_o - T) - \frac{\alpha}{C}(T - Teq)\right\} \; ;$$

Γ_T is the thermal conductivity;

α is the surface heat transfer coefficient;

C is the specific heat capacity of the layer fluid; and

Teq is the equilibrium temperature.

In general, for the property, ϕ, the conservation equation is:

$$\frac{\partial \phi}{\partial x} + (a+b\omega)\frac{\partial \phi}{\partial \omega} = \frac{\partial}{\partial \omega}\left(c\frac{\partial \phi}{\partial \omega}\right) + d \qquad ,(3.3.23)$$

(longitudinal convection) (lateral convection) (diffusion) (sources and sinks)

where,

$$a \equiv \frac{\{\dot{m}'_v + (z\dot{m}''_h)_I\}}{(\psi_E - \psi_I)} ;$$

$$b \equiv \frac{\{(z\dot{m}''_h)_E - (z\dot{m}''_h)_I - (\dot{m}'_v)_E\}}{(\psi_E - \psi_I)} ;$$

$$c \equiv \frac{z^2 \rho U \Gamma_\phi}{(\psi_E - \psi_I)^2} ;$$

$$d \equiv \frac{1}{\rho U z} S_\phi .$$

The pressure-gradient terms, containing $\frac{\partial P}{\partial x}$ and $\frac{\partial P}{\partial y}$, represent the net driving forces on the layer fluid due to the variations in density and layer depth in the respective directions. These terms are derived from first principles in Appendix A.

For the floating layer, the expressions are:

$$\frac{\partial P}{\partial x} = g\left\{\left(\frac{\rho}{2\rho_o} - \frac{\Delta\rho}{2\rho_o}\right)z\frac{\partial \Delta\rho}{\partial x} + \frac{\Delta\rho}{\rho_o}\rho\frac{\partial z}{\partial x}\right\} ,$$

and, (3.3.24)

$$\frac{\partial P}{\partial y} = g\left\{\left(\frac{\rho}{2\rho_o} - \frac{\Delta\rho}{2\rho_o}\right)z\frac{\partial \Delta\rho}{\partial y} + \frac{\Delta\rho}{\rho_o}\rho\frac{\partial z}{\partial y}\right\} ,$$

where,

ρ_o is the density of the supporting liquid mass,

ρ is the density of the layer fluid, and

$\Delta\rho \equiv \rho_o - \rho$.

For the full-depth layer, the expressions are:

$$\frac{\partial P}{\partial x} = g \{\frac{z}{2} \frac{\partial \rho}{\partial x} + \rho (\frac{\partial z}{\partial x} + \frac{\partial z_o}{\partial x})\} ,$$

and, (3.3.25)

$$\frac{\partial P}{\partial y} = g \{\frac{z}{2} \frac{\partial \rho}{\partial y} + \rho (\frac{\partial z}{\partial y} + \frac{\partial z_o}{\partial y})\} ,$$

3.3.2 Finite-difference equations

The partial-differential equations of the type (3.3.23) must be discretized to obtain the finite-difference equations. This is done by integrating them over the finite-difference grid, (described in subsection (3.2.4)) for each of the variables. At each grid node the resulting equations are of the form:

$$D_i \phi_{i,d} = A_i \phi_{i+1,d} + B_i \phi_{i-1,d} + C_i \quad ;(3.3.26)$$

where,

i is the grid node subscript varying from 1 at the I boundary to N at the E boundary;

$$A_i \equiv \frac{(z\Gamma_\phi)_{i+\frac{1}{2}}}{(y_{i+1}-y_i)_u} - \tfrac{1}{2} z \dot{m}''_{h,i+\frac{1}{2}} \quad ;(3.3.27)$$

$$B_i \equiv \frac{(z\Gamma_\phi)_{i-\frac{1}{2}}}{(y_i-y_{i-1})_u} + \tfrac{1}{2} z \dot{m}''_{h,i-\frac{1}{2}} \quad ;(3.3.28)$$

$$C_i \equiv \left\{\frac{\phi_{i,u}}{\delta x_i} + \frac{S_{\phi,u}}{\rho U z}\right\}_i (\psi_E - \psi_I)\ (\omega_{i+\frac{1}{2}} - \omega_{i-\frac{1}{2}}) \qquad ;(3.3.29)$$

$$D_i \equiv A_i + B_i + \left\{\frac{1}{\delta x_i} - \frac{S_{\phi,p}}{\rho U z}\right\}_i (\psi_E - \psi_I)\ (\omega_{i+\frac{1}{2}} - \omega_{i-\frac{1}{2}}) \qquad .(3.3.30)$$

Equation (3.3.12) may be expressed as:

$$\phi_{i,d} = A'_i\ \phi_{i+1,d} + B'_i\ \phi_{i-\frac{1}{2},d} + C'_i \qquad ;(3.3.31)$$

where,

$$A'_i \equiv A_i/D_i,$$

$$B'_i \equiv B_i/D_i, \qquad .(3.3.32)$$

$$C'_i \equiv C_i/D_i$$

Equations of the type (3.3.26) are derived for each ϕ variable, at each of the internal grid nodes, (i=2 to i=N-1) at any cross-stream station. When the coefficients A,B,C,D have been calculated, the resulting set of simultaneous equations, for each ϕ, is solved with a single sweep of a Tri-diagonal Matrix Algorithm (TDMA).

To conclude this section on the governing equations, some auxiliary information is given on the treatment of the source terms and the boundary conditions.

3.3.3 Auxiliary information

(i) Treatment of Source Terms

In the context of this discussion, the phrase, "source terms" is used broadly, to represent all the terms of equation (3.3.11) other than the first three. This treatment enables the same computer code to be used for a wide variety of cases, with the "source terms" alone needing modification.

The source term, S_ϕ is linearised in the same way as done by Patankar and Spalding (1972), as:

$$S_\phi = S_{\phi,U} + S_{\phi,P} \cdot \phi \qquad .(3.3.33)$$

This permits the source term to depend on both upstream (or previous iteration) and downstream values, $S_{\phi,U}$ and $S_{\phi,P}$, being calculated from the former, and from the latter, respectively. The level of implicitness is thereby increased, leading to enhanced stability, if $S_{\phi,P}$ is negative.

In the simplest cases of the floating-layer and full-depth flows with which the governing equations are illustrated in this section, the source terms for the various ϕ's are:

Table 3.1: Source terms for floating-layer flows.

ϕ	$S_{\phi,P}$	$S_{\phi,U}$
U	$-\dot{m}''_V$	$\dot{m}''_V U_o - z\frac{\partial P}{\partial x}$
V	$-\dot{m}''_V$	$\dot{m}''_V V_o - z\frac{\partial P}{\partial y}$
T	$-\frac{\alpha}{C} - \dot{m}''_V$	$\dot{m}''_V T_o + \frac{\alpha}{C} Teq$

Table 3.2: Source terms for full-depth flows.

ϕ	$S_{\phi,P}$	$S_{\phi,U}$
U	-	$-z\frac{\partial P}{\partial x}$
V	-	$-z\frac{\partial P}{\partial y}$
T	$-\frac{\alpha}{C}$	$\frac{\alpha}{C} Teq$

When the flow is more complicated, as is the case in flows with curvature, or in the presence of wind effects, etc., additional terms are required. However, the discussion of these is deferred till the later sections where these special cases are considered.

(ii) Treatment of Boundary Conditions

The values of ϕ_i, on the boundaries, (i=1 and i=N) must be specified before the set of finite-difference equations represented by (3.3.12) can be solved. These boundary conditions are treated in two ways:

(a) The value of ϕ is prescribed on the boundary;

(b) the value of ϕ on the boundary is deduced from the known gradient of ϕ at the boundary.

An example of the first is a wall boundary at which the velocities are zero. The second case may be a symmetry axis, at which the gradient of ϕ is equal to zero. The implication of the latter is that: $\phi_{boundary} = \phi_{near\ boundary}$. This condition is incorporated in to the finite-difference equations by setting the coefficients of the boundary ϕ's, in equations (3.3.12) equal to zero.

3.4 Solution Procedures

3.4.1 Classification of flow types

The partial-differential equations governing the flow of heat, mass and momentum in the surface layer and their finite-difference equivalents were described in the preceding section. In this section, the methods of solving the latter are described. Three cases are discernible, depending on the methods of evaluating the pressure terms in the momentum equations.

The first case, the simplest, is the "parabolic" case, in which the pressure terms are either known beforehand or are negligible. In the second case, the pressure terms are

significant and unknown, but their influences may travel only in the downstream direction. This is the "hyperbolic" case, applicable to supercritical (Froude number greater than unity) flow problems. A solution sequence, based on the SIMPLE* algorithm of Patankar and Spalding (1972) is employed. The solution is achieved by a single calculation sweep in a downstream marching-integration manner from the initial to the final plane of the flow domain. The third case, the "semi-elliptic" or "partially-parabolic" case applies to flows in which influences from downstream may travel upstream solely through pressure effects. This corresponds to subcritical (Froude number less than unity) surface-layer flow problems. A repeated downstream marching-integration sequence, similar to those employed by Pratap (1975) and Singhal (1977) must now be employed.

These three cases are now discussed in detail.

3.4.2 The "parabolic" case

The task is to solve the finite-difference equation (3.3.17):

$$\phi_{i,d} = A'_i \phi_{i+1,d} + B'_i \phi_{i-1,d} + C'_i \qquad .(3.3.17)$$

For the variables U,V and T, respectively, equation (3.3.17) may be expressed as:

$$U_{i,d} = A_i^U U_{i+1,d} + B_i^U U_{i-1,d} + C^U + D_P^U (P_{i,d}-P_{i,u}) \quad ;(3.4.1)$$

$$V_{i+\frac{1}{2},d} = A_i^V V_{i+1\frac{1}{2},d} + B_i^V V_{i-\frac{1}{2},d} + C^V + D_P^V \left(\frac{P_{i+1,d}+P_{i+1,u}}{2} - \frac{P_{i,d}+P_{i,u}}{2}\right) \quad ;(3.4.2)$$

*NOTE: SIMPLE stands for Semi-Implicit Method for Pressure-Linked Equations.

$$T_{i,d} = A_i^T T_{i+1,d} + B_i^T T_{i-1,d} + C^T \qquad ;(3.4.3)$$

where,

$$D_P^U \equiv \{- (\psi_{i+\frac{1}{2}} - \psi_{i-\frac{1}{2}})/(\rho U z dx)_i\}/D_i,$$
$$D_P^V \equiv \{- (\psi_{i+1} - \psi_i)/(\rho U z dy)_{i+\frac{1}{2}}\}/D_i \qquad .(3.4.4)$$

Since the pressures are either known or are negligible, in this case, all the coefficients of equations (3.4.1) - (3.4.3) can be explicitly calculated. The solution sequence is then as follows.

(1) The values of the velocities (U) and (V) and temperature (T) are prescribed at the inlet plane. Their values, at the next downstream plane, must now be evaluated.

(2) The coefficients of the finite-difference equations are calculated using values of the flow properties at the upstream plane. The U-velocity distribution is now obtained by the application of a single sweep of the Tri-diagonal Matrix Algorithm (TDMA) to the set of simultaneous equations (3.3.12) for U. The V-velocity and temperature distributions are similarly obtained.

(3) The continuity equation:

$$\Delta y_{i,d} = \frac{\Delta\psi_{i,d}}{(\rho U z)_{i,d}} \qquad ,(3.4.5)$$

is then used to compute the cross-stream locations of the grid nodes at the downstream plane.

(4) Since upstream values of the flow properties were used in calculating the coefficients of the finite-difference

equations, the resulting solution may not be accurate. The coefficients are therefore recalculated with the most recently computed flow property values, and the whole calculation sequence repeated. About three such iterations are usually needed to obtain a converged solution.

(5) The flow properties at this downstream plane are now fully determined. A new forward step is now taken to determine the flow properties at the next downstream location, utilising steps (2), (3) and (4).

(6) The marching-integration process is continued until the final cross-stream plane is reached. The problem has then been fully solved.

3.4.3 The "hyperbolic" case

In most flows of practical importance, the pressure distribution is not known "a priori", but must be calculated simultaneously with the other flow properties. However, in supercritical flows, pressure influences can only travel in the downstream direction.

The solution sequence employed in this case is as follows:

(1) The values of the flow properties are prescribed at the inlet plane as in the parabolic case, above.

(2) At the first downstream plane, the coefficients of the finite-difference equations are similarly calculated, using upstream values of the flow properties. The downstream pressures are unknown so they are assigned guessed values (usually the upstream ones). These are called P*s.

The velocities and temperatures are then calculated from equations (3.4.1) - (3.4.3). The computed velocities are:

$$U^*_{i,d} = A^U_i U^*_{i+1,d} + B^U_i U^*_{i-1,d} + C^U + D^U_P (P^*_{i,d} - P_{i,u}) \quad ,(3.4.6)$$

$$V^*_{i+\frac{1}{2},d} = A^V_i V^*_{i+1\frac{1}{2},d} + B^V_i V^*_{i-\frac{1}{2},d} + C^V + D^V_P \left(\frac{P^*_{i+1,d}+P_{i+1,u}}{2} + \frac{P^*_{i,d}+P_{i,u}}{2}\right) \quad .(3.4.7)$$

(The velocities are starred to indicate that they were calculated from guessed pressures.)

(3) The continuity equation (3.4.5) is used to calculate the downstream cell-widths:

$$\Delta y^*_{i,d} = \frac{\Delta\psi_{i,d}}{(\rho U z)^*_{i,d}} \quad .(3.4.8)$$

The cell-widths are also calculated from the angles of inclination of the grid lines as:

$$\Delta y_{i,d} = \Delta y_{i,u} + dx \,(\tan \alpha_{i+\frac{1}{2}} - \tan \alpha_{i-\frac{1}{2}}) \quad ,(3.4.9)$$

where,

$$\alpha_{i+\frac{1}{2}} = \tan^{-1}\left(\frac{V}{U}\right)_{i+\frac{1}{2}} - \mathrm{Sin}^{-1}\left(\frac{\dot{m}''_h}{\rho\sqrt{U^2+V^2}}\right)_{i+\frac{1}{2}} \quad .(3.4.10)$$

and,

$$\alpha_{i-\frac{1}{2}} = \tan^{-1}\left(\frac{V}{U}\right)_{i-\frac{1}{2}} - \mathrm{Sin}^{-1}\left(\frac{\dot{m}''_h}{\rho\sqrt{U^2+V^2}}\right)_{i-\frac{1}{2}}$$

It is necessary, for kinematic compatibility, that the two cell-widths should be the same. However, this will only be true if the pressure field have been guessed correctly. This is not usually the case, so the kinematic compatibility errors are calculated from the differences in the two cell-widths.

The aim is to eliminate these errors by applying some corrections to the pressure field. This condition is used to derive a pressure-correction equation, which is solved by TDMA to yield the pressure corrections, p''s. The full derivation of the pressure-correction equation is presented in App.B.

(4) The pressures, layer depths and velocities are corrected from:

$$\begin{aligned} P_{i,d} &= P^*_{i,d} + P'_{i,d} \\ z_{i,d} &= z^*_{i,d} + z'_{i,d} \\ U_{i,d} &= U^*_{i,d} + D^U_P \, (P'_{i,d}) \\ V_{i+\frac{1}{2},d} &= V^*_{i+\frac{1}{2},d} + D^V_P \, \left(\frac{P'_{i+1,d}}{2} - \frac{P'_{i,d}}{2}\right) \end{aligned} \qquad .(3.4.11)$$

(5) Because of the non-linearity of the differential equations, it is necessary to repeat steps (2), (3) and (4), using updated coefficients. As in the parabolic case, about 3 iterations are required to obtain a converged solution.

(6) The integration march then proceeds to the next forward step, and so on until the final cross-stream plane is reached. The solution is then complete.

3.4.4 The "partially-parabolic" case

In subcritical flows, pressure influences can travel both upstream and downstream. If attention is restricted to the class of flows with a predominant flow direction in which convective influences always travel from upstream to downstream, the elliptic effects are then restricted solely to the pressures. Hence the terms "semi-elliptic" or "partially-parabolic": both terms being synonymous. The consequences of this are that:

(i) the pressures for the whole flow field must be stored;

(ii) a single marching-integration sweep from the initial to the final plane of the flow domain is inadequate for a complete solution: many sweeps are now required. The solution sequence for this case is as follows:

(1) The values of the flow properties are prescribed at inlet, as previously. The whole two-dimensional pressure field is now assigned guessed values.

(2) The coefficients of the finite-difference equations are calculated, as in the hyperbolic case. The temperatures and velocities are then evaluated. The velocities are evaluated from:

$$U^*_{i,d} = A^U_i U^*_{i+1,d} + B^U_i U^*_{i-1,d} + C^U + D^U_P (P^*_{i,d} - P^*_{i,u}),$$

and

$$V^*_{i+\frac{1}{2},d} = A^V_i V^*_{i+1\frac{1}{2},d} + B^V_i V^*_{i-\frac{1}{2},d} + C^V + D^V_P \left(\frac{P^*_{i+1,d}+P^*_{i+1,u}}{2} - \frac{P^*_{i,d}+P^*_{i,u}}{2}\right) \quad .(3.4.12)$$

(3) Step three is as in the hyperbolic case. However, since both the upstream and downstream pressures are guessed, they should, in principle, both be corrected. But, if the marching-integration manner of the solution scheme is to be maintained, only one set of pressures can be corrected at any cross-stream location. The upstream pressures are therefore corrected; the correction to the downstream pressures would be effected during the following integration step, and so on, until the final plane at which the pressures must be prescribed as boundary conditions.

It would be recalled that, in the hyperbolic procedure, the downstream pressures are always corrected. One of the reasons for this difference in the treatments of subcritical and supercritical flows is that, to achieve a stable procedure it is necessary for the coefficients of the pressure-correction equation to be positive, and the present practice ensures that. The mathematical proof of this is shown in Appendix B. It should be noted that the pressure-correction equation is a "null-equation" with all its terms tending to zero as convergence is approached. Only the terms that would lead to convergence need be included.

(4) The flow properties are corrected as follows:

$$\begin{aligned} P_{i,u} &= P^{*}_{i,u} + P'_{i,u} \\ z_{i,u} &= z^{*}_{i,u} + z'_{i,u} \\ U_{i,d} &= U^{*}_{i,d} \\ V_{i+\frac{1}{2},d} &= V^{*}_{i+\frac{1}{2},d} + D^{V}_{P}\left(\frac{P'_{i+1,u}}{2} - \frac{P'_{i,u}}{2}\right) \end{aligned} \qquad ;(3.4.13)$$

To ensure that the average pressure level, at the cross-section, remains unchanged, the corrected pressures must be reduced by the overall average of the pressure corrections. Thus, finally

$$P_{i,u} = P_{i,u} - \overline{P'} \qquad ;(3.4.14)$$

where,

$$\overline{P'} = \frac{1}{(y_E - y_I)} \int P'_{i,u}\, dy.$$

Similarly, the layer depths must be adjusted, as

$$z_{i,u} = z_{i,u} - \overline{z'} \qquad ;(3.4.15)$$

where,

$$\overline{z'} = \frac{1}{(y_E - y_I)} \int z'_{i,u}\, dy.$$

(5) The coefficients of the finite-difference equations are now recalculated, and steps (2), (3) and (4) are then repeated, as is done in the hyperbolic case.

(6) If the flow is confined, the total calculated downstream flow width should be equal to the width of the confining duct. When this is not so, a uniform overall correction is applied to each of the pressures, layer depth and velocities at the downstream plane to ensure compatibility. The full derivation of the overall pressure and velocity corrections is given in Appendix C. The resulting correction equations are:

$$P_{i,d} = P_{i,d} + \overline{P}'$$

$$z_{i,d} = z_{i,d} + \overline{z}' \qquad .(3.4.16)$$

$$U_{i,d} = U_{i,d} - D_P^U \overline{P}'$$

This step is not necessary in the hyperbolic case, because overall continuity is automatically satisfied once local continuity is satisfied.

(7) The integration march then proceeds to the next forward step, and so on until the final plane is reached. The whole solution sequence must now be repeated, using the newly calculated (and stored) pressure field as an improved guess of the actual pressure field. It is necessary to repeat these marching-integration sweeps of the whole flow domain until further sweeps do not produce appreciable change in the computed flow properties. The actual number of sweeps required is problem dependent.

3.4.5 Summary

The methods of achieving the solution of the finite-difference equations for surface-layer flows increase in complexity in the order: parabolic; hyperbolic; partially-parabolic. In all three cases, marching integration in the downstream direction is employed.

In the parabolic case, the pressure field is known "a priori": the velocity and temperature fields are then simply evaluated, plane by plane.

In the hyperbolic case, the pressure field is unknown and must be calculated. A guess-and-correct method is used to calculate the pressures and velocities: but, once the solution at any plane is obtained, it cannot be affected by events at any downstream plane. In the partially-parabolic case, the pressure field is also unknown, and a guess-and-correct method is used to compute the pressure and velocity fields. However, downstream effects can travel upstream through the pressures, hence a repeated marching-integration process is employed.

3.5 Calculation of Flows with Curvature

To conclude this chapter, the procedure for calculating flows with curvature is described. Flow curvature occurs in surface layers either through the imposition of curved boundaries or through crossflow interaction.

3.5.1 Rotating-grid system

The rotating-grid system is employed in computing curved surface-layer flows. This is illustrated in Figure 3.6. The s-grid lines are lines along which the normalised stream functions, ω are constant, and the n-grid lines are lines normal to a reference s-grid line, usually denoted by S_{IC_L}. The U-velocities are in the direction of the reference s-grid line, and the V-velocities are normal to them, i.e., in the direction of the n-grid lines.

In general, the radius of curvature, R and the angle of inclination, θ of the s-grid lines are continously changing. They may be calculated for each cell by the following relations:

$$\theta_i = \theta_{IC_L} + \tan^{-1}\left(\frac{V}{U}\right)_i - \sin^{-1}\left(\frac{\dot{m}''_h}{\rho\,(U^2+V^2)_i^{\frac{1}{2}}}\right) \qquad ,(3.5.1)$$

and,

$$R_i = \frac{R_{IC_L} + (n_i - n_{IC_L})}{\cos(\theta_i - \theta_{IC_L})} \qquad .(3.5.2)$$

The latest computed values of the flow properties are used in these calculations.

In bounded flows, the reference s-grid line is chosen as one of the boundaries. θ_{IC_L} and R_{IC_L} are then computed from the shape of the boundary. However, if the flow curvature is produced by crossflow interaction in surface-layer flows, the choice of the reference grid line is not so obvious. The jet trajectory must be computed by solving a jet-bending equation.

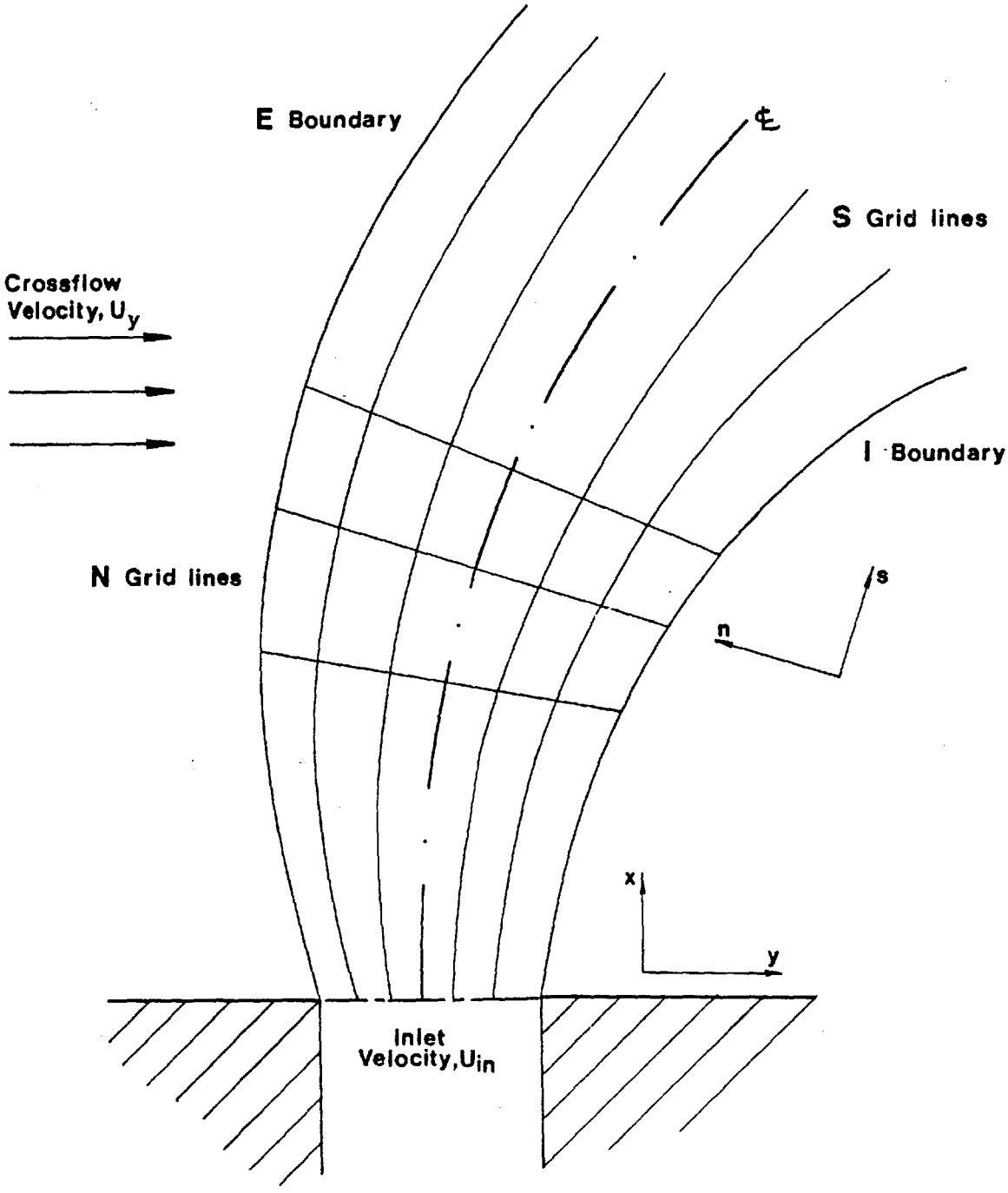


Fig.3.6: The Rotating (S-N) Grid System

The reference grid line is then assumed to lie on the computed trajectory. The relevant partial-differential equations are now described.

3.5.2 Relevant partial-differential equations

The main difference between the rotating-grid system and the coordinate system derived for straight flows in section 3.3 is the presence of curvature effects in the former. The terms representing the curvature effects are simply incorporated into the equations derived for straight flows. Such curvature terms have been employed by Pratap (1975) in the computation of flows in curved channels.

The resulting equations are:

Longitudinal momentum equation

$$\frac{\partial U}{\partial S} + (a + b\omega)\frac{\partial U}{\partial \omega} + \frac{V}{R} = \frac{\partial}{\partial \omega}\left(c\frac{\partial U}{\partial \omega}\right) + \frac{1}{\rho U z}\left\{\dot{m}''_v (U_o - U) - \frac{\partial}{\partial n}\left(z\mu\frac{U}{R}\right)\right.$$

$$\left. + \frac{2}{R}\left(z\mu\frac{\partial U}{\partial n} - z\mu\frac{U}{R}\right) - z\frac{\partial P}{\partial S}\right\} \qquad ;(3.5.3)$$

Lateral momentum equation

$$\frac{\partial V}{\partial S} + (a + b\omega)\frac{\partial V}{\partial \omega} - \frac{U}{R} = \frac{\partial}{\partial \omega}\left(c\frac{\partial V}{\partial \omega}\right)$$

$$+ \frac{1}{\rho U z}\left\{\dot{m}''_v (V_o - V) + \frac{2}{R} z\mu\frac{\partial V}{\partial n} - z\frac{\partial P}{\partial n}\right\} \qquad ;(3.5.4)$$

Temperature equation

$$\frac{\partial T}{\partial s} + (a + b\omega)\frac{\partial T}{\partial \omega} = \frac{\partial}{\partial \omega}\left(c\frac{\partial T}{\partial \omega}\right) + \frac{1}{\rho U z}\left\{\dot{m}''_V (T_o - T)\right.$$

$$\left. + \frac{1}{R}\left(z\,\Gamma_T \frac{\partial T}{\partial n}\right) - \frac{\alpha}{C}(T - Teq)\right\} \qquad ;(3.5.5)$$

where,

a, b and c are as defined, previously in section 3.3.

Equations (3.5.3), (3.5.4) and (3.5.5) may be expressed in (s∿ω) coordinates in the general form:

$$\frac{\partial \phi}{\partial s} + (a + b\omega)\frac{\partial \phi}{\partial \omega} = \frac{\partial}{\partial \omega}\left(c\frac{\partial \phi}{\partial \omega}\right) + d \qquad .(3.5.6)$$

It will be noted that this is the same as equation (3.3.23), already discussed in sub-section 3.3.1 for straight flows.

This similarity of equations is achieved by including all the curvature terms in the source term, d, which is given by:

$$d \equiv \frac{1}{\rho U z} S_\phi = \frac{1}{\rho U z}\left(S_{\phi,P}\cdot\phi + S_{\phi,u}\right) \qquad .(3.5.7)$$

The source terms $S_{\phi,P}$ and $S_{\phi,u}$ for the various ϕ's, are:

Table 3.3: Source terms for surface-layer flows with curvature.

ϕ	$S_{\phi,P}$	$S_{\phi,u}$
U	$-z\frac{\mu}{R^2} - \dot{m}''_V$	$\dot{m}''_V U_o - z\frac{\partial P}{\partial S} + z\frac{\mu}{R}\frac{\partial U}{\partial n} - z\frac{\rho UV}{R}$
V	$-z\frac{\mu}{R^2} - \dot{m}''_V$	$\dot{m}''_V V_o - z\frac{\partial P}{\partial n} + z\frac{\mu}{R}\frac{\partial V}{\partial n} + z\frac{\rho U^2}{R}$
T	$-\frac{\alpha}{C} - \dot{m}''_V$	$\dot{m}''_V T_o + \frac{\alpha}{C} Teq + z\frac{\Gamma_T}{R}\frac{\partial T}{\partial n}$

It may be noted that, if the flow is straight, $R \to \infty$, all the curvature terms disappear. The source terms then reduce to those given for straight flows in Table 3.1.

3.5.3 Calculation of jet trajectory

Most of the methods that have been used to calculate the trajectory of a jet in crossflow treat the jet as if it were a solid body, being deflected by the pressure-drag force acting normal to its axis. Such methods were applied by Abramovich (1963), Crowe and Riesenbieter (1967), Vizel and Mostinskii (1965), and Platten and Keffer (1968) to submerged circular jets in crossflow.

The present method of calculation uses the concept that:

(i) the jet is deflected by the net force acting on it in the direction normal to its axis, i.e., the sum of the pressure forces and the momentum of the entrained fluid, in this direction;

(ii) the deflection is restrained by the total axial momentum of the jet.

The jet-bending equation is then:

$$\frac{1}{R_{IC_L}} \int_I^E z\rho U^2 dn = U_y \sin\theta_{IC_L} \left(\int_{I,E} \dot{m}''_h \, dz + \int_I^E \dot{m}''_V \, dn \right) + \int_I^E z \frac{\partial P}{\partial n} \cdot dn \qquad .(3.5.8)$$

The integrands are evaluated numerically, and the solution of the equation yields R_{IC_L}.

θ_{IC_L} is then obtained from:

$$\theta_{IC_L,d} = \theta_{IC_L,u} + \frac{\delta s_{IC_L}}{R_{IC_L}} \qquad .(3.5.9)$$

The calculation sequence employed at any cross-stream location is:

- Using upstream values of R_{IC_L} and θ_{IC_L}, the momentum and temperature equations (3.5.1), (3.5.2) and (3.5.3) are first solved. The pressure-correction equations are then solved.

- The obtained velocity and pressure fields are used in equation (3.5.8) to evaluate $R_{IC_L,d}$. Subsequently, θ_{IC_L} is calculated from equation (3.5.9).

- The θ_i's and R_i's are now calculated from equation (3.5.6) and (3.5.7). The solution of the momentum, temperature and pressure-correction equations is then repeated.

- This iteration process is carried out until convergence is achieved. This usually requires about 8 iterations for convergence.

3.6 Concluding Remarks

The mathematical basis of this study of surface-layer flows has been discussed in this chapter. The main features of the method of analysis are given in the first section. This is followed by a discussion of the governing partial-differential equations and their discretization into finite-difference ones. The procedures for solving these finite-difference equations are then presented. The chapter concludes with a discussion of the special procedure developed for treating surface-layer flows with curvature.

Application of the model to surface-layer flow problems will now be presented in subsequent chapters.

CHAPTER 4

PREDICTION OF FLOWS WITH ANALYTICAL SOLUTION

4.1 Introduction

In this chapter, numerical solutions of the differential equations are compared with analytical solutions to three flow problems. The first problem is the "uniform" flow of water within a curved domain. This is used to validate the parabolic procedure as well as the procedure for calculating flows with curvature. The second problem is the radial spreading of a buoyant surface pool of water. This serves to validate the hyperbolic procedure. Finally, the developing flow of water in a two-dimensional channel is predicted as a validation of the parabolic procedure in the presence of viscous effects. The analytical solutions of the first two problems are derived in this study, while the analytical solution to the third problem is presented by Schlichting (1968).

4.2 Uniform Flow in Curved Domains

4.2.1 Problem specification

To test the mathematical accuracy of the rotating-grid procedure, and the parabolic solution procedure, a flow situation is devised by superposing a curved flow domain on a uniform, constant-depth, constant-direction flow of water. The curved flow domain is defined by prescribing the boundary shapes.

Computations are performed for six flow configurations. These configurations are illustrated in Figures 4.1(a) and (b). In all the six cases, the internal, (I) boundary is an arc of a circle of radius 12. In the first three cases, the external, (E) boundary is a circular arc of radius 14, with its centre displaced in the uniform flow direction by distances, a = 0, 1.0, and 1.9, respectively. In the remaining three cases, the E boundary is a straight line making angles, θ_E = +14.3°, 0°, and -14.3°, respectively with the uniform flow direction. At the beginning of the calculation domain, the I-boundary makes an angle of 29° with the uniform flow direction, and at the end, the corresponding angle is -73°. The I-boundary is chosen as the reference s-grid line.

4.2.2 Computational details

The computational details are as follows:

Table 4.1: Computational details for the uniform-flow calculations.

VARIABLE	VALUE
Number of cross-stream grids, N	11
Number of forward steps	700
Size of forward step, $\frac{\delta s}{R_I}$	2.5×10^{-3}
Number of iterations at any cross-stream station	5
Computer time in CDC6600 secs	30

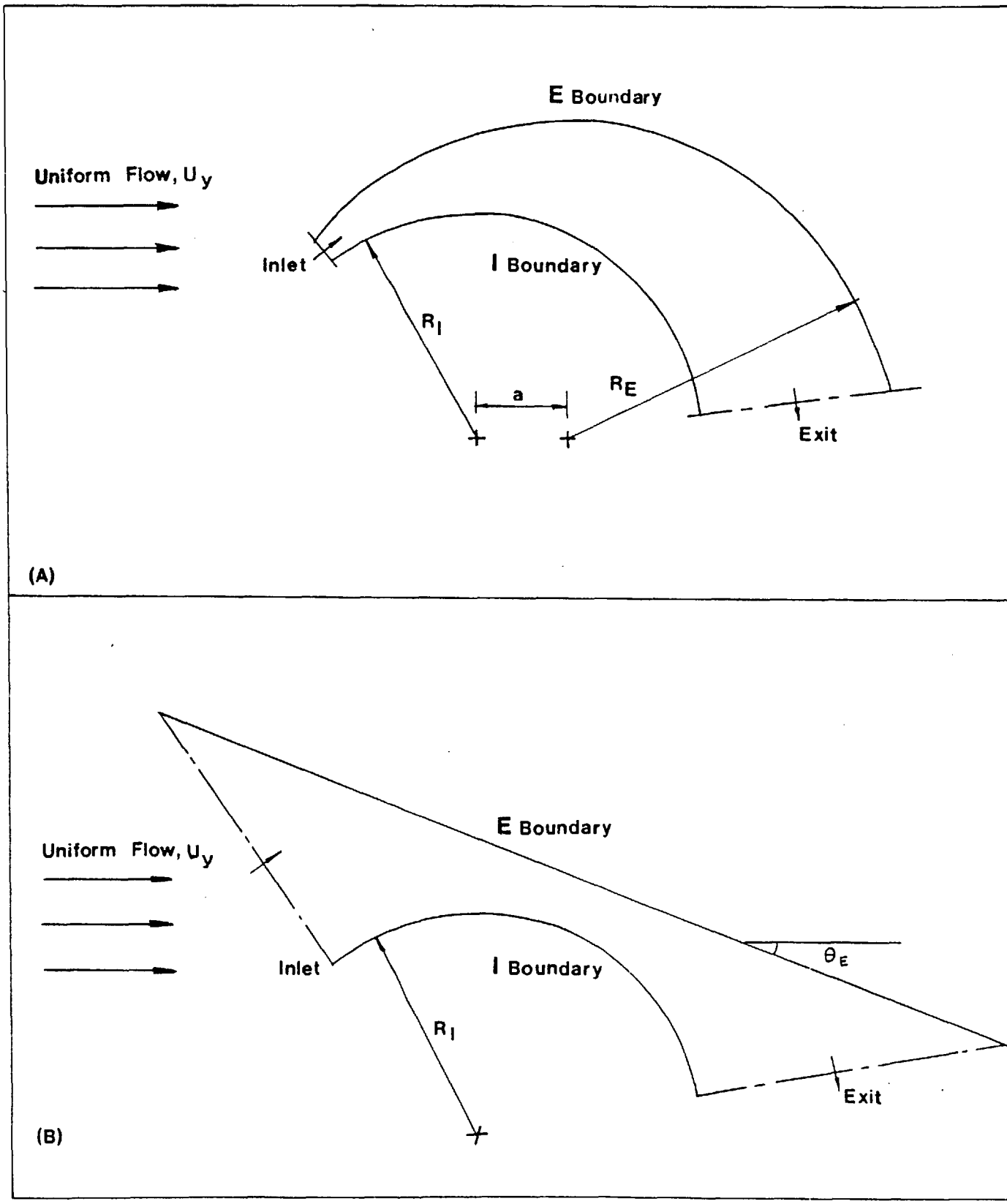


Fig.4.1: Calculation Domain for Uniform - Flow Computations

Boundary Conditions

The boundary conditions are prescribed as follows:

At inlet,

$$U = U_y \cos \theta_{IN} \,, \qquad V = U_y \sin \theta_{IN} \,. \tag{4.2.1}$$

At the I and E boundaries,

$$\left(\frac{\partial U}{\partial n}\right)_{I,E} = 0 \,,$$

$$(V)_{I,E} = U_y \sin \theta_{I,E} \,,$$

$$(\dot{m}''_h)_I = \rho U_y \sin \theta_I \,,$$

$$(\dot{m}''_h)_E = \rho U_y \sin \theta_E \,. \tag{4.2.2}$$

4.2.3 Results and discussion

The exact solutions of the velocities is obtained by simply resolving the uniform flow velocity in the respective directions. Hence, the longitudinal velocity, U, at any cross-stream station, is given by:

$$\frac{U}{U_{IN}} = \frac{\cos \theta_I}{\cos \theta_{IN}} \,, \tag{4.2.3}$$

where,

θ_I is the angle of inclination of the reference s-grid line (in this case, the I-boundary).

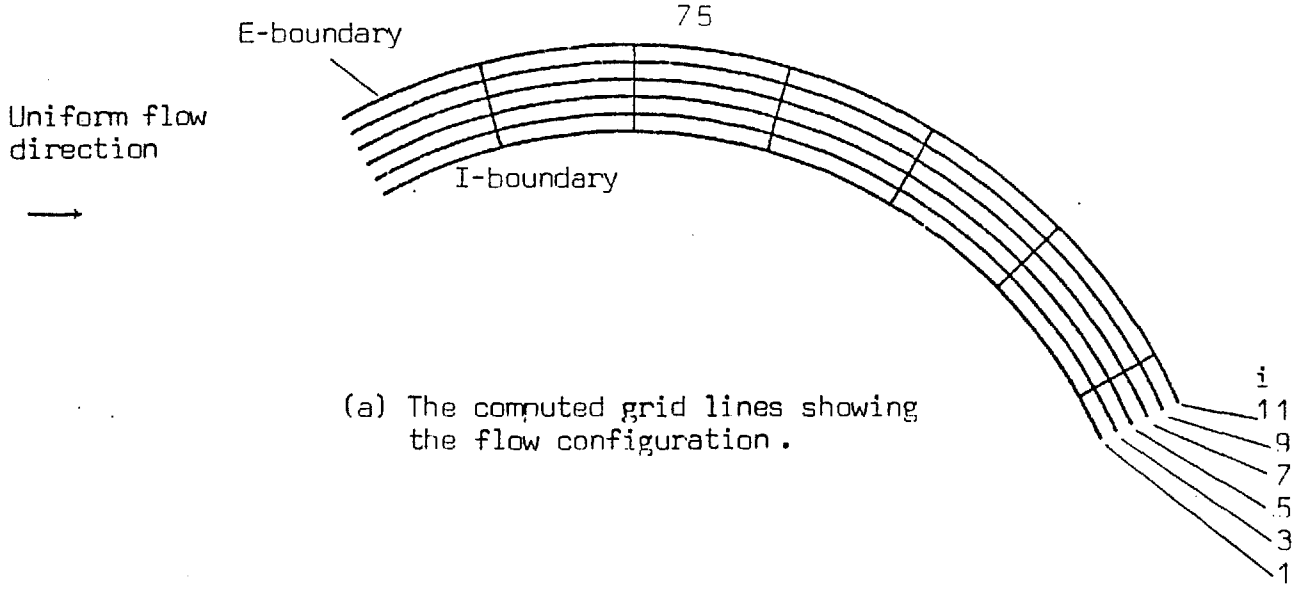
The exact solution of the angle of inclination of the other s-grid lines, θ_i, is obtained from geometrical consideration as shown in Appendix D. The result is:

$$\theta_i = \frac{R_{i,d} \text{ Cos } \theta_{I,d} - R_{i,u} \text{ Cos } \theta_{I,u}}{R_{i,d} \text{ Sin } \theta_{I,d} - R_{i,u} \text{ Sin } \theta_{I,u}} \qquad ,(4.2.4)$$

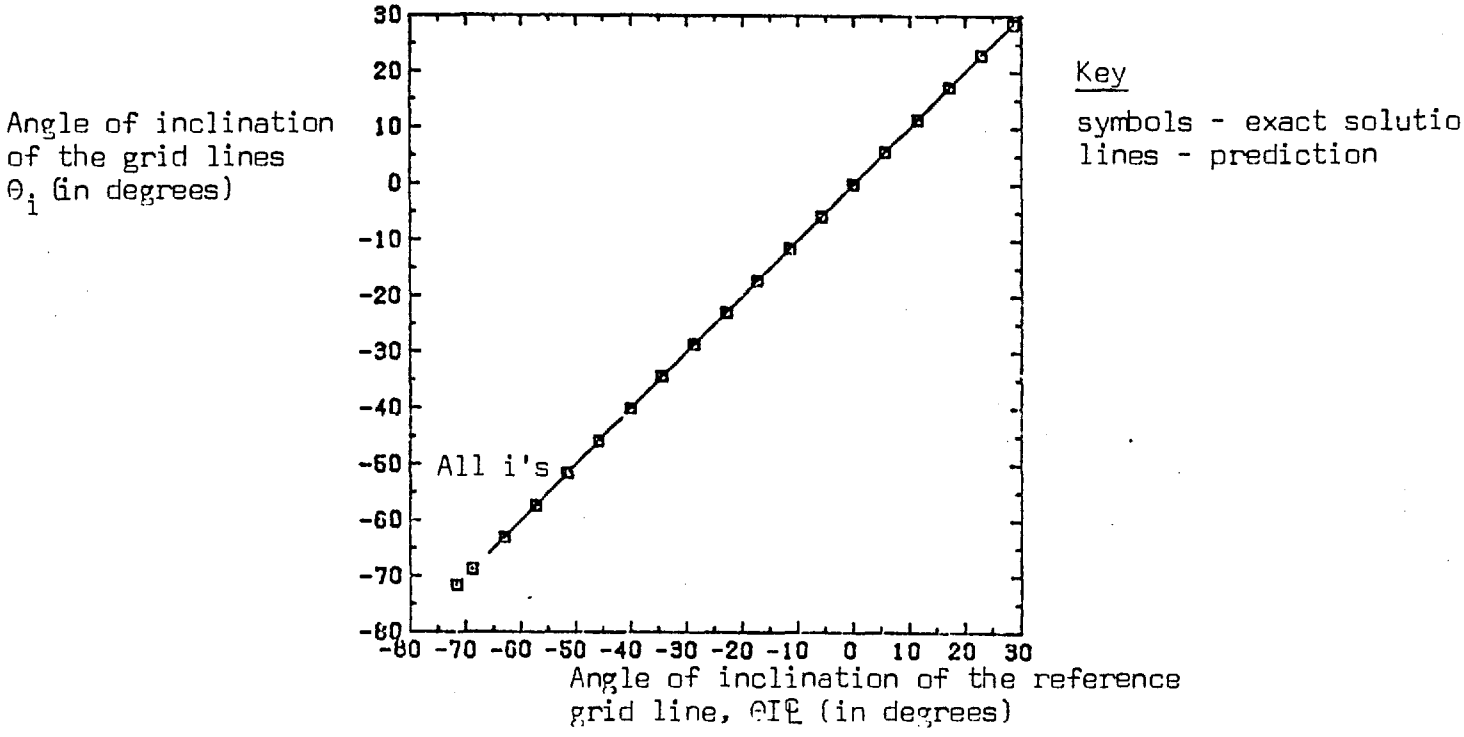
where,

R_i is the distance from the nodal point of cell i to the centre of curvature of the I boundary.

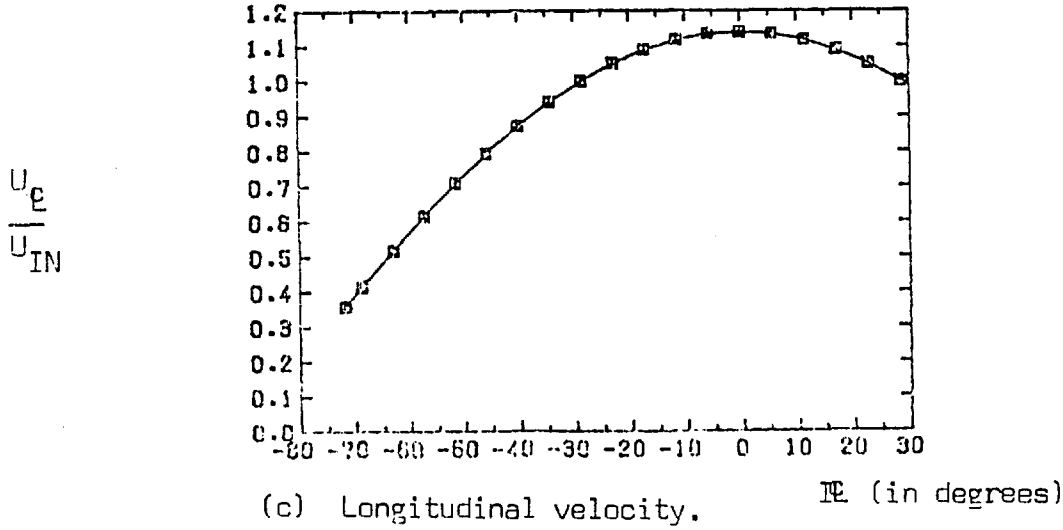
Figures 4.2 - 4.7 show the results of the computations for the six cases described. Each of these figures show the computed s-grid lines, the comparison of the computed angles of inclination with the exact solution, and the comparison of the computed longitudinal velocity with the exact solution. The agreement is seen to be excellent in all cases; in spite of the high degrees of non-orthogonality of the computational grid lines in the last three cases. The maximum error in the computed longitudinal velocity was about 0.2%. These comparisons show that the parabolic solution procedure is correct, and that the rotating-grid procedure is mathematically accurate.



(a) The computed grid lines showing the flow configuration.

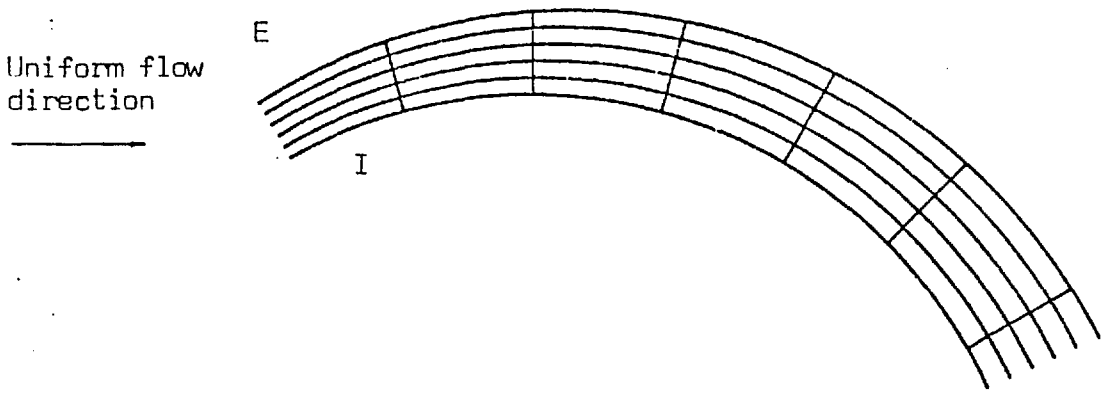


(b) Angles of inclination of the grid lines.

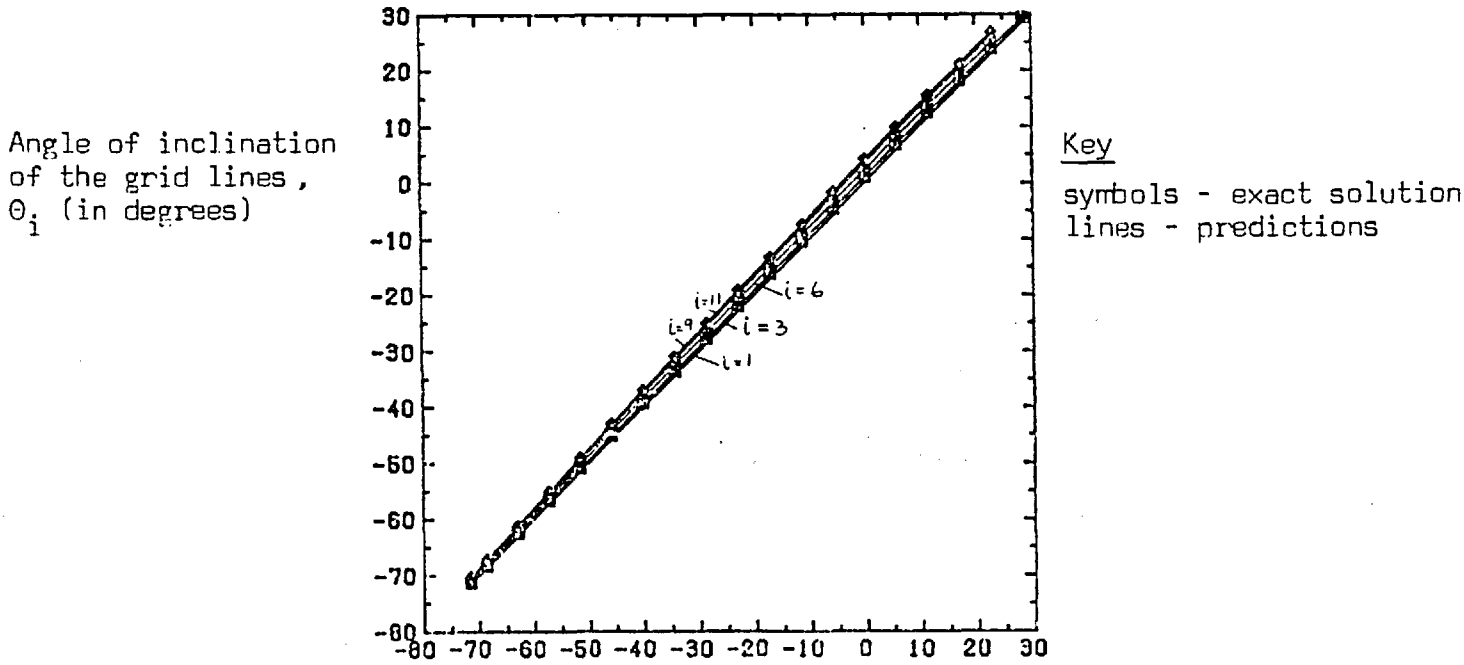


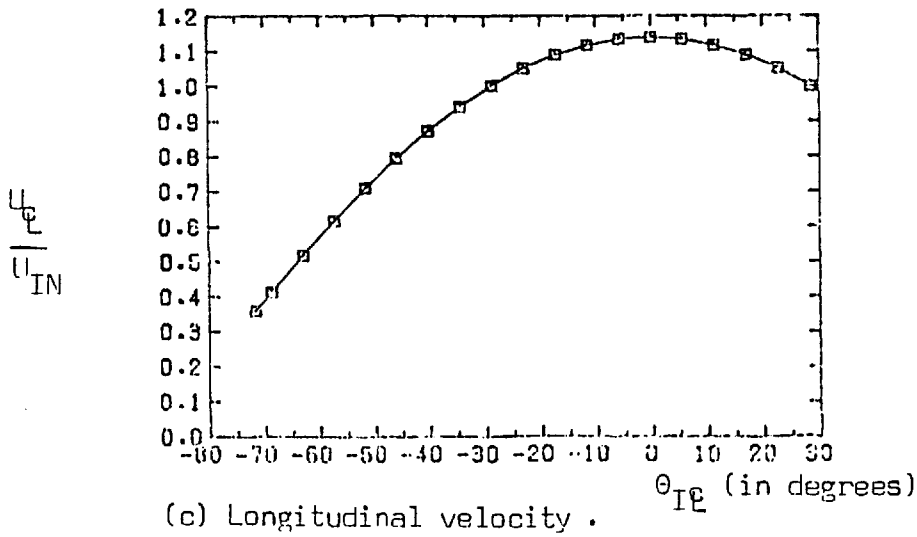
(c) Longitudinal velocity.

FIG. 4.2: Predictions of uniform flow in curved domain: $R_I = 12$, $R_E = 14$, distance between centres, $a = 0$.



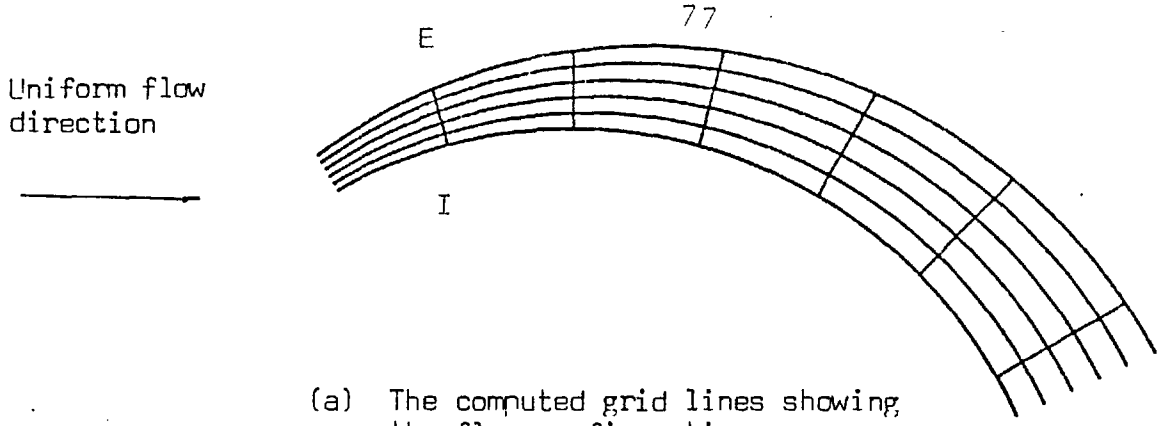
(a) The computed grid lines showing the flow configuration.



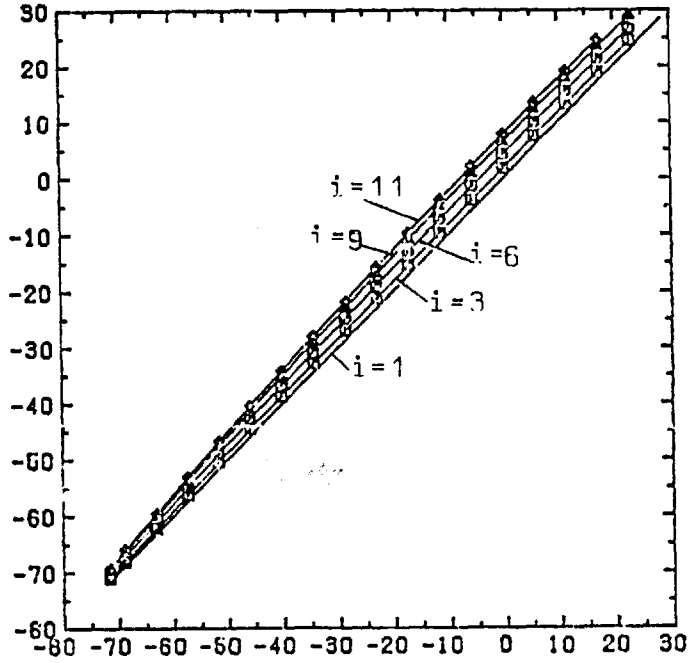


(c) Longitudinal velocity.

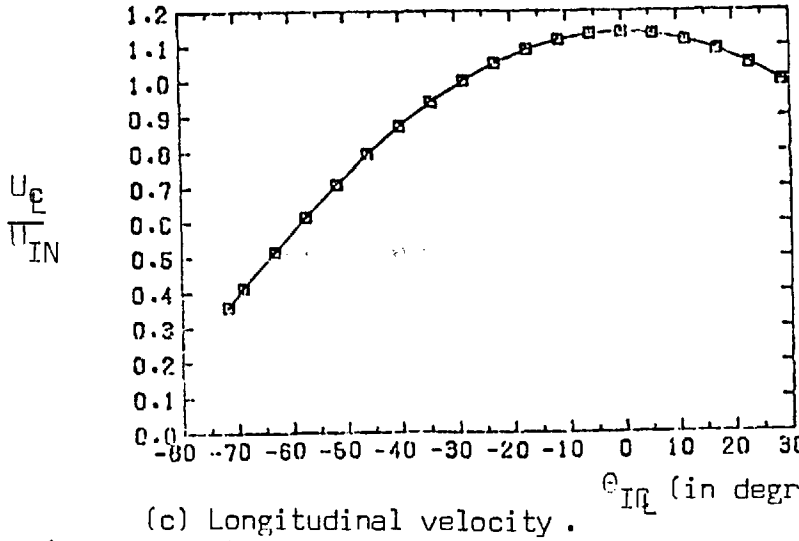
FIG. 4.3: Prediction of uniform flow in curved domain: R_I = 12, R_E = 14, distance between centres, a = 1.0.



(a) The computed grid lines showing the flow configuration.

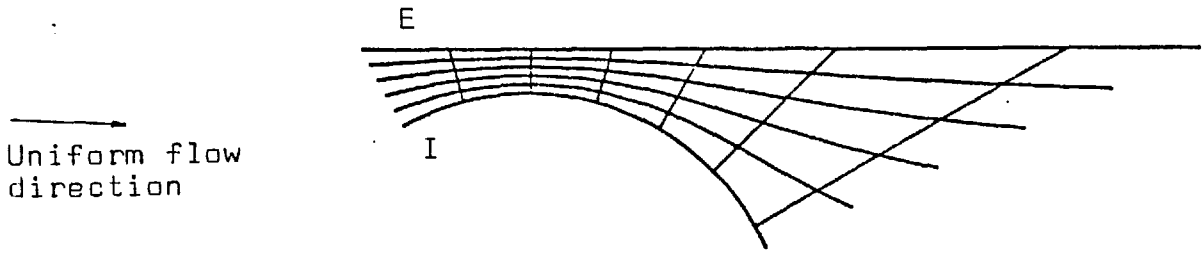


(b) Angle of inclination of the grid lines.

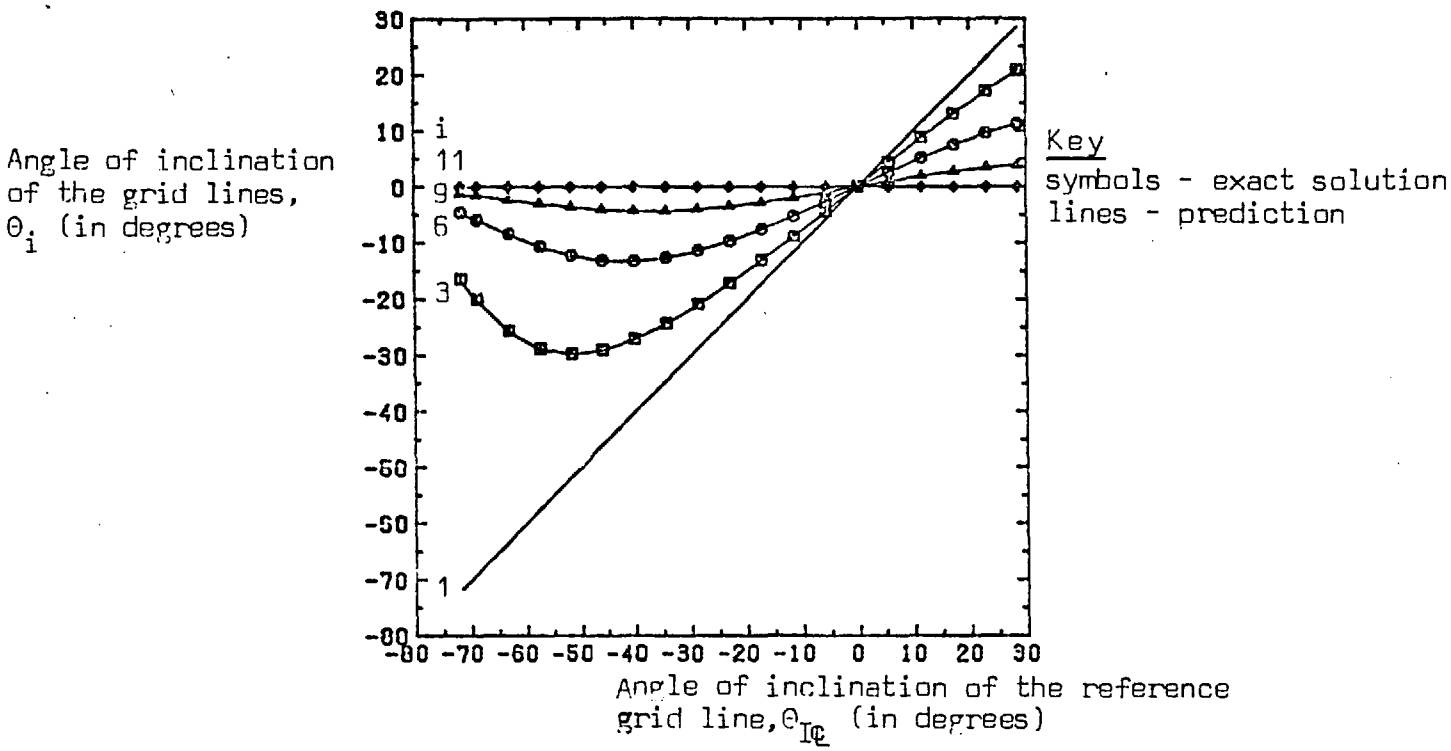


(c) Longitudinal velocity.

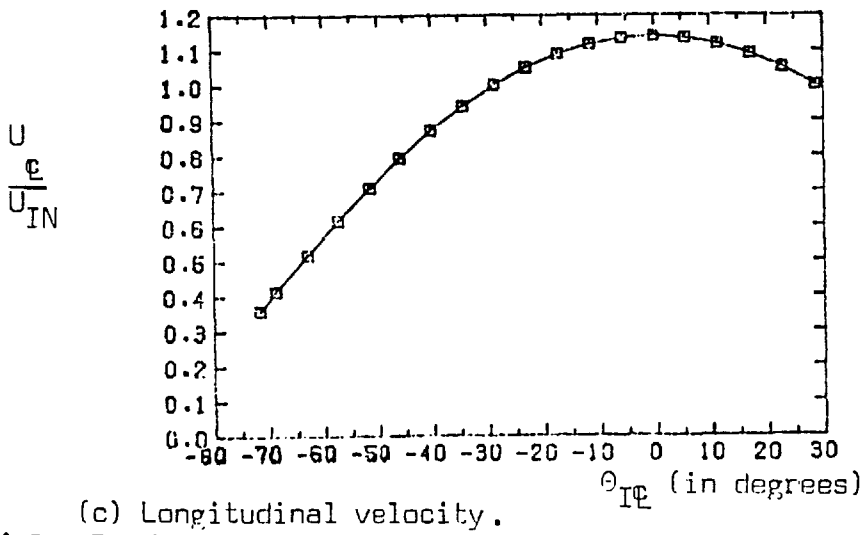
FIG. 4.4 Prediction of uniform flow in curved domain: $R_I = 12$, $R_E = 14$, distance between centres, a = 1.9.



(a) The computed grid lines showing the flow configuration.

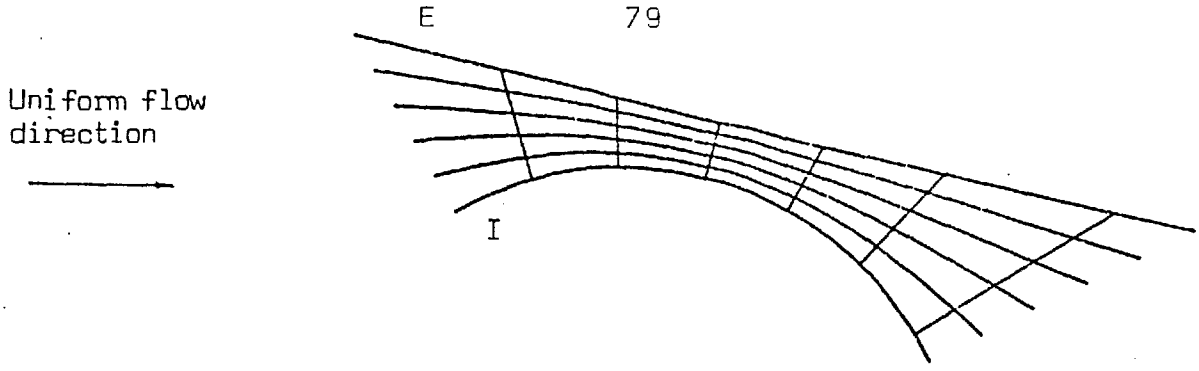


(b) Angles of inclination of the grid lines.

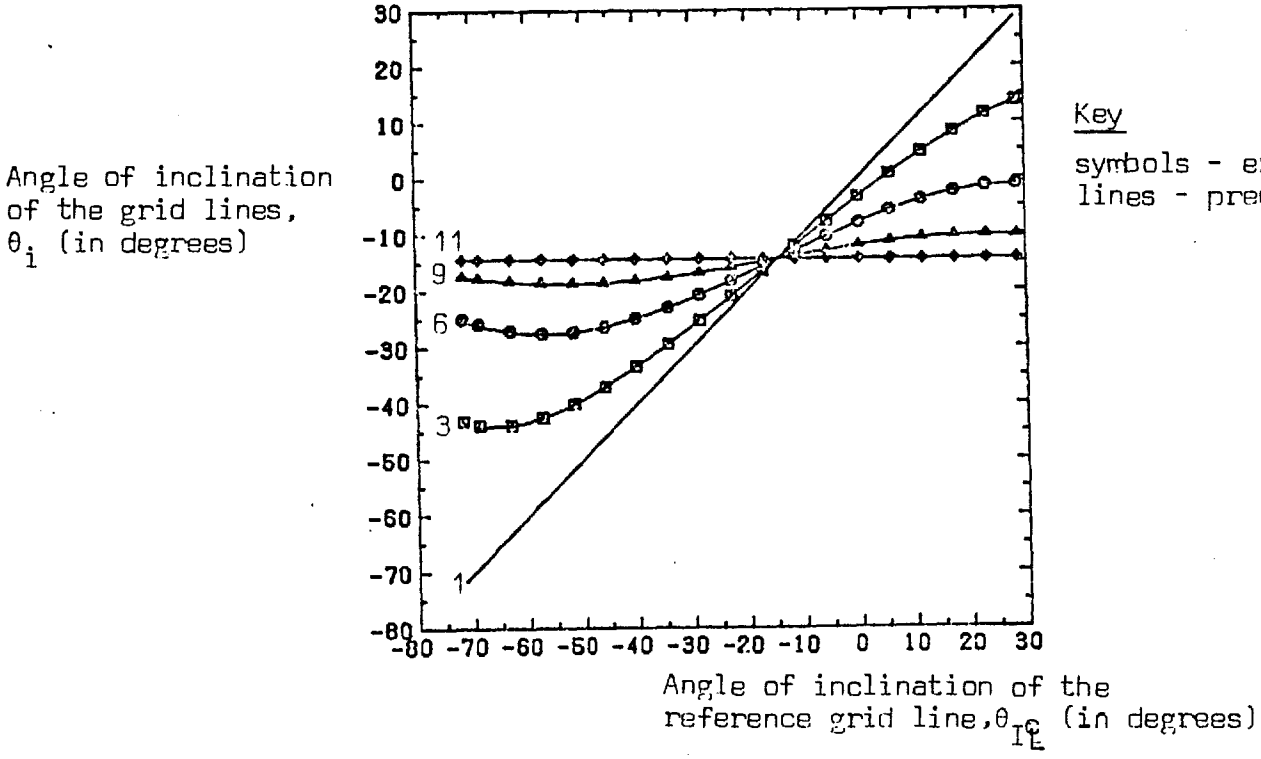


(c) Longitudinal velocity.

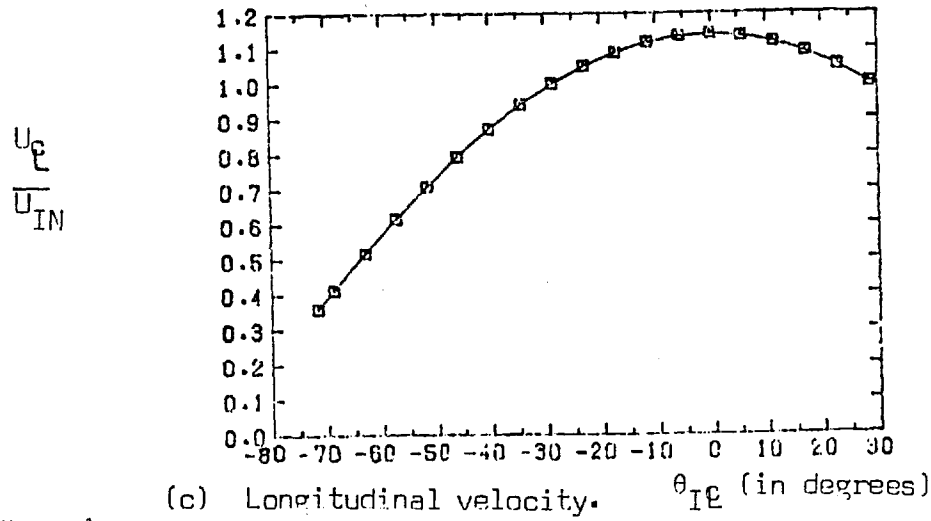
FIG. 4.5: Predictions of uniform flow in curved domain: $R_I = 12$, $\theta_E = 0$.



(a) The computed grid lines showing the flow configuration.

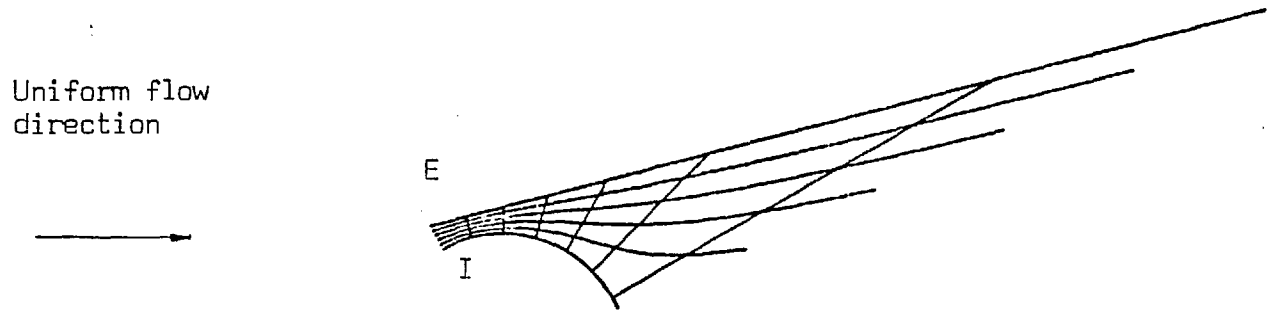


(b) Angles of inclination of the grid lines.

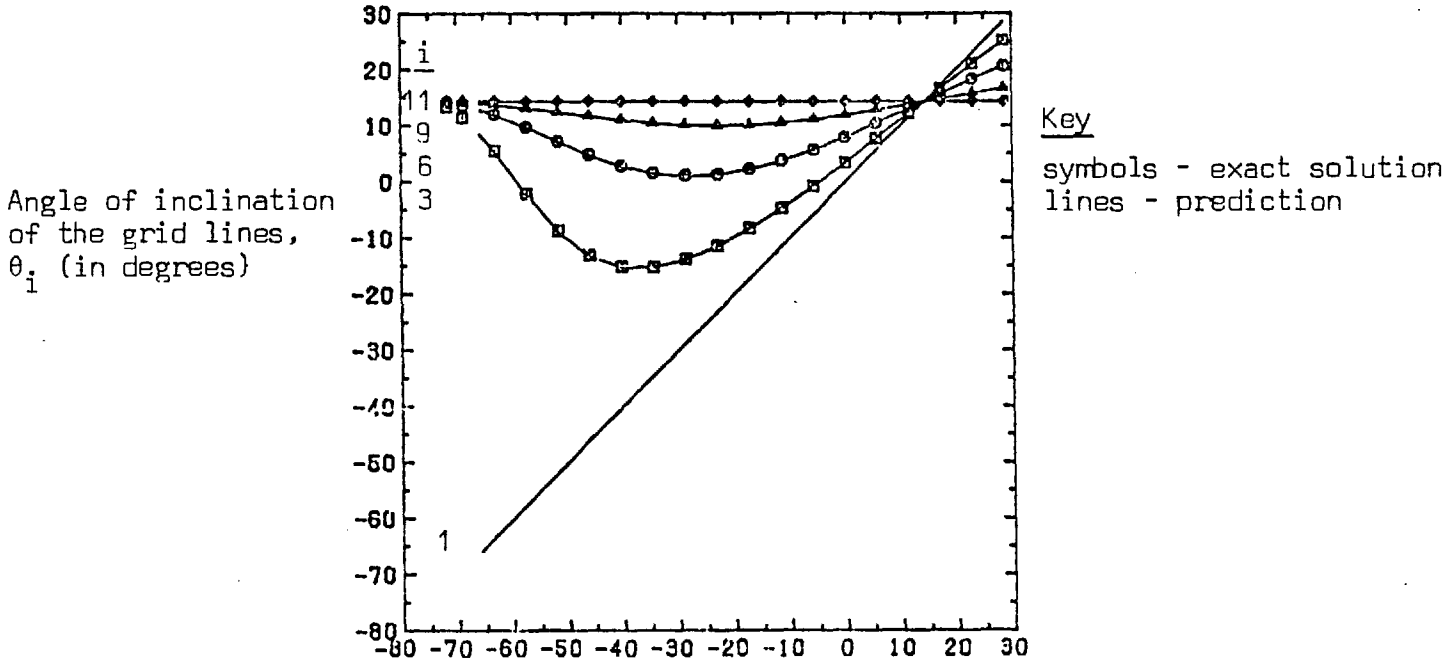


(c) Longitudinal velocity.

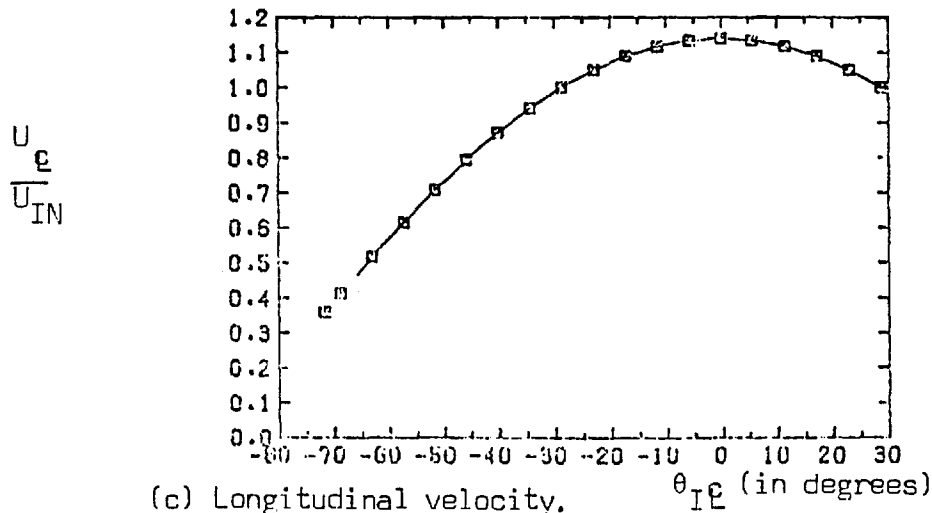
FIG. 4.6: Prediction of uniform flow in curved domain $R_I = 12$, $\theta_E = -14.3^o$.



(a) The computed grid lines showing the flow configuration.



(b) Angles of inclination of the grid lines.



(c) Longitudinal velocity.

FIG. 4.7: Prediction of uniform flow in curved domain $R_I = 12$, $\theta_E = 14.3°$.

4.3 The Radial Pool Problem

4.3.1 Problem specification

To test the mathematical accuracy of the hyperbolic solution procedure, the steady supercritical flow of warm water issuing from a steady source and spreading radially above cold stagnant water is predicted. An exact analytical solution of this problem can be derived if heat and mass transfers to and from the pool are neglected. The derivation of the exact solution is given in Appendix E. Figure 4.8 illustrates the flow situation and a typical grid distribution.

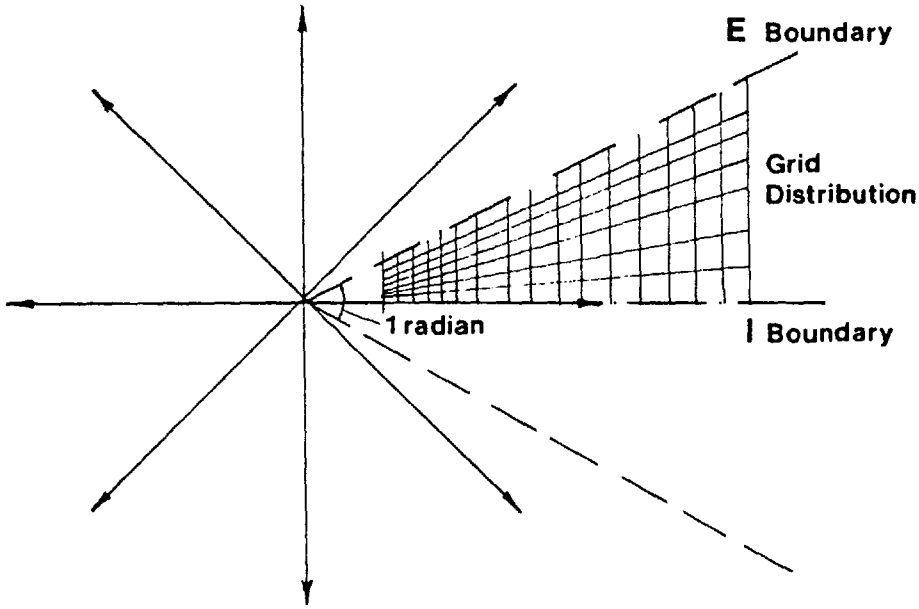
Computations are performed for two test cases:

(i) Flow with initial Froude number = 1.19;

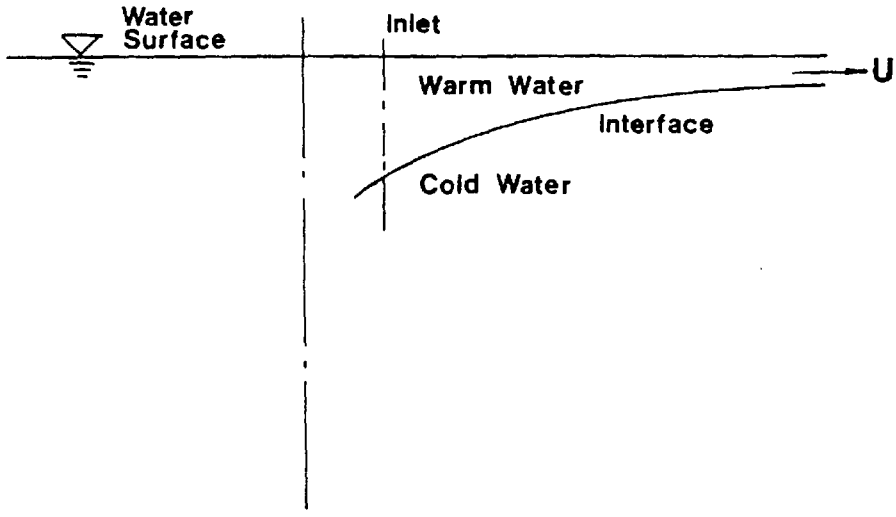
(ii) Flow with initial Froude number = 9.36.

4.3.2 Computational details

Preliminary calculations showed that the longitudinal velocity changed rapidly near the inlet, but more gradually further downstream, so an expanding grid is employed in the longitudinal direction. The practice is to increase the value of the forward step size, δx, by a constant factor, FRA, as the marching integration progresses from the inlet to the exit plane. In each case, the exit plane is 40 initial half-widths downstream.



Plan



Vertical Section

Fig. 4.8: Flow Domain and Grid Distribution for Steady Radial Pool Problem

Some important computational information are:

Table 4.2: Computational details for the radial pool problem.

FROUDE NUMBER	1.19	9.36
Number of cross-stream grid points, N	20	20
Number of forward steps	410	275
Initial forward step size, $\frac{\delta x}{b}$	1×10^{-2}	4×10^{-2}
Incremental factor, FRA	1.01	1.01
Number of iterations at each cross-stream plane	6	6
Computer time in CDC 6600 secs,	112	80

Grid-dependency tests are carried out in each case by varying N, $\frac{\delta x}{b_o}$, and FRA. Figures 4.9 and 4.10 show the predicted longitudinal velocity variations, using various grid sizes, for the cases Fr. = 1.19 and 9.36, respectively. The low sensitivity of the predictions to the changes in grid sizes may be noted.

Boundary Conditions

The inlet conditions, and the conditions along the E boundary are prescribed from the exact solution, derived in Appendix E. There exists a unique relationship between the radial distance from the virtual origin of the flow to any point and the values of the flow variables, U, V and Z at that point.

Hence, the variables are evaluated as follows:

(1) The following equation is solved to yield Z,

$$R\sqrt{(C_1-2\lambda z)}-Q_{IN} = 0 \qquad ;(4.3.1)$$

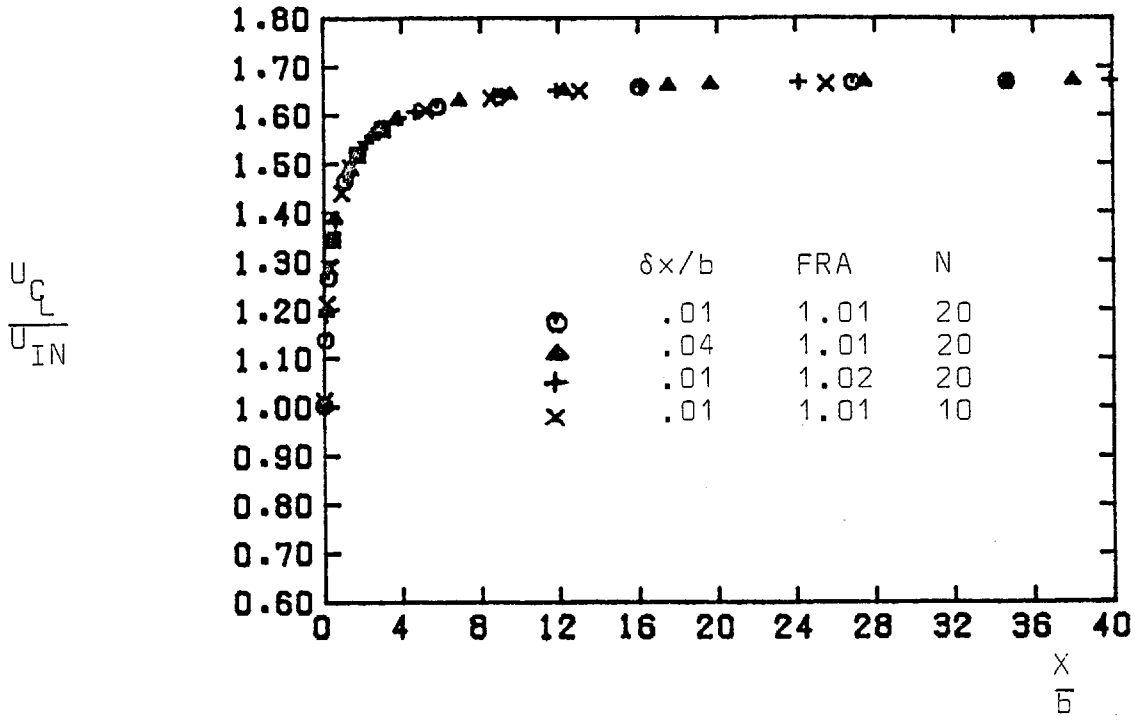


FIG. 4.9: TEST FOR GRID-DEPENDENCE; FR=1.19.

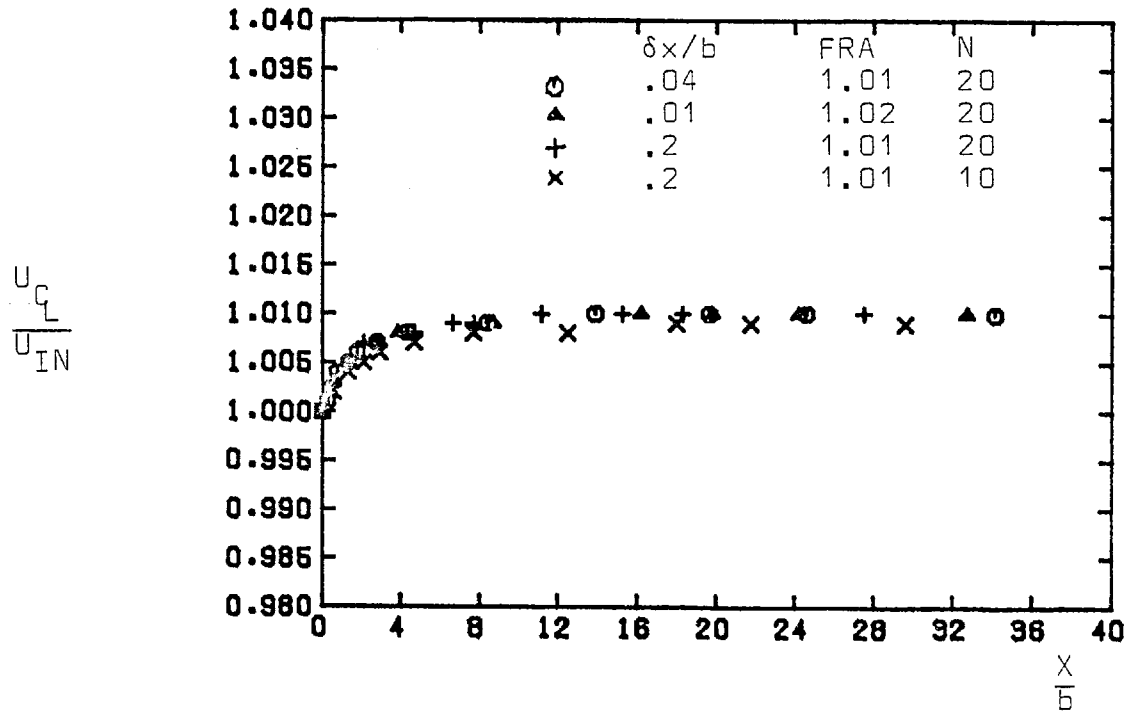


FIG. 4.10: TEST FOR GRID-DEPENOENCE; FR=9.36.

(2) The lateral velocity, V, is then calculated from the relation,

$$V=\sqrt{(C_1-2\lambda z)}\ \sin\theta \qquad ;(4.3.2)$$

(3) The longitudinal velocity, u is calculated from the relation,

$$U=\sqrt{(C_1-2\lambda z)}\ \cos\theta \qquad ;(4.3.3)$$

where,

$$\lambda \equiv \frac{\Delta\rho}{\rho} g,$$

$$C_1 = U_{IN} + 2\lambda z_{IN},$$

$$Q_{IN} \equiv (UzR)_{IN},$$

*R is the radial distance from the origin to the point,

θ is the angle of inclination of the s-grid line to the x-axis,

The I-boundary is a symmetry axis, hence, the following conditions are prescribed along it:

$$V_I = 0,$$

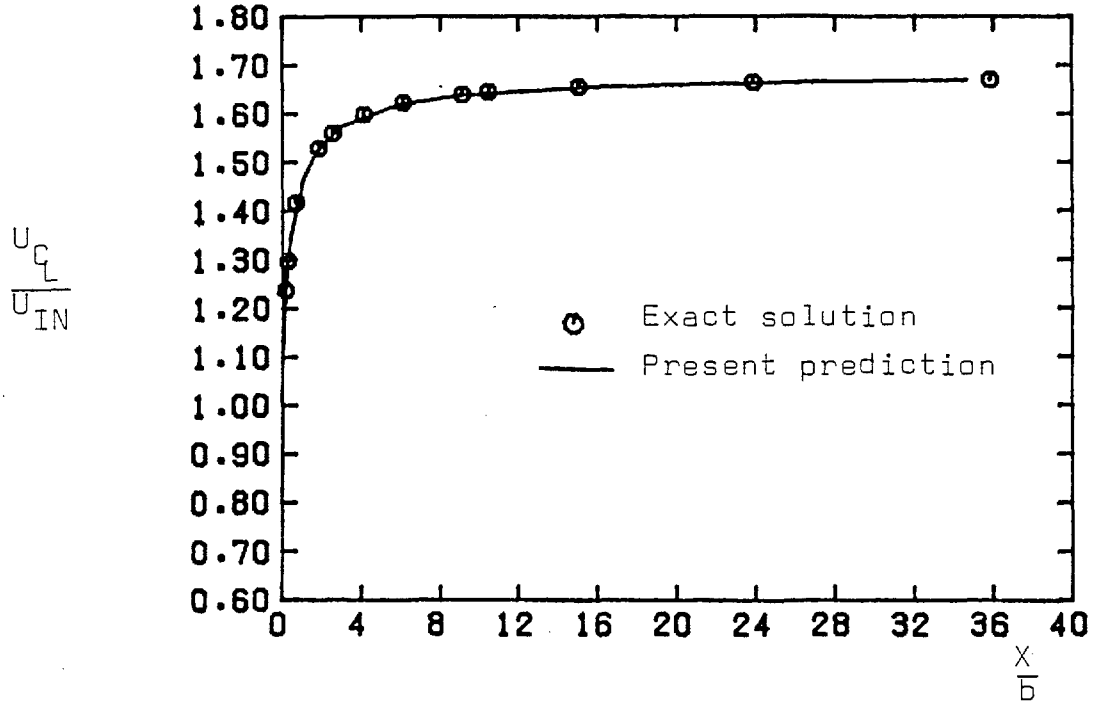
$$\frac{\partial U}{\partial y} = 0, \qquad (4.3.4)$$

$$\frac{\partial z}{\partial y} = 0.$$

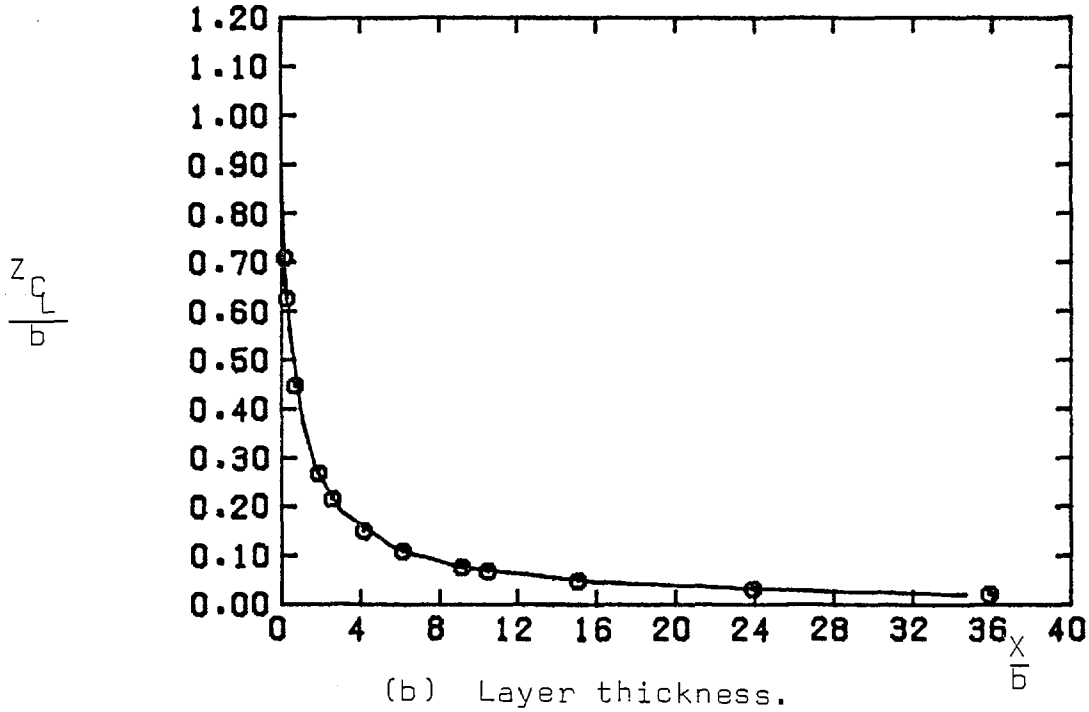
4.3.3 Results and discussion

The predictions of the longitudinal variations of the longitudinal velocity and the layer depth are comapred with the exact solutions, for the two Froude numbers in Figures 4.11 and 4.12, respectively. It is seen that the agreement is excellent in both cases. It may, therefore, be concluded that the hyperbolic solution procedure is mathematically accurate.

*NOTE: Since attention is confined to a segment of 1 radian, R is also equal to the length of the arc subtended by this angle.

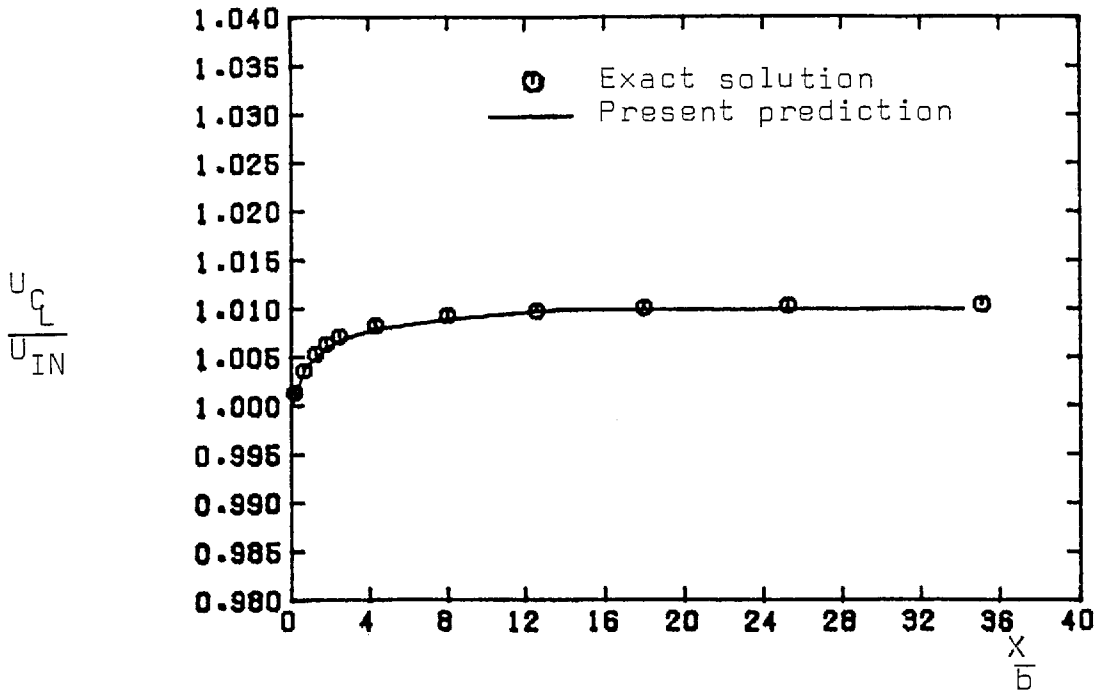


(a) Longitudinal velocity.

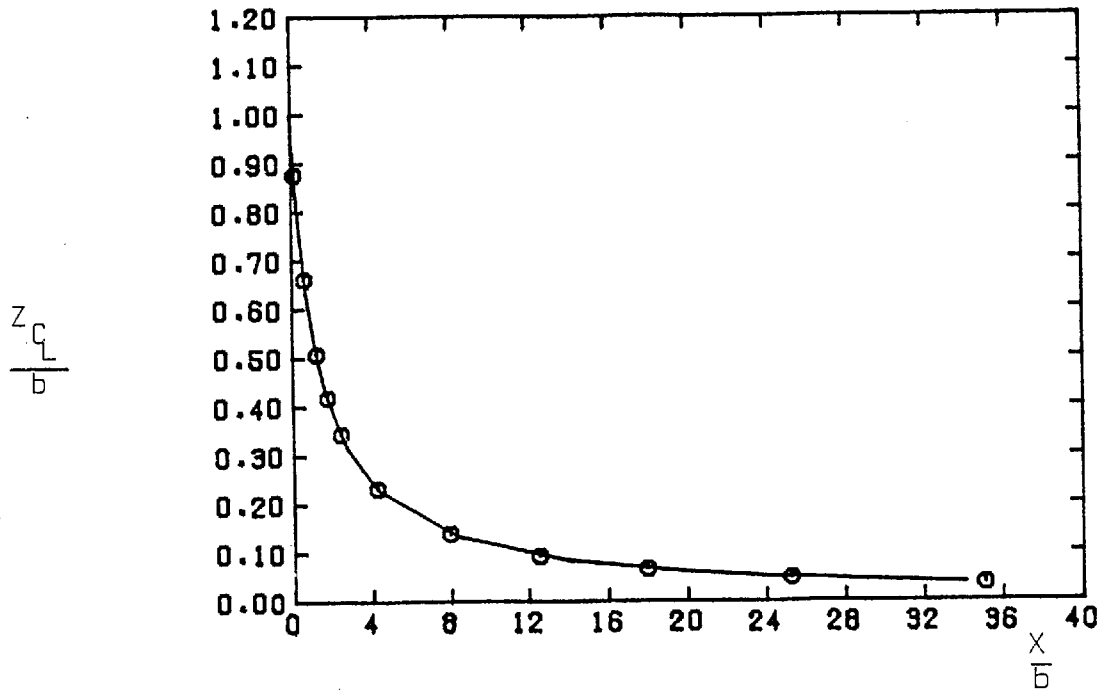


(b) Layer thickness.

FIG. 4.11: COMPARISON OF THE PREDICTED PROPERTIES OF THE RADIAL POOL WITH THE EXACT SOLUTION; FR=1.19.



(a) Longitudinal velocity.



(b) Layer thickness.

FIG. 4.12: COMPARISON OF THE PREDICTED PROPERTIES OF THE RADIAL POOL WITH THE EXACT SOLUTION; FR=9.36.

4.4 Subcritical Laminar Channel Flow

4.4.1 Problem specification

Subcritical flows in channels are, in general, elliptic or partially-parabolic. However, in the presence of viscous effects, the flows may often be treated as parabolic if recirculation zones are absent. This occurs when the viscous forces predominate over the pressure forces, as is the case in developing flows in straight channels. Schlichting (1968) presented an analytical solution of the developing flow in a two-dimensional channel. The solution was obtained by matching together two integration schemes: one being carried out in the downstream direction and the other in the upstream direction. The first scheme started from a plug profile and treated the problem as the development of boundary layers, along the walls, in an accelerated flow. The second scheme started from a fully-developed parabolic profile and calculated deviations from this asymptotic flow, in the upstream direction. The two solutions were then matched at a station where both still applied.

4.4.2 Computational details

As with the previously reported computations, grid-dependency tests were carried out. The computational details for grid-independent results are:

Table 4.3: Computational details for subcritical laminar channel flow.

VARIABLE	VALUE
Number of cross-stream grid points, N	20
Number of forward steps	100
Forward step size, $\frac{\delta x}{bRe}$	10^{-3}
Number of iterations at each cross-stream plane	3
Computer time in CDC 6600 secs.	6

Boundary Conditions

The initial and boundary conditions employed in the computations are:

At inlet,

$$\begin{aligned} U &= U_{IN} \\ V &= 0 \\ z &= z_{IN} \end{aligned} \qquad .(4.4.1)$$

The I-boundary is a symmetry axis along which,

$$\begin{aligned} \frac{\partial U}{\partial y} &= 0 \\ V &= 0 \\ \frac{\partial z}{\partial y} &= 0 \end{aligned} \qquad .(4.4.2)$$

Finally, the E-boundary is a wall along which,

$$\begin{aligned} U &= 0 \\ V &= 0 \\ \frac{\partial z}{\partial y} &= 0 \end{aligned} \qquad .(4.4.3)$$

4.4.3 Results and discussion

The rate of development of the laminar velocity profiles in the channel depends on the Reynolds number of the flow. This dependence is removed by normalising the axial distance from inlet with the Reynolds number, thus:

$$\bar{x} = \frac{x}{b\ Re} \qquad .(4.4.4)$$

The present predictions are compared with the analytical solution of Schlichting in Figure 4.13. The agreement is seen to be quite good.

4.5 Concluding Remarks

In this chapter, model predictions were compared with analytical solutions to three flow problems. The agreement was very good in each case. One of the comparisons showed that the rotating-grid procedure for computing layer flows with curvature is mathematically accurate. The parabolic and the hyperbolic solution procedures have also been validated. These lend confidence to the use of these procedures in the prediction of real flow situations in forthcoming chapters.

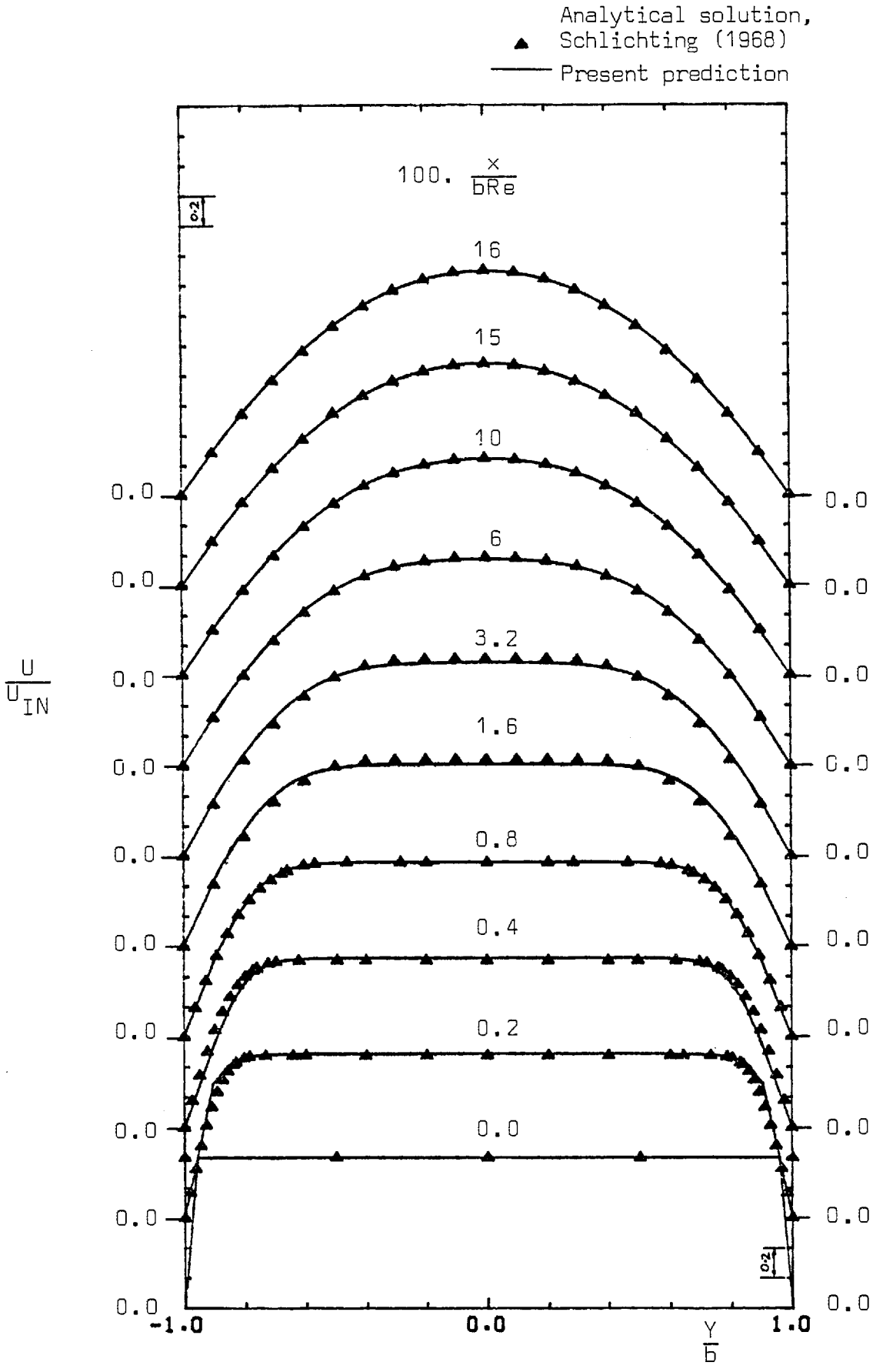


FIG. 4.13: PREDICTION OF THE LAMINAR DEVELOPING FLOW IN A STRAIGHT OPEN CHANNEL

CHAPTER 5

PREDICTION OF HEATED SURFACE DISCHARGES

5.1 Introduction

In this chapter, the predictions of heated surface discharges in both laboratory and field situations are reported. The extensive study of the available experimental data on heated surface discharges carried out by Dunn et al (1975) resulted in the conclusions that fairly accurate measurements in well-controlled laboratory experiments existed, but the field measurements were not very reliable. Field data may therefore not be suitable for quantitative comparisons with mathematical models, although on average they will show the right qualitative trends. The objective of the present work is to achieve good quantitative comparisons with the laboratory data, whilst seeking only qualitative agreement with the field data. All the flows considered in this chapter are supercritical, so the hyperbolic solution procedure is employed throughout.

The chapter commences with a discussion of the mathematical treatment of various physical phenomena affecting the dispersion of heated surface discharges. The predictions of laboratory discharges into stagnant surroundings are then presented, followed by the predictions of laboratory discharges into moving ambients. The chapter ends with the comparisons of the present model predictions with predictions by other authors of a few laboratory and field data.

5.2 Treatment of Relevant Physical Phenomena

The flow and heat transfer of heated surface discharges are influenced by various physical phenomena. The ways in which

some of the most important are represented mathematically are discussed in this section. Special emphasis is laid on the simplicity of the models; in line with the philosophy of the present study.

Entrainment of Ambient Fluid

The most important means of jet dilution and temperature reduction in the near-field is through the entrainment of ambient fluid. Vertical entrainment through the bottom of the layer is, in general, much more important than lateral entrainment through the sides, because of the much larger surface area of the former.

The vertical entrainment rate is calculated from the relation:

$$\dot{m}''_V = E \rho (U - U_o) \qquad ,(5.2.1)$$

where,

E is the entrainment coefficient, which incorporates the effect of buoyancy in damping turbulent entrainment. It may be deduced from the experimental data of Chu and Vanvari (1975) as:

$$E = 0.048e^{-12.5Ri} \qquad ,(5.2.2)$$

where,

Ri is the overall Richardson number.

The lateral entrainment rate is calculated from the relation:

$$\dot{m}''_h = \alpha_h \rho (U - U_o) \qquad ,(5.2.3)$$

where,

$$\alpha_h = 0.048.$$

Layer Spreading

The rate of spread of the surface layer is prescribed indirectly by specifying the lateral velocity boundary condition at the edge of the layer. This is taken as the sum of a buoyant and a non-buoyant contributions. The buoyant contribution is taken as equal to the rate of spread of density wedges, deduced by Benjamin (1968) and Kao (1977) as:

$$U\left(\frac{db}{dx}\right)_{buoyant} = \left(2.0\ \frac{\Delta\rho}{\rho}\ gz\right)^{\frac{1}{2}} \qquad .(5.2.4)$$

The non-buoyant contribution is taken as the rate of spread of non-buoyant two-dimensional jets, thus:

$$\left(\frac{db}{dx}\right)_{non\text{-}buoyant} = 0.22 \qquad .(5.2.5)$$

Therefore at the E-boundary, the lateral velocity boundary condition* is

$$V_E = 0.22\ U_E + \left(2.0\ \frac{\Delta\rho}{\rho}\ gz_E\right) \qquad .(5.2.6)$$

Surface Heat Transfer

Heat is transferred to and from the water surface by the processes of convection, conduction, evaporation, radiation condensation, etc. There exist many elaborate methods for calculating each of these contributions. Spalding (1975) and Stolzenbach (1976) presented some of these. The method adapted here is to lump the effects of all these together in a heat transfer rate $\dot{Q}$", which is calculated from the relation:

$$\dot{Q}" = -\alpha(T - Teq) \qquad ,(5.2.7)$$

*NOTE: This treatment ensures that when the jet is highly buoyant, the buoyant contribution dominates, and when the jet is only mildly buoyant, the non-buoyant contribution dominates.

where,

α is the heat transfer coefficient,

and T_{eq} is the equilibrium temperature, i.e., the temperature that the water body would attain in the absence of the discharge.

Both T_{eq} and α depend on several factors which are usually difficult to determine. Stolzenbach (1976) argued that T_{eq} could be replaced by the ambient temperature T_o, if α was suitably adjusted. Experimental studies show that α is of order 0.001 - 0.003. The higher value is used in the present calculations except, where a different value is suggested by the authors of the experimental data. Sundaram and Wu (1973) argued that surface heat transfer is relatively unimportant in the near-field, in which the present model and most of the other existing mathematical models are valid. The present calculations do show this to be true, but it is, nevertheless included, in this model, for completeness, and because it does not introduce additional complexities.

Wind Effects

For heated surface discharges into natural water bodies, the wind exerts a shear stress, τ_s on the water surface which may be calculated from the relation:

$$\tau_s = \tfrac{1}{2} C_f \rho_{air} U_w^2 \qquad (5.2.8)$$

where,

$C_f/2$ is the shear-stress coefficient having a magnitude of about 0.003,

and, U_w is the wind speed at some short distance above the water surface. A formula for calculating this distance, based on field data, is presented by Sundaram and Wu (1973).

In the present numerical model, the x and y components of the wind shear stress are included as source terms of the respective momentum equations.

Equation of State

The equation of state relates density variations to the salinity, temperature, constituent concentration and pressure of the layer.

In the heated surface discharges being investigated, only the effects of temperatures are important: fresh-water flow is presumed. Many sophisticated formulae for relating density to temperature variations exist in the oceangraphic literature, for example, Hill (1962). However, a simple relation is used in this case, namely

$$\frac{\Delta\rho}{\rho} = - \beta\Delta T \qquad ,(5.2.9)$$

where,

$$\Delta\rho \equiv \rho_o - \rho \ ,$$

$$\Delta T \equiv T_o - T,$$

and β is the coefficient of expansion of water.

The value of β varies with temperature, so an average value for the temperature range of the experimental measurements is used.

5.3 Computational Details

In discharges into stagnant ambients, only one half of the layer needs to be treated, resulting in a saving in the computational grid requirement. However, in discharges into crossflowing streams, or when a transversely-blowing wind is present, the whole layer needs to be considered. Temperature decay is usually more rapid near the discharge than further downstream, so small forward step sizes are taken in the earlier region. The practice adopted is to increase the next forward step size by a constant factor, FRA, after each forward step has been taken. Grid-dependency tests are carried out to ensure that the presented results are independent of the grid sizes in both directions.

Some typical computational details are tabulated below, for discharges into both stagnant* and crossflowing ambients.

Table 5.1: Computational details for the predictions of heated surface discharges.

VARIABLE	Value for Stagnant Ambient	Value for Crossflowing Ambient
Number of cross-stream grid points, N	11	19
Number of forward steps	200	140
Initial size of forward step, $\frac{\delta x}{b}$	0.06	0.15
Incremental factor, FRA	1.01	1.01
Number of iterations at each cross-stream station	3	8
Computer time in CDC 6600 secs	40	100

*NOTE: The computational details for discharges into coflowing ambients are similar to those for stagnant ambient discharges.

Boundary Conditions

The initial conditions are prescribed as uniform everywhere, thus:

At inlet,

$$\begin{aligned} U &= U_{IN} \\ V &= 0 \\ z &= z_{IN} \\ T &= T_{IN} \end{aligned} \qquad .(5.3.1)$$

In the discharges into stagnant or coflowing surroundings, the I-boundary is a symmetry axis, along which,

$$\begin{aligned} \frac{\partial U}{\partial y} &= 0 \\ V &= 0 \\ \frac{\partial z}{\partial y} &= 0 \\ \frac{\partial T}{\partial y} &= 0 \end{aligned} \qquad .(5.3.2)$$

The E-boundary is a free boundary, with the following prescribed conditions:

$$\begin{aligned} \frac{\partial U}{\partial y} &= 0 \\ V_E &= 0.22\, U_E + \left(2.0\, \frac{\Delta\rho}{\rho}\, g z_E\right)^{\frac{1}{2}} \\ \frac{\partial z}{\partial y} &= 0 \\ \frac{\partial T}{\partial y} &= 0 \end{aligned} \qquad .(5.3.3)$$

In the discharges into crossflowing surroundings, both the I- and E-boundaries are free boundaries: one spreading in the direction of the ambient crossflow and the other against it.

The prescribed boundary conditions are:

$$\left(\frac{\partial U}{\partial n}\right)_{I,E} = 0$$

$$V_I = V_o - 0.22\, U_E - \left(2.0\, \frac{\Delta\rho}{\rho}\, g z_I\right)$$

$$V_E = V_o + 0.22\, U_E + \left(2.0\, \frac{\Delta\rho}{\rho}\, g z_E\right) \qquad ,(5.3.4)$$

$$\left(\frac{\partial z}{\partial n}\right)_{I,E} = 0$$

$$\left(\frac{\partial T}{\partial n}\right)_{I,E} = 0$$

where,

V_o is the lateral component of the crossflow velocity.

5.4 Prediction of Laboratory Discharges into Stagnant Surroundings

Of the numerous experimental investigations of heated discharges into stagnant surroundings (see Table 2.1), the ones with the most detailed measurements are those of Pande and Rajaratnam (1975b) and Wiuff (1977). Pande and Rajaratnam investigated five discharge flow conditions of which three are suitable for comparison with the present predictions. Wiuff investigated only one discharge flow condition; with the experiment being repeated several times. The present predictions are compared extensively to these four data sets.

The characteristic conditions of the discharges are:

Table 5.2: Discharge parameters for the main comparisons.

Run	Discharge Froude Number	Initial Aspect Ratio	Authors
1	2.59	1.00	Pande and Rajaratnam (1975b)
2	1.67	1.00	
3	1.32	3.06	
4	3.60	1.40	Wiuff (1977)

The present predictions are also compared to centre-line temperature decay data by Stolzenbach and Harleman (1971), Tamai et al (1969), and Hayashi and Shuto (1967).

In all the results presented in this section, the temperatures are normalised as,

$$T^+ \equiv \frac{T - T_o}{T_{IN} - T_o} \qquad ;(5.4.1)$$

the velocities are normalised as,

$$U^+ = \frac{U}{U_{IN}} \qquad ;(5.4.2)$$

and the distances are normalised as,

$$x^+ = \frac{x}{D} ,$$

$$y^+ = \frac{y}{D} , \qquad (5.4.3)$$

and $$z^+ = \frac{z}{D} ,$$

where,

D is the square root of the initial area of the discharge.

Figure 5.4.1 shows the comparison of the predicted lateral temperature distributions, at 8 cross-stream planes, to the experimental measurements of Run 1, (Froude number = 2.59.) The agreement is seen to be fairly good. It may be noted that, at planes near the outfall, the predictions do not extend laterally as far as the measurements. The reason for this is that the predictions are necessarily restricted to the main region of the jet in which the flow remains supercritical. The computation of mixed supercritical/subcritical flow is beyond the scope of the present study. It is seen that the predicted profiles spread almost linearly, in agreement with most experimental observations of warm surface jets.

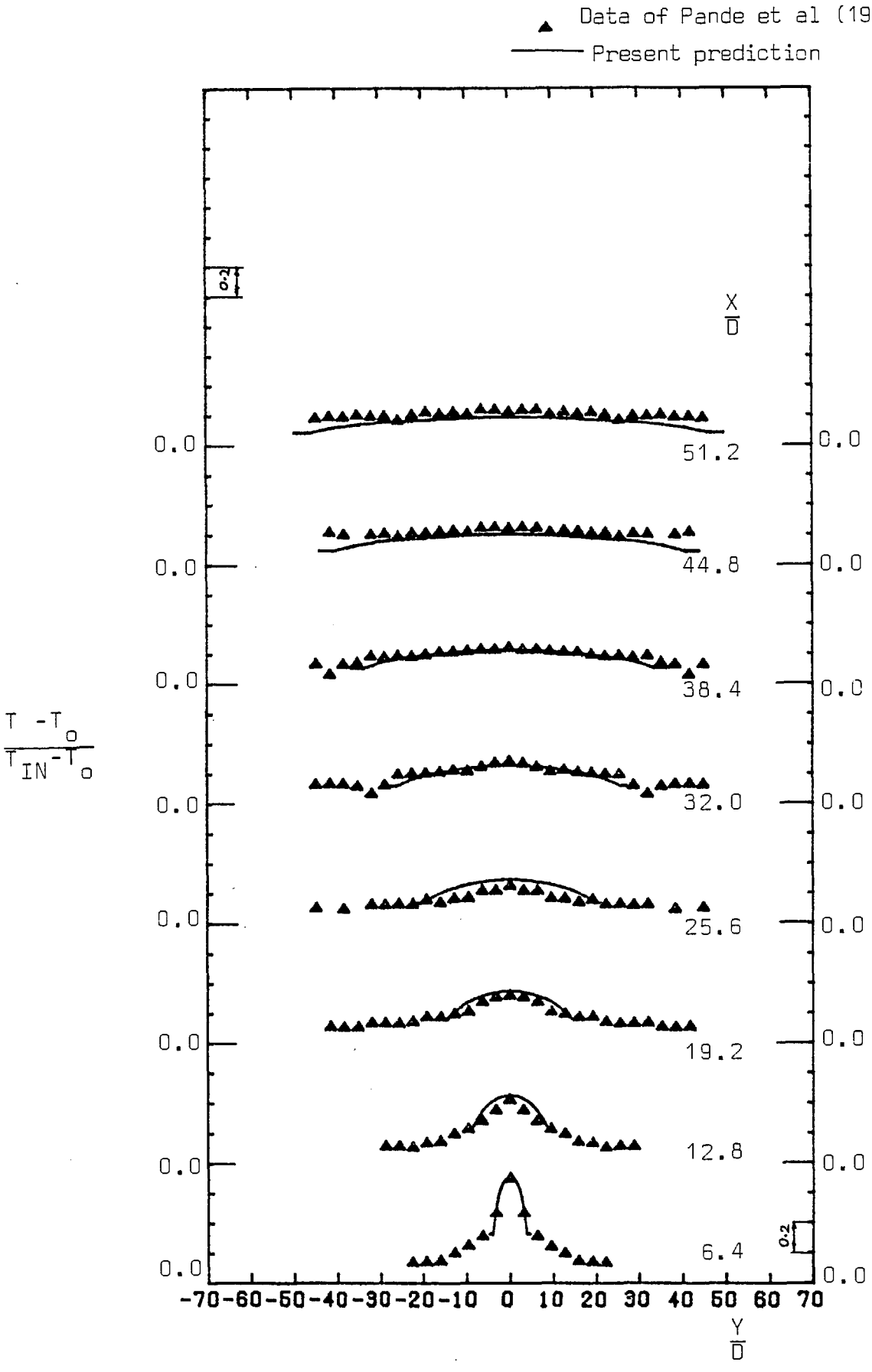


FIG. 5.4.1: PREDICTION OF THE TEMPERATURE DISTRIBUTION IN A HEATED SURFACE DISCHARGE; FR=2.59, A.R.=1.

Figure 5.4.2 shows the comparison of the predicted lateral distributions of the longitudinal velocities, at 9 cross-stream planes, with the measurements for the same experimental run. The agreement is also fairly good. Similar comparisons are shown for the remaining two experimental runs of Pande and Rajaratnam, (Froude numbers = 1.67 and 1.32) in Figures 5.4.3 and 5.4.4, and Figures 5.4.5 and 5.4.6, respectively. The agreement is seen to be mostly satisfactory, with the temperature predictions being somewhat the better. Figures 5.4.7 - 5.4.9 show the decays of the centre-line temperatures, for the 3 runs, and Figures 5.4.10 - 5.4.12 show the decays of the centre-line velocities. These are seen to be well predicted. Figure 5.4.13 shows the predicted temperature and velocity contours for Run 1. The temperature contours are in the upper half, and the velocity contours are in the lower half of this figure. It is seen that the temperatures decay faster than the velocities and the area within any given isotherm is smaller than the area within the corresponding isovel. These effects are even more pronounced in the contours for the Froude number = 1.67 case, shown in Figure 5.4.14. The reason for this is that the buoyancy produces an acceleration, through the pressure gradients, which increases the velocities but has no direct effect on the temperatures. This buoyancy effect becomes stronger as the Froude number decreases. Figure 5.4.15 shows the predicted contours for the Froude number = 1.32 case. The temperature contours are seen to be quite flat near the centre-line and the maximum temperatures are sometimes

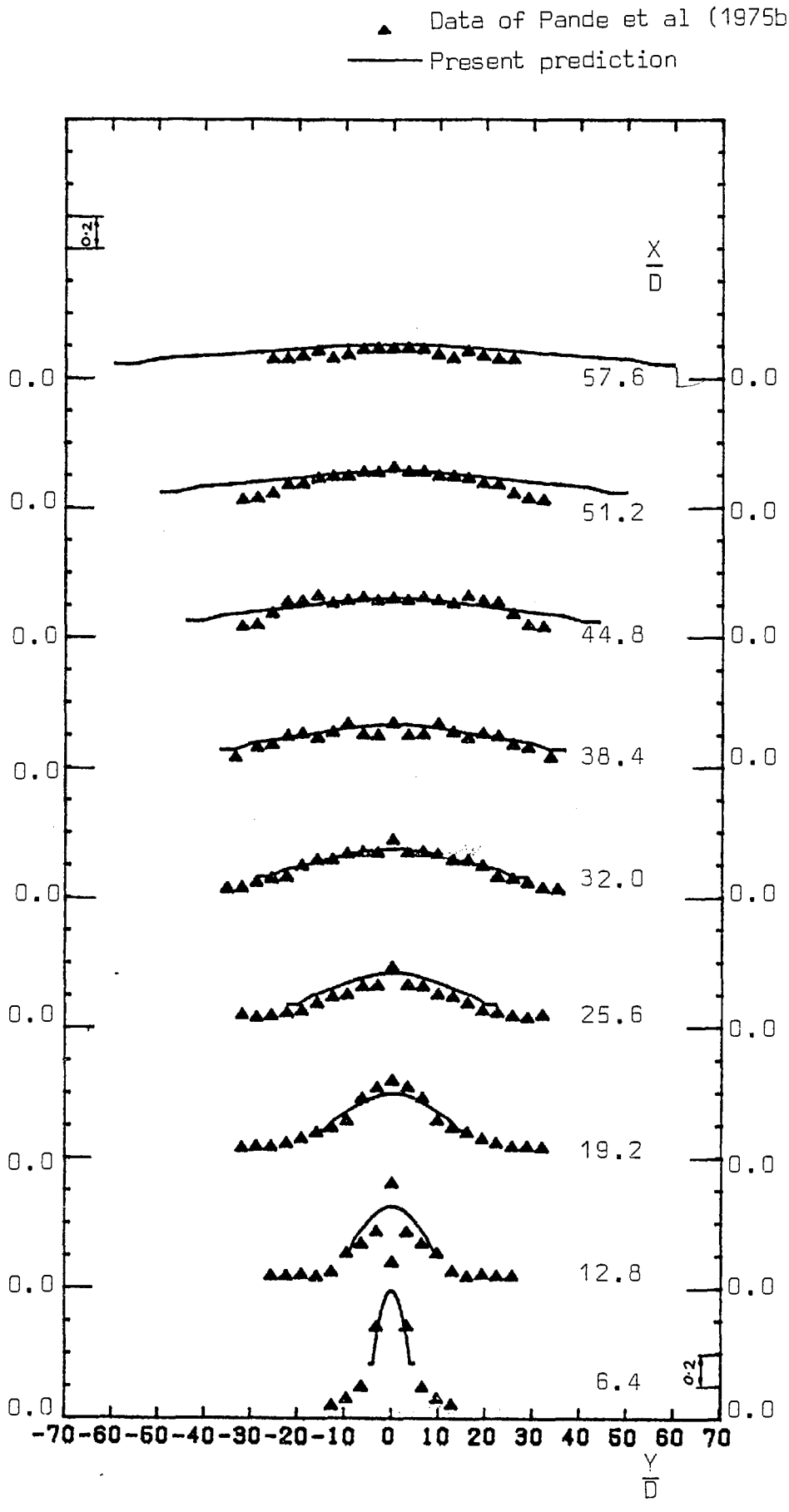


FIG. 5.4.2: PREDICTION OF THE LONGITUDINAL VELOCITY DISTRIBUTION IN A HEATED SURFACE DISCHARGE; FR=2.59, A.R.=1.

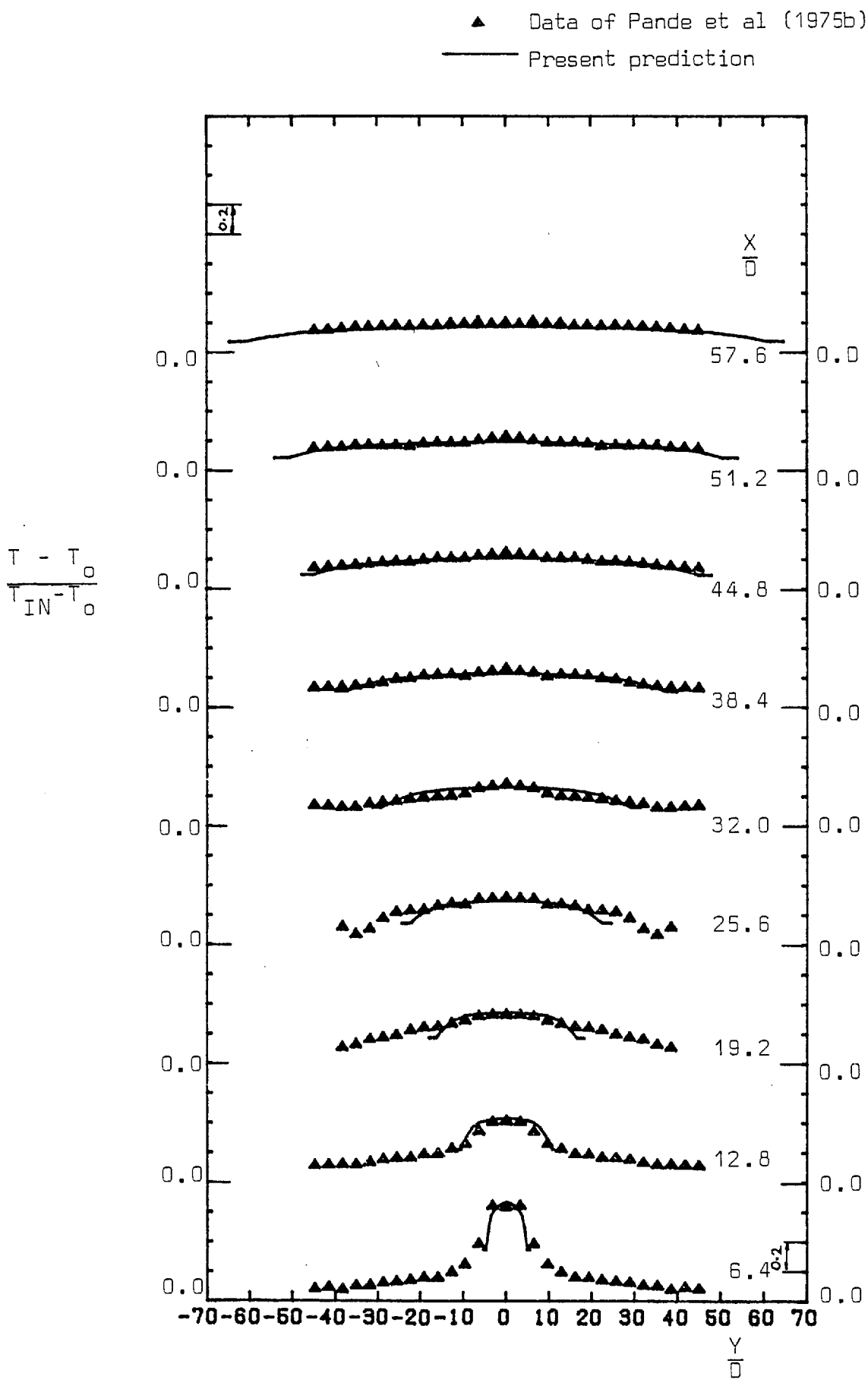


FIG. 5.4.3: PREDICTION OF THE TEMPERATURE DISTRIBUTION IN A HEATED SURFACE DISCHARGE; FR=1.67, A.R.=1.

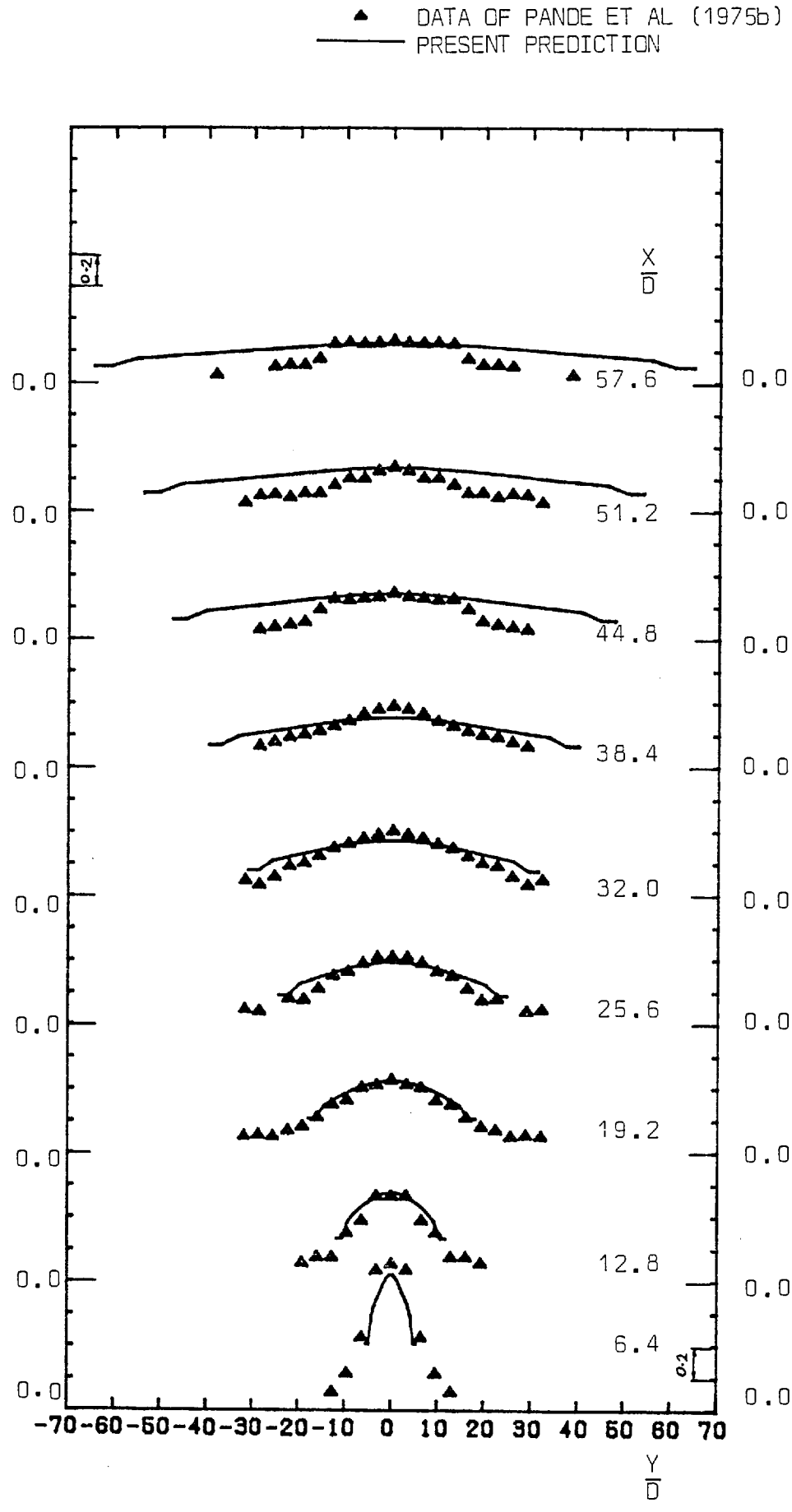


FIG. 5.4.4: PREDICTION OF THE LONGITUDINAL VELOCITY DISTRIBUTION IN A HEATED SURFACE DISCHARGE, FR=1.67, A.R.=1.

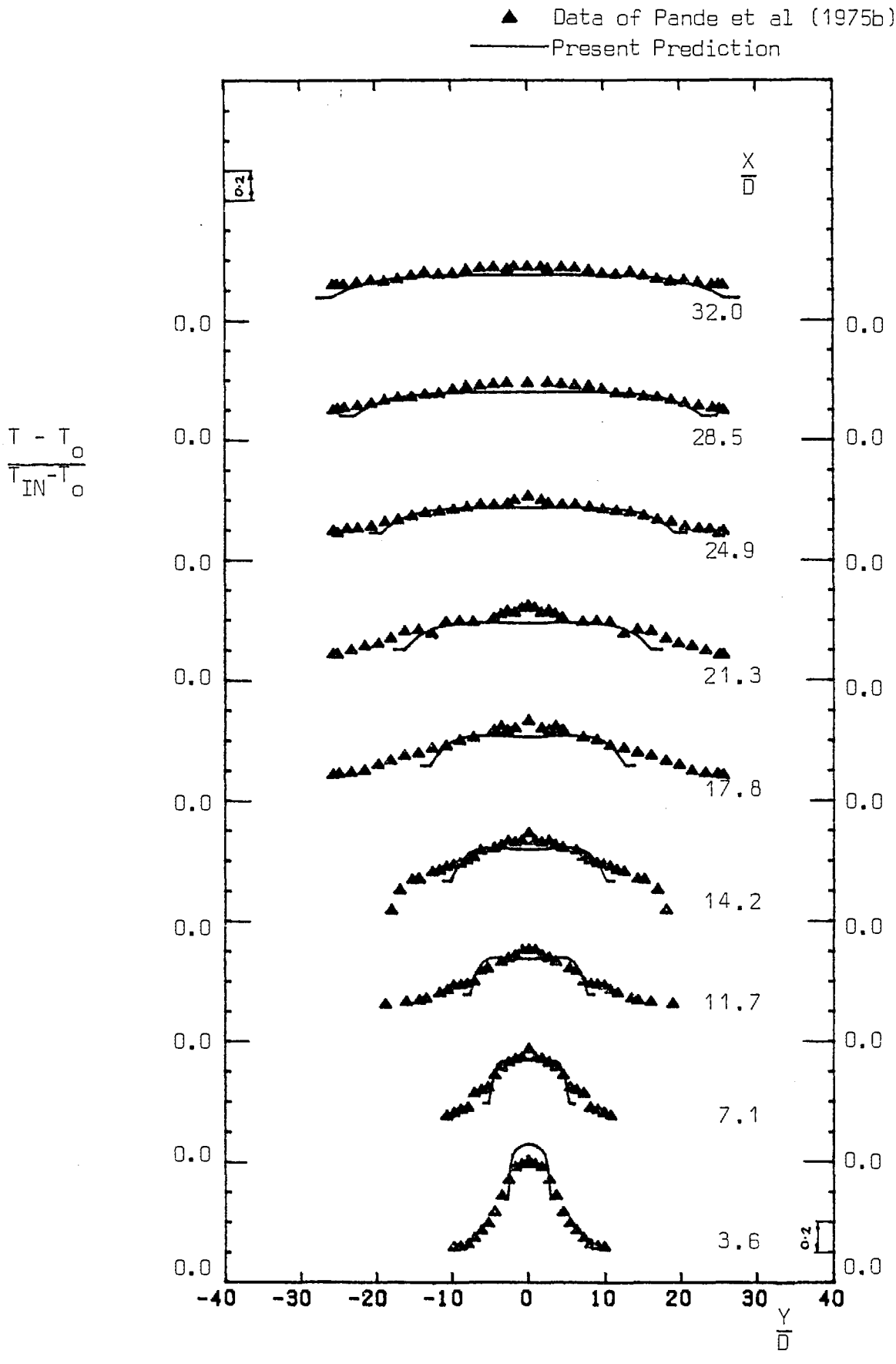


FIG. 5.4.5: PREDICTION OF THE TEMPERATURE DISTRIBUTION IN A HEATED SURFACE DISCHARGE; FR=1.32, A.R.=3.06

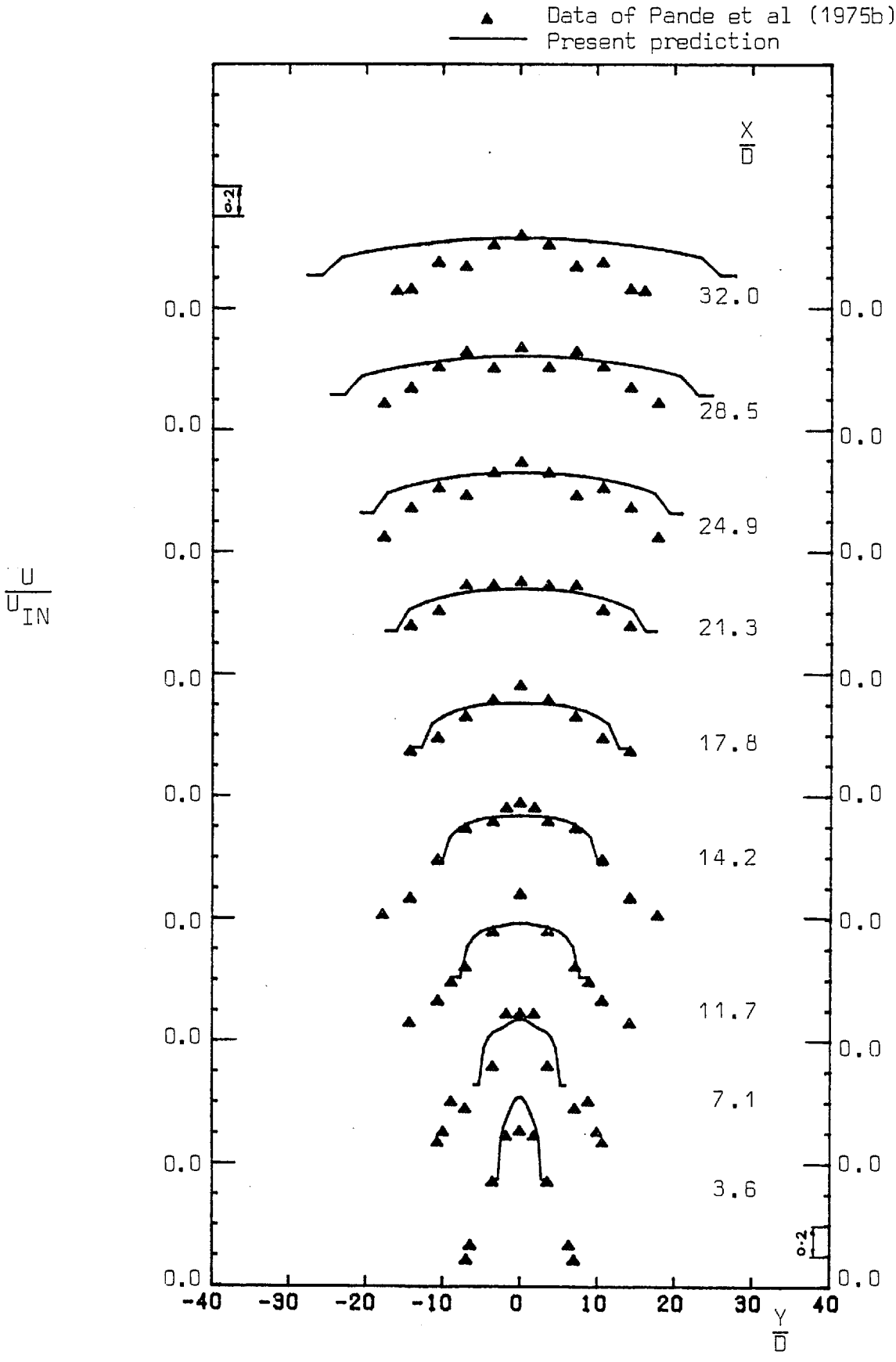


FIG. 5.4.6: PREDICTION OF THE LONGITUDINAL VELOCITY DISTRIBUTION IN A HEATED SURFACE DISCHARGE; FR=1.32, A.R.=3.06.

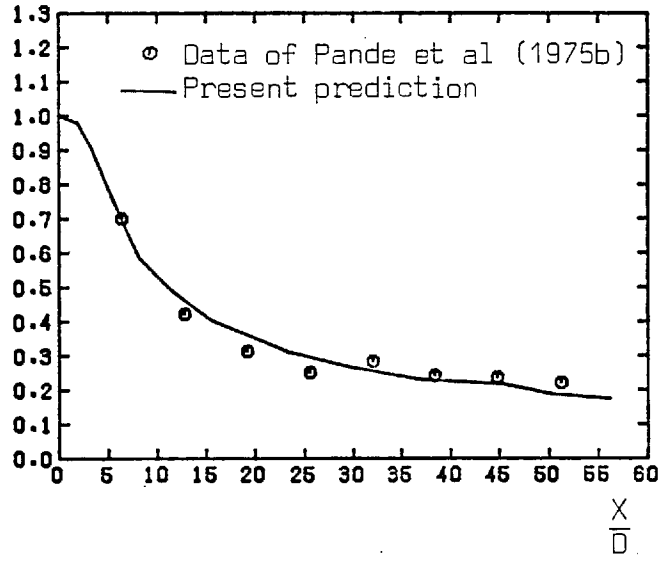


FIG. 5.4.7: CENTRE-LINE TEMPERATURE DECAY; FR=2.59, A.R.=1.

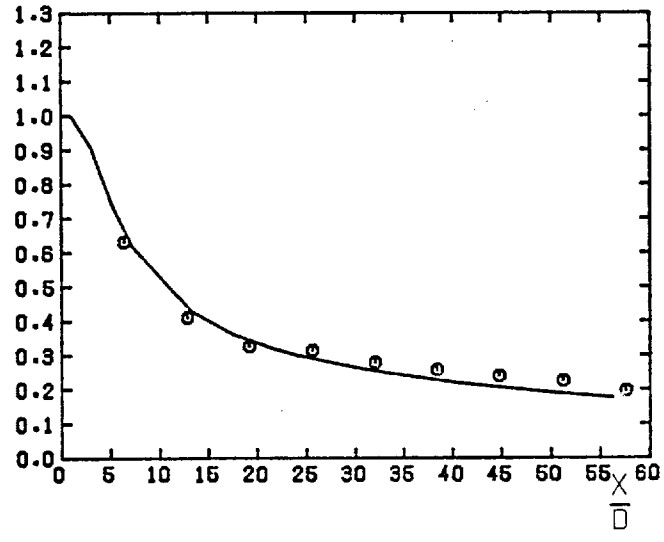


FIG. 5.4.8: CENTRE-LINE TEMPERATURE DECAY; FR=1.67, A.R.=1.

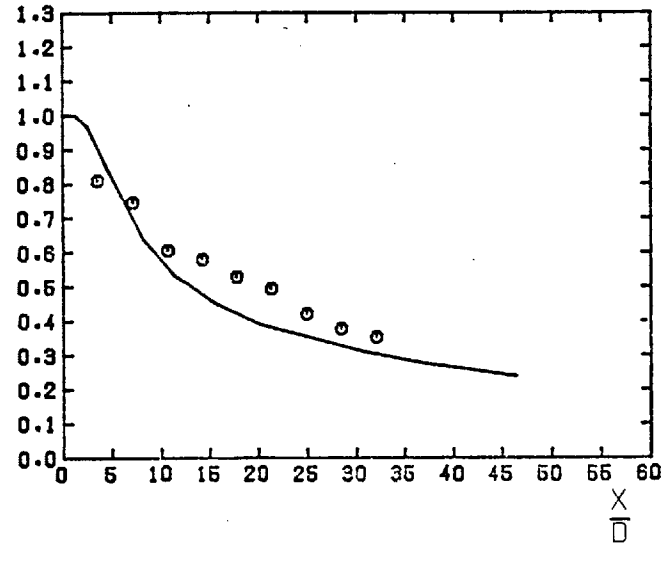


FIG. 5.4.9: CENTRE-LINE TEMPERATURE DECAY; FR=1.32, A.R.=3.06.

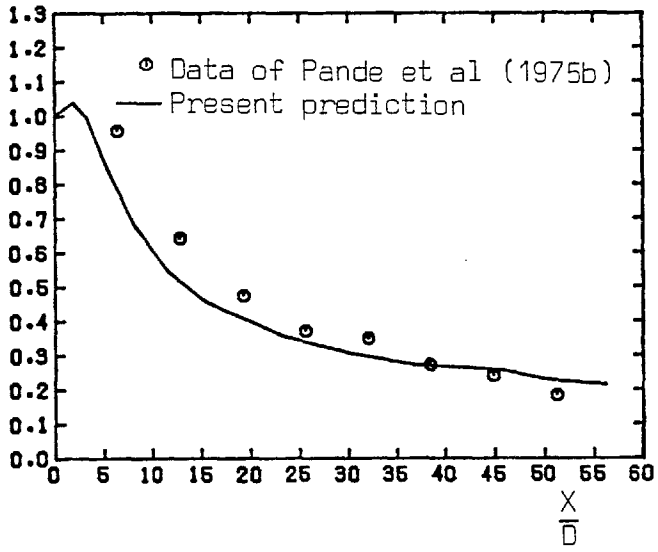


FIG. 5.4.10: CENTRE-LINE VELOCITY DECAY; FR=2.59, A.R.=1.

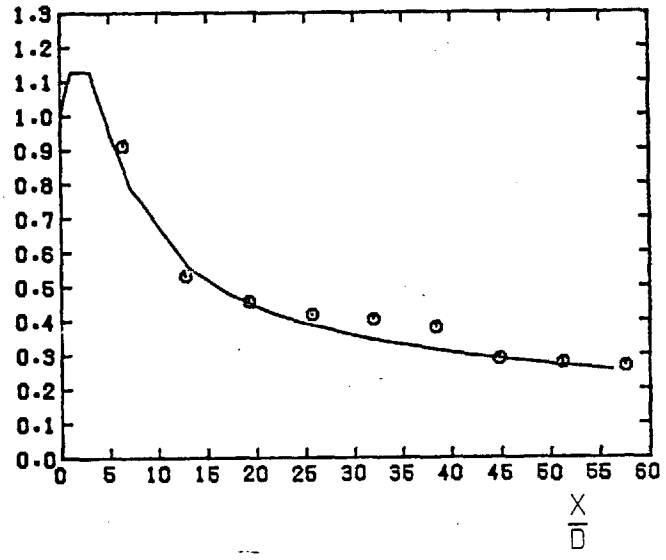


FIG. 5.4.11: CENTRE-LINE VELOCITY DECAY; FR=1.67, A.R.=1.

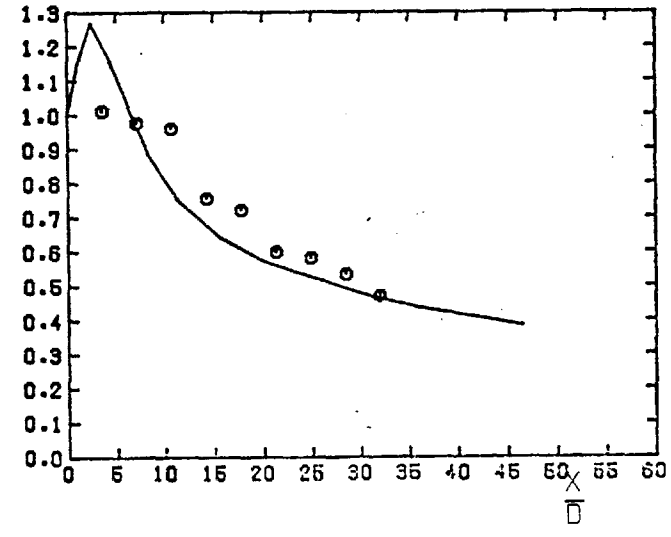


FIG. 5.4.12: CENTRE-LINE VELOCITY DECAY; FR=1.32, A.R.=3.06.

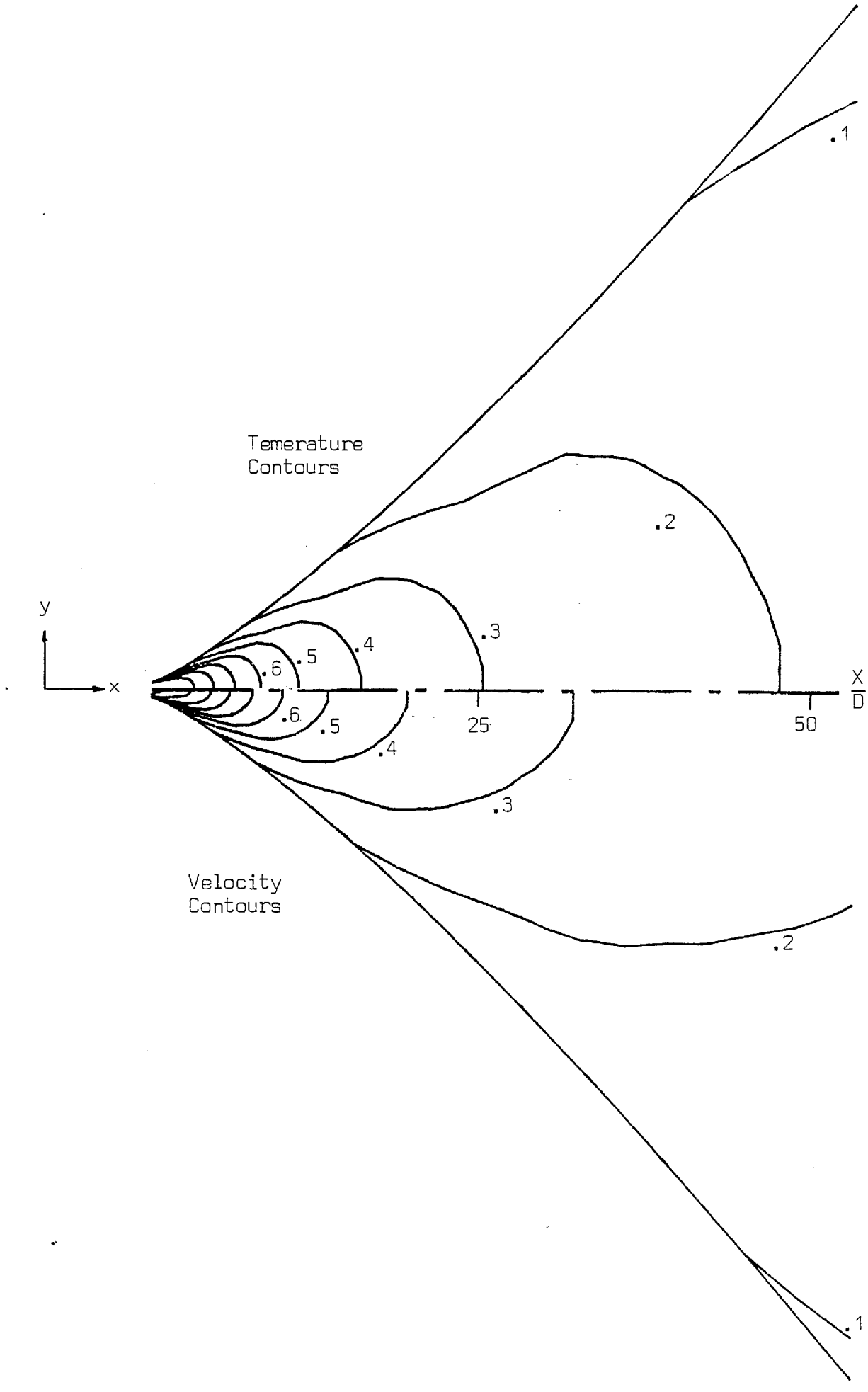


FIG. 5.4.13: PREDICTED TEMPERATURE AND VELOCITY CONTOURS; FR=2.59, A.R.=1.

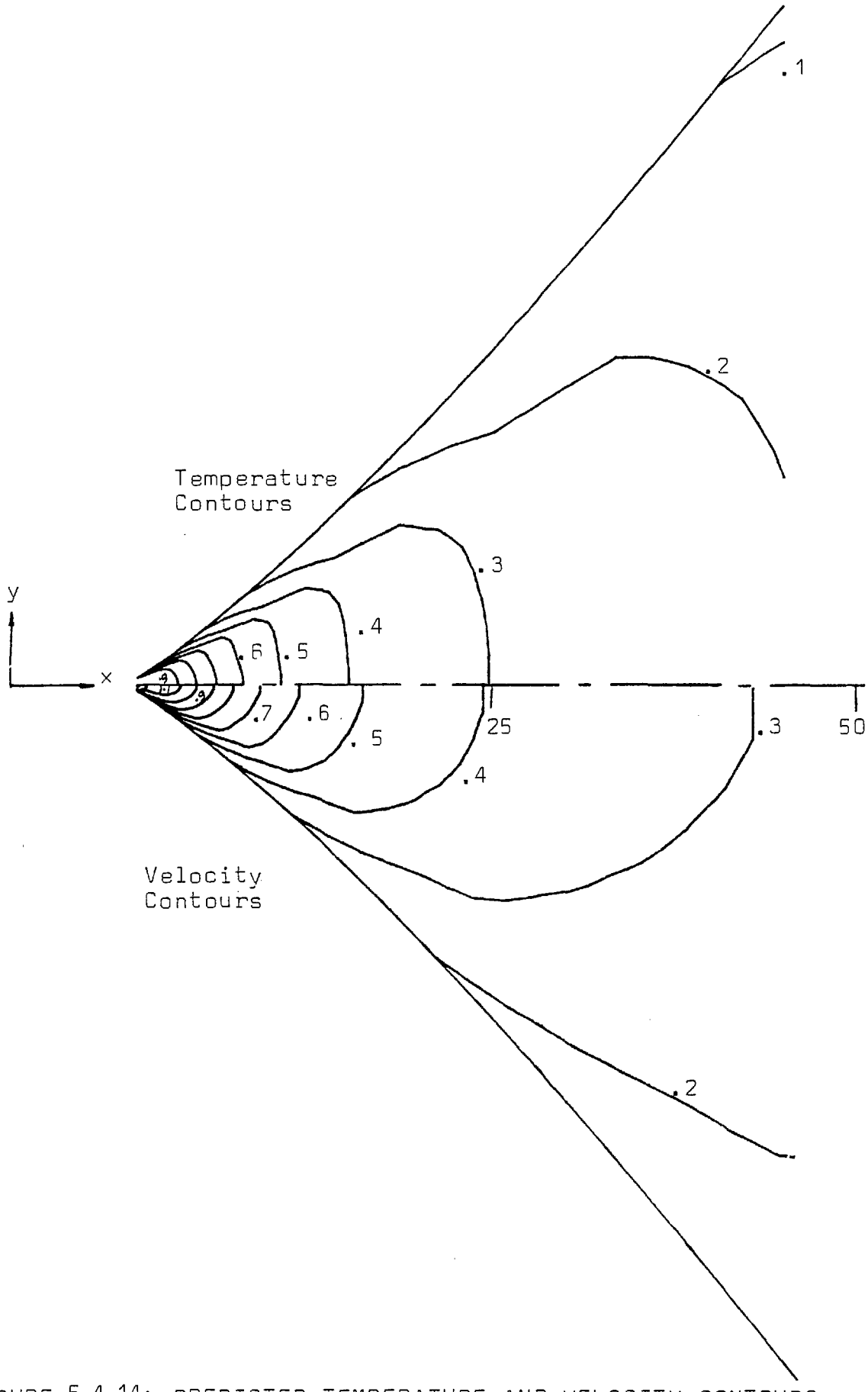


FIGURE 5.4.14: PREDICTED TEMPERATURE AND VELOCITY CONTOURS, FR=1.67, A.R.=1.

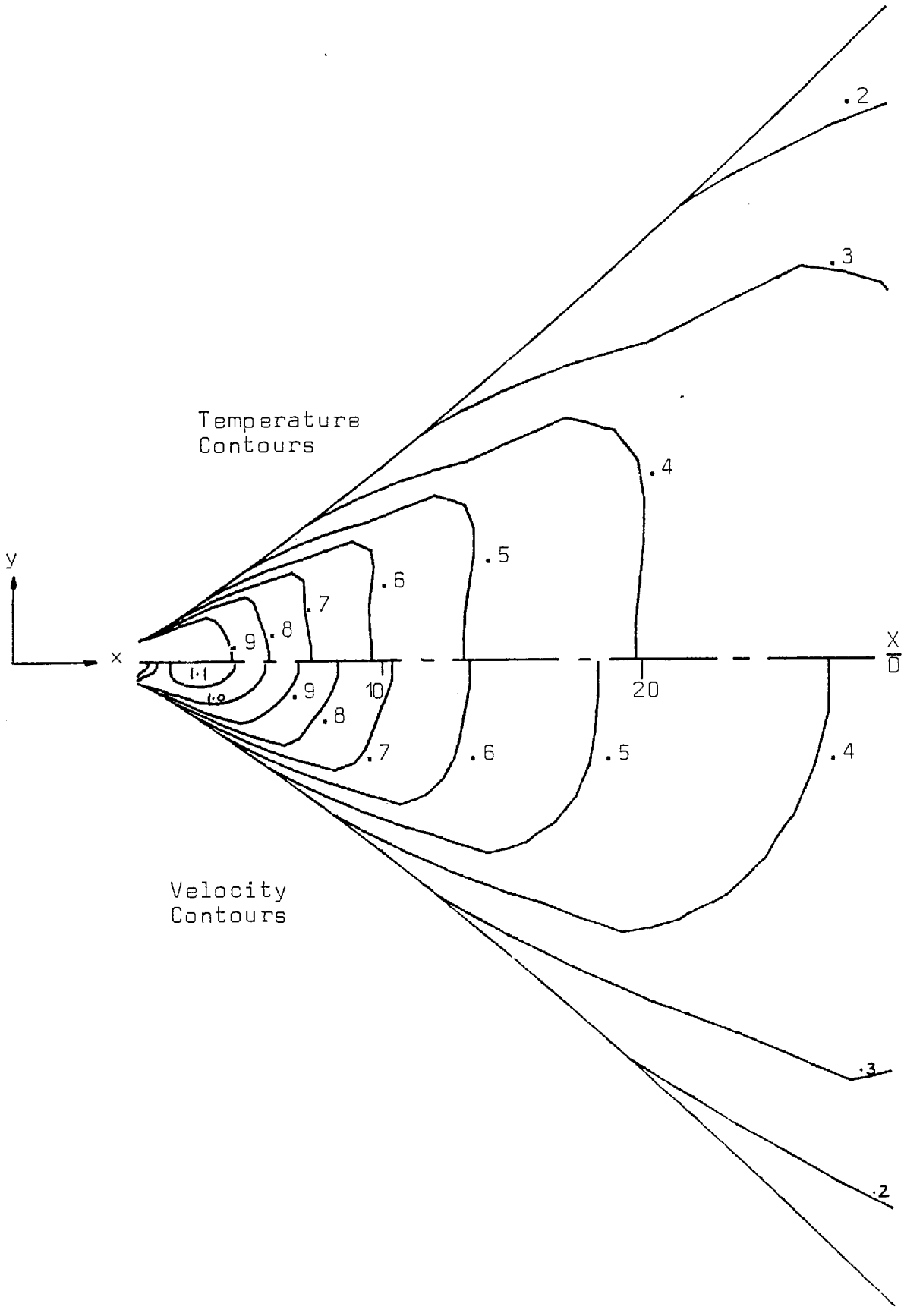


FIG. 5.4.15: PREDICTED TEMPERATURE AND VELOCITY CONTOURS; FR=1.32, A.R.=3.06.

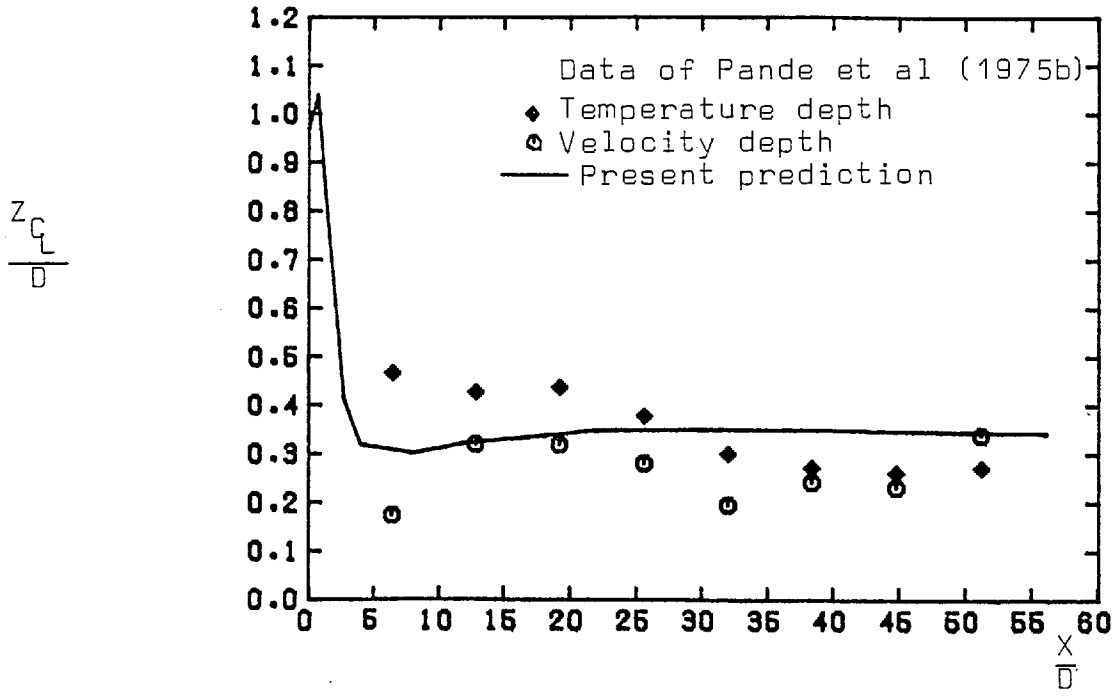
displaced away from the centre-line. It appears that the buoyancy effects are so strong, in this case, that the higher temperatures are convected, laterally, away from the centre-line.

In Figure 5.4.16, the predicted longitudinal variation of the centre-line layer depth and the average cross-sectional layer depth are compared with the corresponding measurements of the temperature and velocity half-depths,* for the case of Froude number = 2.59. The present mathematical formulation assumes that the temperature and velocity layer depths are the same. These appear to lie around the average of the temperature and velocity half-depths presented in Figure 5.4.16. Figure 5.4.17 shows similar comparisons for the case of Froude number = 1.67. On the whole, the temperature half-depths seem bigger than the velocity half-depth, and the predicted layer depth appear to agree better with the latter. Figure 5.4.18 shows the comparisons of the predicted and measured layer depths for the lowest Froude number case. The velocity layer depths are consistently bigger, in this case, and the predicted depths are seen to agree well with them.

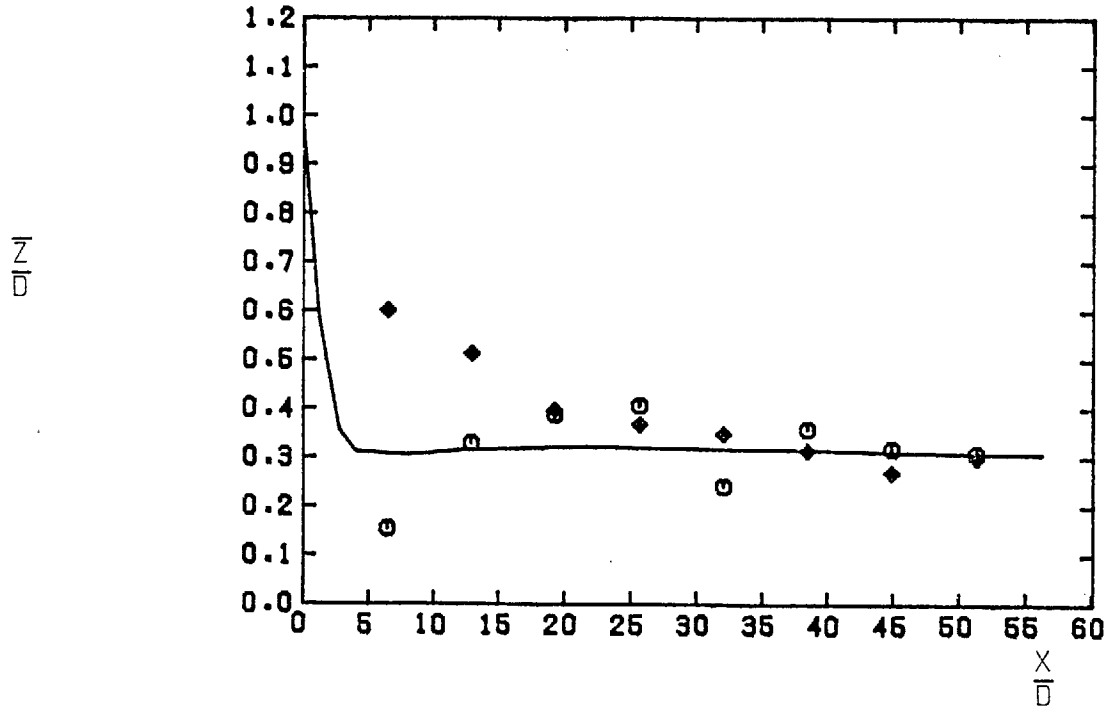
The comparisons of the present predictions with Wiuff's experimental data (Run 4) are now presented. The predicted lateral distributions of temperature are compared with measured data, at seven cross-stream planes, in Figure 5.4.19. The horizontal line at the end of each curve indicates the presumed boundary condition, which appears to agree well with the trend of the data; though the lateral extents of the data

---

*NOTE: The velocity or temperature half-depth is defined as the depth at which the value of the velocity or temperature is equal to half the surface value.

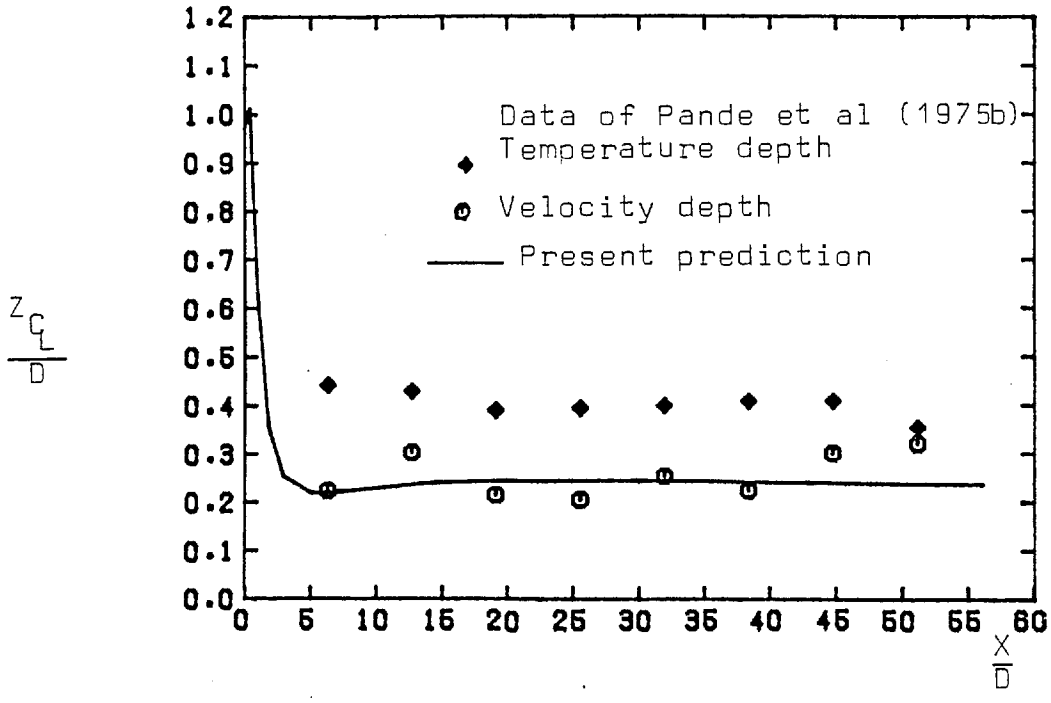


(a) Centre-line half-depth.

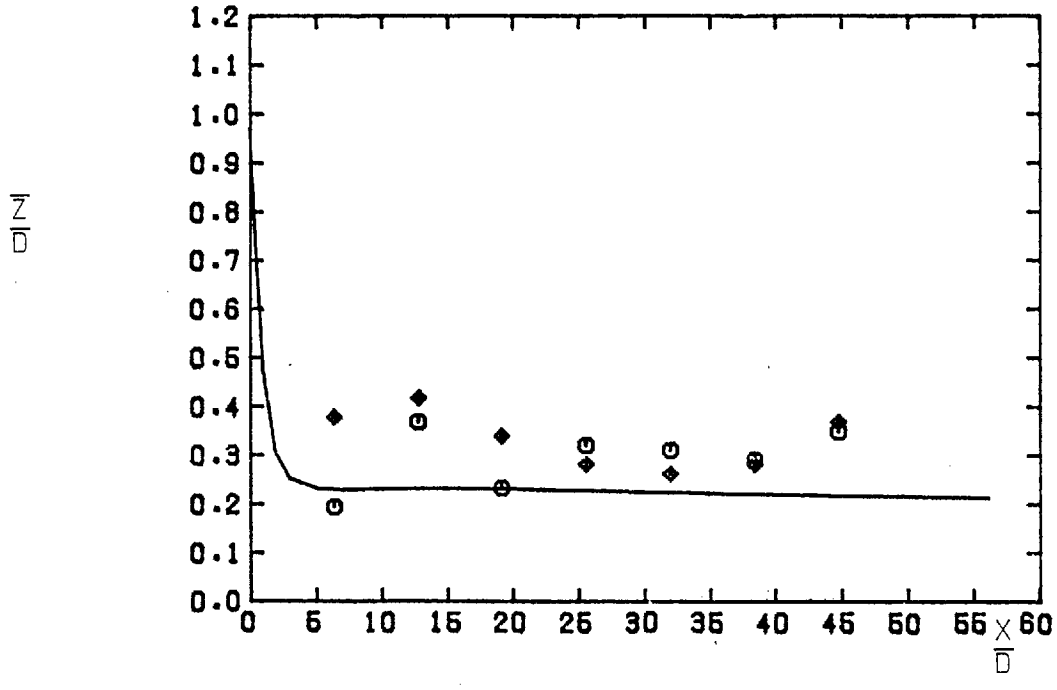


(b) Cross-sectional average half-depth.

FIG. 5.4.16: PREDICTION OF THE LAYER DEPTHS; FR=2.59, A.R.=1.

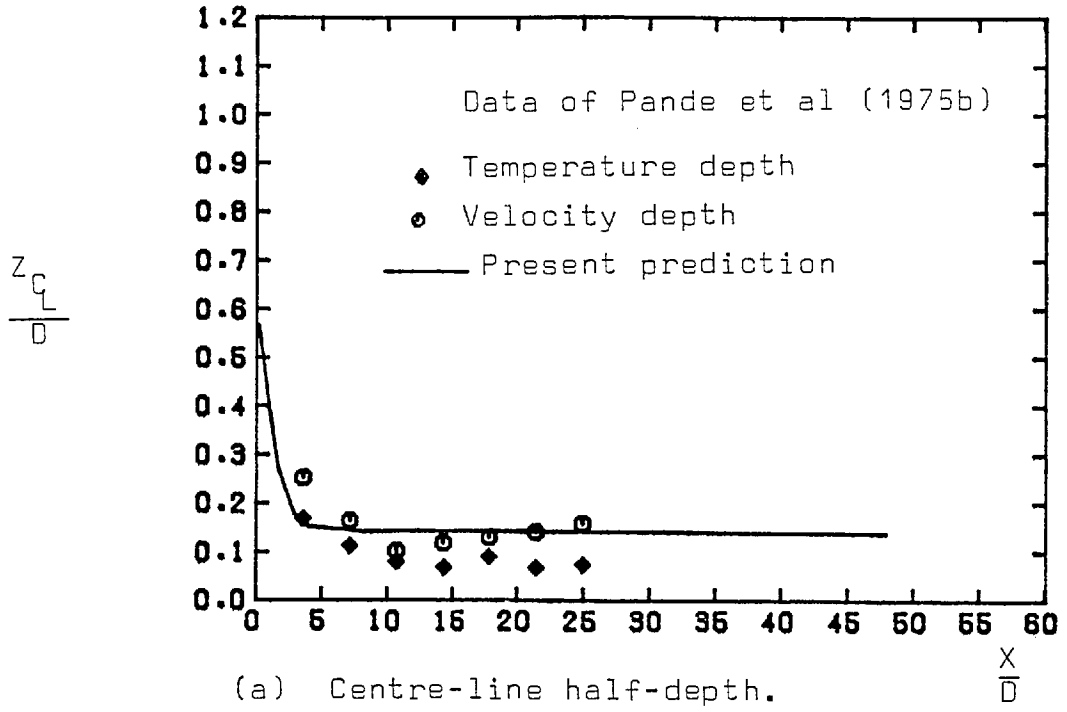


(a) Centre-line half-depth.

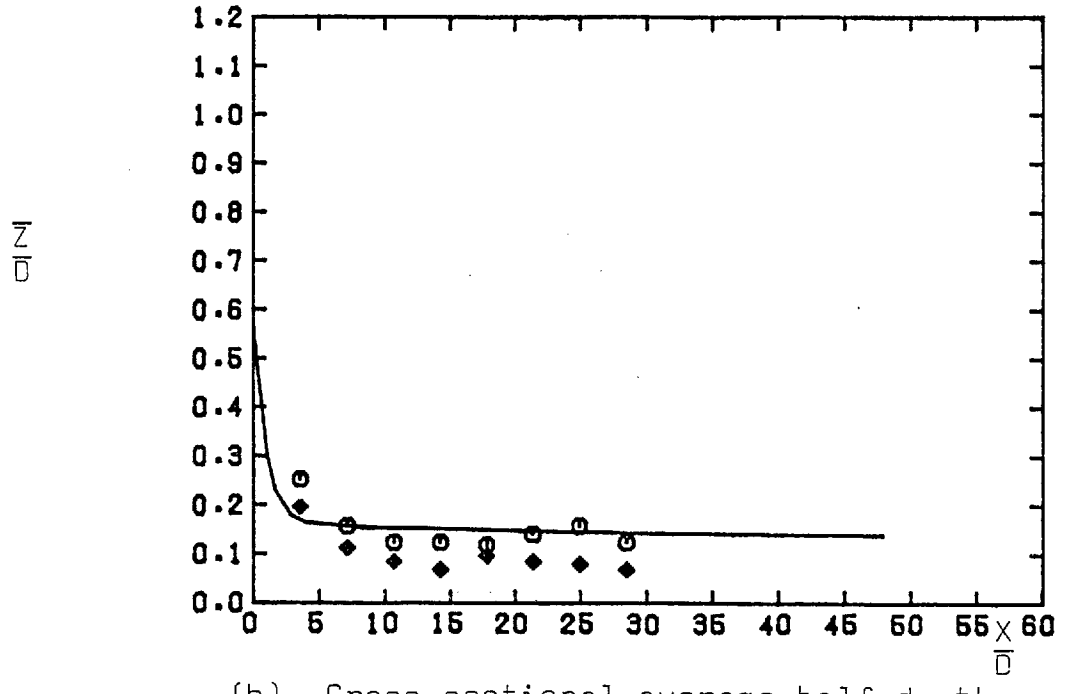


(b) Cross-sectional average half-depth.

FIG. 5.4.17: PREDICTION OF THE LAYER DEPTHS; FR=1.67, A.R.=1.



(a) Centre-line half-depth.



(b) Cross-sectional average half-depth.

FIG. 5.4.18: PREDICTION OF THE LAYER DEPTHS; FR=1.32, A.R.=3.06.

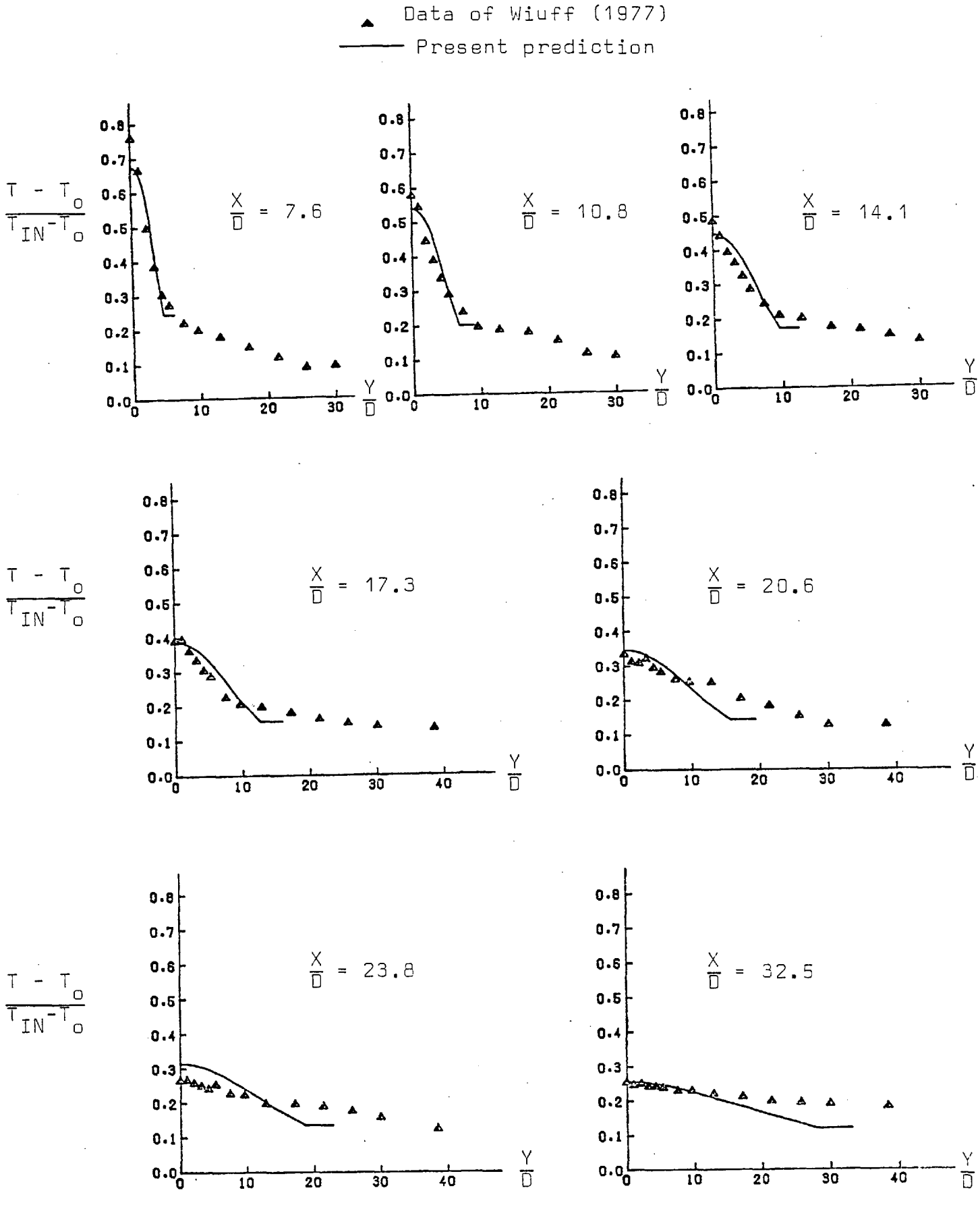


FIG. 5.4.19: PREDICTION OF THE TEMPERATURE DISTRIBUTION IN A HEATED SURFACE DISCHARGE; FR=3.60, A.R.=1.40.

are greater than those of the predictions, as previously discussed. The agreement between the predictions and the data is fair, though, in the last few cross-stream planes, the measured temperature profiles appear flatter than predicted. Figure 5.4.20 shows the comparison of the predicted lateral distributions of the longitudinal velocity, at eight cross-stream planes, with the measured ones. The agreement seems fairly good. The centre-line temperature and velocity decays are shown in Figures 5.4.21 and 5.4.22, respectively. The agreement is also fair. The scatter in the measured velocities is probably due to the velocity measurements having been made over many experimental runs. Figure 5.4.23 shows a comparison of the predicted lateral distributions of the transverse velocities, at six cross-stream planes, with the measured data. The agreement appears satisfactory.

The present predictions are now compared with other experimental data as tabulated below:

Table 5.3: Discharge parameters for the other predictions.

Run	Discharge Froude Number	Initial Aspect Ratio	Authors
1	2.35	0.35	Stolzenbach and Harleman (1971)
2	4.44	5.8	
3	5.22	2.4	
4	6.66	0.51	
5	9.56	1.0	
6	1.55	1.0	Hayashi and Shuto (1969)
7	3.30	1.0	Tamai, Wiegel and Tornberg (1969)
8	8.40	1.0	
9	9.50	1.0	
10	11.0	1.0	
11	11.3	1.0	

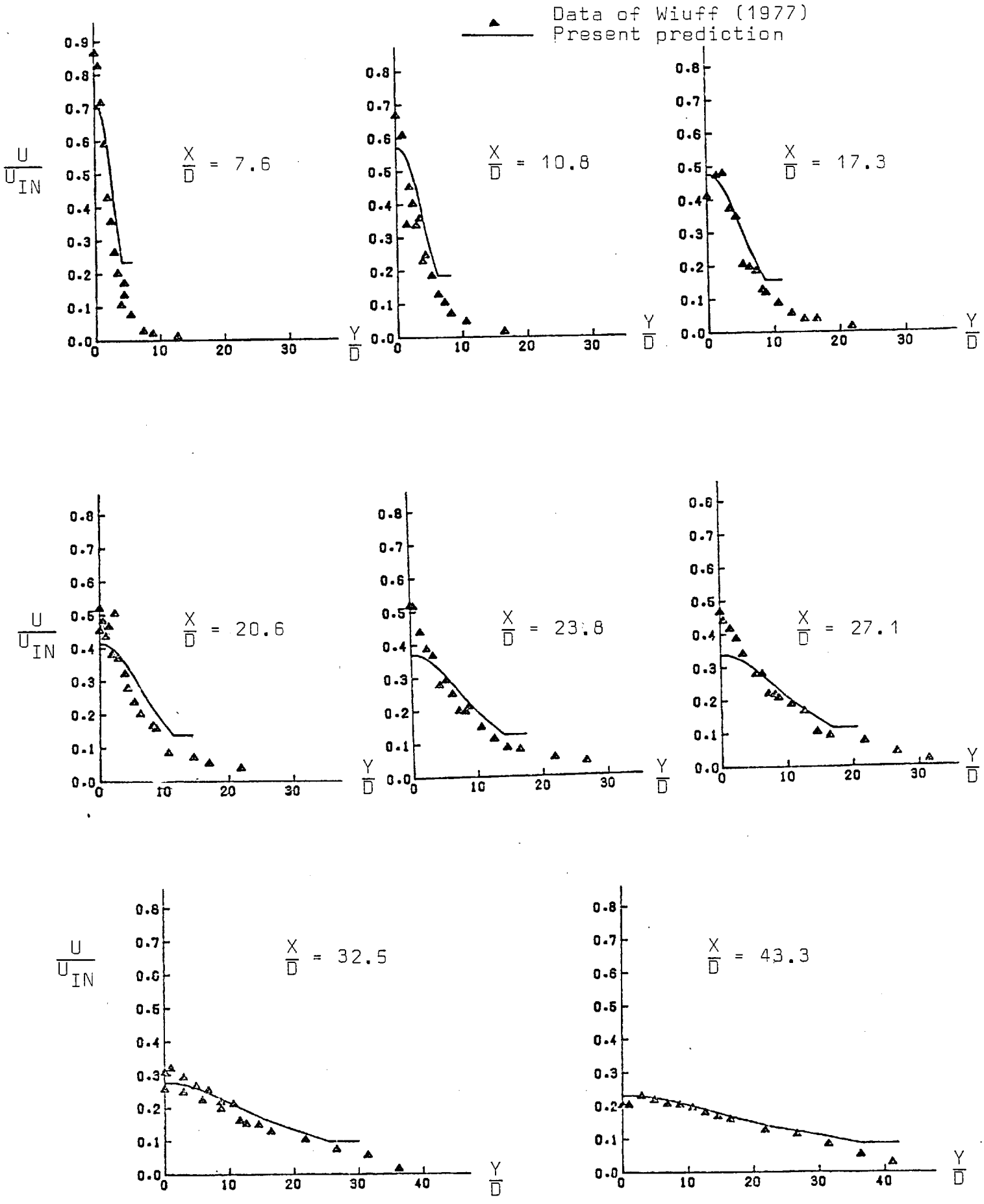


FIG. 5.4.20: PREDICTION OF THE LONGITUDINAL VELOCITY DISTRIBUTION IN A HEATED SURFACE DISCHARGE; FR=3.60, A.R.=1.40.

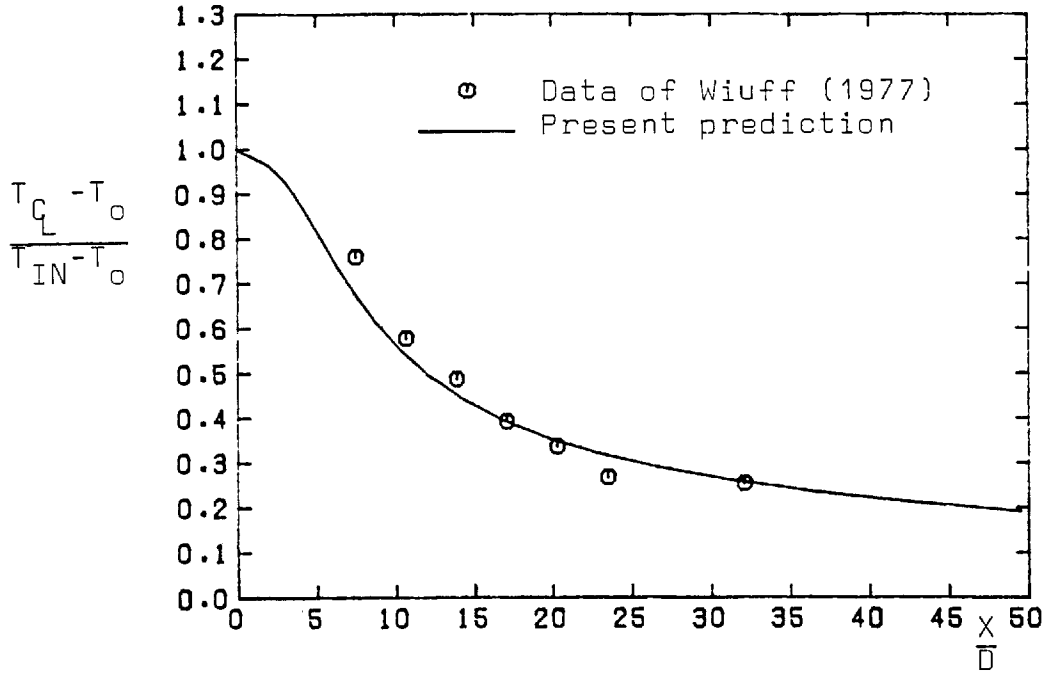


FIG. 5.4.21: CENTRE-LINE TEMPERATURE DECAY; FR=3.6, A.R.=1.40.

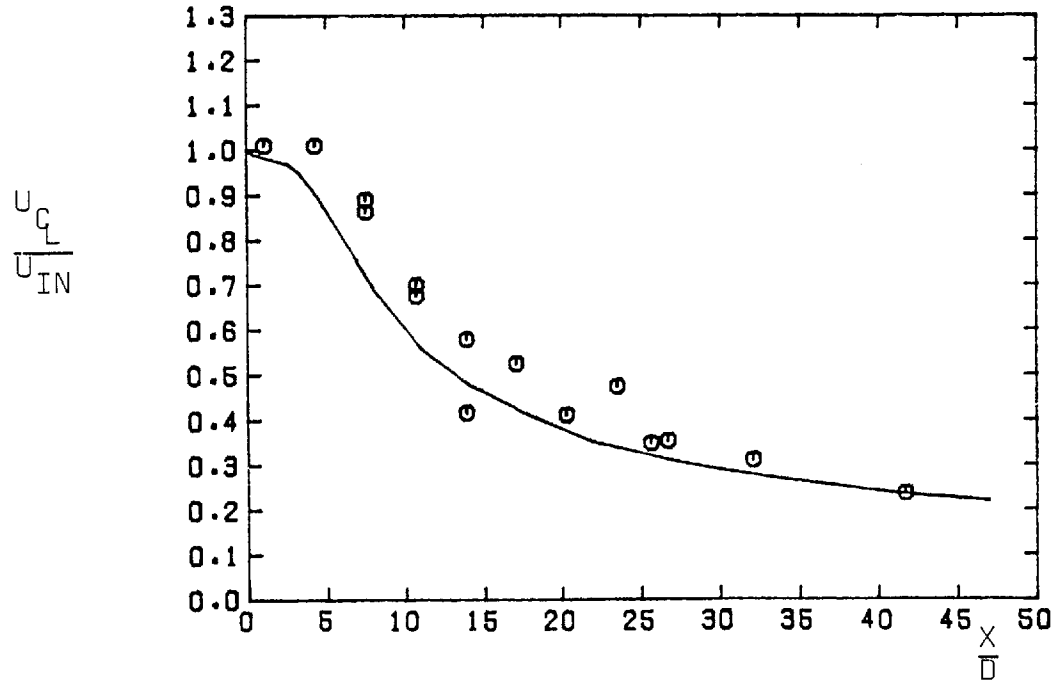


FIG. 5.4.22: CENTRE-LINE VELOCITY DECAY; FR=3.60, A.R.=1.40.

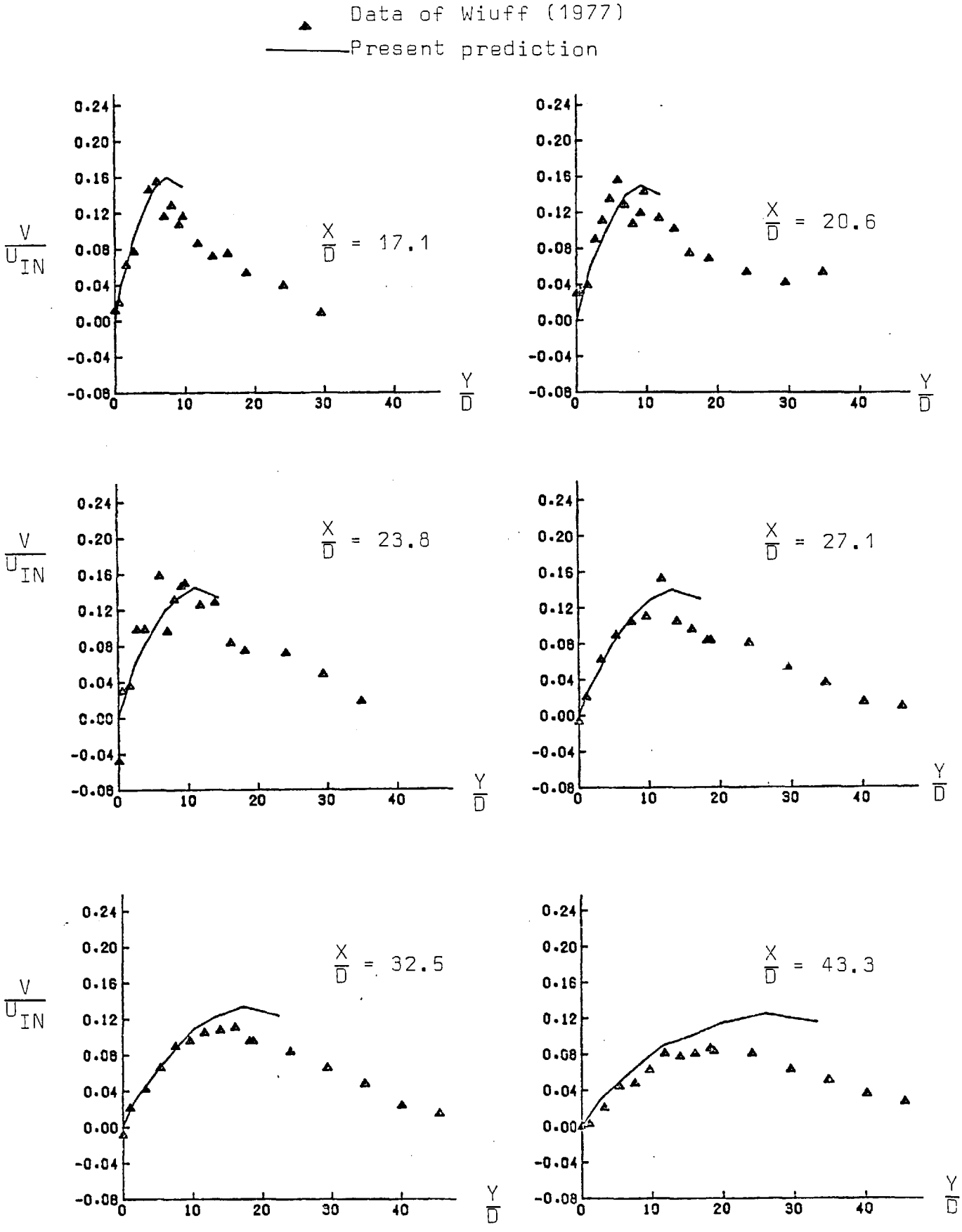


FIG. 5.4.23: PREDICTION OF THE LATERAL VELOCITY DISTRIBUTION; FR=3.60, A.R.=1.40.

In most of these experiments, only temperature measurements were undertaken; even then only centre-line decays were presented. In a few cases, the temperature half-widths and half-depths were also presented. The present predictions are compared only with the measured centre-line temperature decays. Figures 5.4.24 - 5.4.32 show these comparisons. In two cases, two data sets with similar initial conditions have been plotted together. These are runs 5 and 9, (Froude numbers = 9.56 and 9.50, respectively), and runs 10 and 11, (Froude numbers = 11.0 and 11.3, respectively). In each case the aspect ratio is equal to 1.0. The agreement is seen to be mostly satisfactory in all cases.

From the comparisons of the present model predictions with a wide range of experimental data, it may be concluded that the present numerical model is capable of predicting heated surface discharges into stagnant ambients, under laboratory conditions, fairly well.

5.5 Prediction of Laboratory Discharges into Moving Ambient Fluid

Heated surface discharges into moving surroundings may be classified into two* categories, depending on whether the ambient fluid is coflowing or crossflowing. In this section, the predictions of discharges into coflowing ambients are presented first, followed by the predictions of discharges into crossflowing ambients.

---

*NOTE: A possible third category of discharges into counter-flowing ambient fluid is beyond the scope of the present work.

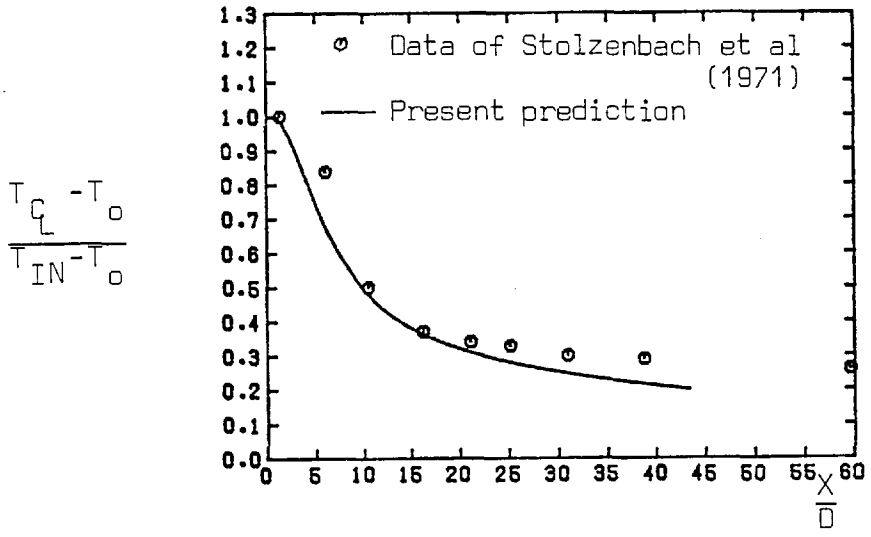


FIG. 5.4.24: CENTRE-LINE TEMPERATURE DECAY; FR=2.35, A.R.=0.35.

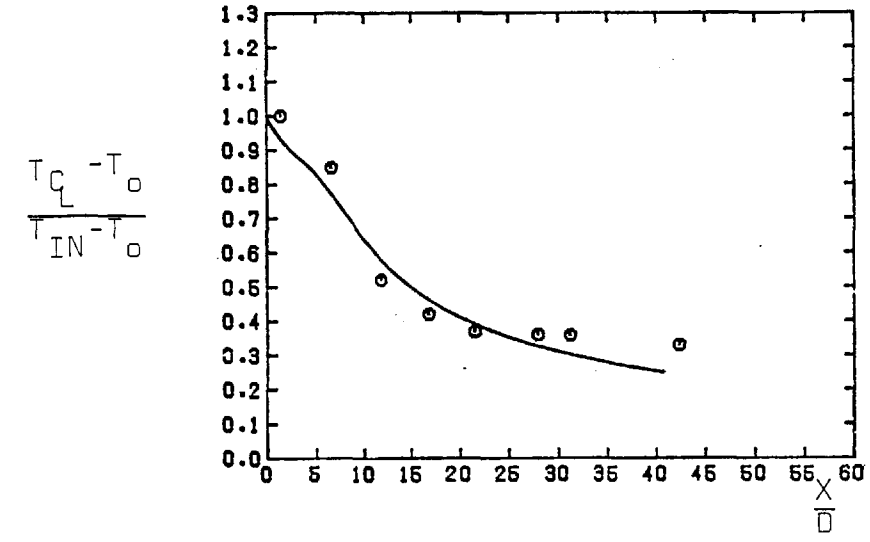


FIG. 5.4.25: CENTRE-LINE TEMPERATURE DECAY; FR=4.44, A.R.=5.8.

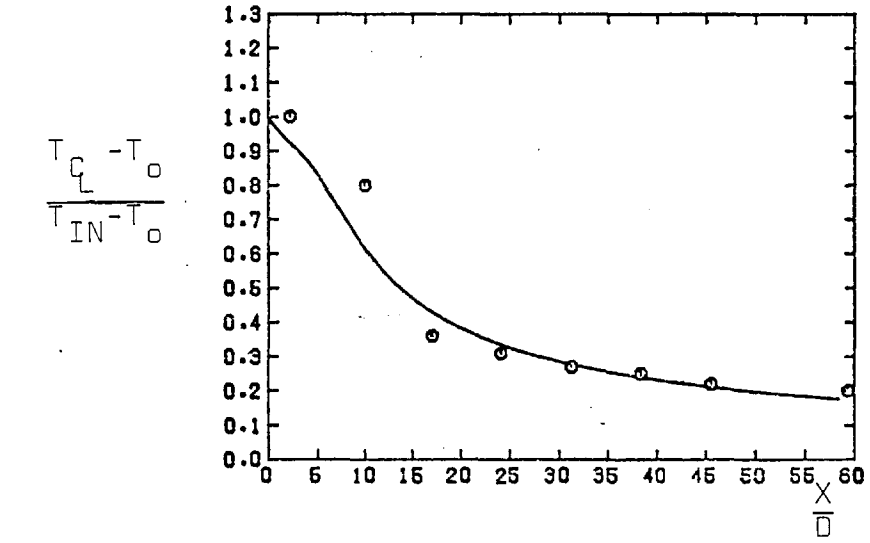


FIG. 5.4.26: CENTRE-LINE TEMPERATURE DECAY; FR=5.22, A.R.=2.4.

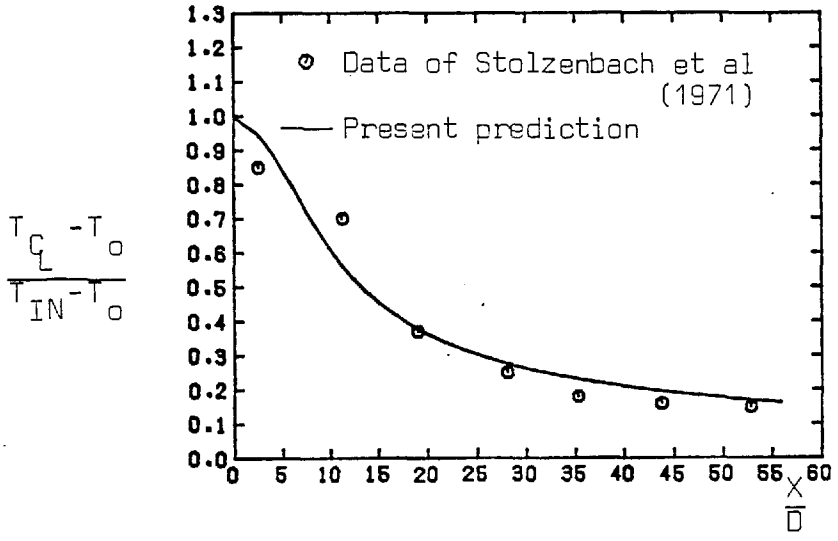


FIG. 5.4.27: CENTRE-LINE TEMPERATURE DECAY; FR=6.66, A.R.=0.51

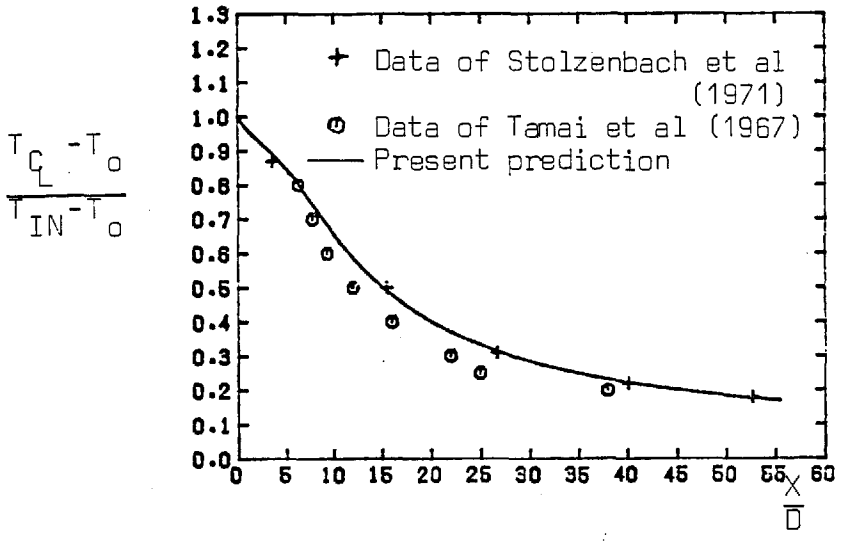


FIG. 5.4.28: CENTRE-LINE TEMPERATURE DECAY; FR=9.53, A.R.=1.

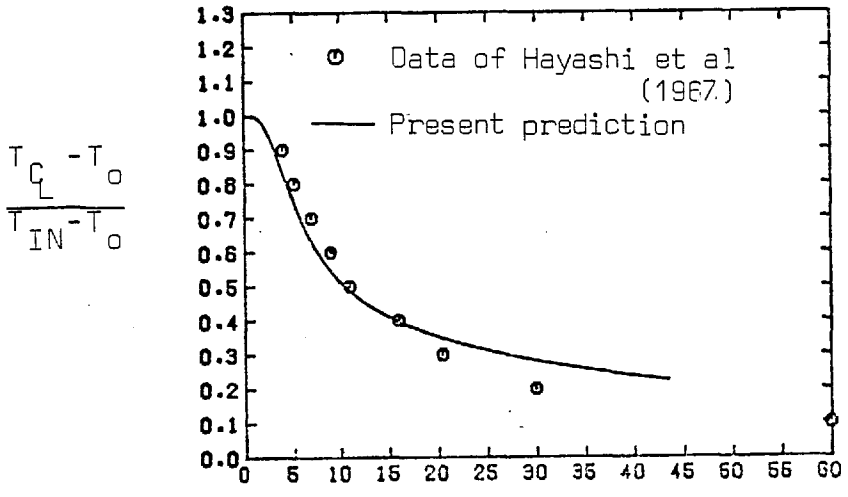


FIG. 5.4.29: CENTRE-LINE TEMPERATURE DECAY; FR=1.55, A.R.=1.

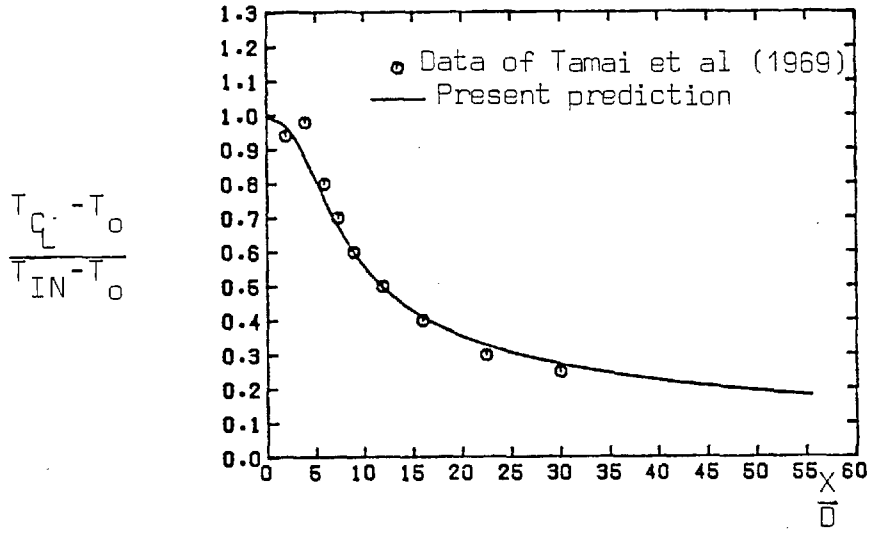


FIG. 5.4.30: CENTRE-LINE TEMPERATURE DECAY; FR=3.30, A.R.=1.

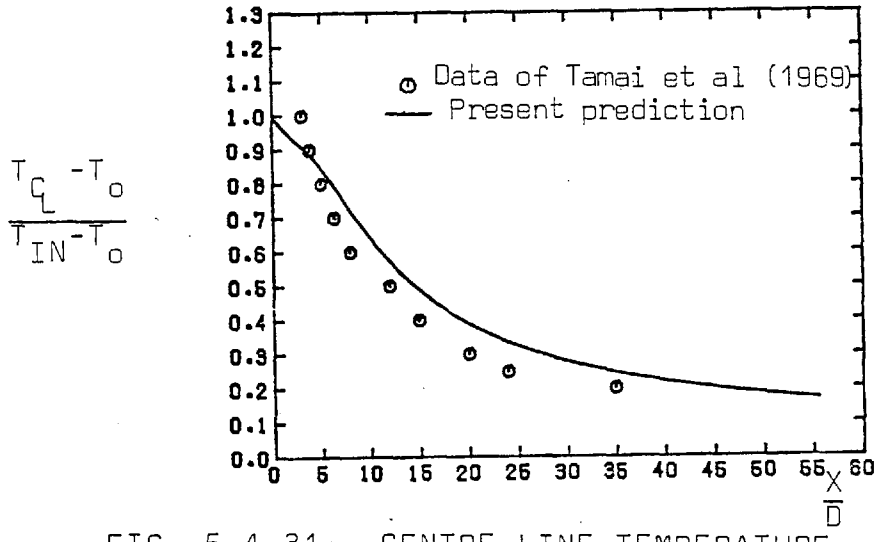


FIG. 5.4.31: CENTRE-LINE TEMPERATURE; FR=8.4, A.R.=1.

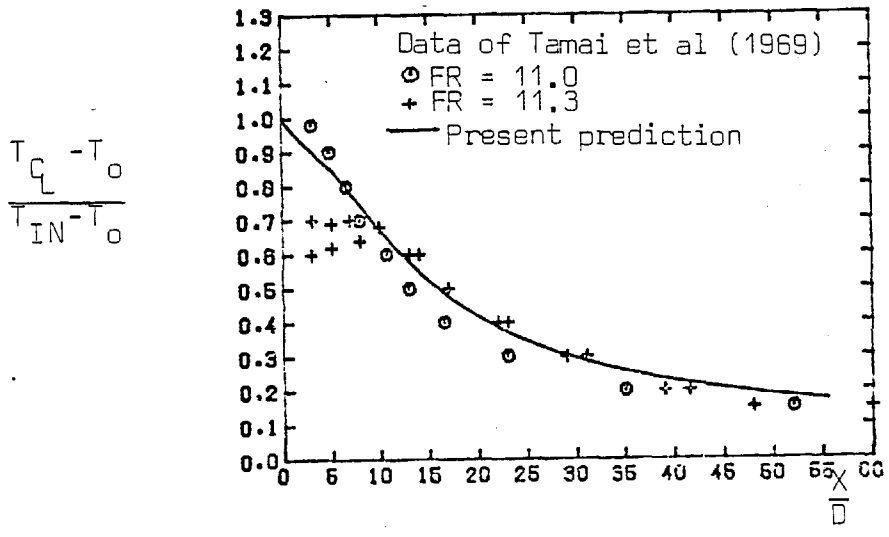


FIG. 5.4.32: CENTRE-LINE TEMPERATURE DECAY; FR=11.5, A.R.=1

5.5.1 Discharges into Coflowing Ambients

No suitable laboratory measurements of heated surface discharges into coflowing streams were found in the literature, so a parametric study is carried out numerically to show the effects of:

(a) ambient to layer fluid velocity ratio;

(b) initial aspect ratio of the layer; and

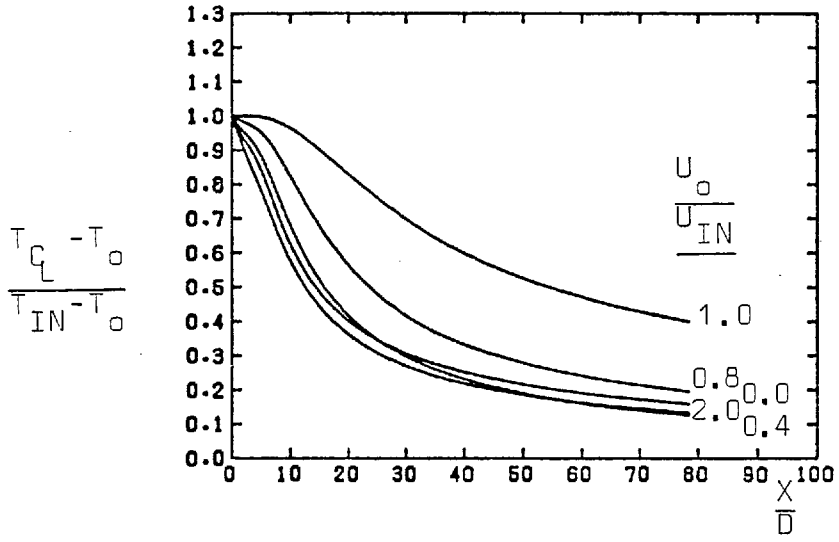
(c) discharge densimetric Froude number.

The test conditions for the parametric study are tabulated below.

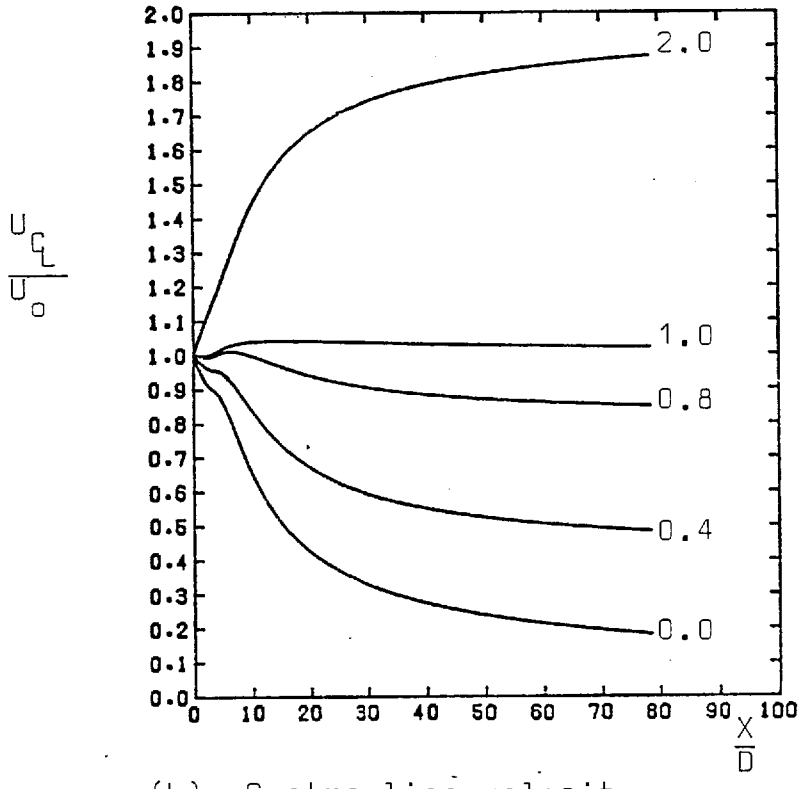
Table 5.4: Flow parameters employed in "coflow" predictions.

DISCHARGE FROUDE NUMBER	INITIAL ASPECT RATIO	AMBIENT TO LAYER FLUID VELOCITY RATIO
4	4	0.0
4	4	0.4
4	4	0.8
4	4	1.0
4	4	2.0
4	1	0.4
4	2	0.4
4	8	0.4
4	16	0.4
2	4	0.4
8	4	0.4
16	4	0.4

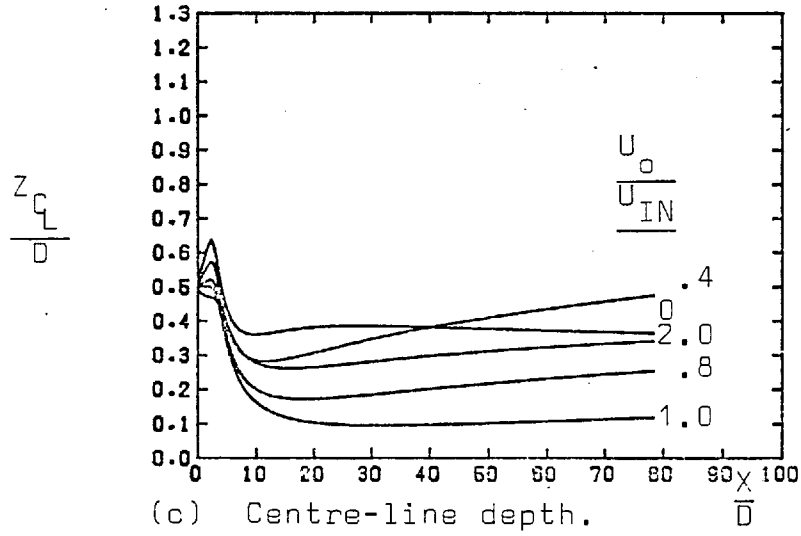
Figure 5.5.1 shows the effect of the velocity ratio on the predicted longitudinal variations of the temperature, velocity,



(a) Centre-line temperature.



(b) Centre-line velocity.



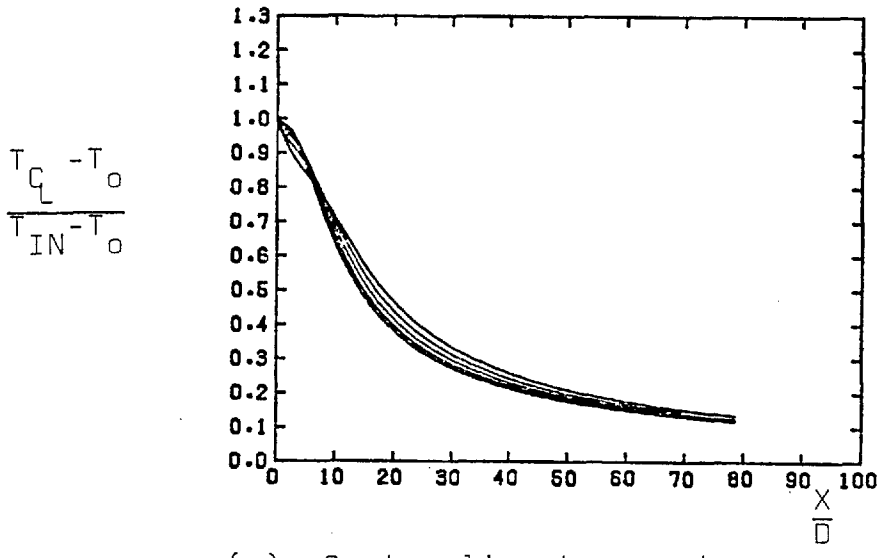
(c) Centre-line depth.

FIG. 5.5.1: EFFECT OF VELOCITY RATIO; FR=4, A.R.=4.

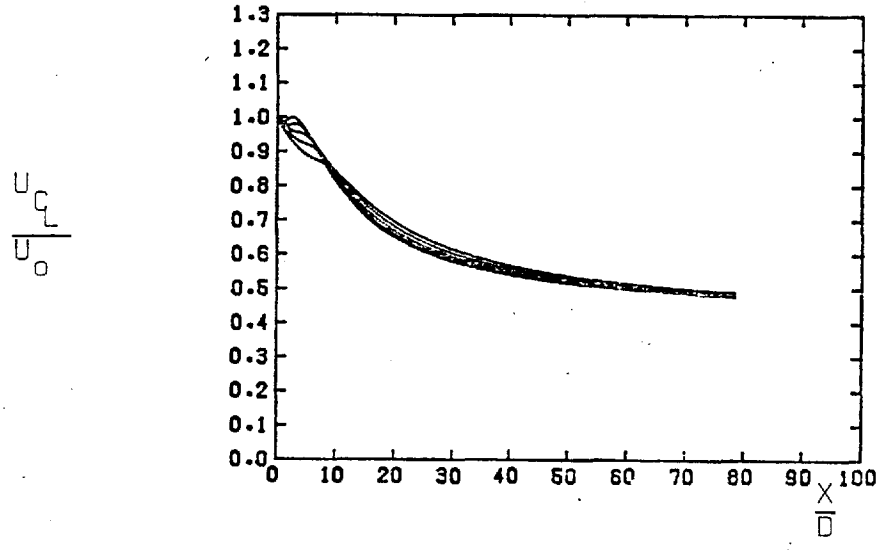
and layer depths along the centre-line. As expected, the flow with the velocity ratio of 1 had the slowest temperature decay rate, followed by the flow with velocity ratio of 0.8. There is very little difference between the temperature decay rates of the remaining three flows. The layer velocities appear to be approaching the ambient fluid velocity asymptotically. The layer depths seem to be greatly influenced by the velocity ratio. The asymptotic depth of the flow with the velocity ratio of 1 is about 0.1D, while that of the flow with zero velocity ratio is about 0.4D. An unexpected result is that the flow with velocity ratio of 0.4 continued to increase in depth and, lower in temperature more rapidly than the other flows, after 80 diameters, when the others had more or less stabilised.

Figure 5.5.2 shows the effect of aspect ratio on the variations of the temperature velocity and layer depth along the centre-line. It is seen that the effect of aspect ratio on the centre-line temperature and velocity is minimal. The effect of aspect ratio on the layer depths is more noticeable. At about 7 diameters downstream, the layer depths converge to a value of about 0.3D, before diverging again. Larger layer depths are predicted, the smaller the aspect ratio.

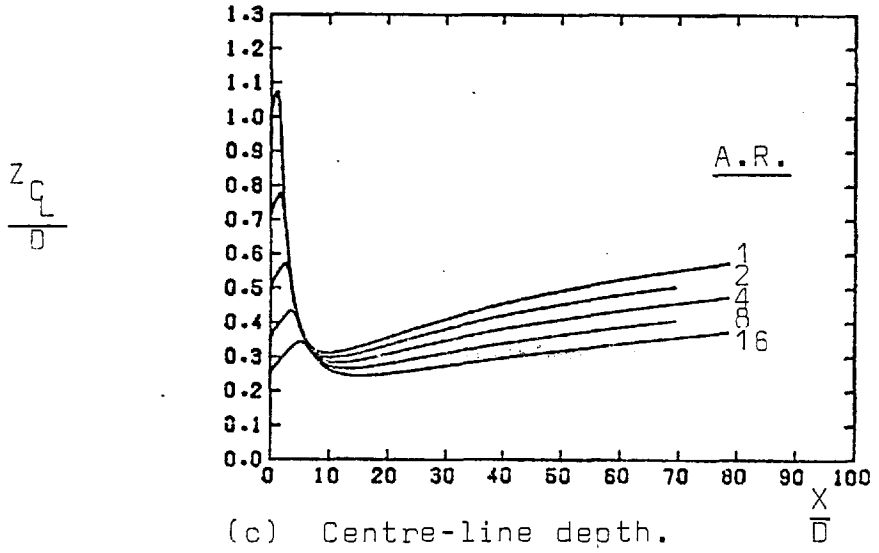
The effect of discharge Froude number on the same layer characteristics, as above, is shown in Figure 5.5.3. Slower temperature decay is predicted, the higher the discharge Froude number. The predicted layer depth increases with increase in Froude number. The velocity variations are not so prominent, and show no clear pattern with changes in Froude number.



(a) Centre-line temperature.

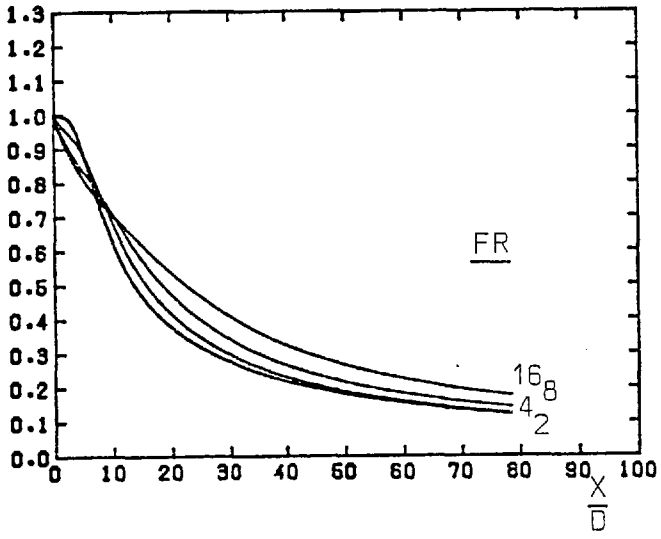


(b) Centre-line velocity.

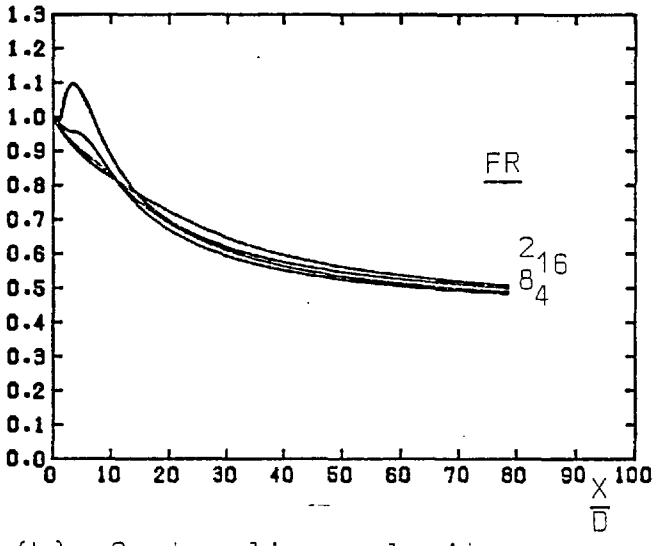


(c) Centre-line depth.

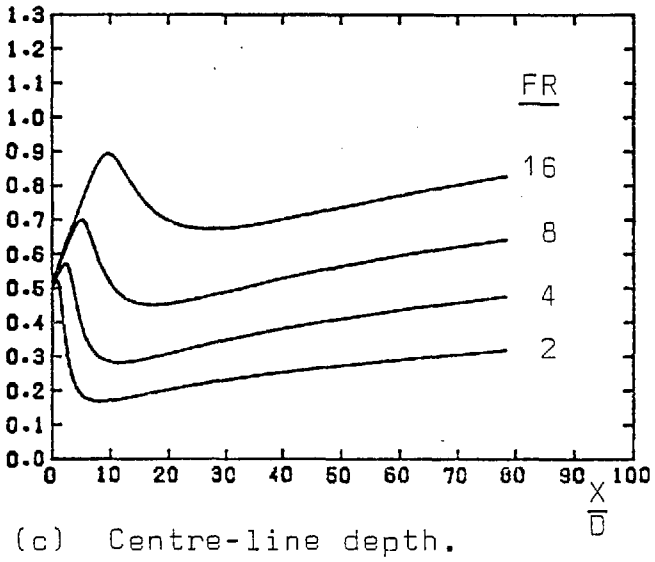
FIG. 5.5.2: EFFECT OF ASPECT RATIO; FR=4, $\frac{U_o}{U_{IN}}$=0.4.



(a) Centre-line temperature.



(b) Centre-line velocity.



(c) Centre-line depth.

FIG. 5.5.3: EFFECT OF FROUDE NUMBER; A.R.=4, $\frac{U_o}{U_{IN}}$=0.4.

5.5.2 Discharges into crossflowing ambients

The present surface-layer model and other surface-jet models should, strictly speaking, not be used to predict surface discharges into crossflowing ambients in which the ambient to discharge velocity ratio is greater than about 0.2. At higher velocity ratios, the crossflow may interact with the discharge to such an extent that a well-defined layer or jet may no longer exist. Observations by Sundaram and Wu (1973) show that the layer may become skewed, so that there is warm water underlying colder water on the downstream side of the crossflow. This condition is clearly unstable. Carter (1969) observed that the layer may be pushed against shore, on the lee-side, and the entrainment is thus cut off on this side. The entrainment requirements on the lee-side may then be satisfied by the recirculation and re-entrainment of already diluted warm-layer water. There are so many factors affecting the flow situation, under these circumstances that a full three-dimensional analysis of the whole flow domain may be required.

In this sub-section, predictions based on the present model are compared with three sets of experimental data by Stolzenbach and Harleman (1971), and another three sets by Stefan et al (1975).

The experimental conditions are tabulated below:

Table 5.5: Discharge parameters for crossflow experiments.

Run	Discharge Froude Number	Initial Aspect Ratio	Ambient to Discharge Velocity Ratio	Authors
1	4.10	0.51	0.115	Stolzenbach and Harleman(1971)
2	5.85	0.51	0.087	
3	6.60	0.51	0.115	
4	3.25	1.0	0.41	Stefan, Bergstedt, and Mrosla (1975)
5	3.25	2.4	0.41	
6	3.25	4.8	0.41	

Comments

Two comments on the values of the ambient-to-discharge velocity ratios are necessary:-

(i) In Stolzenbach and Harleman's experiments, the cross-flow velocity was non-uniform, its profile being given by:

$$U_o = U_{max}\, e^{-0.64\, Z_{IN}^2 \left(\frac{x}{z_{IN}} - 50\right)^2} \qquad ,(5.5.1)$$

where,

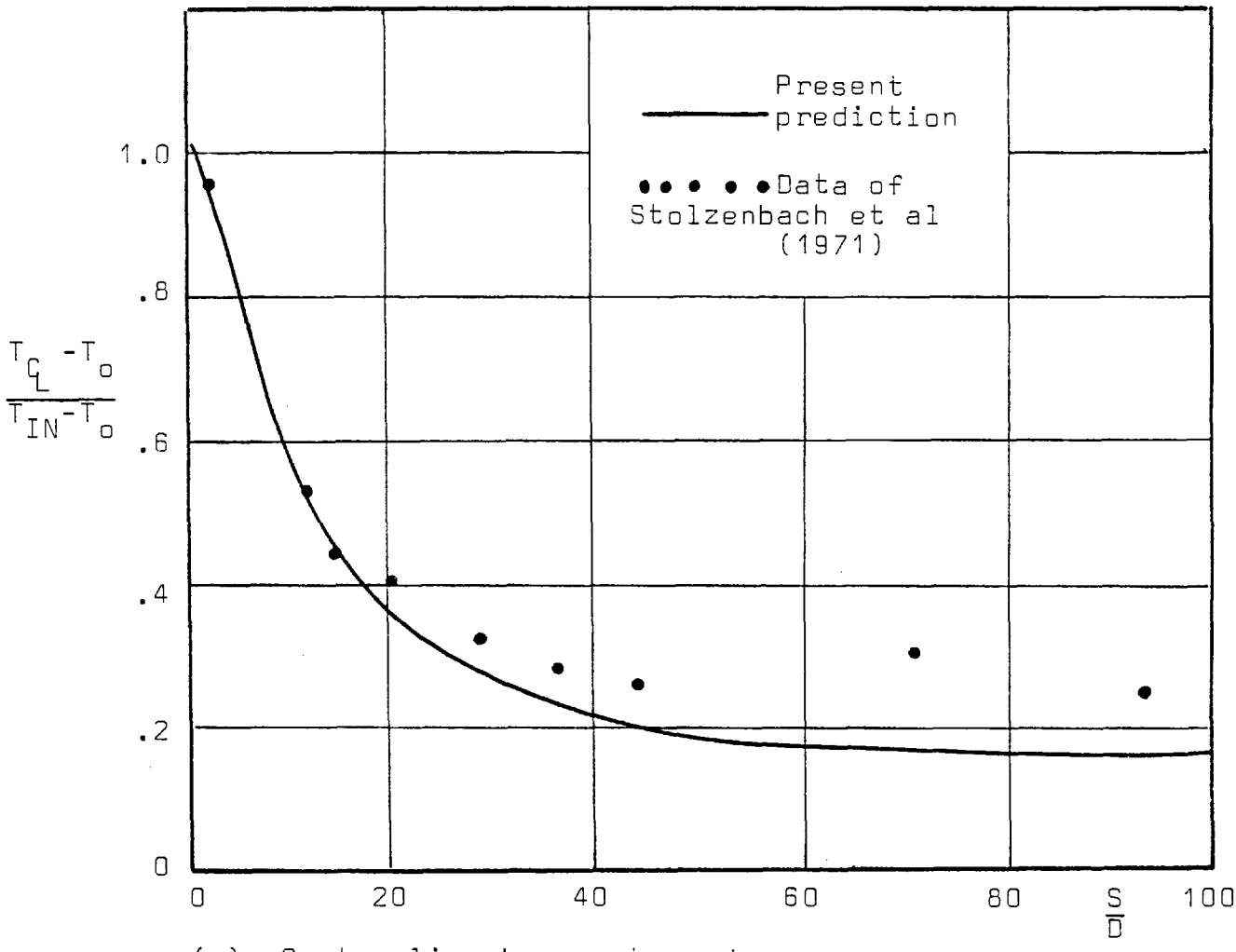
U_{max} is the value used to calculate the ratio given in the table, and all distances are in meters.

(ii) In Stefan et al's experiments, the value of the ambient-to-discharge velocity ratio of 0.41 is higher than the limit suggested in the earlier discussion as appropriate for the application of surface-jet models. However, the experiments were carried out primarily to investigate the initial region of the jet, and the crossflow was applied only in this region.

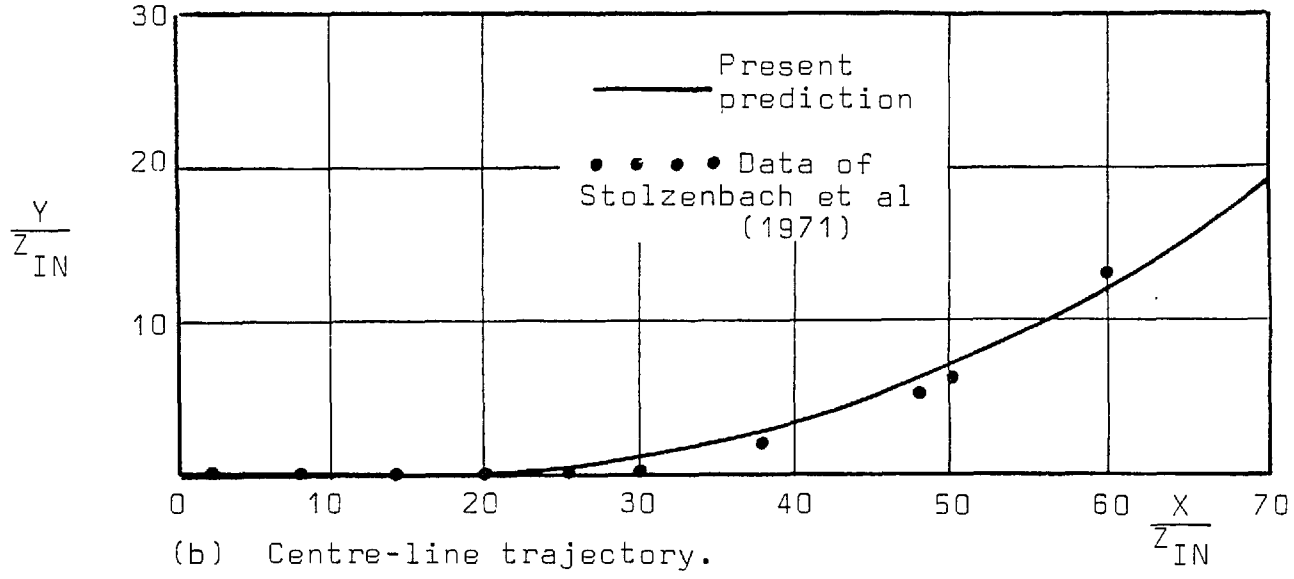
The effect was, therefore, not as adverse as might have been expected, and surface-jet models may be validly applied.

The present predictions are compared with the experimental data of Stolzenbach and Harleman in Figures 5.5.4 - 5.5.6. The predicted centre-line temperature decay and jet trajectory are compared with the first set of experimental data in Figure 5.5.4. The trajectory appears to be correctly predicted. The temperature decay is well predicted up to about 40 diameters, after which, the data show a rise in temperature, while the predicted temperature continues to fall. The mechanism for this rise in temperature is not known. It may be due to thermal instabilities or jet-meandering, both of which have been observed in many thermal plumes. In any case, there are too few measurements in this region for a definite statement to be made. Figure 5.5.5 shows similar comparisons for Run 2. In this case, the temperature decay is fairly well predicted, but there is some deviation in the predicted trajectory. Figure 5.5.6 shows the temperature decay for Run 3. The agreement of the prediction with the experiment is seen to be good.

The predictions of Stefan et al's data are presented in Figures 5.5.7 - 5.5.10. As was stated earlier, these experiments were performed to study the zone of flow establishment in heated water surface jets, so all the measurements were made at distances less than 12 diameters from the discharge port. Figure 5.5.7 shows the decays of the centre-line temperature and velocity for the experimental run with aspect ratio of 1.0. The temperature decay is fairly well predicted,

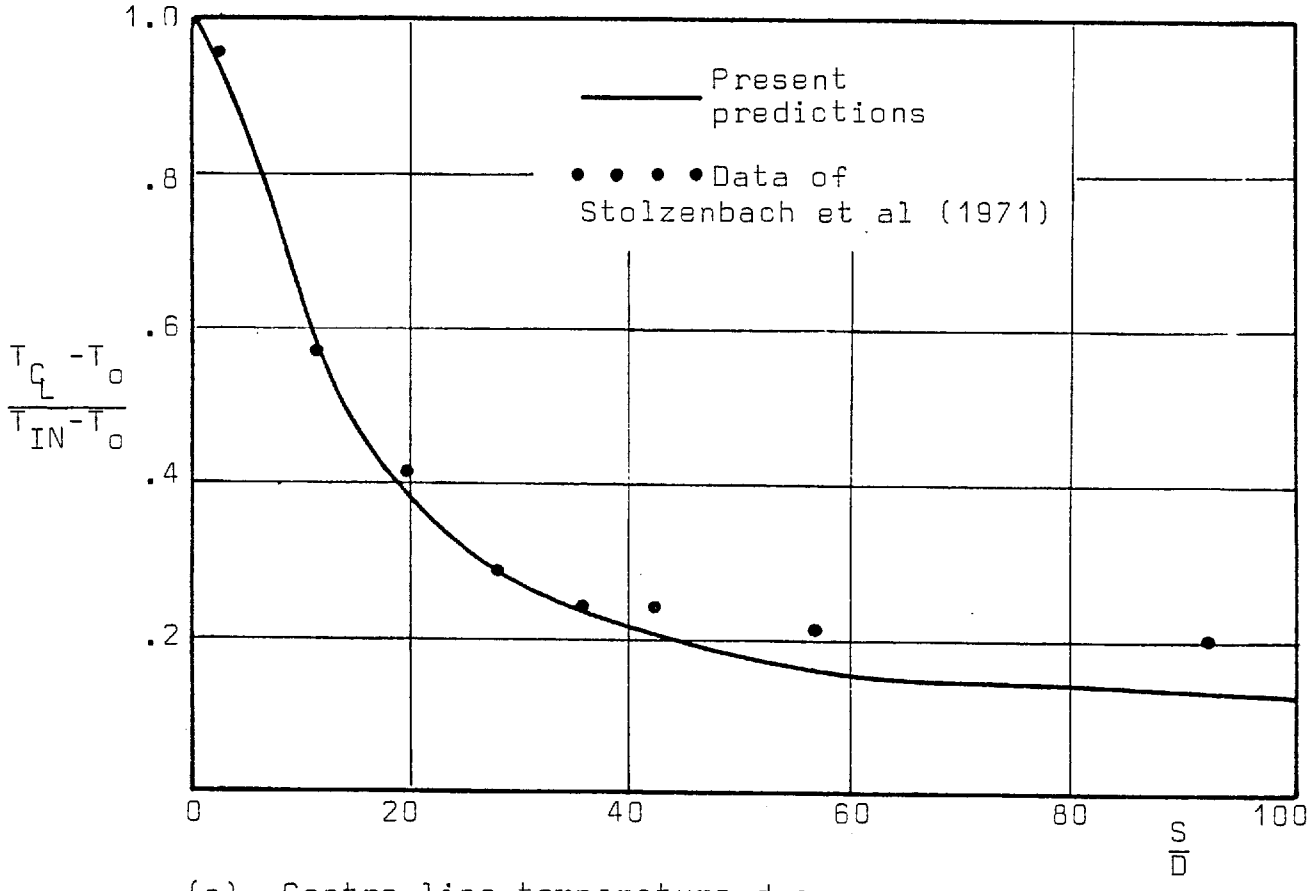


(a) Centre-line temperature decay.

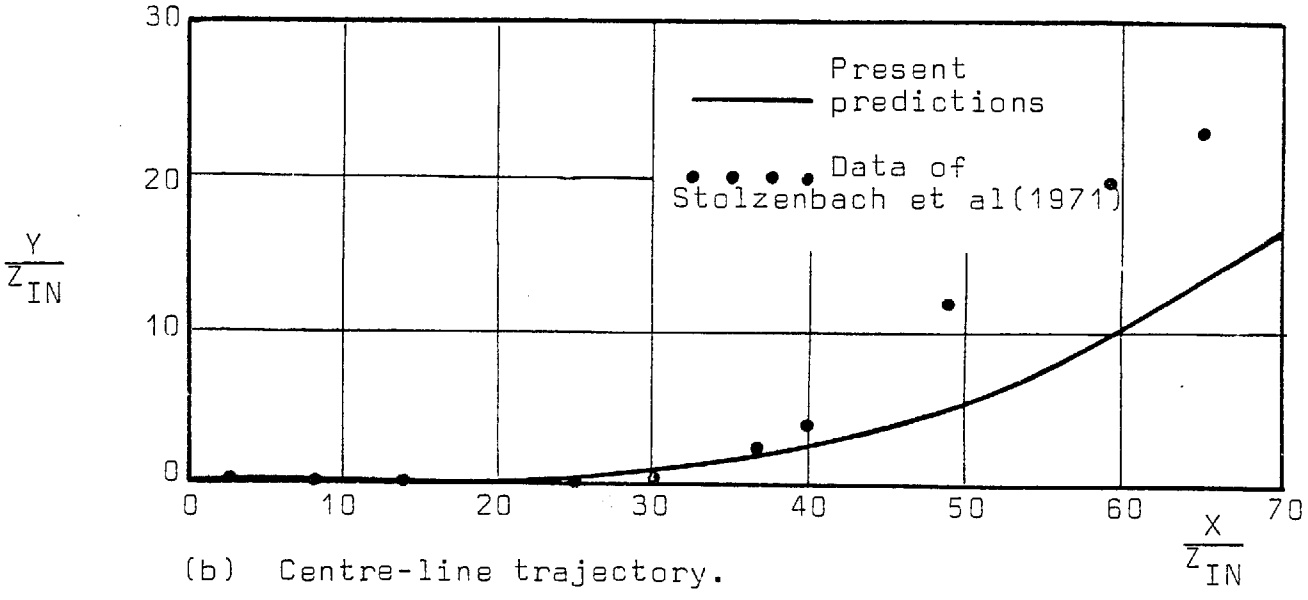


(b) Centre-line trajectory.

FIG. 5.5.4: PREDICTION OF CENTRAL-LINE TEMPERATURE AND TRAJECTORY; FR=4.1, $\frac{V_o}{U_{IN}}$=0.115, A.R.=0.51.



(a) Centre line temperature decay.



(b) Centre-line trajectory.

FIG. 5.5.5: PREDICTION OF CENTRE-LINE TEMPERATURE AND TRAJECTORY; FR=5.85, $\frac{V_o}{U_{IN}}$=0.087, A.R.=0.51.

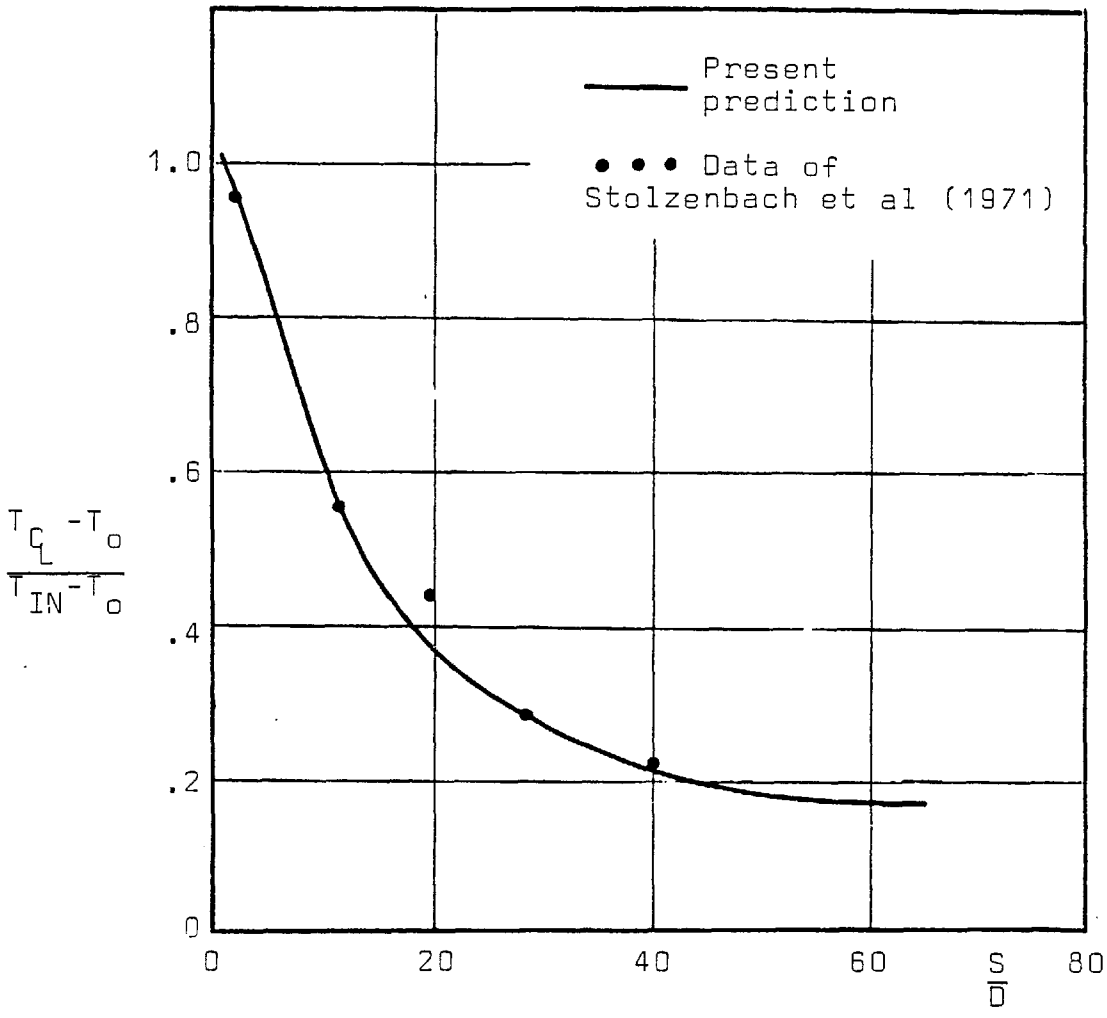
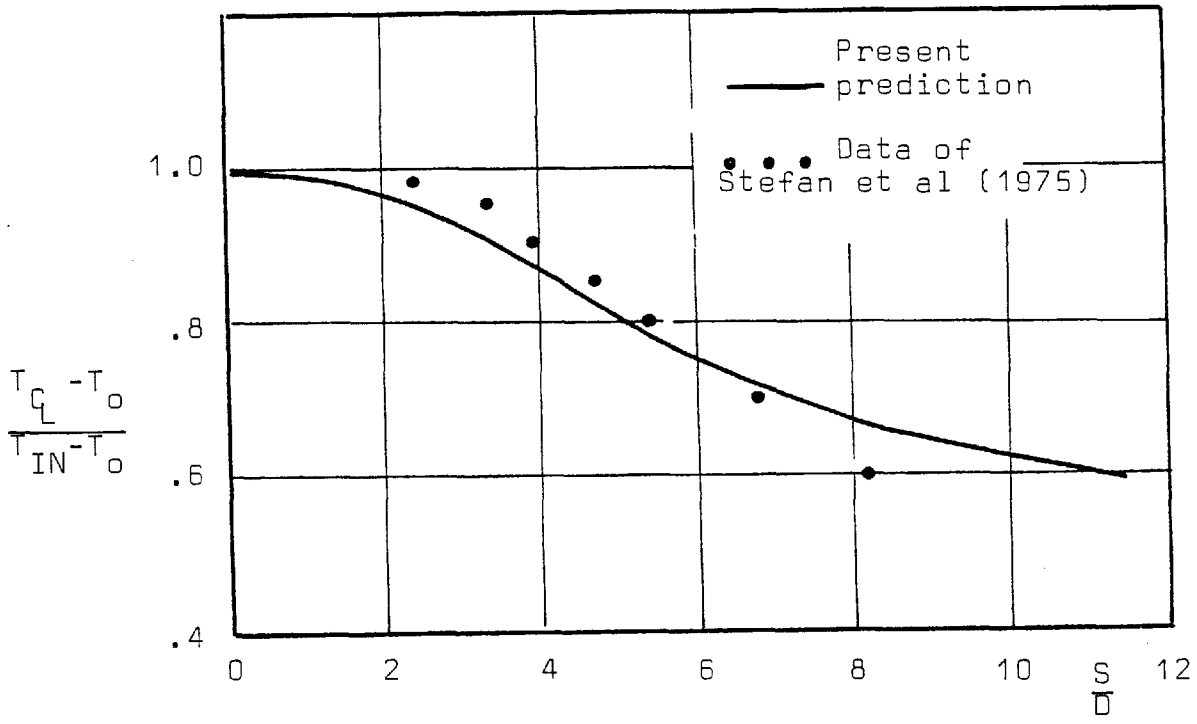
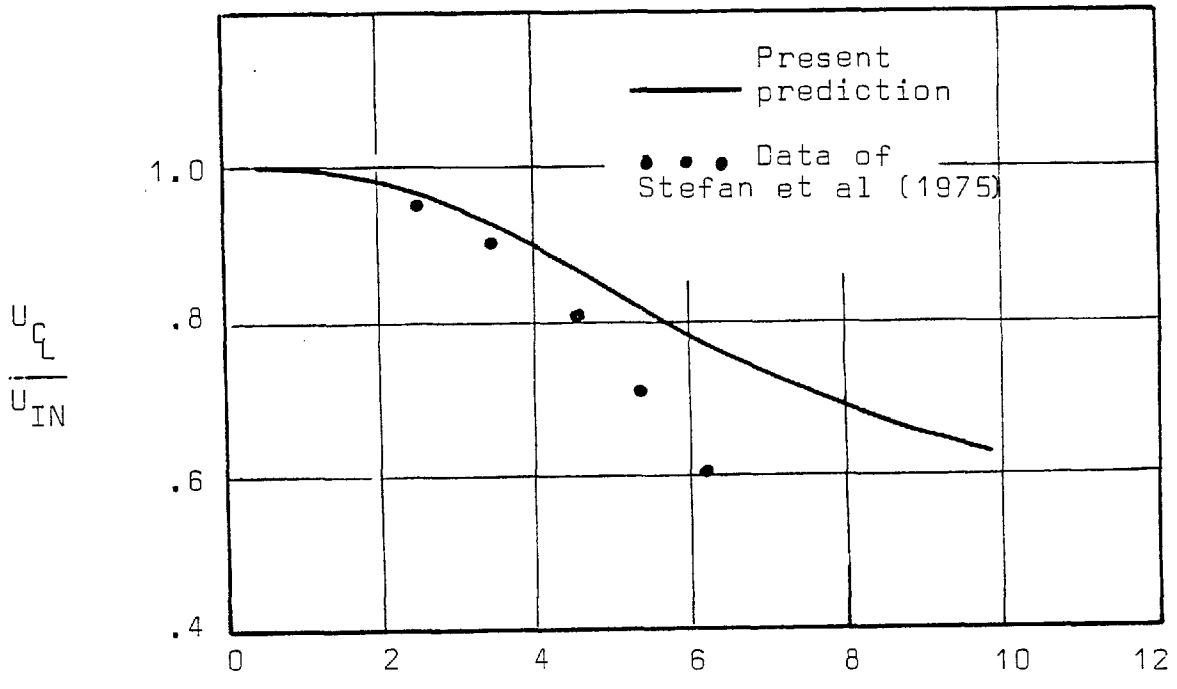


FIG. 5.5.6: PREDICTION OF CENTRE-LINE TEMPERATURE; FR=6.66, $\frac{V_o}{U_{IN}}$=0.115, A.R.=0.51.



(a) Centre-line temperature decay.



(b) Centre-line velocity decay.

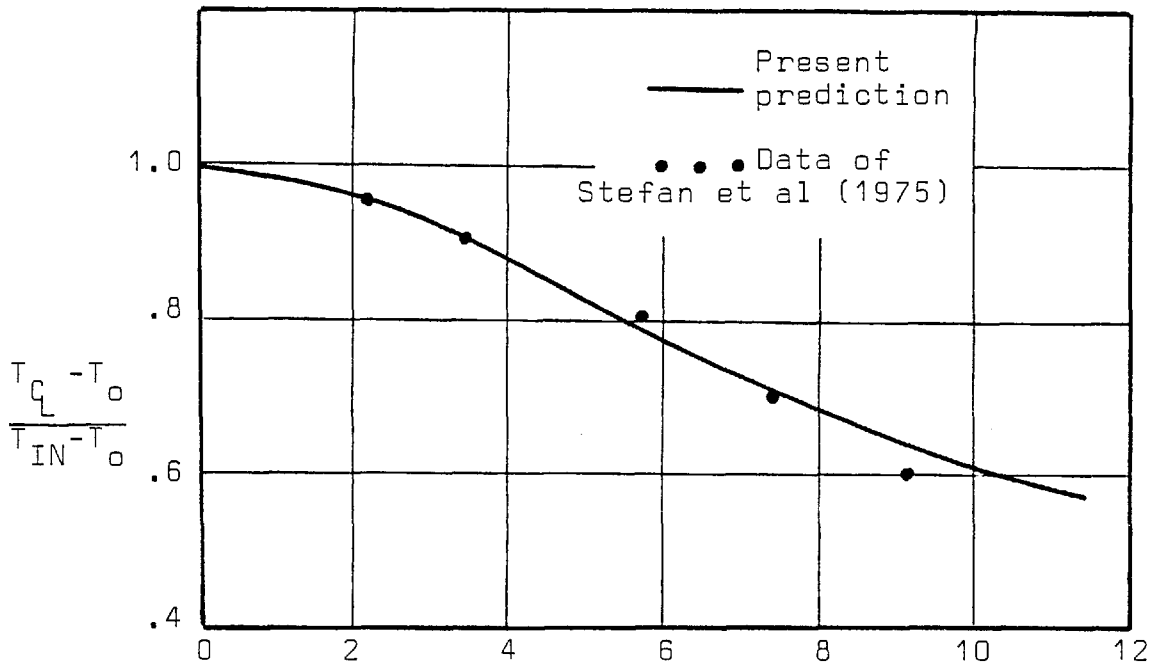
FIG. 5.5.7: PREDICTION OF CENTRE-LINE TEMPERATURE AND VELOCITY; FR=3.25, $\frac{V_o}{U_{IN}}$=0.41, A.R.=1.0.

but the measured velocity appears to decay faster than predicted, in the downstream region. The centre-line temperature and velocity decays for the other two experimental runs, with aspect ratios of 2.4 and 4.8, are presented in Figures 5.5.8 and 5.5.9, respectively. In these cases also, the predictions of the temperature decays are fair. In one case, the velocity decay is slightly under-predicted, while in the other case it is slightly over-predicted.

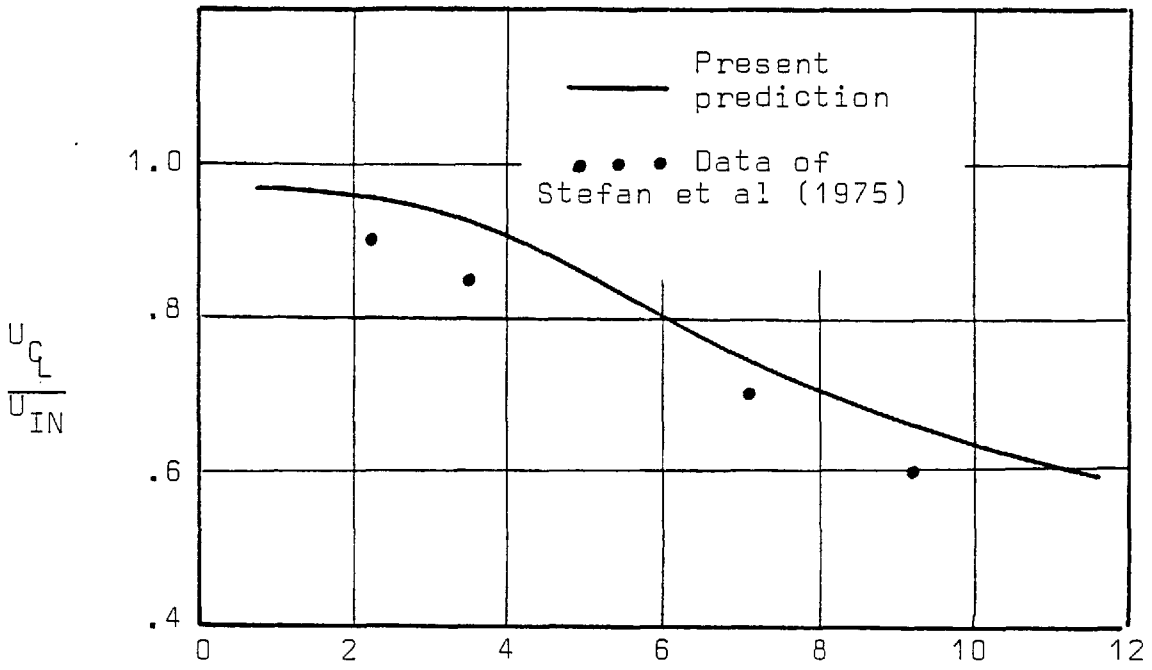
In analogy with the potential core in non-buoyant jet flows, it is commonly assumed that there is a zone of flow establishment within which the centre-line velocity and temperature remain constant. These measurements, in agreement with the predictions, show that the velocity and temperature do not, in fact, remain constant, but vary gradually right from the discharge port.

Figure 5.5.10 shows the comparisons of the predicted jet trajectories with the measurements, for the three experimental runs. The agreement appears satisfactory. The ability of the crossflow to bend over the jet is seen to decrease with increase in aspect ratio.

To complete the crossflow predictions presented in this subsection, some temperature contours and cross-stream profiles are shown for Stolzenbach and Harleman's data, run 2 (Froude number = 5.85, $\frac{U_{max}}{U_{IN}}$ = .087), in Figure 5.5.11. The corresponding velocity contours and profiles are shown in Figure 5.5.12. The temperature and velocity contours are fairly similar, indicating that the buoyancy effects are not very prominent.

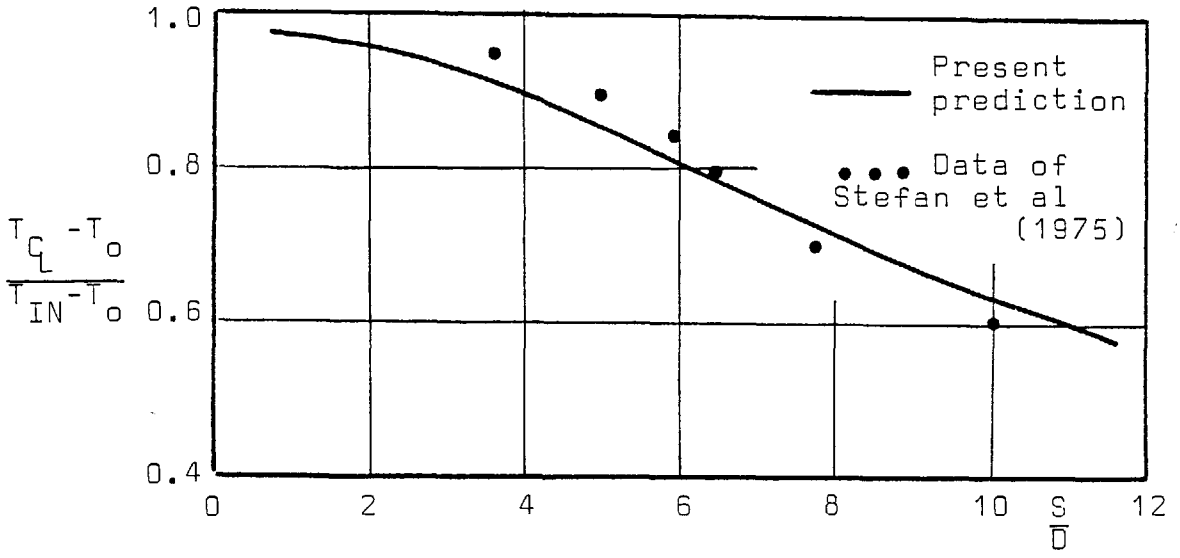


(a) Centre-line temperature decay.

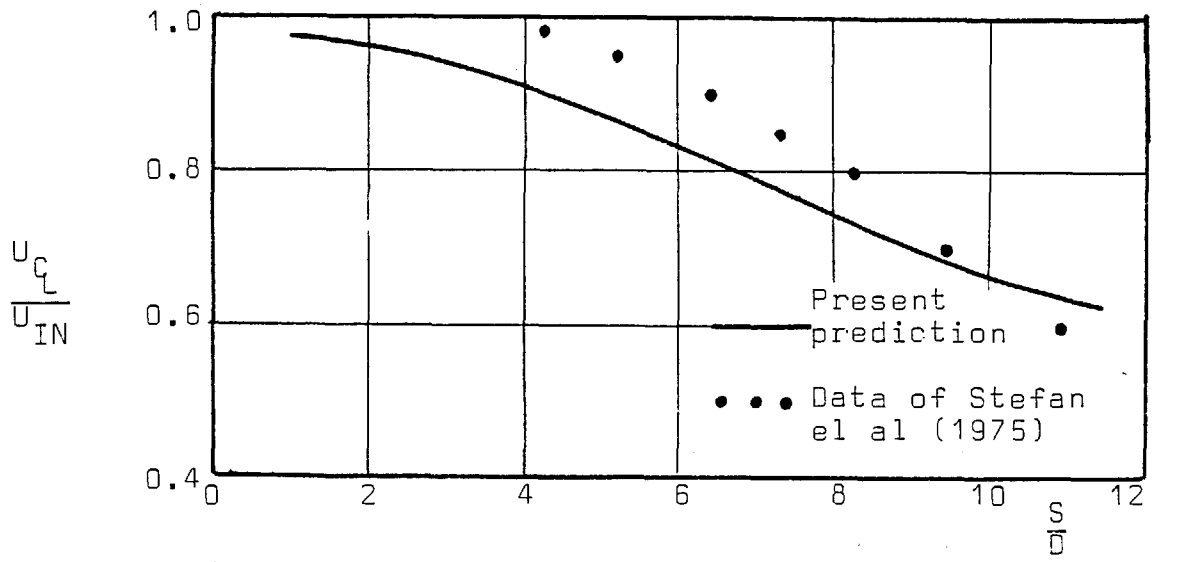


(b) Centre-line velocity decay.

FIG. 5.5.8: PREDICTION OF CENTRE-LINE TEMPERATURE AND VELOCITY; FR=3.25, $\frac{V_o}{U_{IN}}$=0.41, A.R.=2.4.



(a) Centre-line temperature decay.



(b) Centre-line velocity decay.

FIG. 5.5.9: PREDICTION OF CENTRE-LINE TEMPERATURE AND VELOCITY; FR=3.25, $\frac{V_o}{U_{IN}}$=0.41, A.R.=4.8.

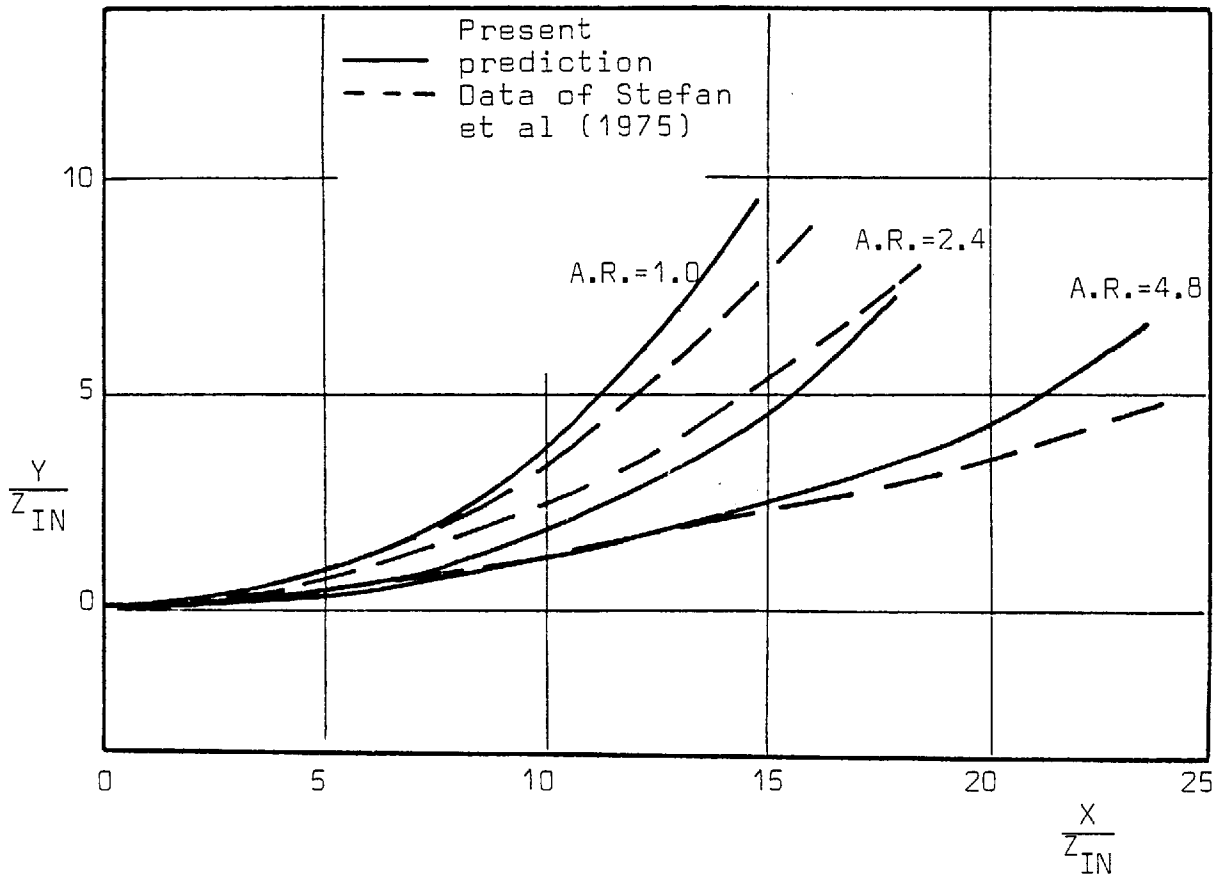


FIG. 5.5.10: PREDICTION OF CENTRE-LINE TRAJECTORIES; FR=3.25, $\frac{V_o}{U_{IN}}$=0.4, A.R.=1.0, 2.4, AND 4.8.

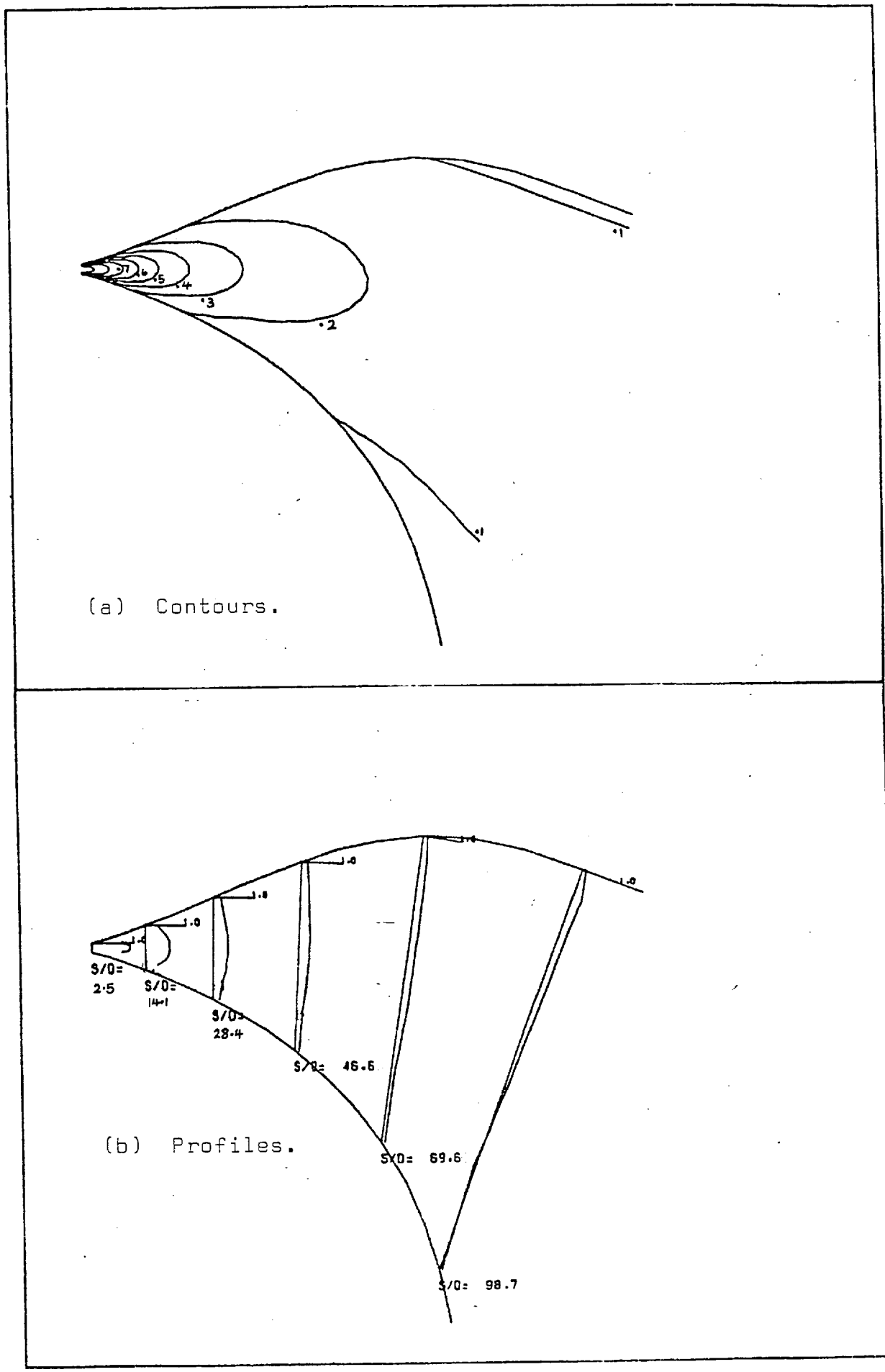


FIG. 5.5.11: PREDICTED TEMPERATURE CONTOURS AND PROFILES; FR=5.85, $\frac{V_o}{U_{IN}}$=0.087, A.R.=0.51.

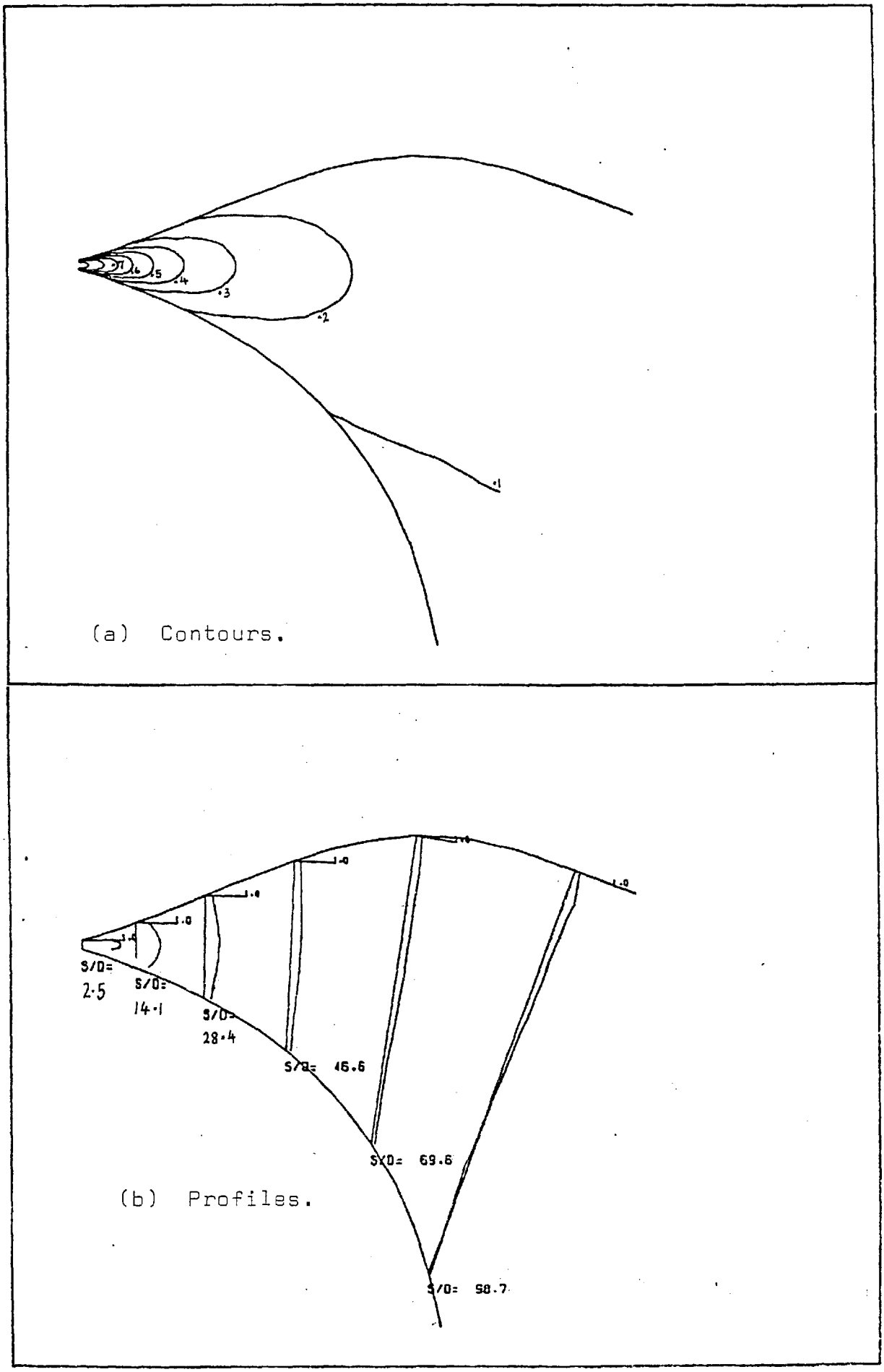


FIG. 5.5.12: PREDICTED VELOCITY CONTOURS AND PROFILES;
FR=5.85, $\frac{V_o}{U_{IN}}$=0.087, A.R.=0.51.

The comparison of the present model predictions with the relatively small range of suitable experimental data found in the literature shows that the model could satisfactorily predict heated surface discharges into crossflowing ambient fluid.

5.6 Comparison of the Present Predictions with Other Model Predictions

In this section, the present model predictions are compared with model predictions by other authors. The test conditions for the first set of comparisons are those of two of Stolzenbach and Harleman's experiments discussed in Section 5.4. These are:

Run 2, (Fr. = 4.44 and A.R. = 5.8), and

Run 5, (Fr. = 9.56 and A.R. = 1.0).

Predictions* by the integral models of Stolzenbach and Harleman, and Prych and the "semi-empirical" model of Pritchard are compared with the present predictions and the experimental data. The comparisons of the longitudinal variations of the centre-line temperature decay, half-width and half-depth are shown in Figure 5.6.1, for Run 2. There is nothing to choose between the two integral models and the present model predictions, though the Stolzenbach and Harleman's model is slightly superior in predicting the half-width, and the present one is slightly superior in predicting the depth. The "semi-empirical" model performed very poorly. Figure 5.6.2 show similar comparisons for Run 5. The statements made above also apply

---

* NOTE: These predictions are adapted from Dunn et al (1975). The models have been reviewed in Chapter 2.

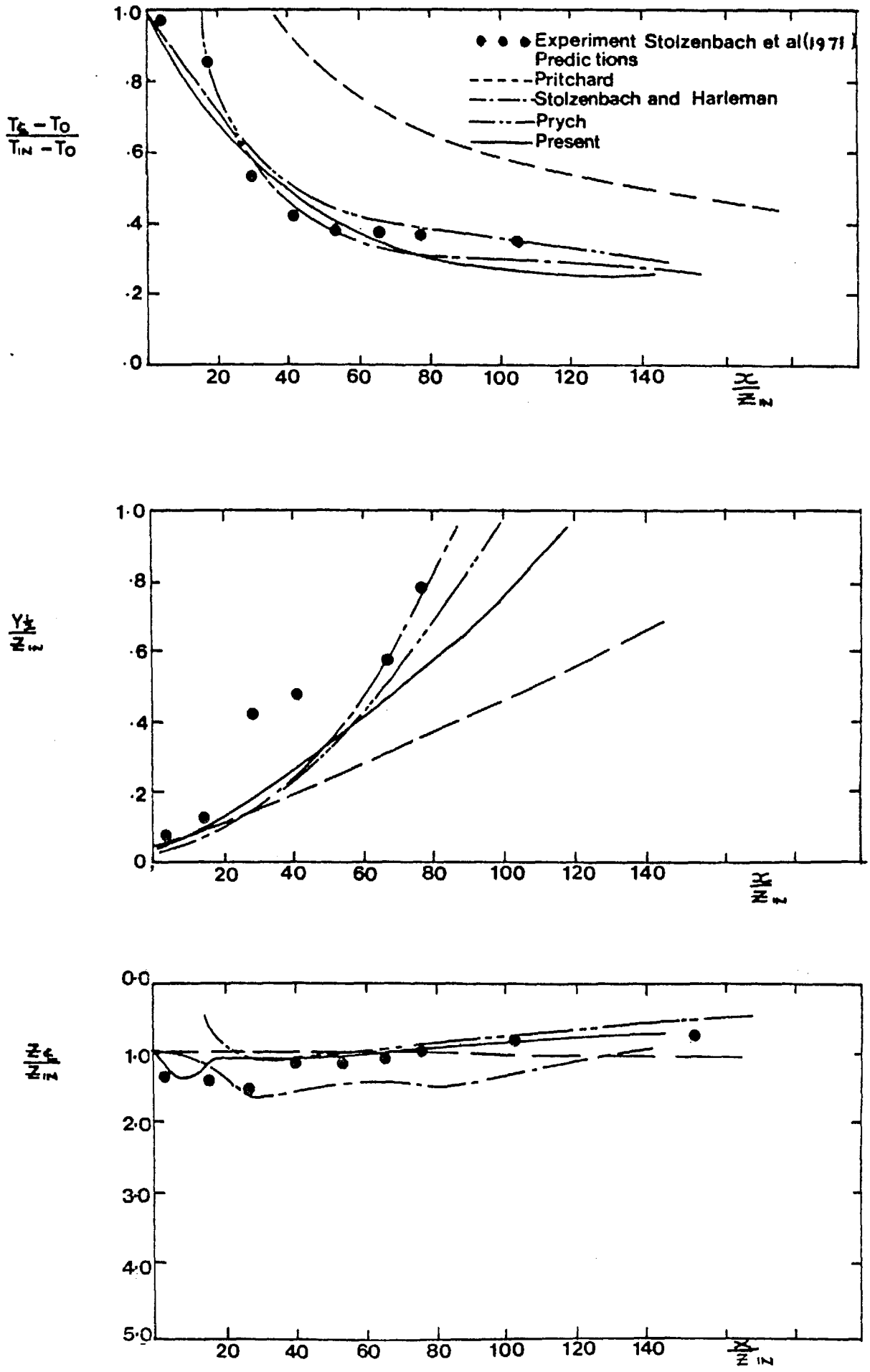


FIG. 5.6.1: COMPARISON OF VARIOUS MODEL PREDICTIONS OF A HEATED SURFACE DISCHARGE; FR=4.44, A.R.=5.8.

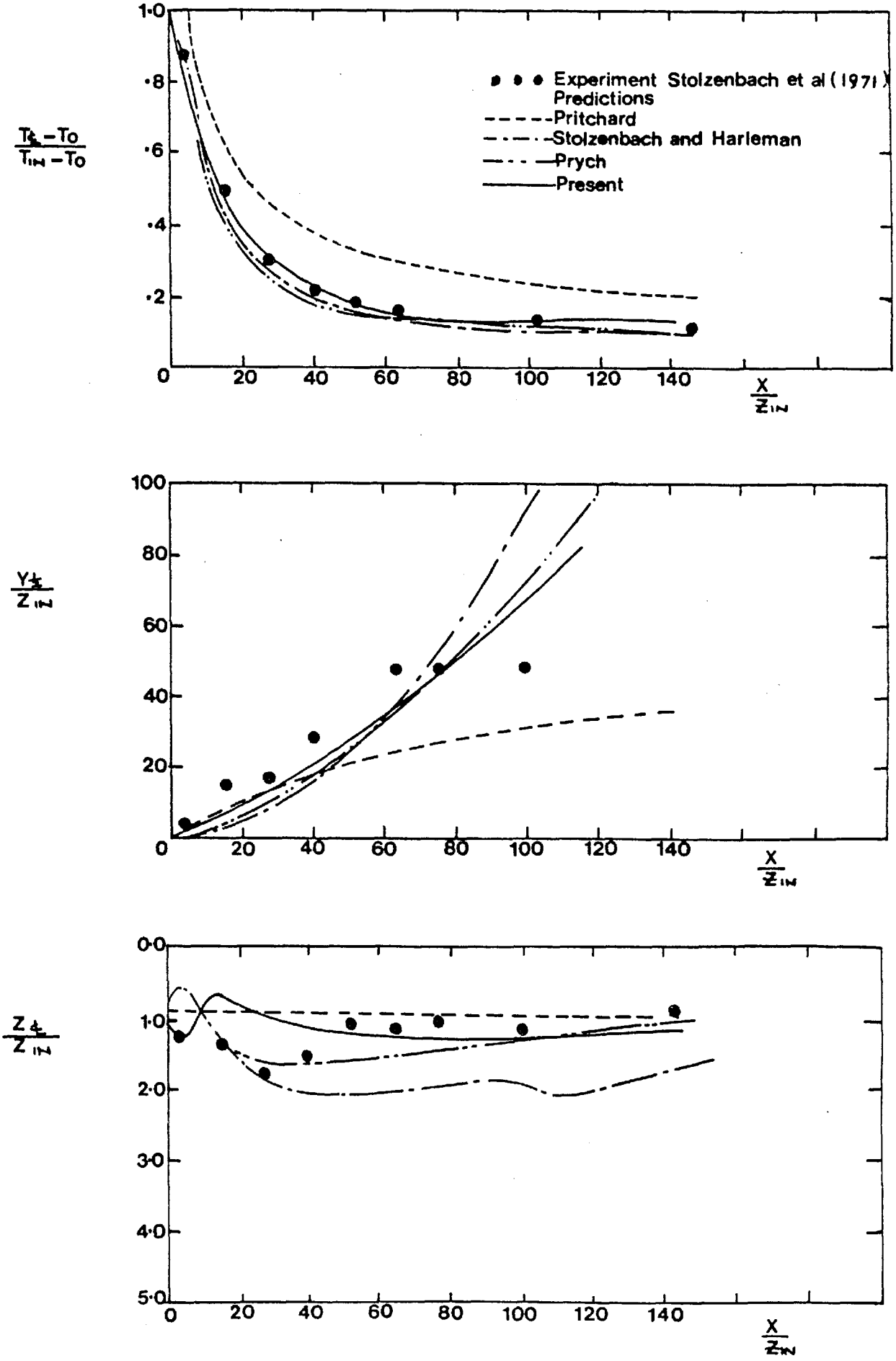


FIG. 5.6.2: COMPARISON OF VARIOUS MODEL PREDICTIONS OF A HEATED SURFACE DISCHARGE; FR=9.56, A.R.=1.0.

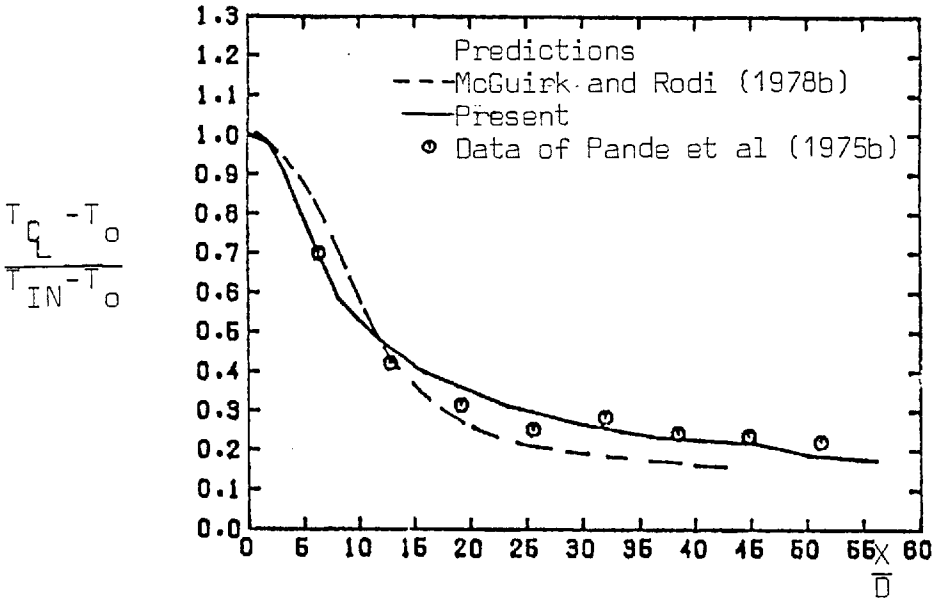
in this case. The reason that Pritchard's model performed so poorly is probably that the predictions with this model depend greatly on the type of experimental data which have been used to calibrate it.

The second set of comparisons is between the three-dimensional numerical model predictions of McGuirk and Rodi (1978b), and the present model predictions, of Pande and Rajaratnam's experimental data discussed in Section 5.4. The test conditions are:

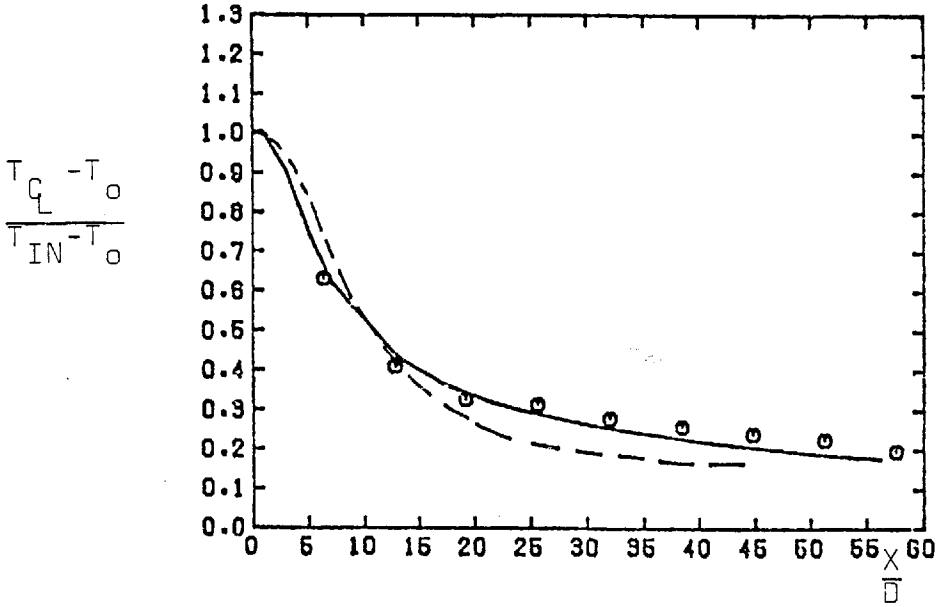
Run 1, (Fr. = 2.59, A.R. = 1),
Run 2, (Fr. = 1.67, A.R. = 1), and
Run 3, (Fr. = 1.32, A.R. = 3.06).

Figure 5.6.3 shows the predictions of the centre-line temperature decays for the three runs. McGuirk and Rodi's model consistently predicts higher temperatures, near the outfall, and lower temperatures, further downstream, than the present model. The present model predictions are slightly better. Figure 5.6.4 shows the predictions of the centre-line velocity decay for Runs 1 and 3. The same trend as for the temperature predictions is repeated. However, the sharp rise in velocity near the outfall predicted by the present model is not predicted by McGuirk and Rodi's model, which indicates that the latter is not as sensitive to buoyancy effects.

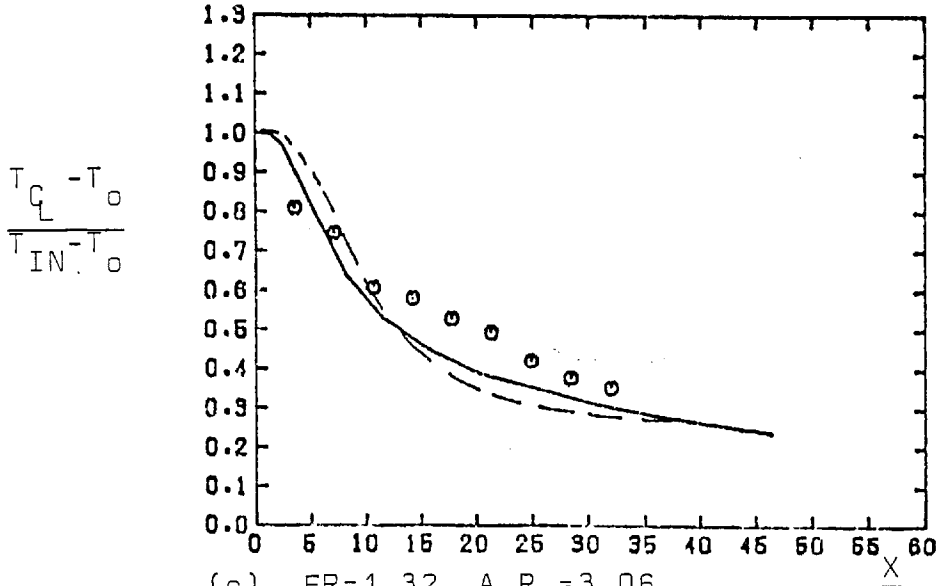
It may be concluded that the present model would perform as well, if not better than, the most popular models currently in use for predicting heated surface discharges into stagnant ambient fluid.



(a) FR=2.59, A.R.=1.

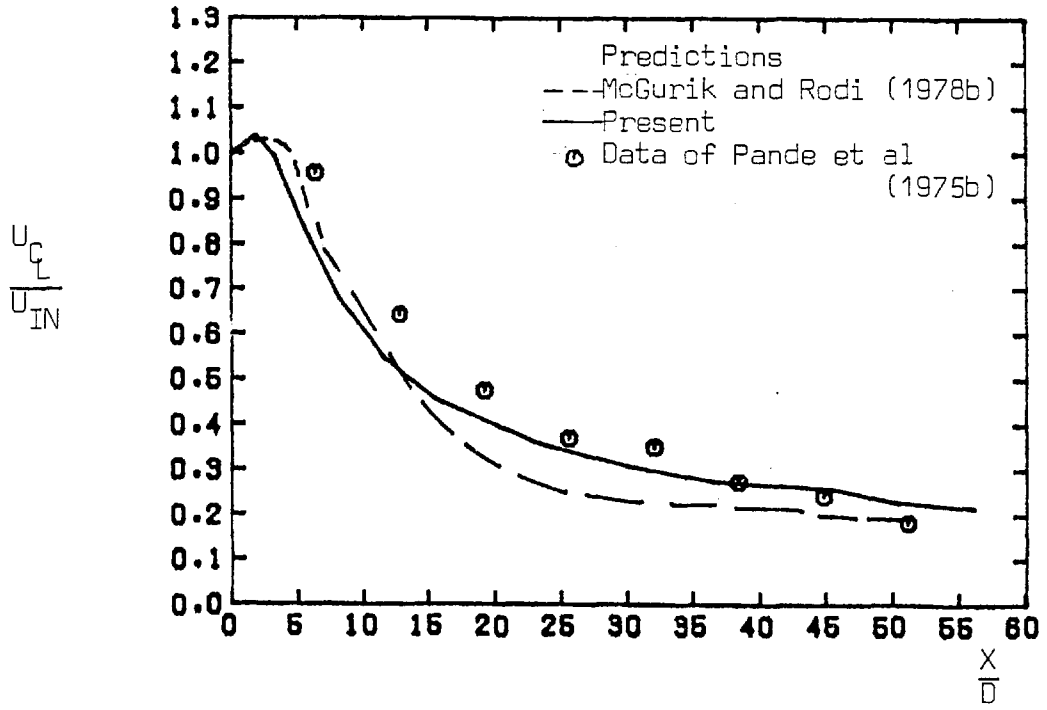


(b) FR=1.67, A.R.=1.

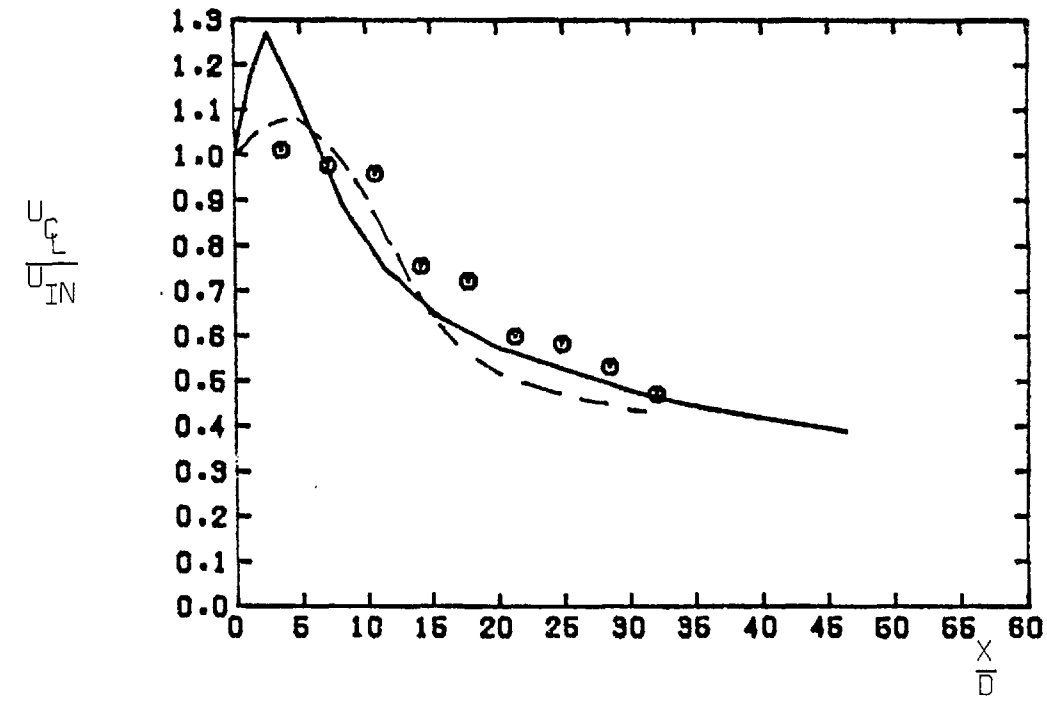


(c) FR=1.32, A.R.=3.06.

FIG. 5.6.3: COMPARISON OF TWO MODEL PREDICTIONS OF CENTRE-LINE TEMPERATURE DECAY OF HEATED SURFACE DISCHARGES.



(a) FR=2.59, A.R.=1.



(b) FR=1.32, A.R.=3.06.

FIG. 5.6.4: COMPARISON OF TWO MODEL PREDICTIONS OF CENTRE-LINE VELOCITY DECAY OF HEATED SURFACE DISCHARGES.

5.7 Prediction of Heated Surface Discharges into Natural Waters

In this section, model predictions are compared with measurements of thermal plumes resulting from prototype discharges. There are so many uncertainties surrounding the existing field data that no comparisons with them can be conclusive. Indeed, the present comparisons are made partly to illustrate this observation. Two data sets are used as test cases. The first is a set of 11 thermal plume maps produced as a result of an aerial survey of the thermal discharge from Pilgrim Nuclear Power Station into Cape Cod Bay, Plymouth, Massachusetts, carried out by the Coastal Research Corporation.

The second set of data is one of the sets of measurements carried out by the Energy and Environmental Systems Division of Argonne National Laboratory, of the thermal discharge from Point Beach Nuclear Power Station into Lake Michigan, on May 23, 1972.

Figure 5.7.1, (adapted from Dunn et al (1975)) shows the 11 centre-line temperature decay data resulting from Coastal Research Corporation's aerial survey. The times of the measurements are shown, in the key, in front of the symbols. A striking observation is that there seems to be no correlation between the tidal period and the measured data, as might have been expected. For example, the low tide measurements made at 1302, 1319 and 1331 seem to cover the whole range of the measured data. This would imply that the temperature excess changed by over 100% in less than half an hour. The same applies to the high tide measurements made at 1724 and 1744.

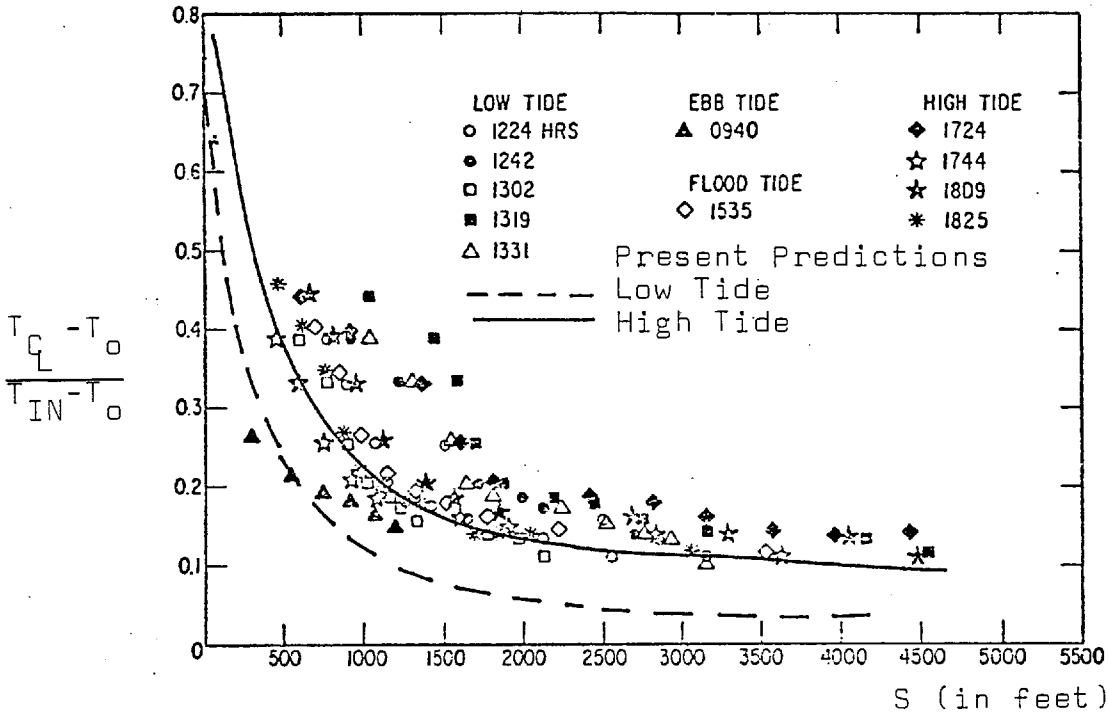


FIG. 5.7.1: PREDICTION OF THE FIELD DATA ON HEATED SURFACE DISCHARGES INTO CAPE COD BAY, MASSACHUSSETTS, MEASURED BY, COASTAL RESEARCH CORPORATION: ADAPTED FROM DUNN ET AL (1975).

In spite of these uncertainties two model predictions of this data set are made. The first corresponds to the high-tide condition, when the discharge parameters are:

Froude number = 2.3, and Aspect ratio = 4.

The second corresponds to the low-tide condition with discharge parameters of:

Froude number = 11.0, and Aspect ratio = 5.

The high-tide prediction of the temperature decay appears to lie within the lower half of the measured data. For the low-tide condition, the predicted temperatures are much too low. The reason for this may be that the specified discharge parameters may not be truly indicative of the thermal discharge. At low tide, the discharge went through a free overfall, during which there might have been considerable momentum dissipation, so that the characteristic Froude number would be lower than the specified value. The true discharge parameters may be more validly determined by measuring the thermal plume a short distance from the discharge channel.

Figure 5.7.2 shows the comparisons of the predictions by the models of Stolzenbach and Harleman, Prych, Pritchard and the present, to the least-squares fit of the Point Beach field data. All the models, except Pritchard's, predicted centre-line temperature and velocity decays that are too rapid. It would be recalled that in the preceding section, when these models were compared to laboratory data, Pritchard's model predicted lower decay rates than the others. In this case, lower decay rates are again predicted, but while the agreement with the

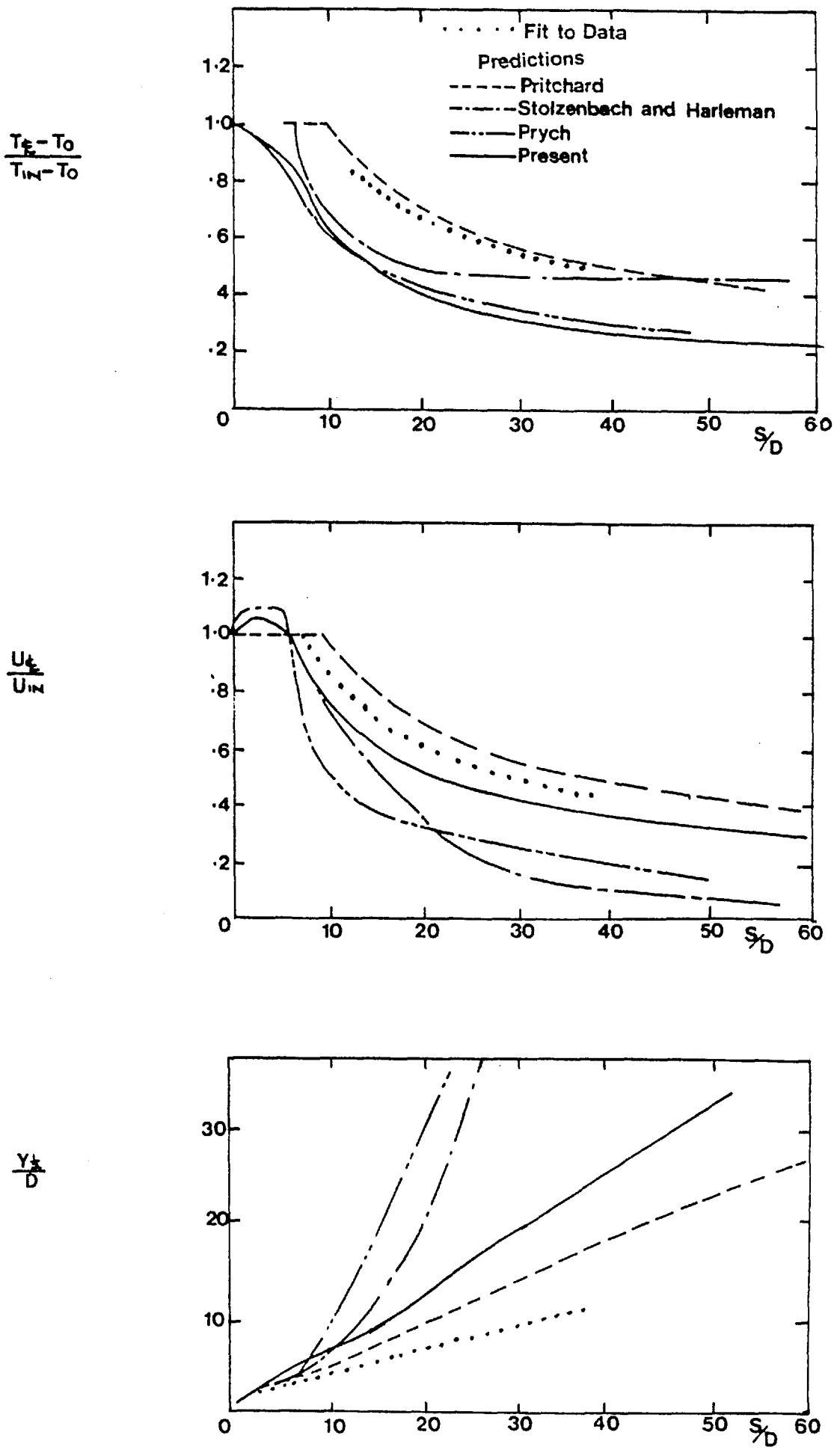


FIG. 5.7.2: COMPARISON OF VARIOUS MODEL PREDICTIONS OF THE FIELD DATA OF THE POINT BEACH THERMAL PLUME ON MAY 23, 1972: ADAPTED FROM DUNN ET AL (1975).

data was poor in the former case it is quite good in the latter. Pritchard's model was calibrated with, amongst other data, field data from Point Beach. It therefore appears to exhibit some of the characteristics of Point Beach data, even when applied to other discharges. The predicted half-widths are also seen to be much higher than the measured. It appears that some of the physical phenomena, such as entrainment of ambient fluid and layer spreading that were modelled with the aid laboratory data may have to be re-modelled for predicting field data. However, this task can not be properly undertaken until good and reliable field data are available.

5.8 Concluding Remarks

In this chapter, the predictions of heated surface discharges into both stagnant and moving ambient fluid were presented. The present numerical model was shown to be capable of predicting heated surface discharges into stagnant or cross-flowing ambient surroundings, in the laboratory fairly well. A parametric study was carried out numerically to show the effects of ambient to discharge velocity ratio, densimetric Froude number and aspect ratio on the prediction of heated surface discharges into coflowing streams. This showed that the velocity ratio has the most prominent effect, and the aspect ratio the least. The comparisons of the present model predictions to predictions by two integral models, one three-dimensional model and one semi-empirical model showed that this model performs as well as the best of these. The semi-empirical model did not predict laboratory data well, but it

was the only one to predict the field data well. Different empirical relations may be required for predicting field data.

This concludes the work on floating-layer flows reported in this thesis. In the next two chapters, full-depth flows are discussed. In the first of these, the predictions of some existing data on supercritical open channel flows are presented; and in the second, the results of the present experimental investigation of supercritical flow of water in channels of varying cross-section are presented.

CHAPTER 6

PREDICTION OF FULL-DEPTH FLOWS

6.1 Introduction

In this chapter, numerous full-depth flows are predicted with the present numerical methods. The emphasis is placed on predicting supercritical flows in open channels. However, some predictions of subcritical flows are also presented to show the contrast between these two types of flow. Most of the predictions of supercritical flows are compared with experimental data and analytical solutions by other authors. The analytical solutions mostly use the method of characteristics.

Some important computational details on the two types of flow predictions are presented in the next section. Then follows the presentation of the supercritical flow predictions. Subcritical flow predictions are presented in the penultimate section, and finally, concluding remarks are made in the last section.

6.2 Computational Details

The same computer code is utilised in predicting both the supercritical and the subcritical flows; with the switch to the use of the hyperbolic or partially-parabolic procedure being made internally, depending on whether the Froude number of the flow is greater or less than one. In predicting the flow of water in a contracting channel, (for example), the following computational details apply:-

Table 6.1: Computational details for predicting supercritical and subcritical water flows in a contracting channel.

Computational Variable	Supercritical flow	Subcritical flow
No. of cross-stream grid points, N	59	19
No. of forward steps	200	50
Forward step size $\frac{\delta x}{b}$	0.03	0.12
Number iteration at each cross-stream plane	3	3
Number of sweeps of the whole calculation domain	1	20
Computer time in CDC 6600 secs.	25	45

The values quoted in the table are for grid-independent results. Such a fine grid distribution is needed in computing supercritical flows in which sharp cross-shock waves occur.

Boundary Conditions

The boundary conditions are prescribed as follows:-

At inlet,

$$\begin{aligned} U &= U_{IN} \\ V &= 0 \\ z &= z_{IN} \end{aligned} \qquad ,(6.2.1)$$

The I-boundary is a symmetry axis along which,

$$\begin{aligned} \frac{\partial U}{\partial y} &= 0 \\ V &= 0 \\ \frac{\partial z}{\partial y} &= 0 \end{aligned} \qquad .(6.2.2)$$

The E-boundary is a wall along which, for the inviscid flows,

$$\frac{\partial U}{\partial y} = 0$$
$$V = 0 \qquad ;(6.2.3)$$
$$\frac{\partial z}{\partial y} = 0$$

and, for the viscous flows,

$$U = 0$$
$$V = 0 \qquad .(6.2.4)$$
$$\frac{\partial z}{\partial y} = 0$$

In the subcritical flow predictions, boundary conditions are also needed for the variable (z) at the exit plane. This is prescribed as:

$$\frac{\partial z}{\partial x} = 0 \qquad .(6.2.5)$$

6.3 Prediction of Supercritical Flows

6.3.1 Flows in channel contractions

The first supercritical flow situation to be predicted is the flow of water in a channel with wall contractions composed of circular arcs. Figure 6.3.1 shows the channel configuration. Figure 6.3.2 shows a comparison of the predicted contours of the water surface profile with the measurements of Ippen et al (1949), for a flow with initial Froude number of 4. It is seen that the predictions agree fairly well with the measurements.

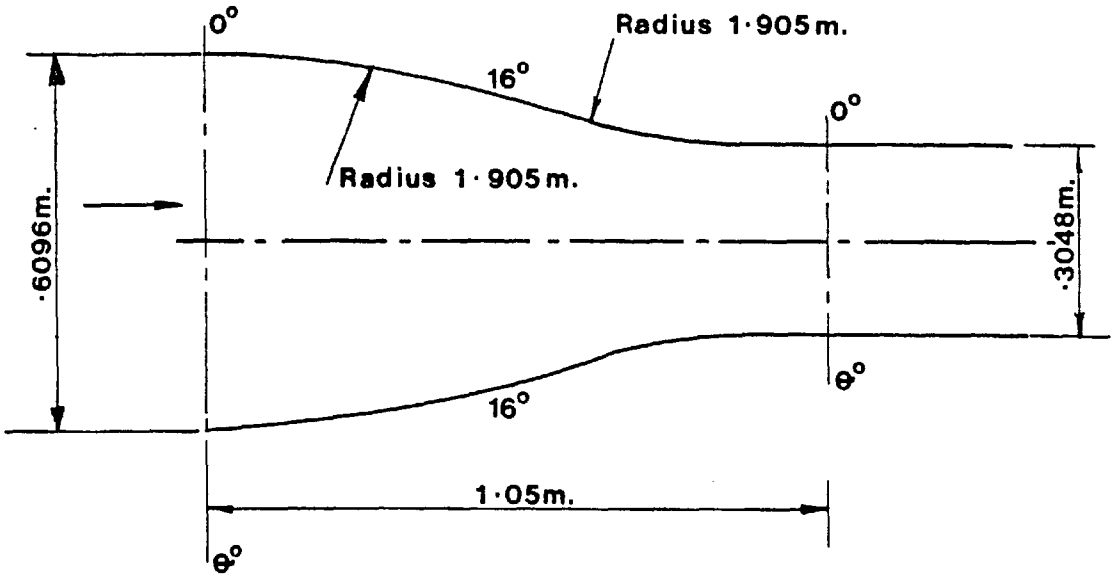


Fig.6.3.1 : Configuration of Channel with Circular Arc Wall Contraction

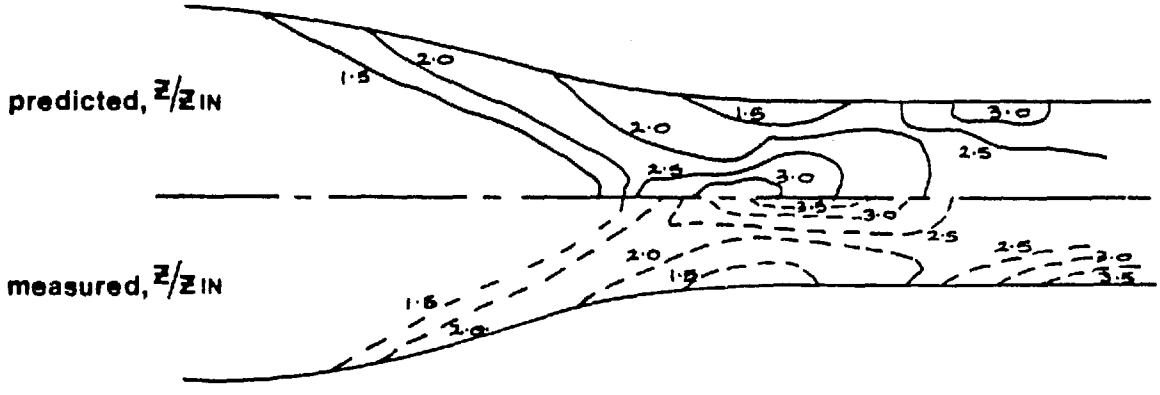
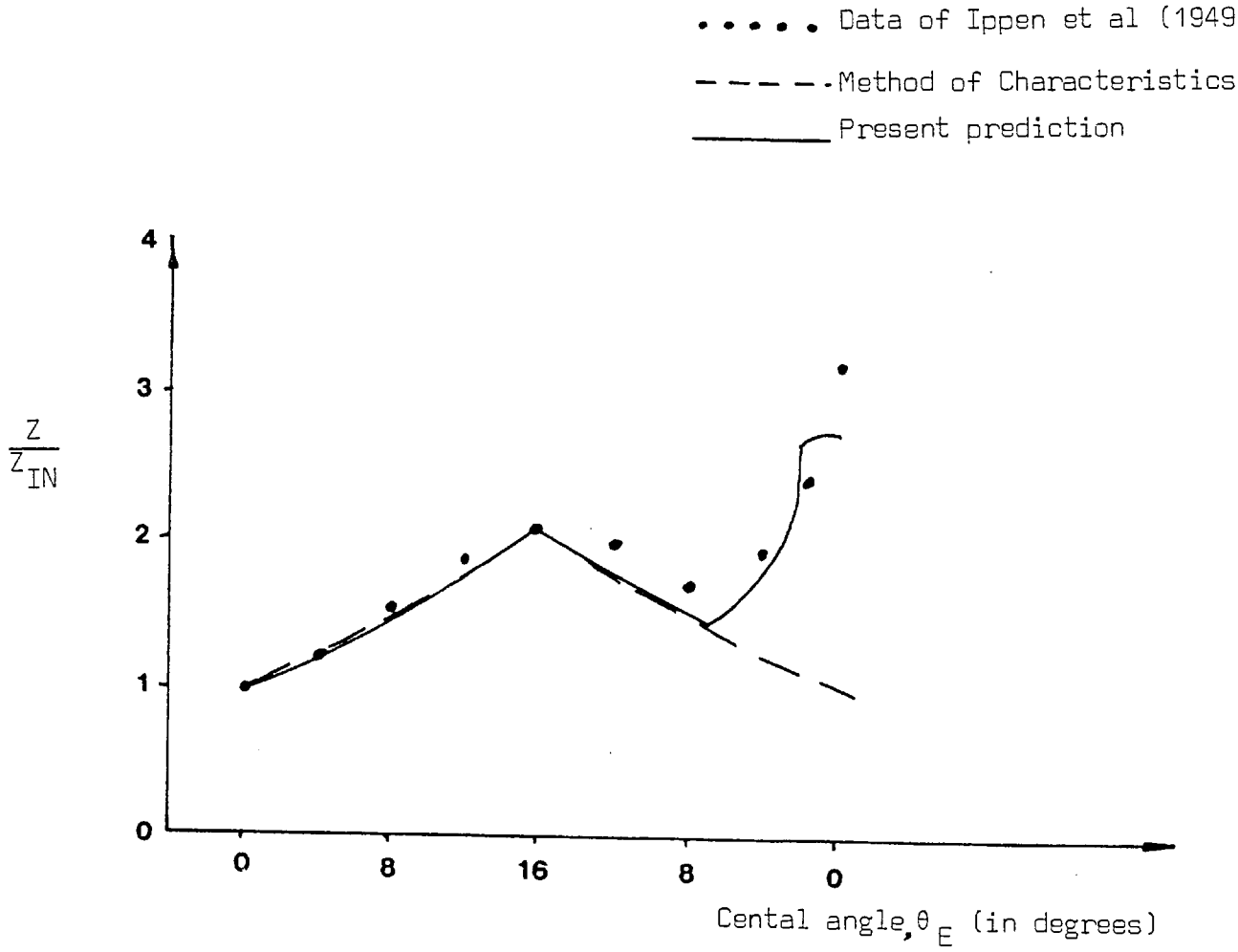


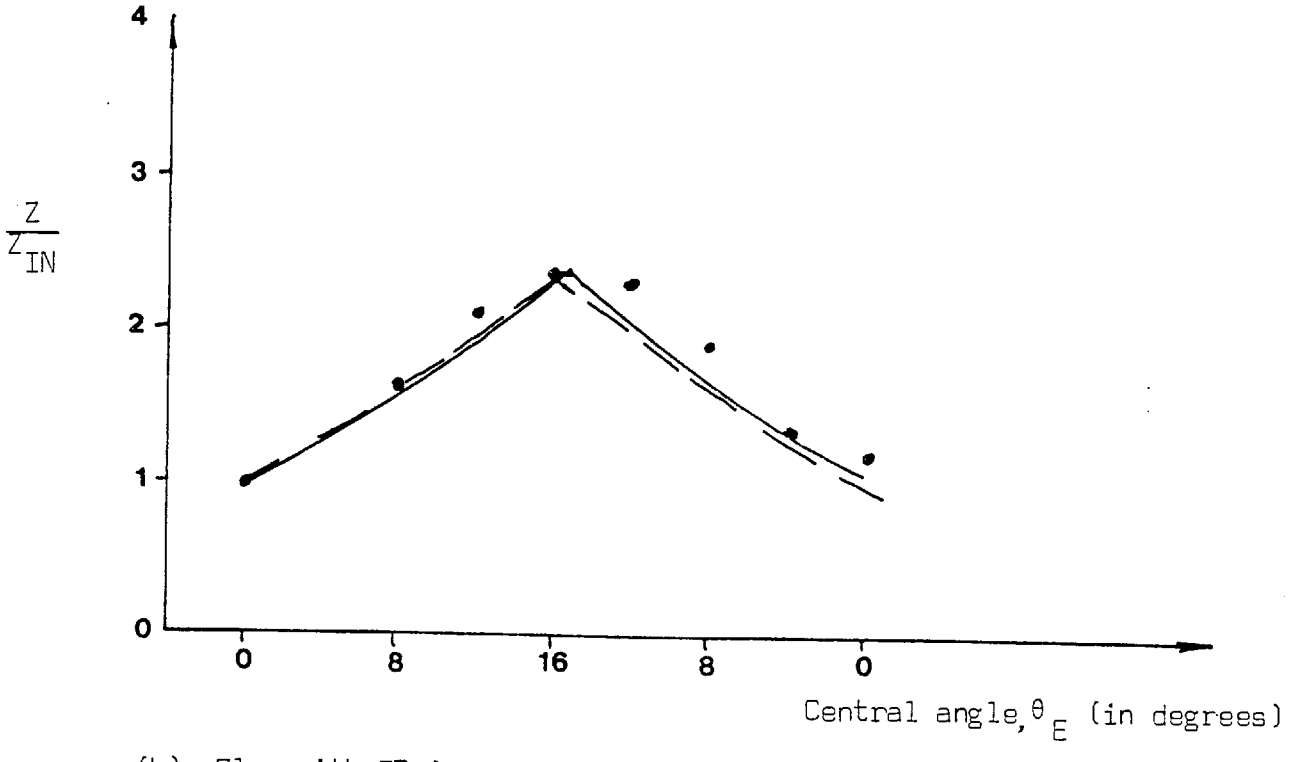
Fig.6.3.2 : Contours of the Water Surface in the Channel for FR=4; Experimental Data by IPPEN et al (1949)

In the same channel, further predictions are made of flows at other initial Froude numbers. Figures 6.3.3 (a) - (d) show the predicted surface profiles along the channel walls, at Froude numbers of 3, 4, 6 and 8, respectively. The points represent the experimental data, and the broken lines, the graphical solution by the method of characteristics, due to Ippen et al (1949). It is seen that, in the first two flows, the present predictions agree fairly well with the measurements. At the two higher Froude number (= 6 and 8), the values of the maximum height of the water surface are well predicted, but their positions are not. At these Froude numbers, the heights of the water surface have risen to three to four times the initial height, and vertical accelerations may not now be negligible. It should be recalled that both the present model, and the method of characteristics neglect vertical accelerations. The present predictions and the solutions with the method of characteristics agree well with each other except in the flow with Froude number of 3, where a second peak in water surface profile is produced at the end of the contracting-channel wall by a wave originating at the other wall, but the characteristic solution did not recognise this.

The second flow situation to be predicted is the supercritical flow of water in a channel composed of straight wall contractions. Figure 6.3.4 illustrates the channel configuration. The predicted contours of the water surface profile, for a flow at Froude number of 4, are compared with the measured surface profile in Figure 6.3.5. It is seen that the agreement is fair. Computations are also performed for flows in the same channel but at Froude numbers of 3, 6, 8 and 10. At either wall,

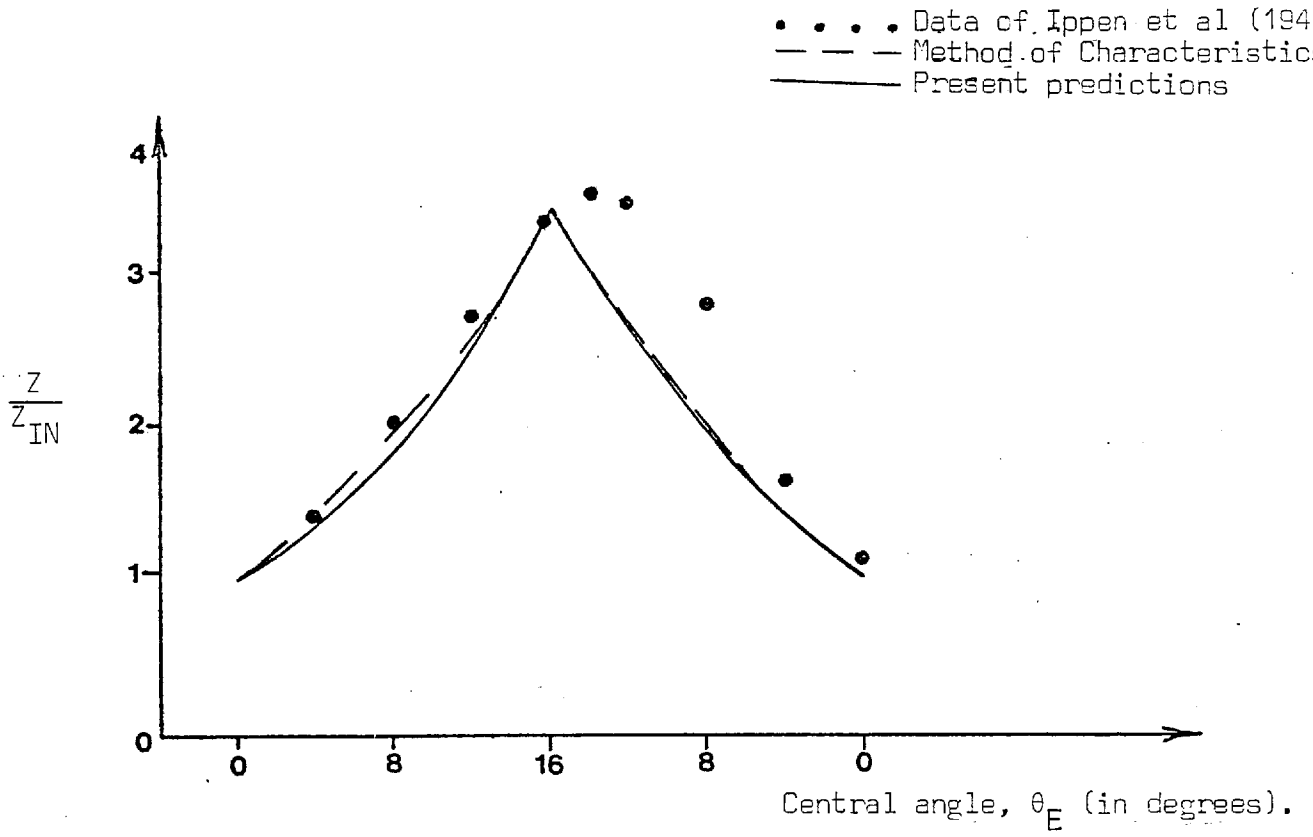


(a) Flow with FR=3.

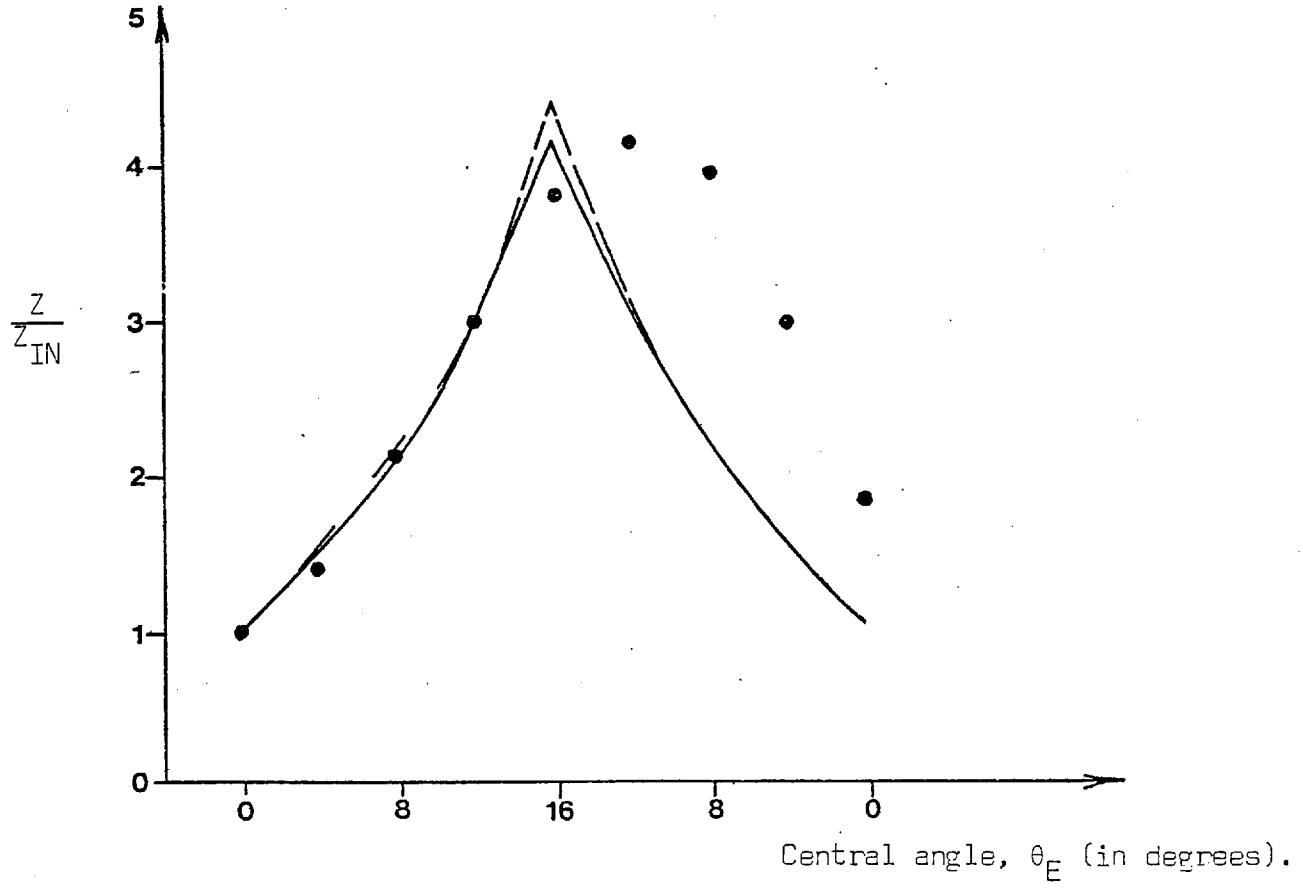


(b) Flow with FR=4.

FIG. 6.3.3: WATER DEPTH RATIO ALONG THE CHANNEL WALL



(c) Flow with FR=6.



(d) Flow with FR=8.

FIG. 6.3.3 (CONTINUED)

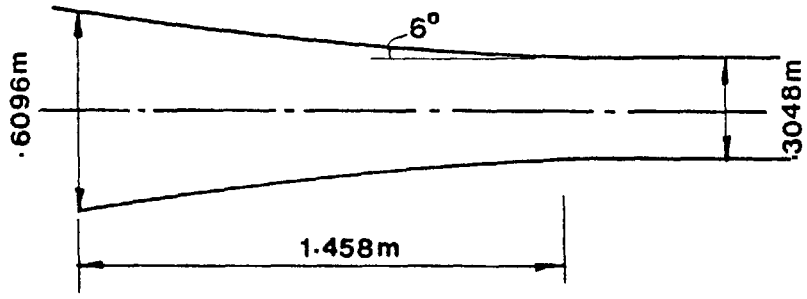


Fig.6.3.4 : Configuration of Channel with Straight Wall Contractions

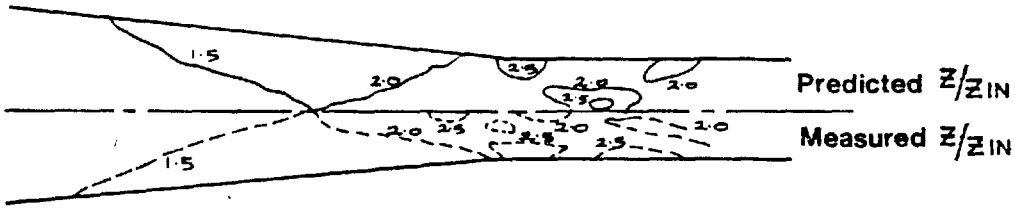


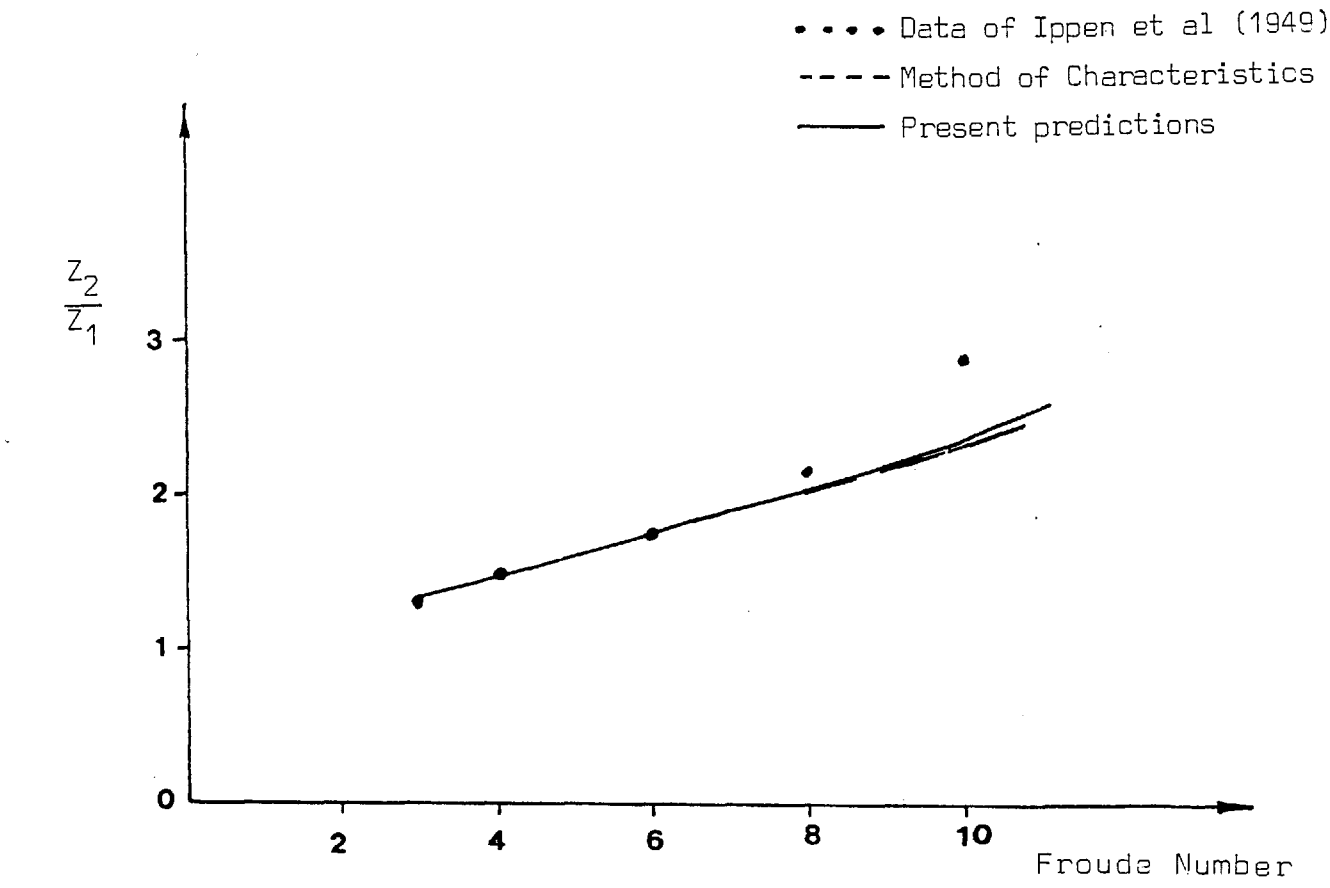
Fig.6.3.5 : Contours of the Water Surface in the Channel for FR = 4; Experimental Data by IPPEN et al (1949)

a sharp and well-defined cross-shock wave is produced. The height of this wave and the corresponding wave angle are presented in Table 6.2 for the five Froude numbers. These results are plotted in Figure 6.3.6.

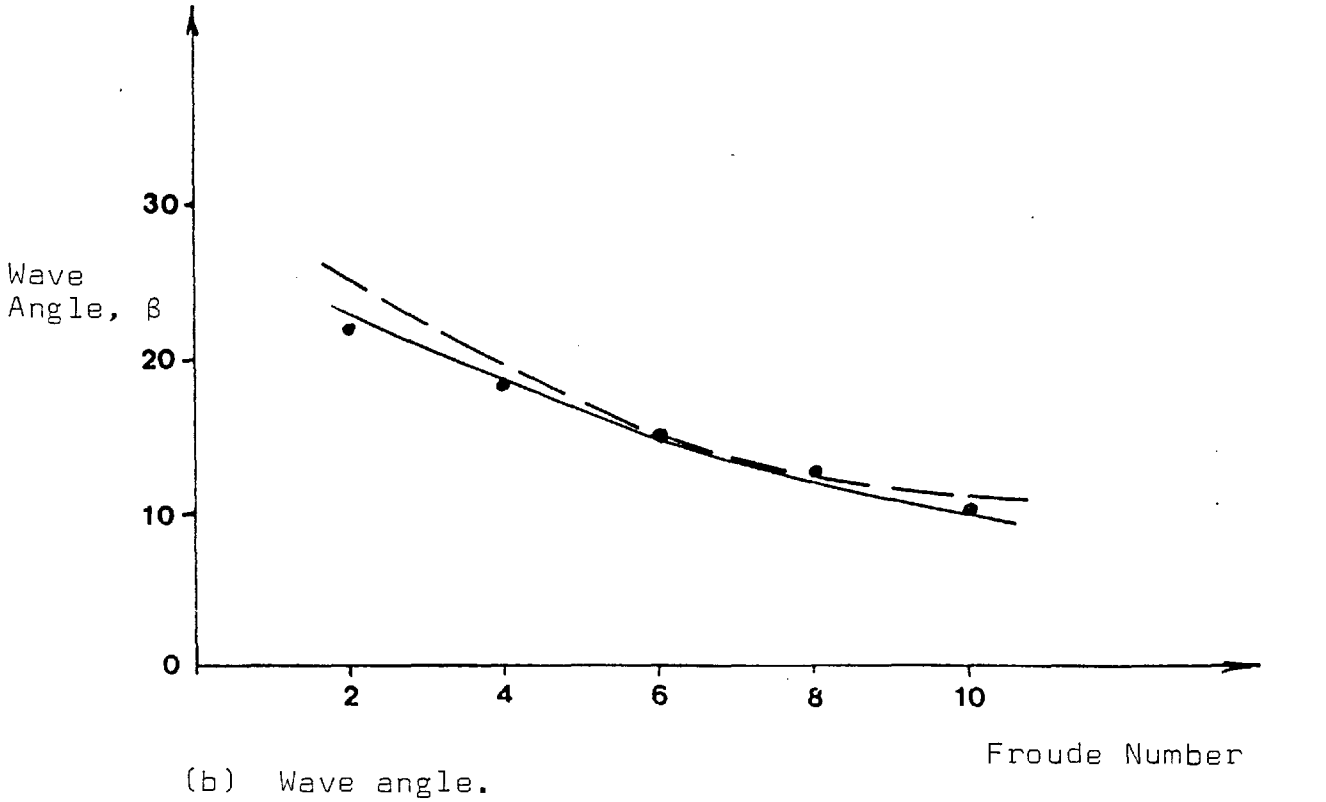
Table 6.2: Prediction of wave height and wave angle in a 6^{o} channel contraction.

	Wave angle β, (in degrees)			Wave height ratio z_2/z_1		
FROUDE No.	Method of Characteristics	Experiment	Present Prediction	Method of Characteristics	Experiment	Present Prediction
3	25.2	22.0	23.6	1.38	1.31	1.35
4	19.5	18.7	18.8	1.47	1.52	1.51
6	15.0	15.2	14.8	1.75	1.73	1.73
8	12.3	12.8	12.0	2.00	2.17	2.07
10	11.1	10.5	10.0	2.30	2.88	2.30

It is seen that the wave heights are well predicted at the lowest three Froude numbers. At Froude numbers of 8 and 10, they are under-predicted. The wave angles are well predicted, by the present method, at all Froude numbers; being slightly superior to the method of characteristics. The initial Froude number of the flow in the channel is now held constant at a value of 3.86, while the wall angles are varied from 3^{o} up to 24^{o} in increments of 3^{o}. The calculated and measured wave angles, and wave heights are presented in Table 6.3.



(a) Height ratio.



(b) Wave angle.

FIG. 6.3.6: VARIATION OF THE HEIGHT AND ANGLE OF THE FIRST WAVE PRODUCED AT THE CHANNEL WALLS, $\theta_{E=6^{o}}$ WITH FROUDE NUMBER.

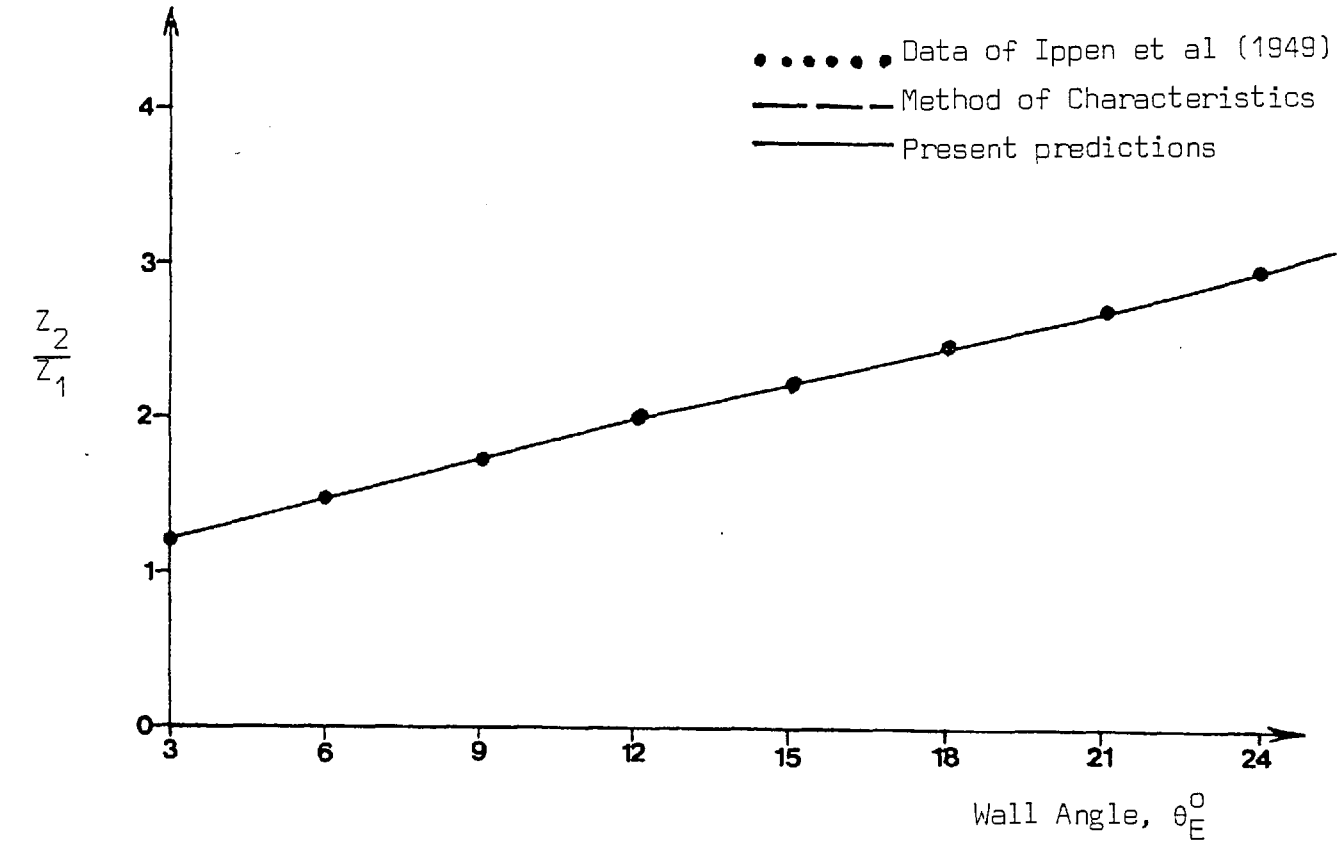
Table 6.3: Prediction of wave height and wave angle in contracting channels, at Froude number = 3.86.

	Wave angle β, (in degrees)			Wave height ratio z_2/z_1		
Wall Angle, θ^o	Method of Characteristics	Experiment	Present Prediction	Method of Characteristics	Experiment	Present Prediction
3	17.6	15.5	17.6	1.21	1.24	1.23
6	20.3	18.3	19.6	1.47	1.47	1.47
9	23.2	22.8	23.3	1.70	1.73	1.72
12	26.5	26.1	26.2	2.00	2.00	1.99
15	29.5	29.9	28.1	2.22	2.22	2.20
18	32.4	34.3	31.6	2.49	2.47	2.45
21	35.8	38.0	35.0	2.72	2.71	2.74
24	39.3	41.3	37.3	2.99	3.01	2.98

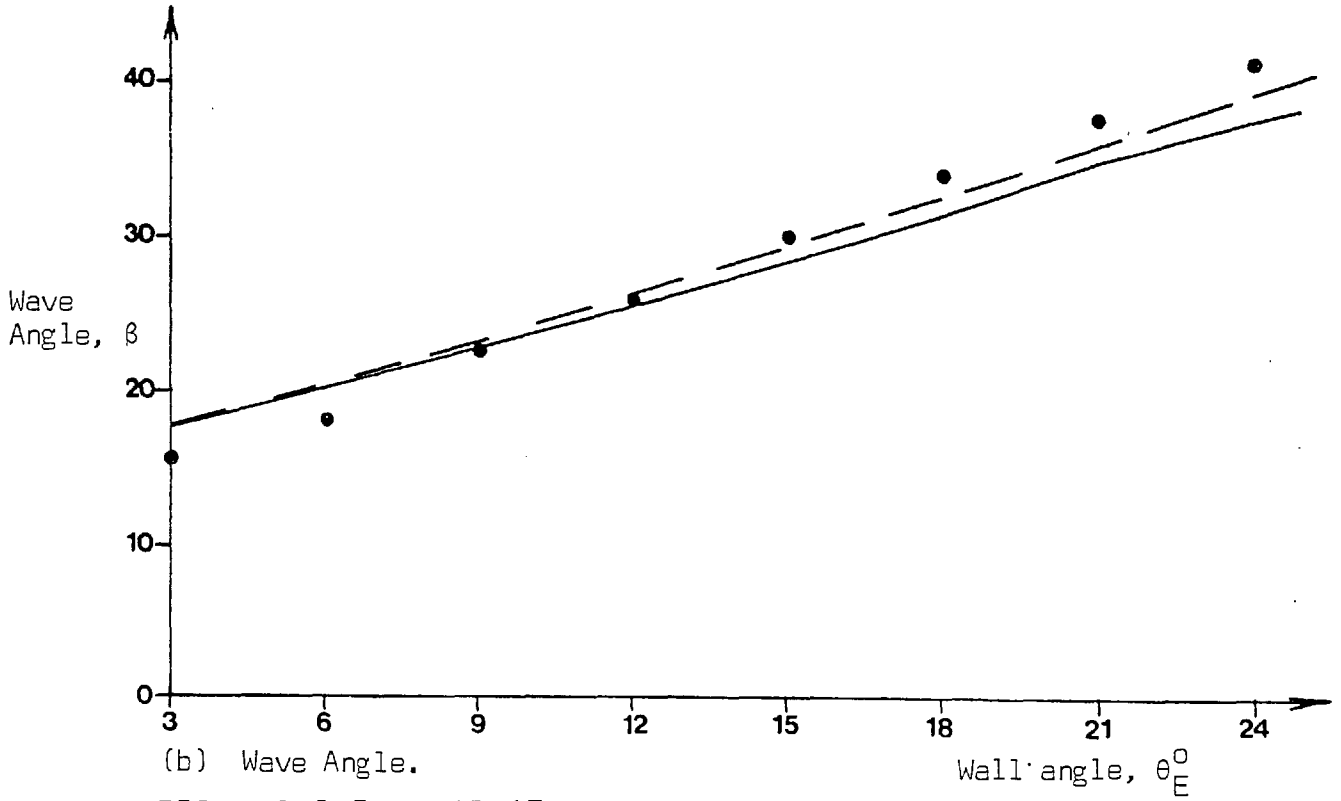
These results are shown graphically in Figure 6.3.7. It is seen that the wave heights are well predicted in all cases, both by the present method and the method of characteristics. However, there is some deviation between the predicted and the measured wave angles. The method of characteristics appears to be slightly superior in predicting the wave angles.

6.3.2 Flow in curved channels

In this section the supercritical flow of water in circular channels is predicted. Two flows are considered. The first is a flow with an initial Froude number of 4.56, and an aspect ratio of 9.58, in a circular channel with inner wall radius of 7.39, and outer wall radius of 7.85. Figure 6.3.8 shows a comparison of the predicted water surface height along the outer wall, with experimental data and the characteristics solution by Knapp (1949). It is seen that the measurements



(a) Height Ratio.



(b) Wave Angle.

FIG. 6.3.7: VARIATION OF THE HEIGHT AND ANGLE OF THE FIRST WAVE PRODUCED AT THE CHANNEL WALLS, WITH WALL ANGLE, FOR FR=3.86.

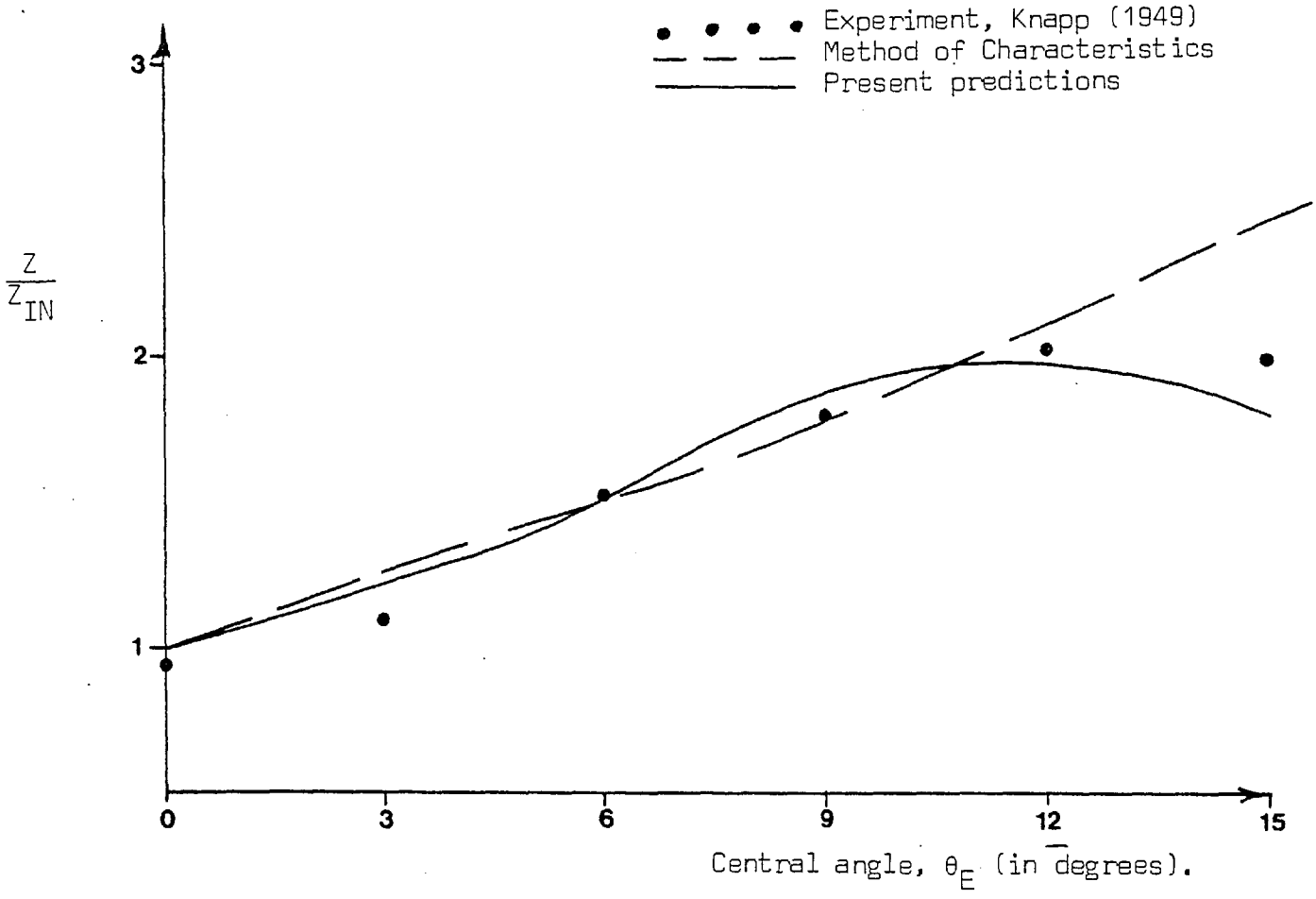


FIGURE 6.3.8: VARIATION OF WATER SURFACE HEIGHT ALONG THE OUTER WALL OF A CIRCULAR CHANNEL, R_I=7.39, FOR FR=4.56, A.R.=9.38.

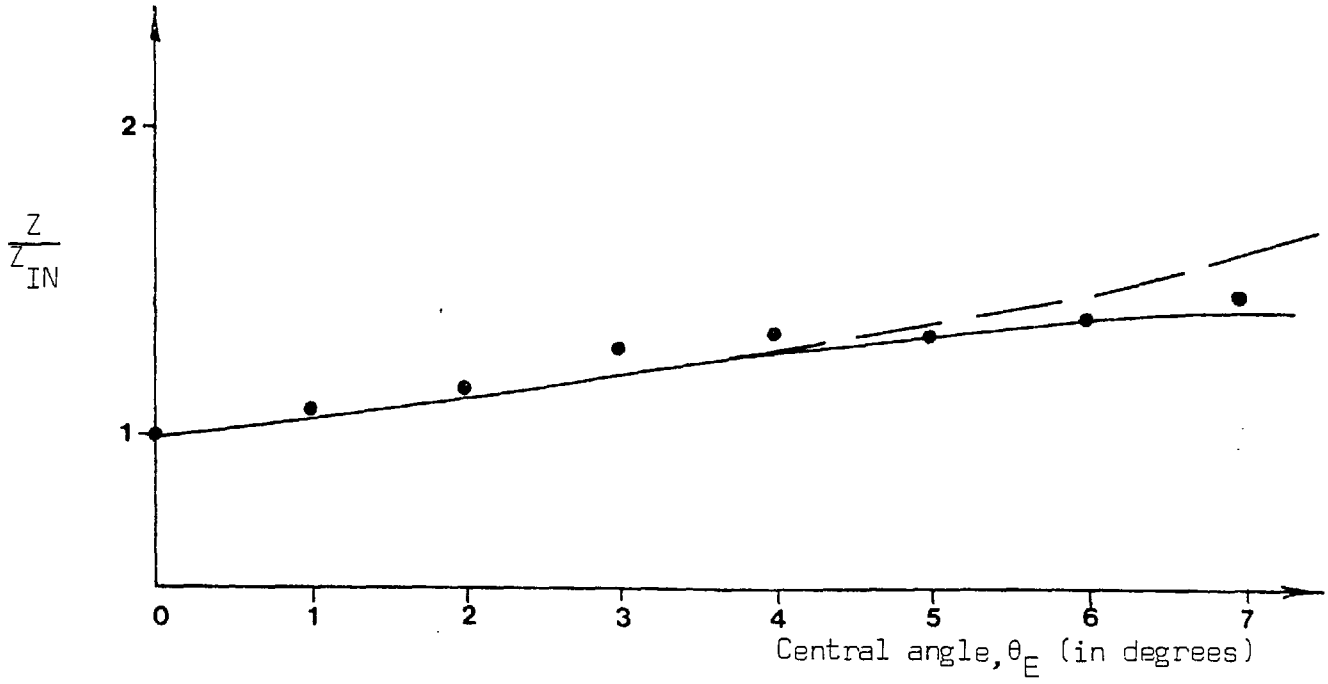


FIG. 6.3.9: VARIATION OF WATER SURFACE HEIGHT ALONG THE OUTER WALL OF A CIRCULAR CHANNEL, R_I=15.0, FOR FR=4.24, A.R.=12.5.

are well predicted. It may be noted that the measured height of the water surface at the outer wall, at inlet, was less than the nominal inlet height, so that the flow entering the curved channel was probably non-uniform. This may be the cause of the small deviations between the predictions and the measurements.

The second computation is performed for a flow with Froude number of 4.24, and aspect ratio of 12.50, in a circular channel with inner radius of 15.01, and outer radius of 15.46. Figure 6.3.9 shows the comparison of the predicted water surface height along the outer wall with the measurements and characteristics solution. It is seen that the measured surface heights are well predicted. In these two cases, the present predictions are superior to the characteristic solutions.

6.4 Prediction of Subcritical Flows

In the present study, the effort has been mostly concentrated on predicting supercritical flows. However, to show the contrast between supercritical and subcritical flows a few predictions of subcritical flows are presented in this section. Computations are performed for two flow situations similar to those of which supercritical predictions were presented in the preceding section. The two cases are flows in the contracting channels, previously shown in Figures 6.3.1 and 6.3.4, i.e. one channel with circular wall contractions, and the other with straight wall contractions.

In each case, two computations are performed: one inviscid, and one viscous. For the viscous flow computations, the turbulent viscosity is prescribed in accordance with Prandtl's mixing length model, as discussed by Launder and Spalding (1972), thus:

$$\mu_t = \rho \ell_m^2 \left|\frac{\partial u}{\partial y}\right| \qquad ,(6.4.1)$$

where,

ℓ_m is the mixing length, prescribed as:

$$\ell_m = Ky, \qquad \text{when } \frac{y}{b} \leq \frac{\lambda}{K} \text{ ;}$$

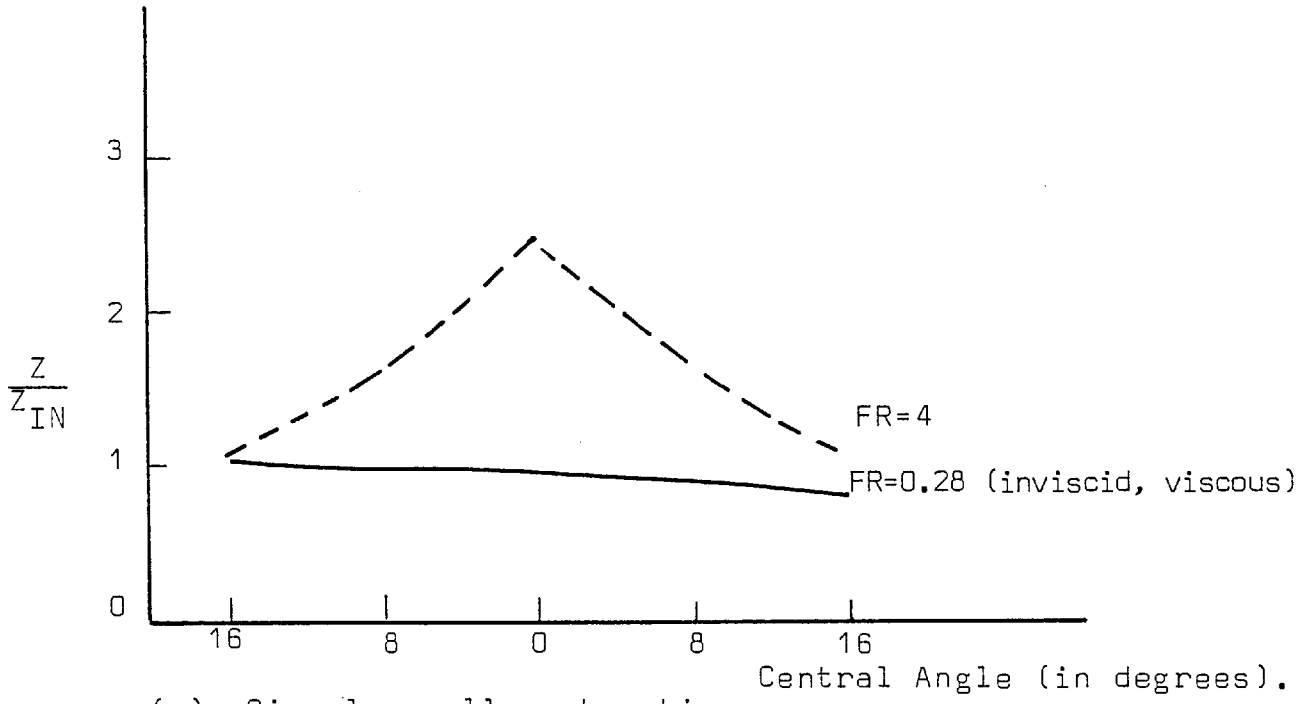
and, (6.4.2)

$$\ell_m = \lambda b, \qquad \text{when } \frac{y}{b} > \frac{\lambda}{k} \text{ ;}$$

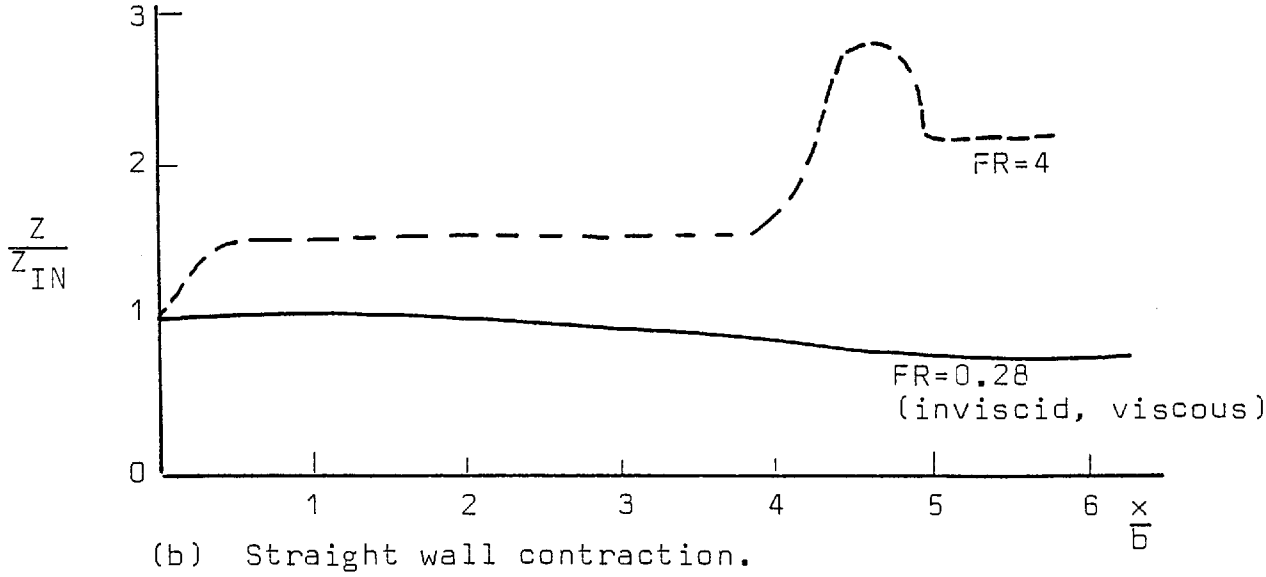
where,

b is the half width of the channel, and λ and K are empirical constants having values of 0.09 and 0.425, respectively.

Figure 6.4.1 shows the predicted layer depth along the channel walls, for the two channels, and by both methods of calculation, for a flow at a Froude number of 0.276. As expected, layer depth variations are very gradual, in contrast with the supercritical flow predictions. The predicted depth is virtually uniform at any cross-section: the maximum variation being less than 0.7% everywhere. There is little difference between the depths predicted by the inviscid and the viscous calculations; the viscous predictions being only slightly lower. Figures 6.4.2 and 6.4.3 show comparisons of the centre-line velocity variations in either channel with those predicted in the corresponding supercritical flows. The velocities are seen to vary in opposite directions, as would be expected.



(a) Circular wall contraction.



(b) Straight wall contraction.

FIG. 6.4.1: PREDICTED LAYER DEPTH ALONG CHANNEL WALL.

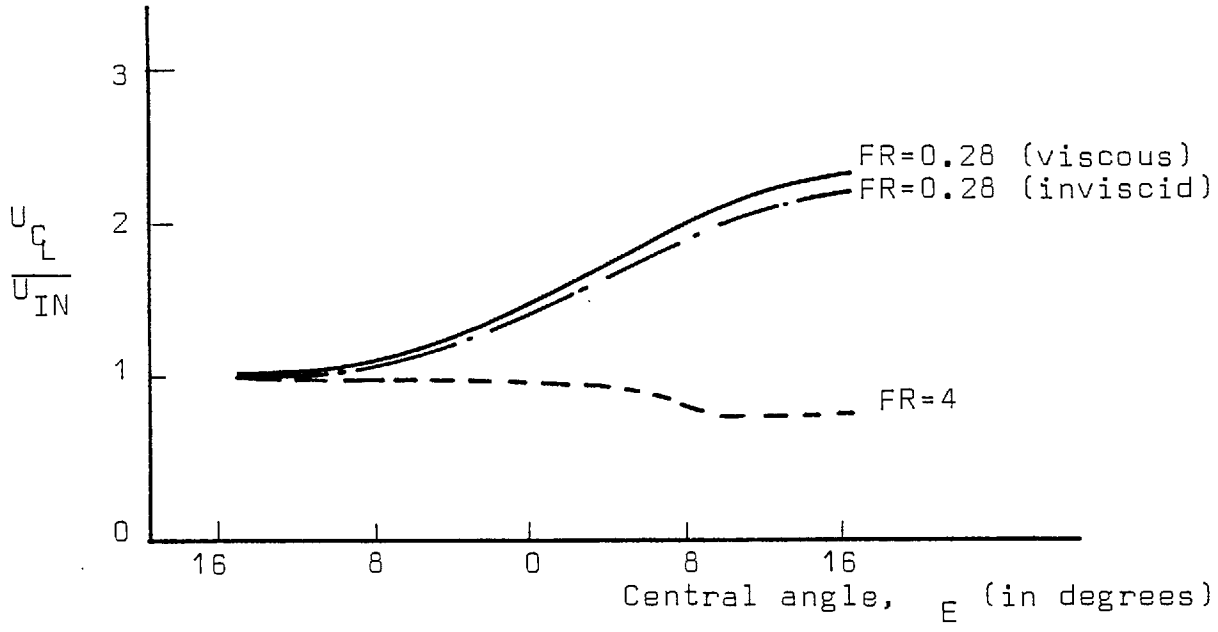


FIG. 6.4.2: COMPARISON OF THE PREDICTED CENTRE-LINE VELOCITY FOR SUBCRITICAL AND SUPERCRITICAL FLOWS IN CIRCULAR-WALL CHANNEL CONTRACTION

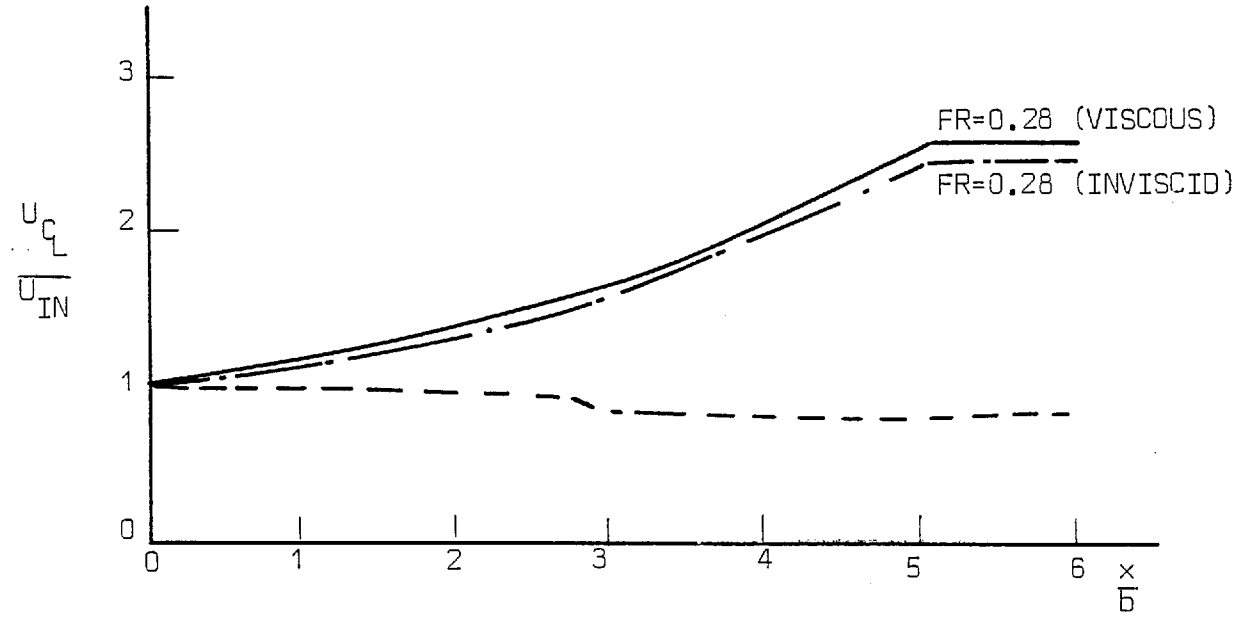


FIG. 6.4.3: COMPARISON OF THE PREDICTED CENTRE-LINE VELOCITY FOR SUBCRITICAL AND SUPERCRITICAL FLOW IN STRAIGHT-WALL CHANNEL CONTRACTION.

The effect of the viscosity is to increase the axial velocity in the central region of the flow. Figure 6.4.4 shows the velocity profiles predicted by both methods, in either channel, at a cross-stream station 5 half-widths from the inlet plane. The viscous flow predictions show uniform velocities everywhere, except near the wall, where it decreases sharply to zero. These predictions show that the effect of assuming inviscid flow is minimal in these channels.

6.5 Concluding Remarks

In this chapter, computations have been presented of full-depth flows in various channels. Most of the predictions were of supercritical flows and have been compared with experimental data and graphical solutions by the method of characteristics reported by other authors. Some subcritical flow predictions of viscous and inviscid flows were also presented.

This concludes the comparison of the present model predictions with experimental data and theoretical solutions by other authors. In the next chapter, the experimental investigation of the present study, and the predictions of the experimental results are reported.

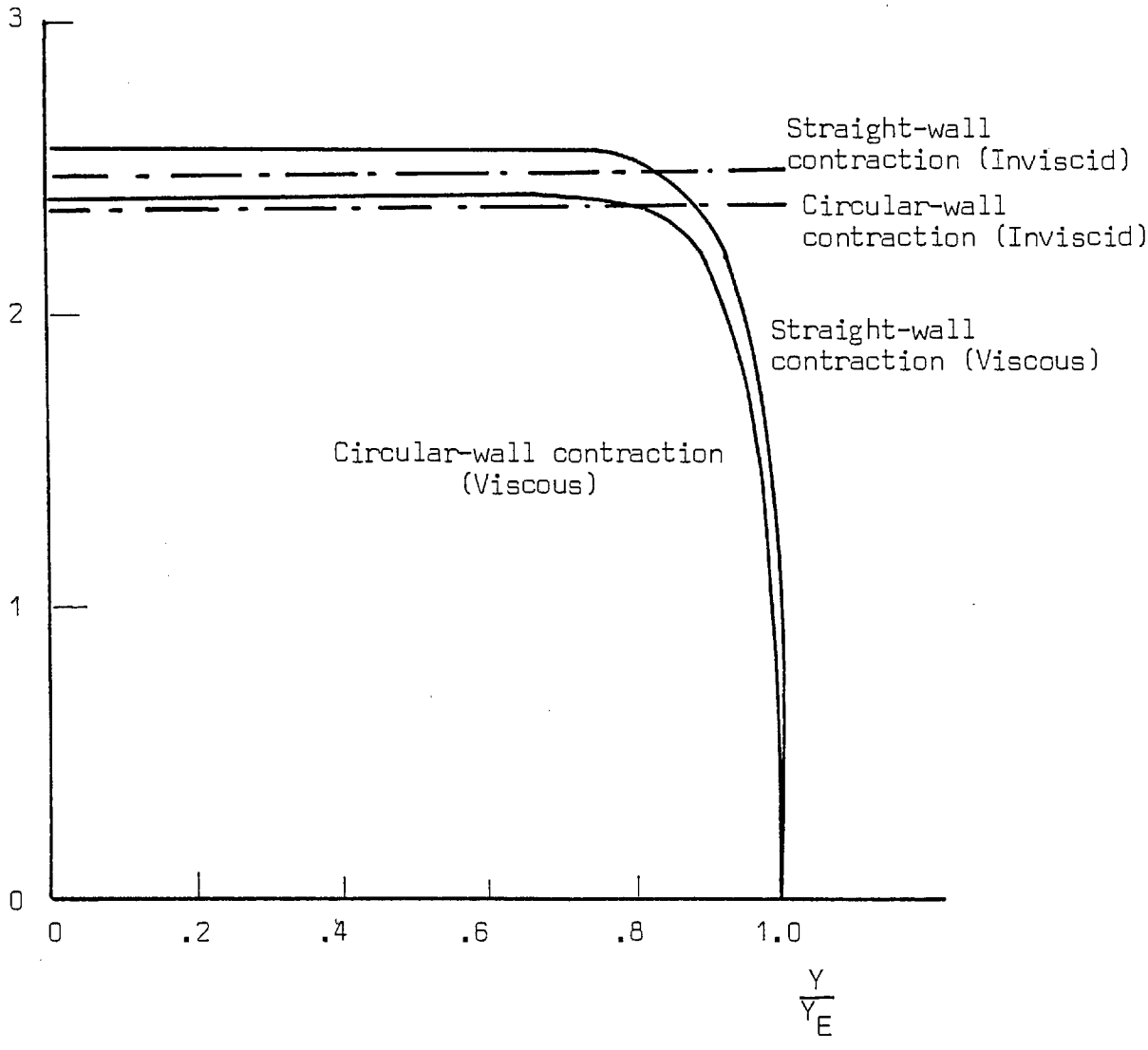


FIG. 6.4.4: PREDICTION OF THE VELOCITY PROFILES IN THE CHANNELS, AT $\frac{x}{b}$ =5; FR=0.28.

CHAPTER 7

EXPERIMENTAL INVESTIGATION

7.1 Introduction

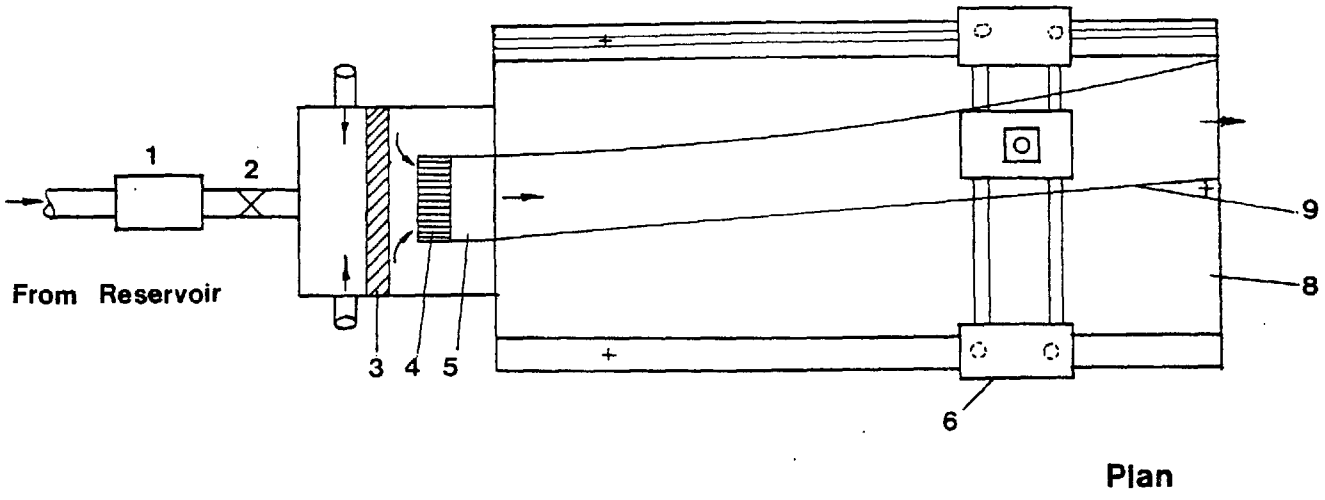
An experimental investigation of the supercritical flow of water in open channels of varying cross-section was conducted to collect data suitable for validating the full-depth layer numerical model. Although many experimental studies of supercritical open-channel flows are reported in the literature, these are either insufficiently detailed or adequate information of the boundary conditions are not provided to enable a fair comparison with the present model predictions to be carried out. Nevertheless some comparisons were presented in the previous chapter. Measurements of the surface elevation of the water layer were made in open channels, whose side walls consisted of: one convex wall*, 10.16 cm., (4in.) high, with radius of curvature 6m.; and the other wall** was either a concave one, radius of curvature 6.203m., or a straight one at an angle of 0^{o}, 5^{o} or 7^{o} to the flow. Both walls had the same height and were about 2 meters long. The initial cross-section of the water flow was 2.54 cm., (1in.) high by 20.32 cm., (8in.) wide. The range of Froude numbers investigated was 1.85 to 2.2. The flow Reynolds number based on the channel width was about 2×10^{5}.

NOTES: * Hereafter called the inner wall or the Internal, (I) boundary.
** Hereafter called the outer wall or the External, (E) boundary.

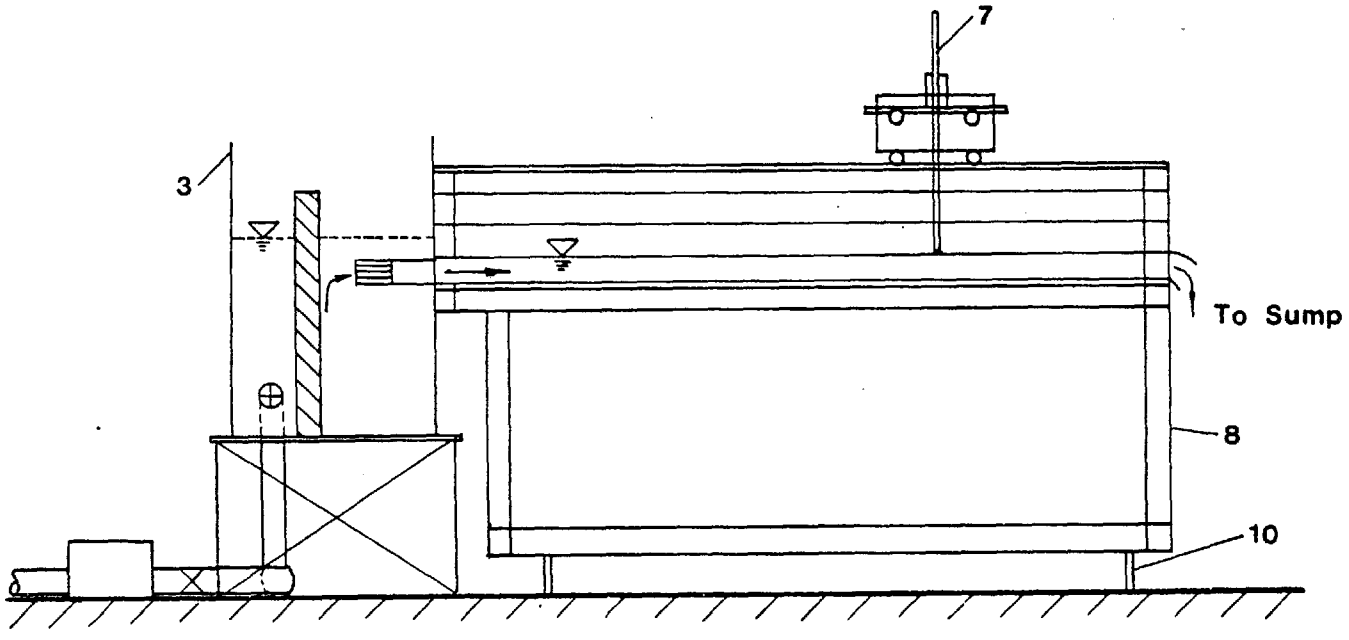
The experimental measurements were made at the Civil Engineering Department of Imperial College, London, in an experimental rig designed and assembled by the author. In this chapter, brief descriptions of the experimental apparatus and procedure are provided, first. The experimental results are then presented. Finally, model predictions are compared with the experimental measurements.

7.2 Experimental Apparatus

A schematic diagram of the experimental apparatus employed in the present investigation is shown in Figure 7.2.1. The photograph in Figure 7.2.2 shows the overall view of the apparatus. This consisted of a settling tank, a flat perspex table and two side walls which were used to form channels of varying cross-sections. The settling tank was a mild-steel tank 46 cm., (18in.) square in cross-section by 69 cm., (27in.) high, painted on the inside and outside to prevent corrosion. Water coming from a large reservoir on the roof of the building, entered the tank through two 5 cm. diameter pipes on its sides. The water then passed through a succession of coarse, cardboard honeycomb, a felt-rubber filter and baffle, a fine Aluminium honeycomb and a perspex rectangular channel. The latter two had the same cross-sectional dimensions as the orifice and were each 7.6 cm. long. They were placed right behind the orifice to make the flow entering the channel as uniform as possible, as well as minimising transverse velocities. The coarse honeycomb and the filter damped out most of the roughness in the flow. The flat table consisted of a 1.8 m., (6ft.) long



Plan



Vertical Section

1 Flowmeter
2 Valve
3 Settling Tank
4 Aluminium Honeycomb
5 Rectangular Channel
6 Tranversing Gear
7 Point Gage
8 Perspex Plate
9 Channel Wall
10 Adjustable Feet

Fig 7·2·1 Schematic Diagram of Experimental Apparatus

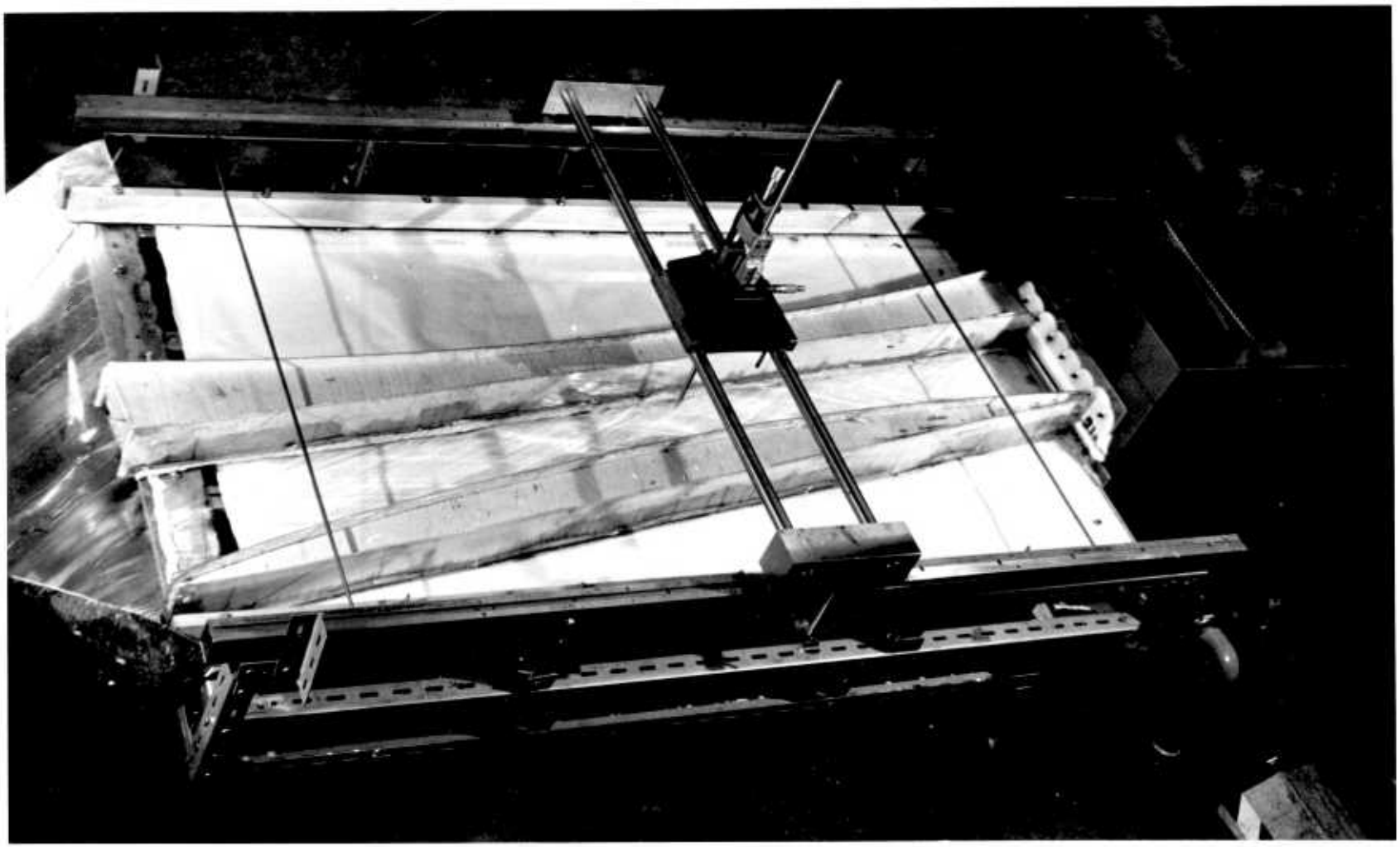


FIG. 7.2.2: OVERALL VIEW OF THE EXPERIMENTAL APPARATUS.

by 0.9 m., (3ft.) wide by 1.25 cm., (o.5in.) thick perspex plate screwed on to a "Handy Angle" frame. This frame also carried the traversing gear. Two side walls, each having two faces, one curved and the other straight, were placed on the flat table to form the flow channel in which the measurements were made. The side walls were made of wooden shells with 3 mm. thick perspex plates screwed on the faces.

The details of the traversing mechanism are shown in Figure 7.2.3. This consisted of two horizontal parallel steel bars, attached to two steel blocks at the ends. Each block was carried by two ball transfers which ran on the two parallel rails, fixed to the "Handy Angle" frame, producing the longitudinal traverse. The probe carrier was an assembly containing 3 micrometer heads which allowed fine movement in the three coordinate directions (x,y,z). The probe, a 50 cm. long by 6 mm. diameter brass rod having a pointed lower end was fixed to this assembly to form the point gage. The lower face of the probe carrier was grooved so that it could be moved on the horizontal bars to achieve the coarse lateral traverse.

The water volume flow rate was measured with a horizontal-dial, rotary-piston type flowmeter, manufactured by Kent Instruments Limited. It was placed between the supply valve and the settling tank. The flowmeter gave an analog reading of the volume of water (in gallons) flowing through the system.

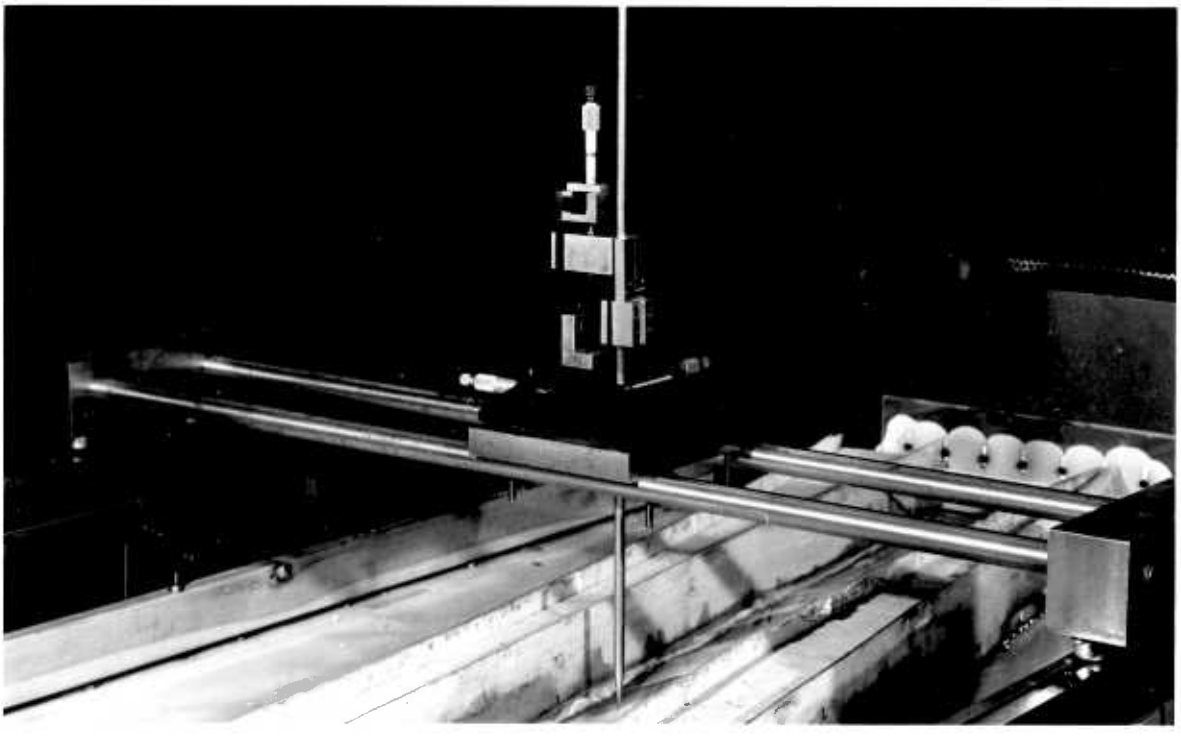


FIG. 7.2.3: THE TRAVERSING MECHANISM.

7.3 Experimental Procedure

The objective was to measure the thickness of the water layer within the channels. The point gage was used to make these measurements.

It might have been desirable to measure the layer flow velocities, as well. However, some serious difficulties made this impractical. On the one hand, the relatively small scale of the experiments would necessitate the use of a fine measuring instrument. The hot-wire anemometer could not be used in water, so a hot-film anemometer, a thermistor, or a very small pitot-static probe might be used. On the other hand, the high speed and turbulence of the flow would require that the probe was fairly sturdy and rigid.

However, the main objection to the use of any of these probes would be the difficulty of interpreting the results. The probe would act as a disturbance to the supercritical flow, thereby generating cross waves (as a disturbance to a supersonic gas flow would generate shock waves). The measured velocity would not be the true velocity at the point in the absence of the probe. While the analysis required to obtain the true velocity at the point is well known in the case of a pitot tube in a supersonic gas flow (as shown by Binder (1961)), the same cannot be said of the supercritical flow case. An instrument that would not interfere with the flow such as a Laser-Doppler anemometer would have to be used. The use of this was not seriously considered as it was not readily available.

Before running the experiments some precautions were taken and some preliminary measurements were made. Precautions were taken to level the water table with a spirit level and to seal the tank and channel against leaks. Bath sealant and plasticine were used for the latter. To facilitate the determination of the water layer thicknesses, the surface elevation of the water table was mapped with the point gage, without any water or channel walls on it. This eliminated the need to repeat this when the water was flowing on it, which would have been more difficult and imprecise. Checks made after fixing the channel walls and turning on the water flow showed that there was no significant change in the surface elevation of the table. The uncertainty in measuring the elevation was within 0.1 mm., (.004in.).

The experimental procedure was then as follows:

(1) The desired channel walls were fixed to the table, and the channel was made water-tight.

(2) The water supply was turned on and adjusted to give the desired flow rate. The system required only a few minutes to settle down.

(3) The elevation of the water surface was then measured with the point gage, at 10 cm. intervals, in the longitudinal direction (up to 120 cm. from the orifice), and 2 cm. intervals, in the lateral direction. This was done by manually screwing the vertical micrometer head until the point of the probe just touched the water surface. This was easily determined because the probe produced a prominent wave pattern on touching the water surface. The uncertainty

in determining the point of touch was everywhere less than 0.4 mm. (0.016in.).

Each experiment lasted for about 3 hours, there being about 130 measuring points. The volume of water flowing through the system, registered by the flowmeter was recorded every 15-30 minutes. It was noted that when the water flowing through the system into the sump was being pumped back into the overhead reservoir, the water flow rate did not vary by more than 0.2% over the 3 hour period. However, when the pump was not working the variation in the water flow rate was about 1%, over the same period. Most of the measurements were taken with the pump switched on. The accuracy of the Kent water flowmeter was stated by the manufacturers to be within 2%.

7.4 Experimental Results

Five sets of experimental measurements were made. The test conditions for these are given in Table 7.1 below.

Table 7.1: Test conditions for experiments.

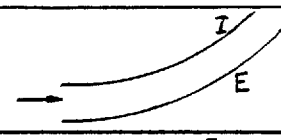
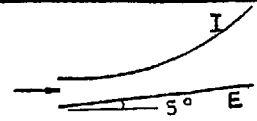
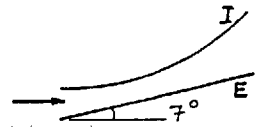
RUN	NOMINAL FROUDE NUMBER	INITIAL ASPECT RATIO	CHANNEL SHAPE (PLAN VIEW)
1	2.20	8	
2	2.20	8	
3	2.20	8	
4	1.85	8	
5	2.10	8	

Figure 7.4.1* shows the measured layer thicknesses in Run 1, at the 12 cross-stream planes. The thicknesses have been non-dimensionalised with the thickness of the water layer at the orifice, Z_{in}. These measurements show that at the first cross-stream plane (10 cm. from the orifice), there was a depression in the layer thickness on either side of the flow at a distance of about 2 cm. from the walls. This would suggest that the flow leaving the orifice was non-uniform; with lateral velocities probably present. The implications of this would be discussed in the next section, where the predictions of the measurements are presented.

Figures 7.4.2 - 7.4.5 show the measured layer thicknesses for the remaining experiments (Runs 2-5, respectively).

The results are presented in tabular form in Appendix F.

7.5 Comparison of Experimental Results with Numerical Predictions

The prediction of the experimental data presented in this section was carried out with the same computer program as was used in the previous chapter. However, as was stated in the preceding section, the flow entering the channel through the orifice was non-uniform, so it was necessary to simulate (or guess) the inlet flow condition to be used in the predictions. In this section, this treatment of the boundary conditions is first described, followed by a statement

---

*NOTE: The channel shape is also shown in the figure. Although some points appear to be outside the channel, the bases which represent the location of these points do lie in the channel.

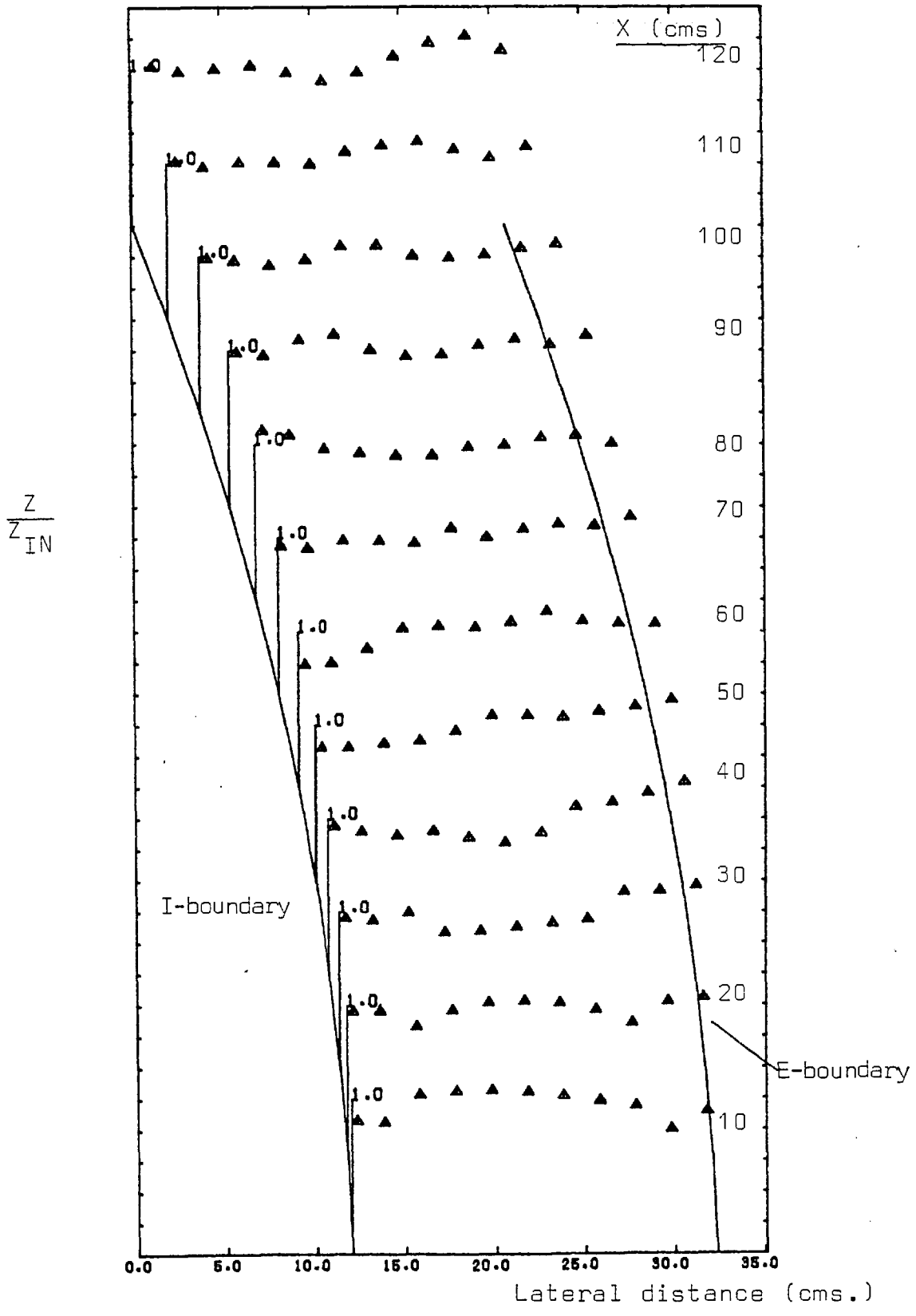


FIG. 7.4.1: MEASURED LAYER DEPTHS IN EXPERIMENTAL RUN 1; FR=2.20, R_I=6.0, R_E=6.2, A.R.=8.

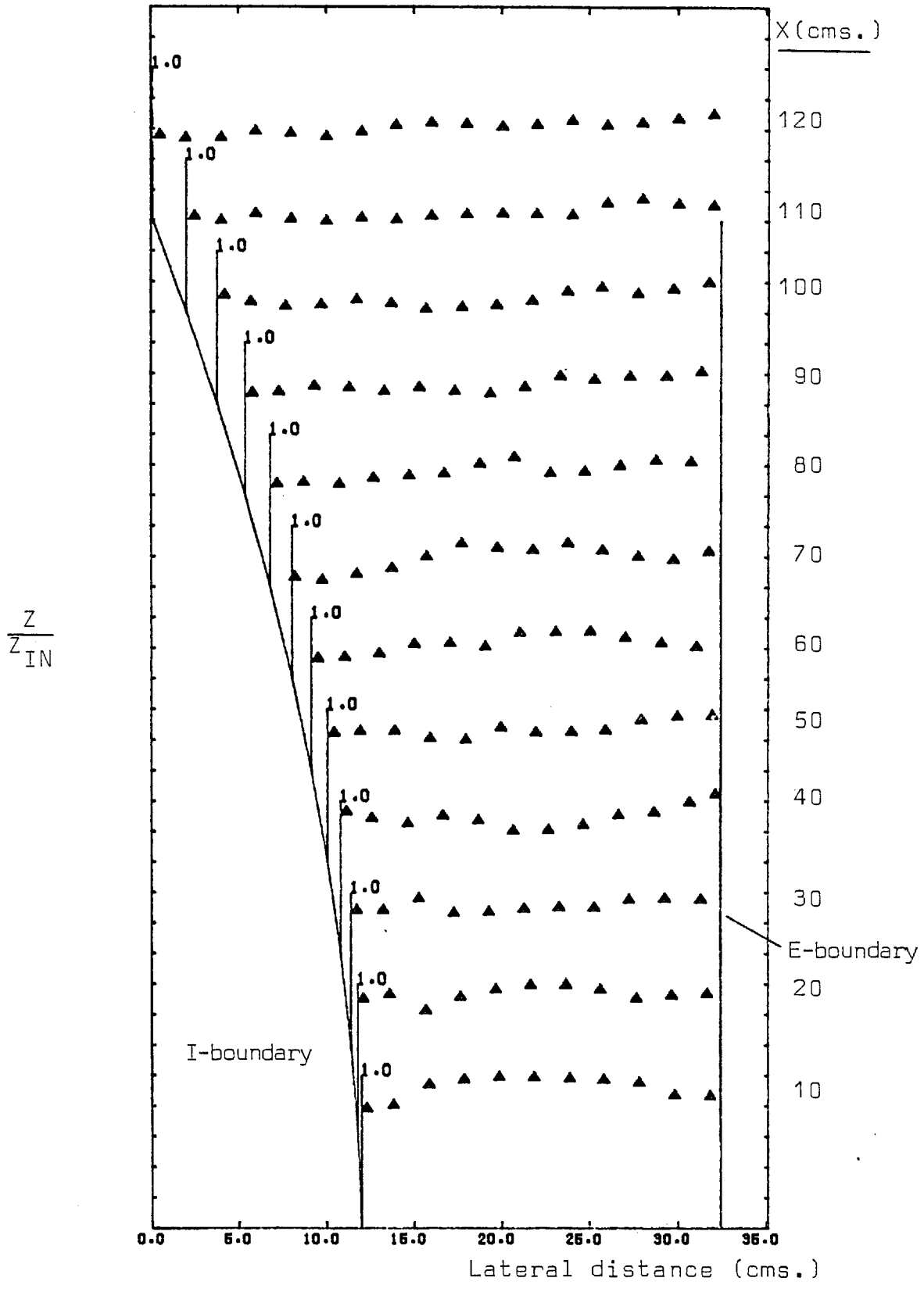


FIG. 7.4.2: MEASURED LAYER DEPTHS IN EXPERIMENTAL RUN 2; FR=2.20, R_I=6.0, θ_E=0°, A.R.=8.

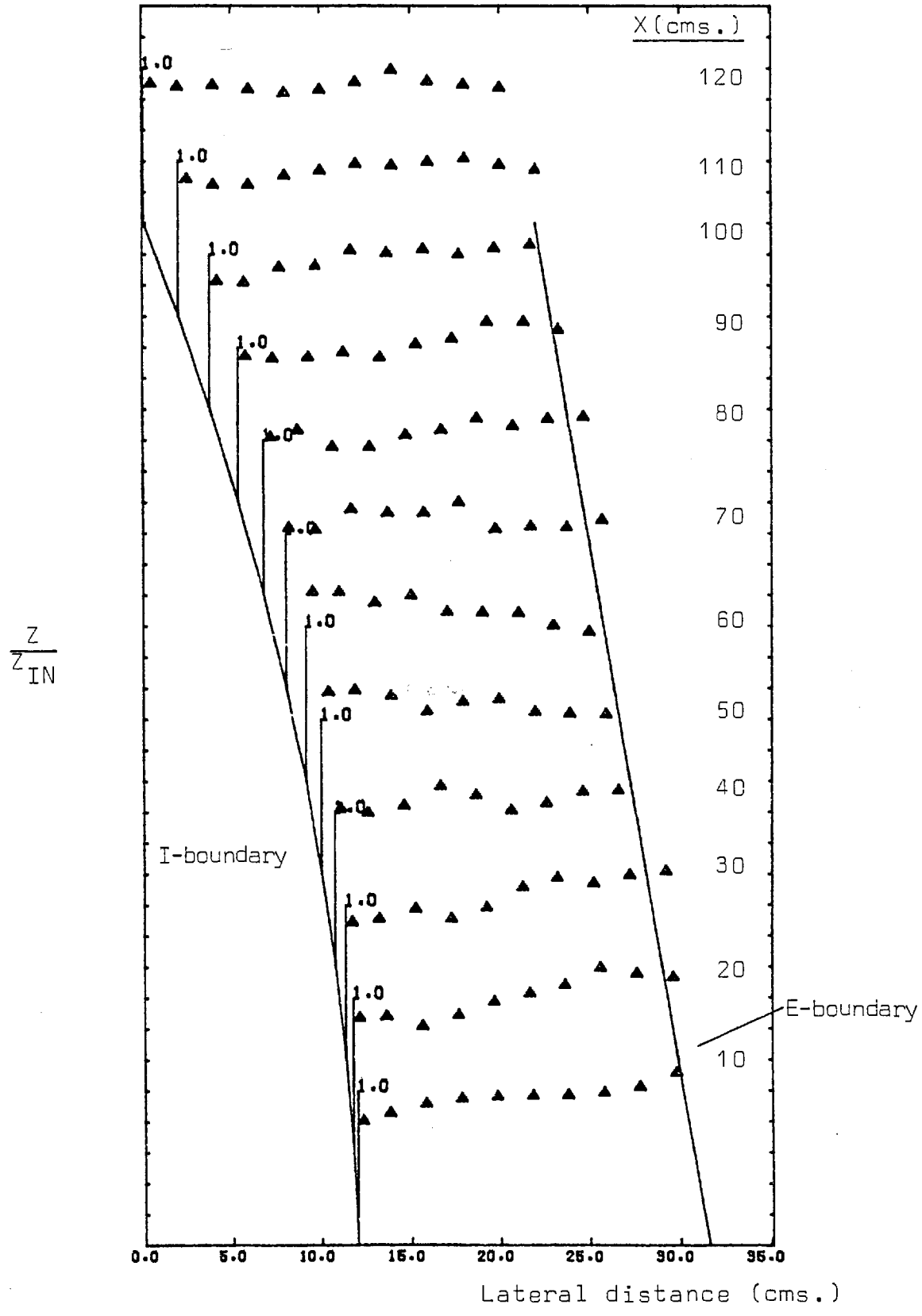


FIG. 7.4.3: MEASURED LAYER DEPTHS IN EXPERIMENTAL RUN 3; FR=2.20, R_I=6.0, θ_E=5°, A.R.=8.

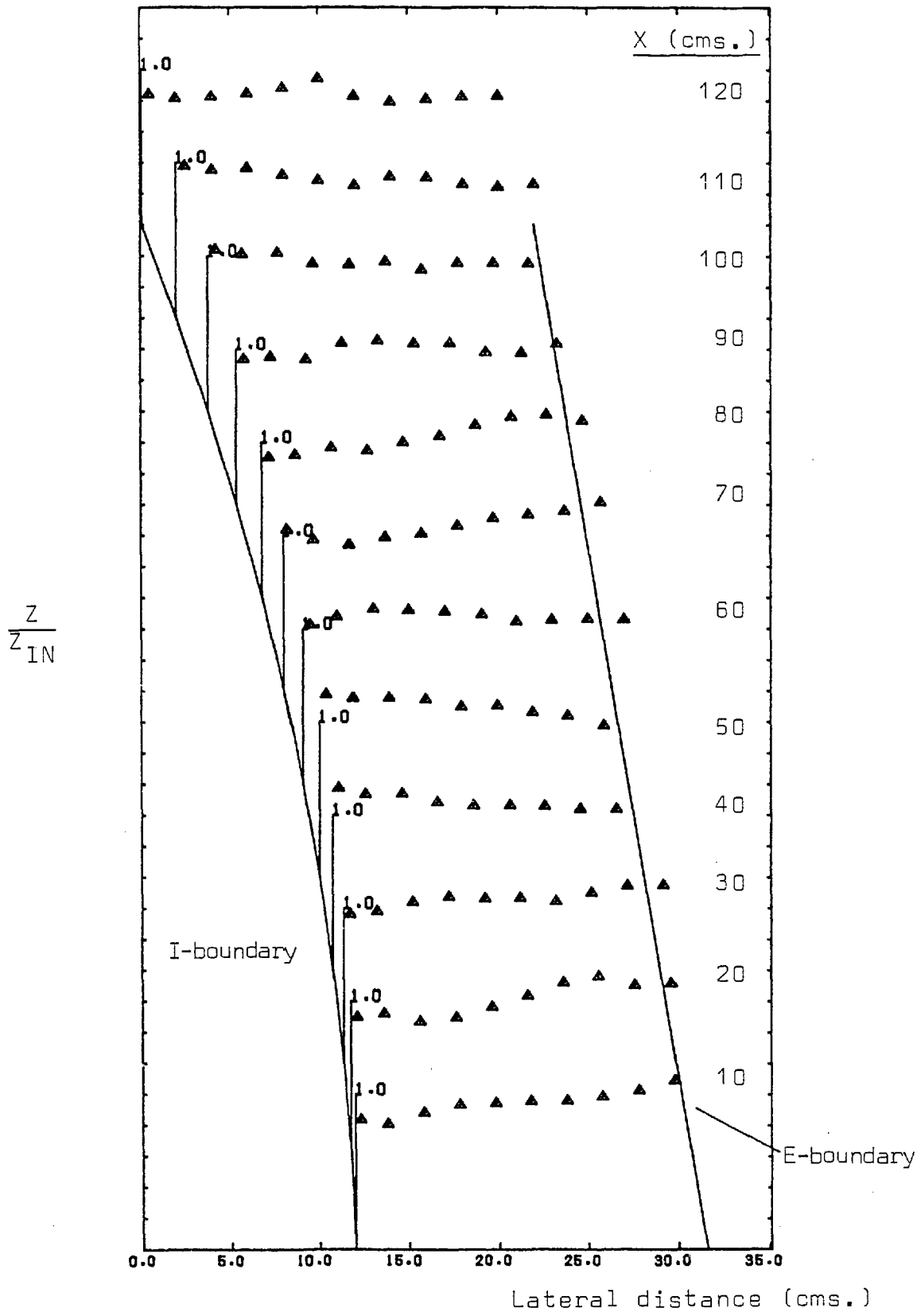


FIG. 7.4.4: MEASURED LAYER DEPTHS IN EXPERIMENTAL RUN 4; FR=1.85, R_I=6.0, θ_E=5°, A.R.=8.

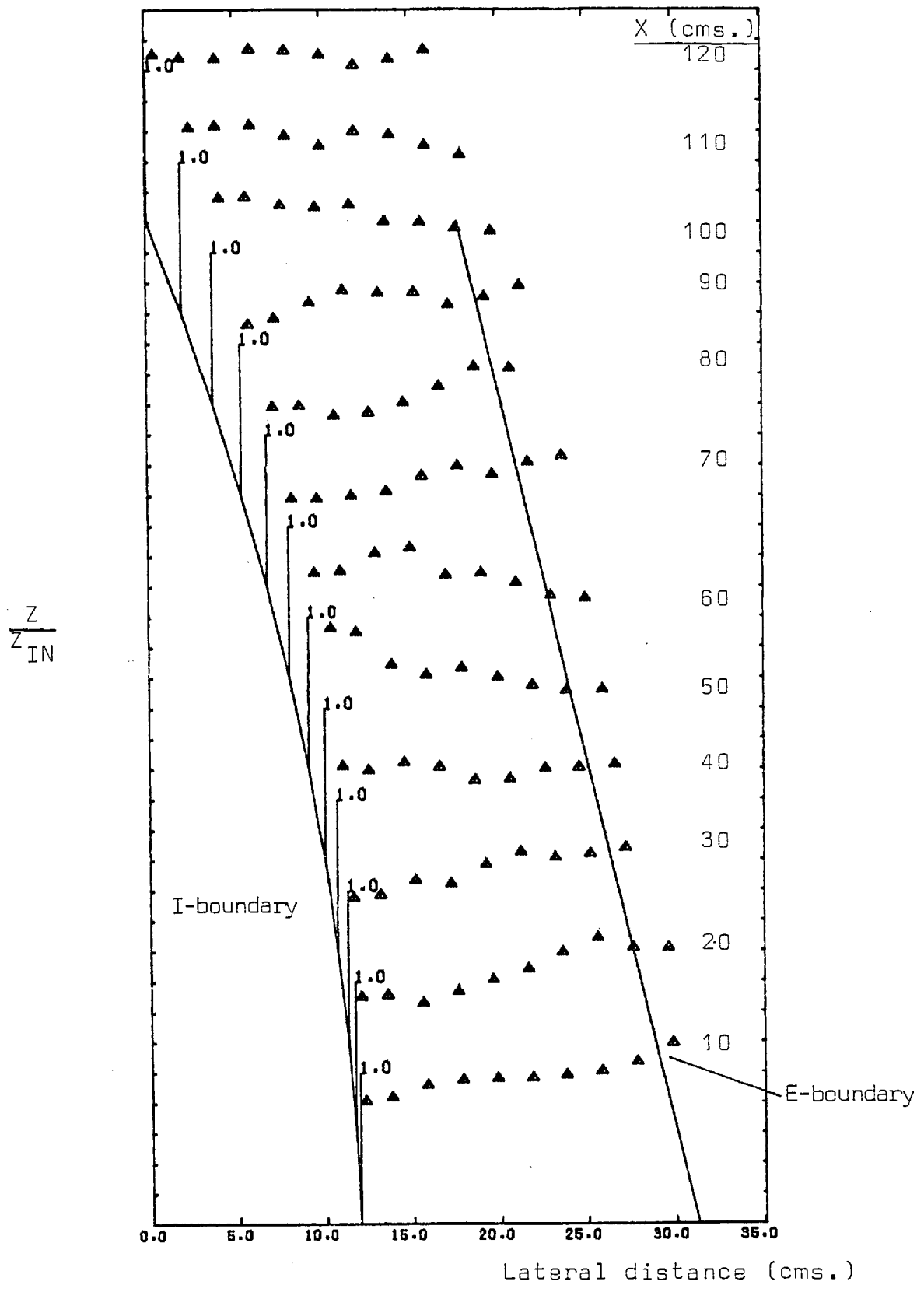


FIG. 7.4.5: MEASURED LAYER DEPTHS IN EXPERIMENTAL RUN 5; FR=2.10, R_I=6.0, θ_E=7°, A.R.=8.

of the computational details. The results are then discussed and concluding remarks made.

7.5.1 Boundary conditions

Two methods of prescribing the initial conditions were considered. In the first method, computation started at the inlet plane with uniform conditions, as usual, and proceeded until the first location at which measurements were made (10 cm. from the orifice). The measured layer thicknesses were then substituted at this location. The corresponding longitudinal velocities were adjusted to keep the flow rate through each grid cell constant, thus

$$U_{adjusted} = \frac{(Uz)_{calculated}}{z_{measured}} \qquad .(7.5.1)$$

Alternatively, the longitudinal velocities were adjusted to keep the total head within each grid cell constant, thus

$$U_{adjusted} = (U^2_{calculated} + 2g(z_{calculated} - z_{measured}))^{\frac{1}{2}} \qquad .(7.5.2)$$

These two treatments of the velocities resulted in practically the same prediction of layer thicknesses, so the former treatment, being simpler was subsequently used.

The second method of prescribing the initial conditions was to guess the distributions of the layer thickness, longitudinal and lateral velocities and input these to the computer program at the beginning of the calculation. For the prediction of the experimental results of Run 5, the best guess was found to be:

$$V = 0.05\, U_{IN} \left(\frac{0.5B-y}{0.5B}\right) ,$$

$$U = U_{IN}/0.9 , \qquad (7.5.3)$$

and

$$z = 0.9 z_{IN} ,$$

where,

U_{IN} is the nominal longitudinal velocity at the orifice,

z_{IN} is the nominal depth of the orifice,

and B is the width of the orifice.

The interpretations of these are:

(i) There are lateral velocities at the channel inlet, having maximum magnitudes of $0.05\, U_{IN}$ at the side, and decreasing linearly towards the centre of the channel.

(ii) The average level of the water in the channel decreased; as was observed in the experiment. This would be the case if a "vena contracta" were present.

(iii) To keep the overall flow rate constant, the longitudinal velocities were correspondingly increased.

These two methods of prescribing the initial conditions were tested by predicting the experimental data of Run 5 with each. The comparisons of the layer thickness distributions are shown in Figures 7.5.1 (a) - (l). The full lines represent the predictions in which the measured layer thicknesses were substituted at the 10 cm. location (i.e. the first method), the broken lines represent the precitions with guessed initial conditions (i.e. the second method),

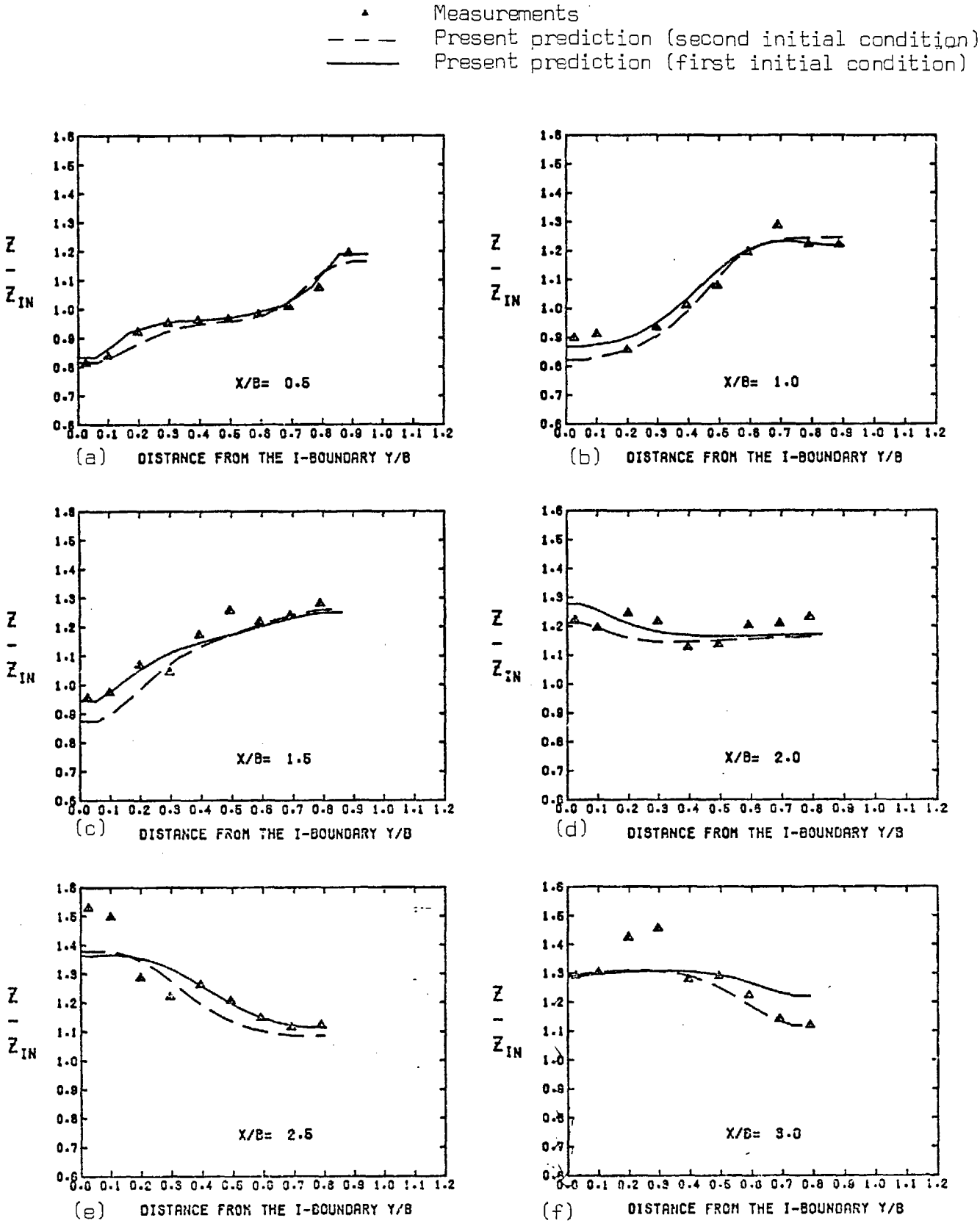


FIG. 7.5.1: PREDICTION OF PRESENT EXPERIMENTAL RUN 5;
FR=2.20, R_I=6.0, θ_E=7°, A.R.=8.

▲ Measurements
– – – Present prediction (second initial condition)
——— Present prediction (first initial condition)

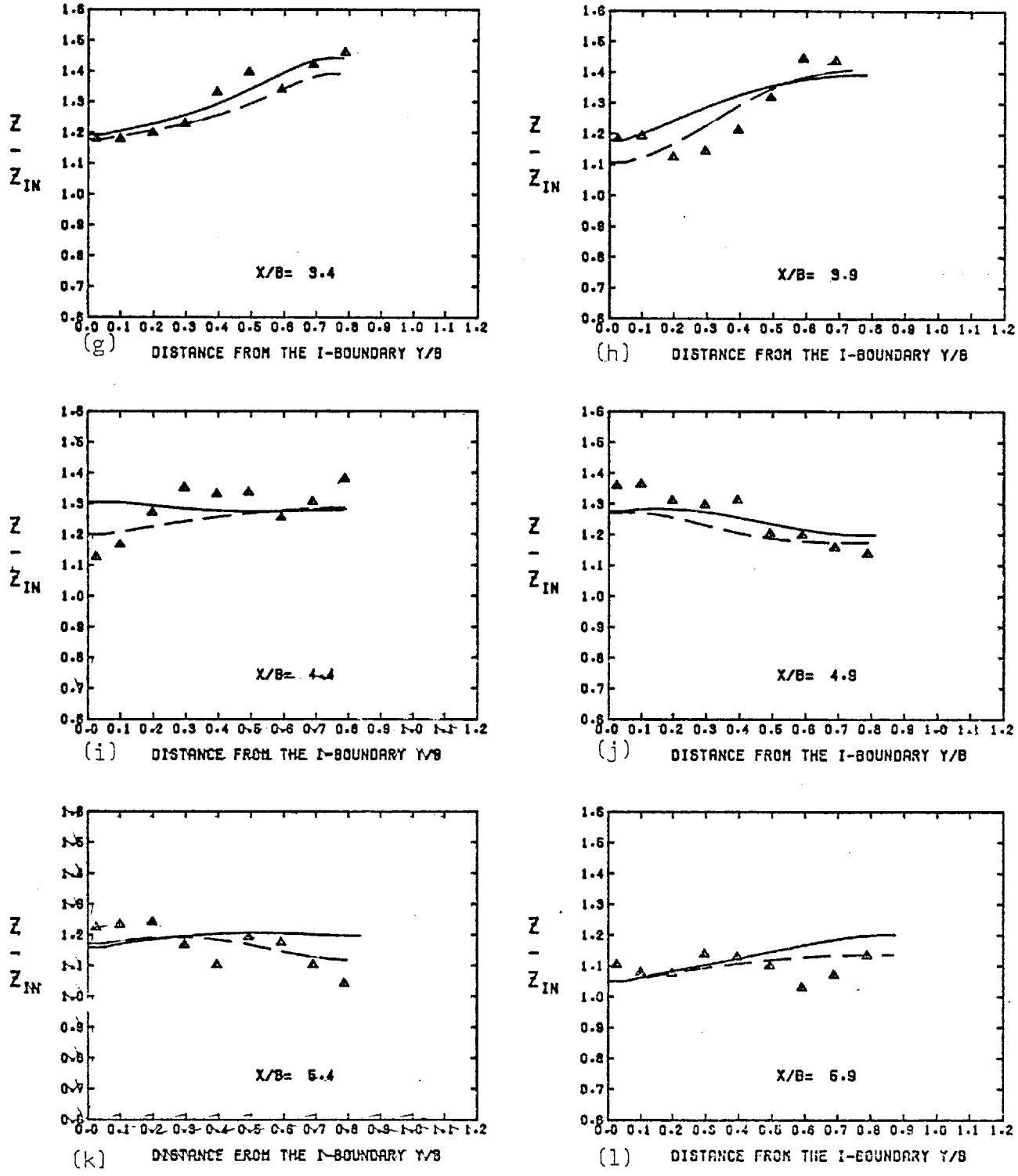


FIG. 7.5.1: (CONTINUED)

and the symbols represent the experimental data. It may be noted that though the are slight difference between the two predictions, their level of agreement with the experimental results is the same. This statement is justified in a later section, where mean square deviations are presented. When using the second method, it was necessary to make new guesses of the initial conditions in predicting the other experimental results. On the other hand, the method of substituting the measured layer thicknesses at the 10 cm. location was simple and straightforward. Hence, the latter was subsequently used for the other predictions. Other boundary conditions were as specified in Chapter 6 for supercritical flows.

7.5.2 Computational details

Some important computational details are:-

Table 7.2: Computational details for predicting the experiments.

VARIABLE	VALUE
Number of cross-stream grid points, N	19
Number of forward steps	120
Forward step size, $\frac{\delta x}{B}$	.05
Number of iterations at each cross-stream location	4
Computer time in CDC 6600 secs.	11

These values are for grid-independent results. Increasing the number of cross-stream grid points to 59 and decreasing the forward step size to, $\frac{\delta x}{B}$ = .0125 did not produce a significant change in the results.

7.5.3 Results and discussion

The predicted layer thicknesses are compared with the experimental results of Run 1 in Figures 7.5.2 (a) - (l). The predicted variations in layer depth at any cross-section, and from one cross-section to the next appear to be fairly gradual. However, the measured layer depths appear to exhibit some substantial variations. These probably originated at the inlet plane, where the flow conditions may have been complex. Any cross waves produced by the non-uniform inlet conditions would be superposed on those originating at the channel boundaries, so it should be possible to predict the general trend of the data; the extra cross waves would then appear as scatter. This general trend is seen to be well predicted. Figure 7.5.3 shows the variations of the layer depths, near the channel walls, in the longitudinal direction. The positions of the peaks and troughs are well predicted, and the agreement between the predictions and the experimental data is fair.

In these predictions and subsequent ones, it was presumed that the perspex floor of the channel exerted a retarding force on the flow, given by:

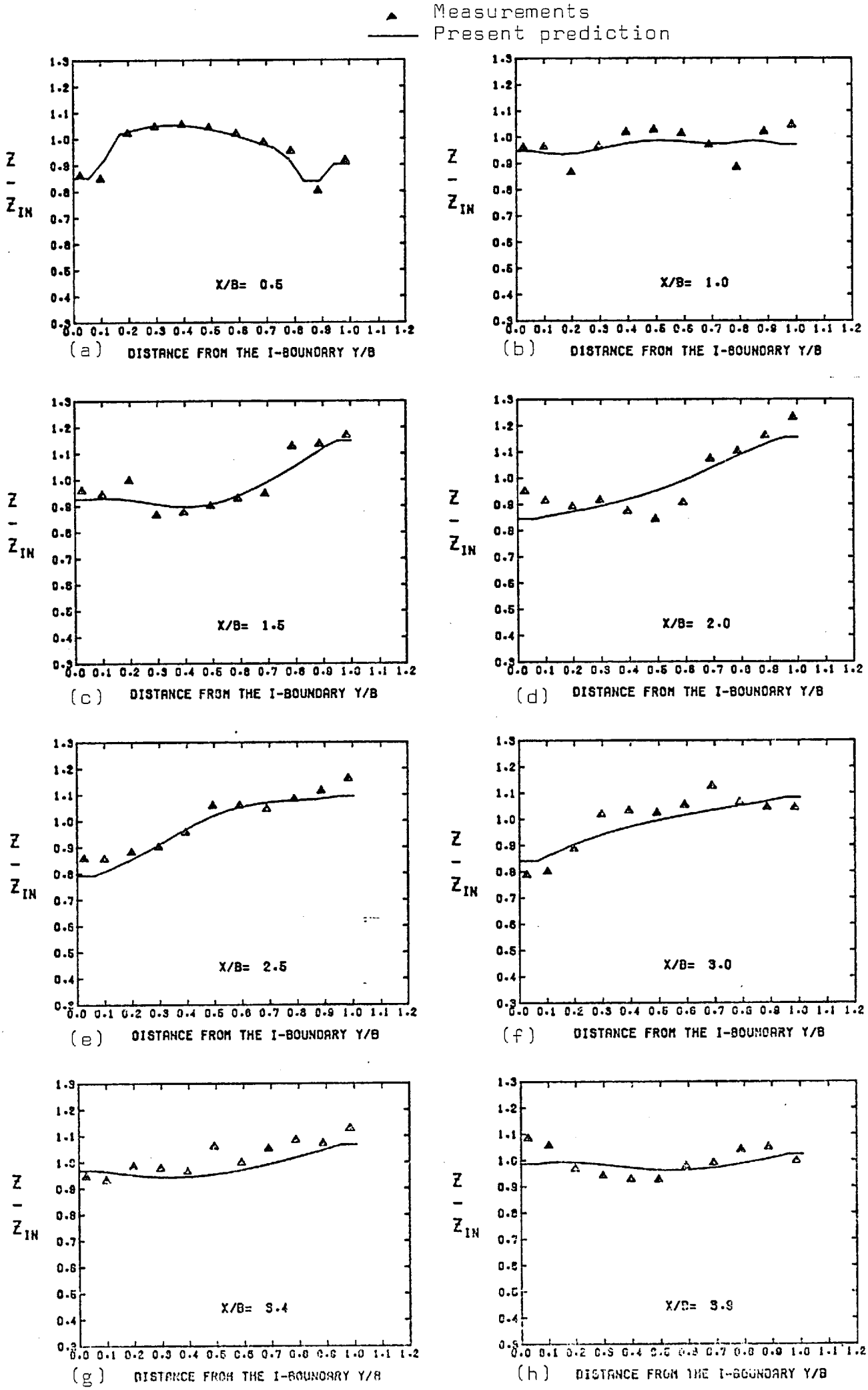


FIG. 7.5.2: PREDICTION OF PRESENT EXPERIMENTAL RUN 1;
FR=2.20, R_I=6.0, R_E=6.2, A.R.=8.

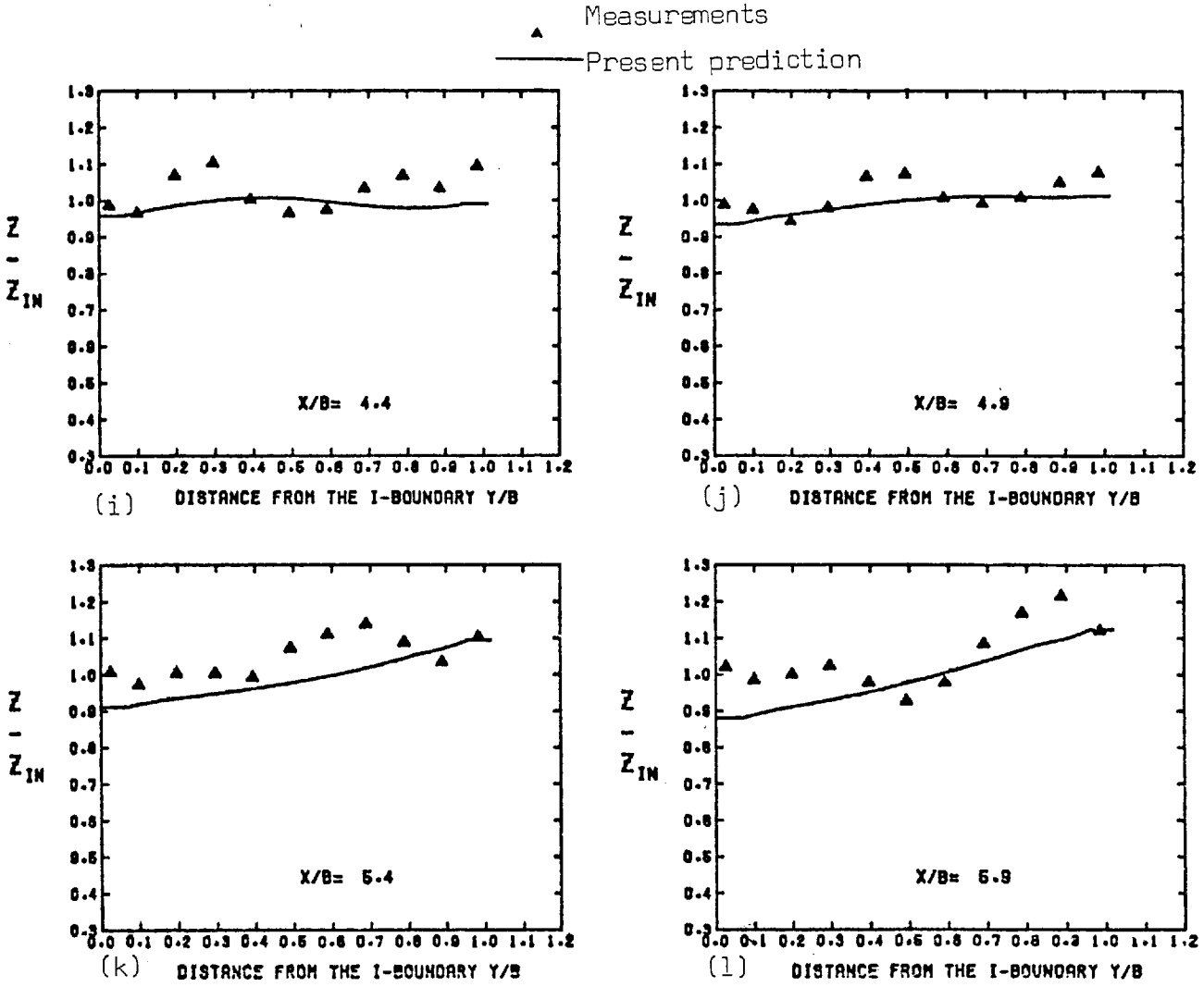


FIG. 7.5.2: (CONTINUED)

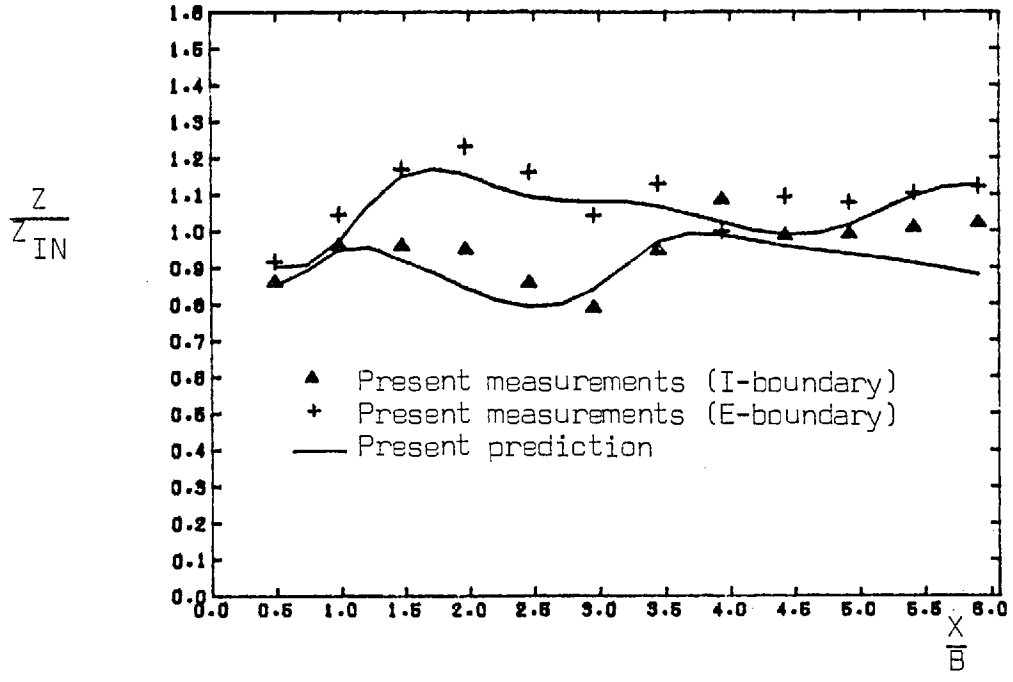


FIG. 7.5.3: PREDICTION OF LAYER DEPTHS ALONG THE WALLS; FR=2.2, R_I=6.0, R_E=6.2, A.R.=8.

In the x-direction,

$$F_x = -.001\rho U(U^2+V^2)^{\frac{1}{2}} \quad , \tag{7.5.4}$$

and, in the y-direction

$$F_y = -.001\rho V(U^2+V^2)^{\frac{1}{2}} \quad ,$$

These expressions were suggested by Spalding (1975), and have been used by McGuirk and Rodi (1978a). A friction coefficient in the range .001-.003 was recommended, and preliminary calculations showed the lower value to be most appropriate in this case; as would be expected since the perspex surface was quite smooth.

Figures 7.5.4 (a) - (l) show the comparison of the predictions of the layer thicknesses with the experimental data of Run 2. In this case, the outer wall was straight and parallel to the initial flow direction. The trend of the data is seen to be well predicted. Figure 7.5.5 shows the variations of the layer thicknesses near the channel walls, in the longitudinal direction. There were effectively only one maximum and no minimum along either wall. The agreement between the predictions and the experiment is fair.

Similar comparisons are shown for Run 3 in Figures 7.5.6 (a) - (l) and Figure 7.5.7, and for Run 4 in Figures 7.5.8 (a) - (l) and Figure 7.5.9. In these two runs, the outer wall made an angle of 5° with the initial flow direction. However, in Run 3 the initial Froude number was 2.20, while Run 4 had an initial Froude number of 1.85. The agreement of the predictions with the experimental data is fair in

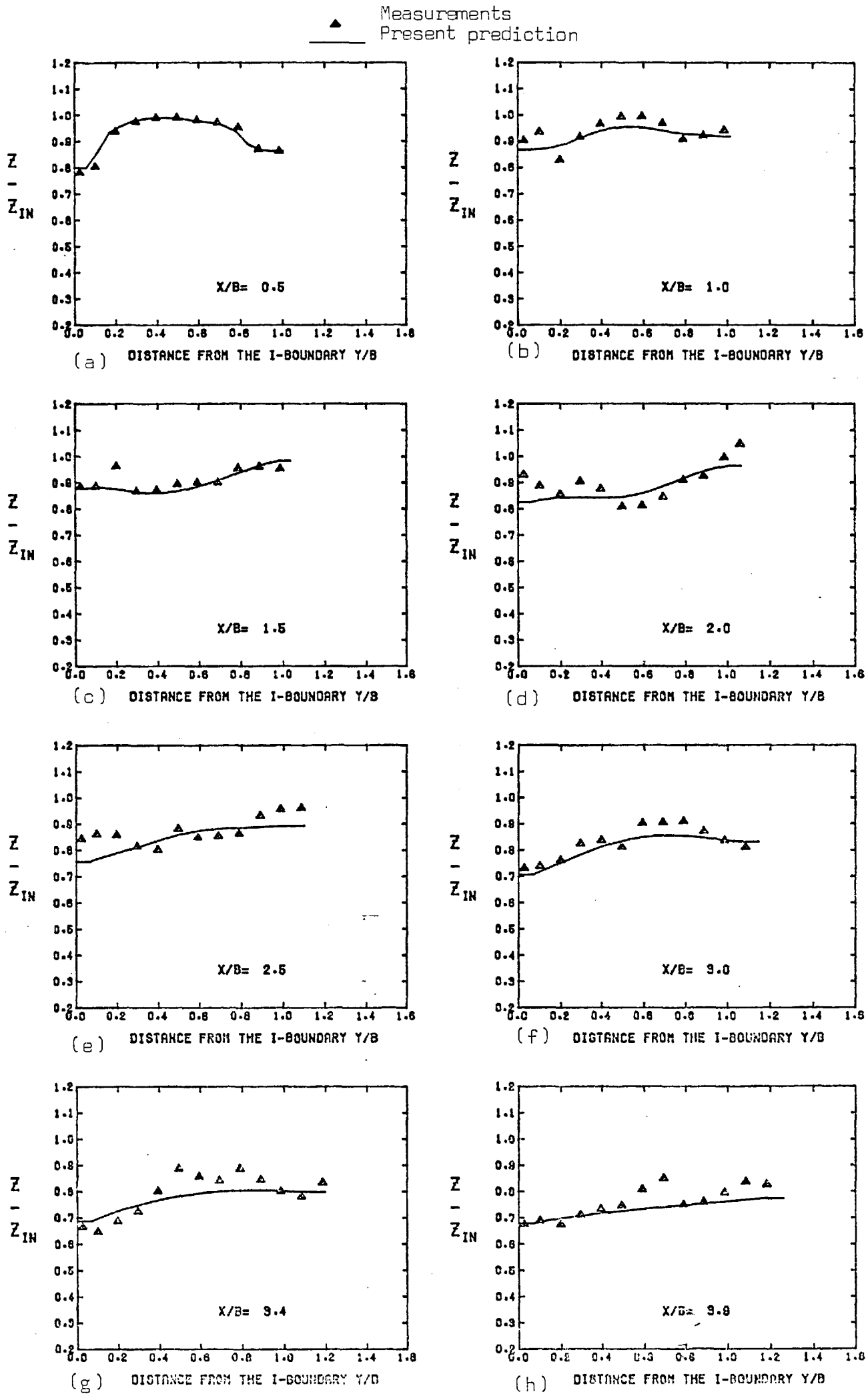


FIG. 7.5.4: PREDICTION OF PRESENT EXPERIMENTAL RUN 2; FR=2.20, R_I=6.0, θ_E=0°, A.R.=8.

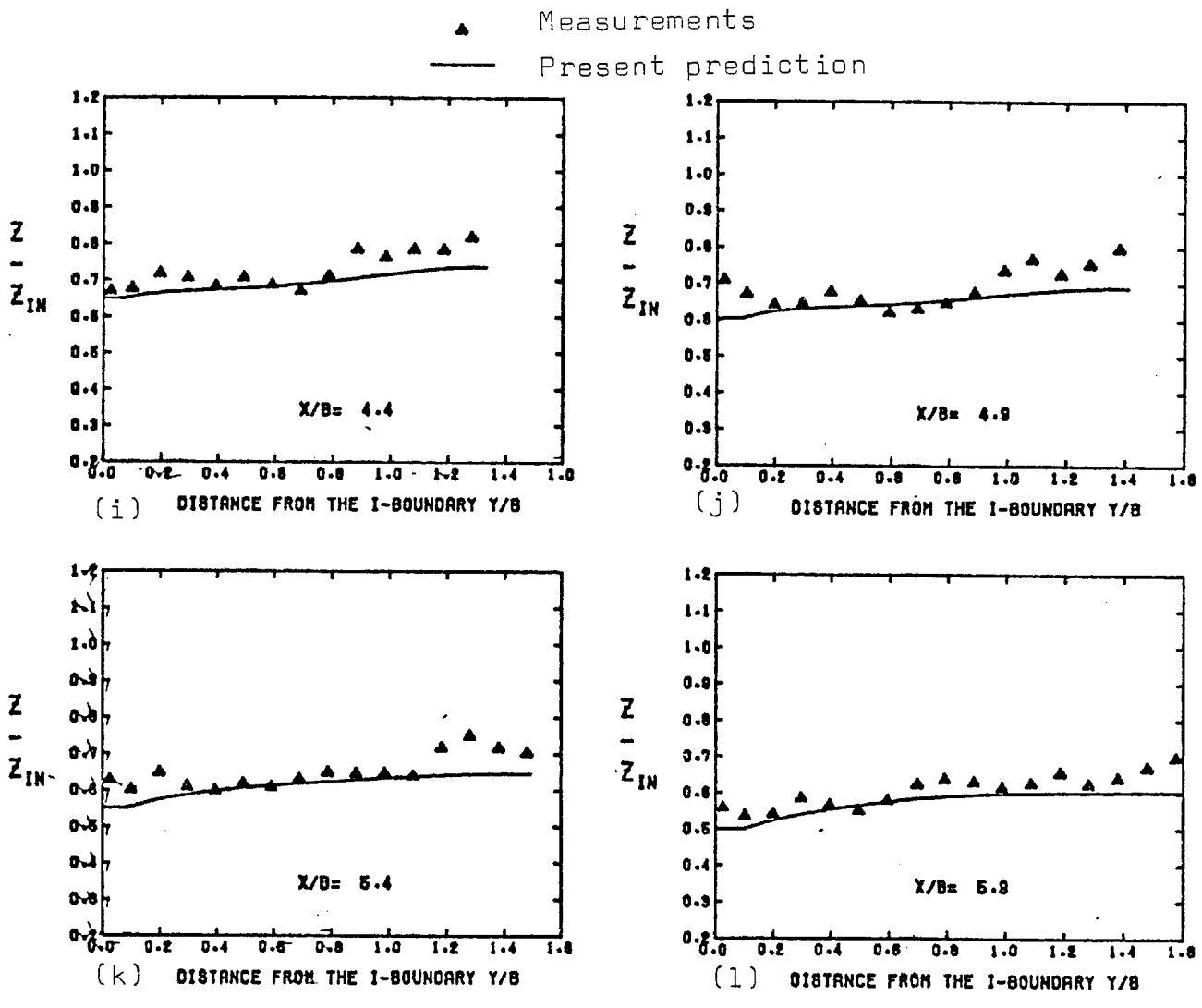


FIG. 7.5.4: (CONTINUED)

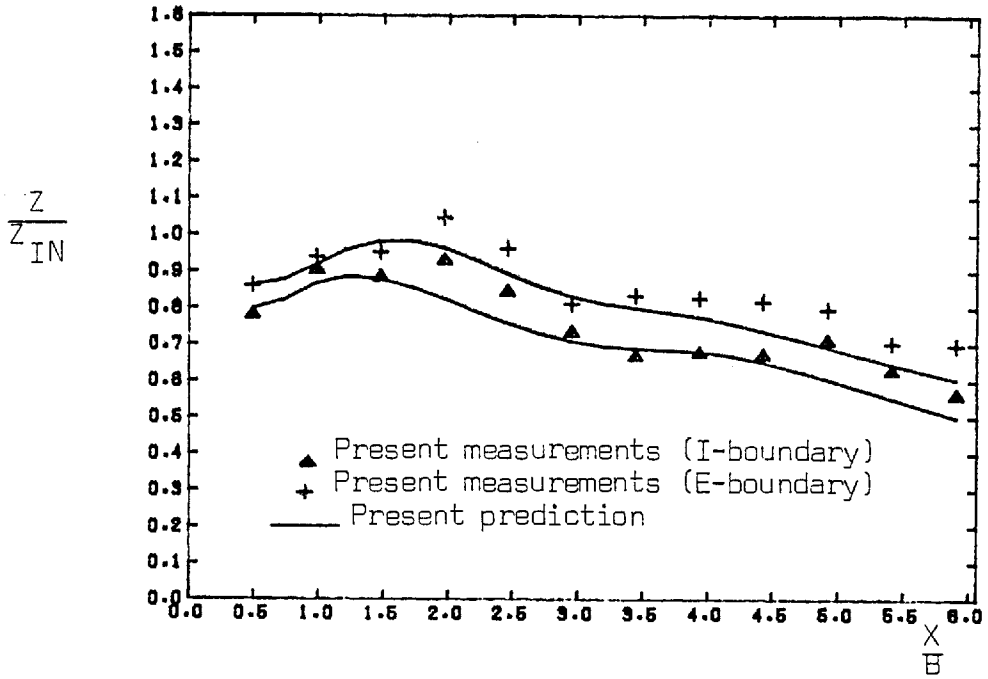


FIG. 7.5.5: PREDICTION OF LAYER DEPTHS ALONG THE WALLS; FR=2.20, R_I=6.0, θ_E=0, A.R.=8.

▲ Measurements
—— Present prediction

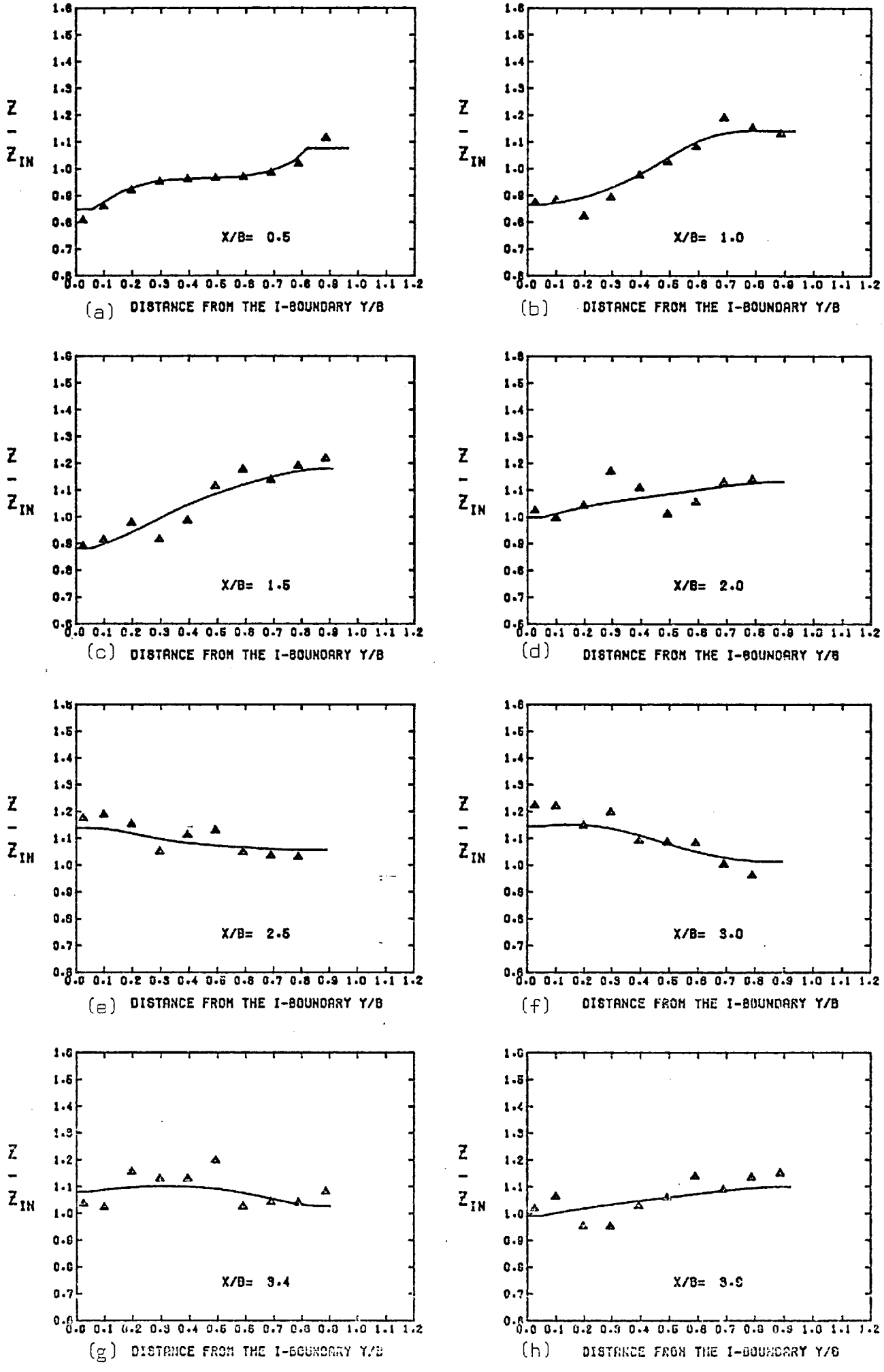


FIG. 7.5.6: PREDICTION OF PRESENT EXPERIMENTAL RUN 3; FR=2.20, R_I= 6.0, $\theta_E=5^0$, A.R.=8.

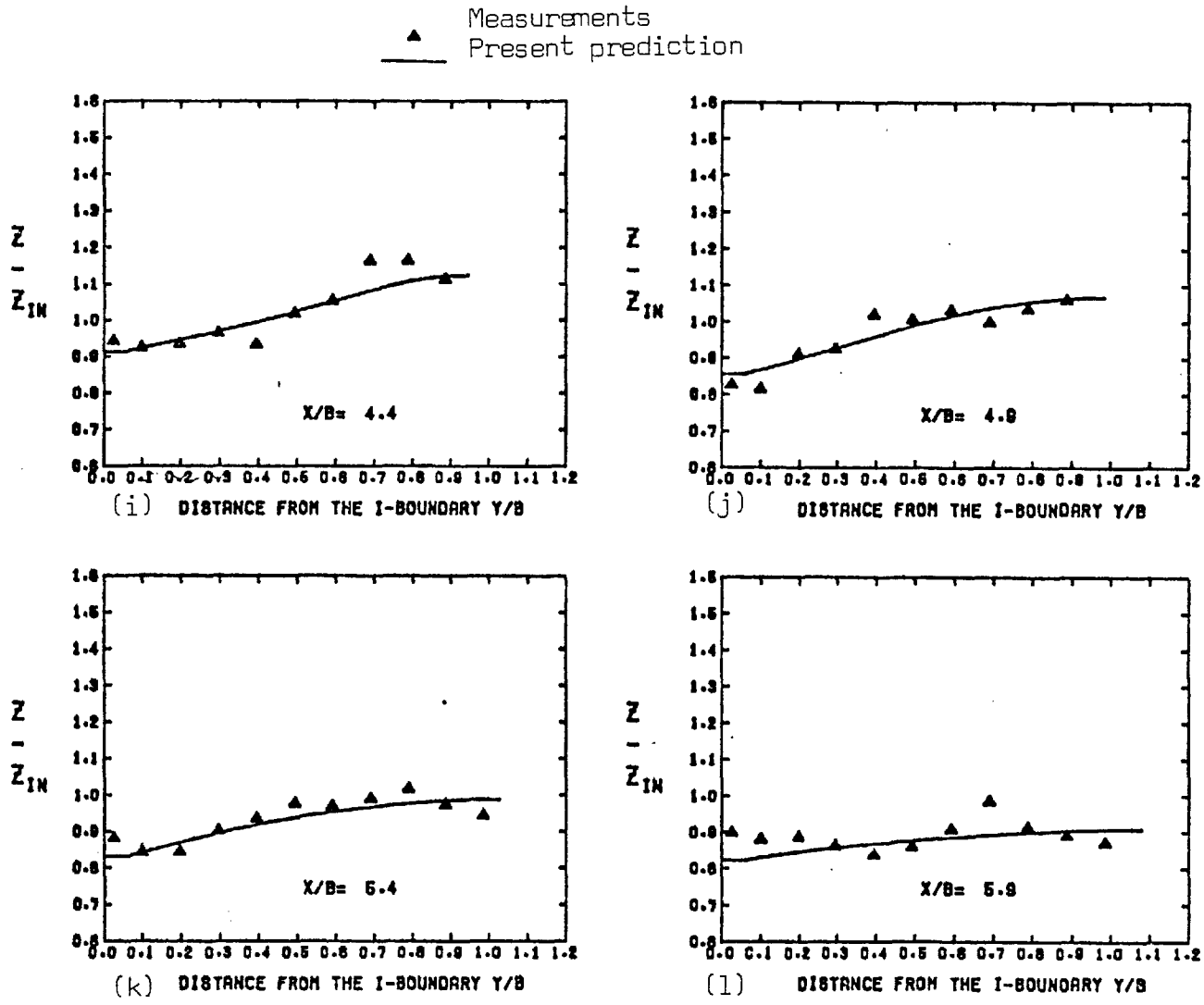


FIG. 7.5.6: (CONTINUED)

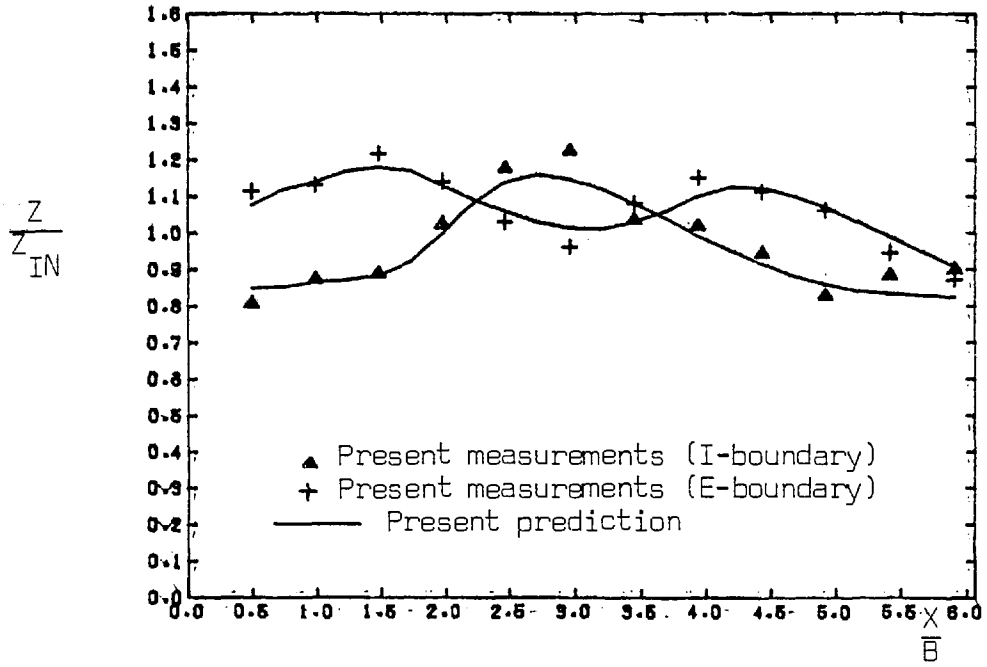


FIG. 7.5.7: PREDICTION OF LAYER DEPTHS ALONG THE WALLS; FR=2.20, R_I=6.0, θ_E=5°, A.R.=8.

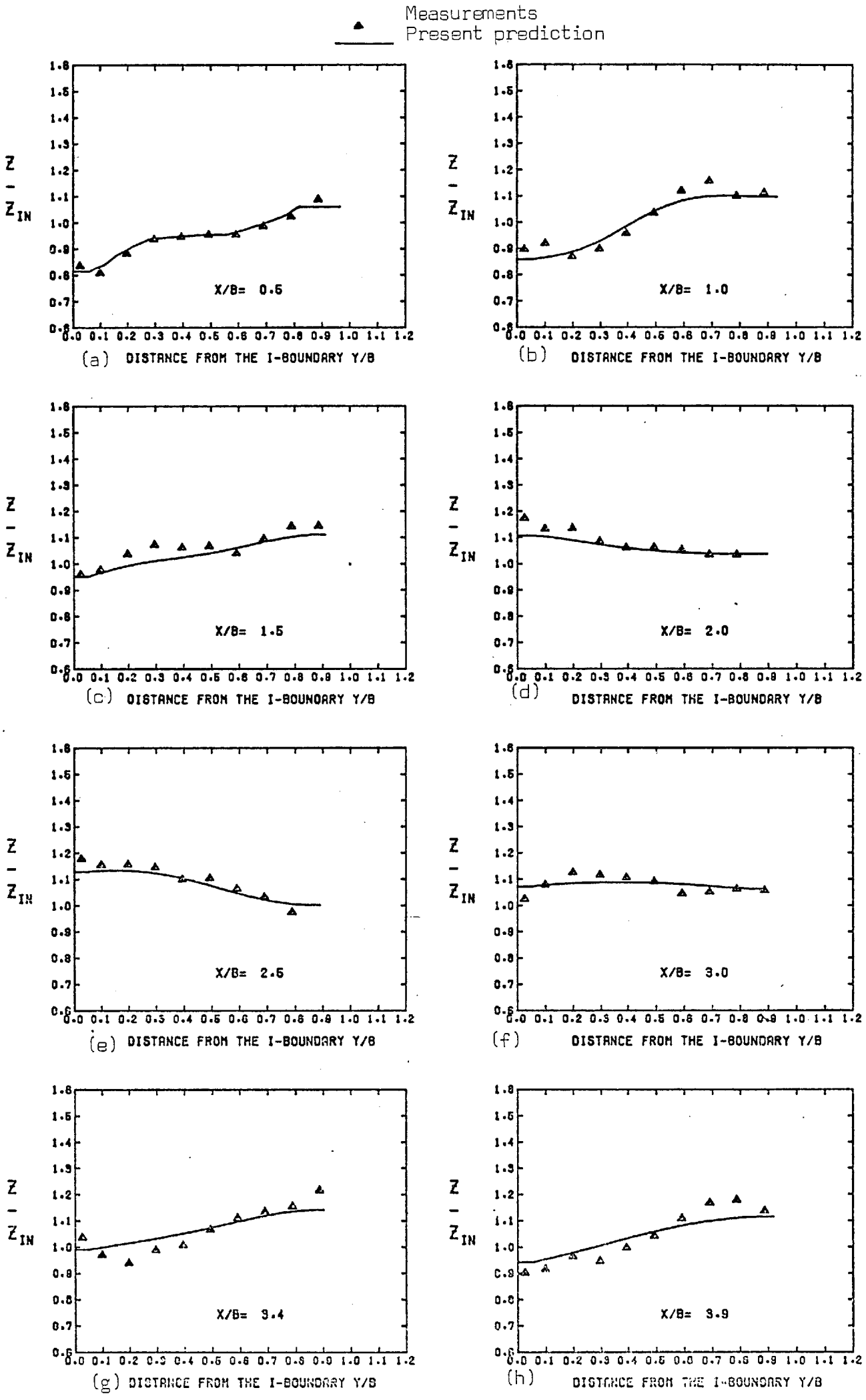


FIG. 7.5.8: PREDICTION OF PRESENT EXPERIMENTAL RUN 4; FR=1.85, R_I=6.0, θ_E=5°, A.R.=8.

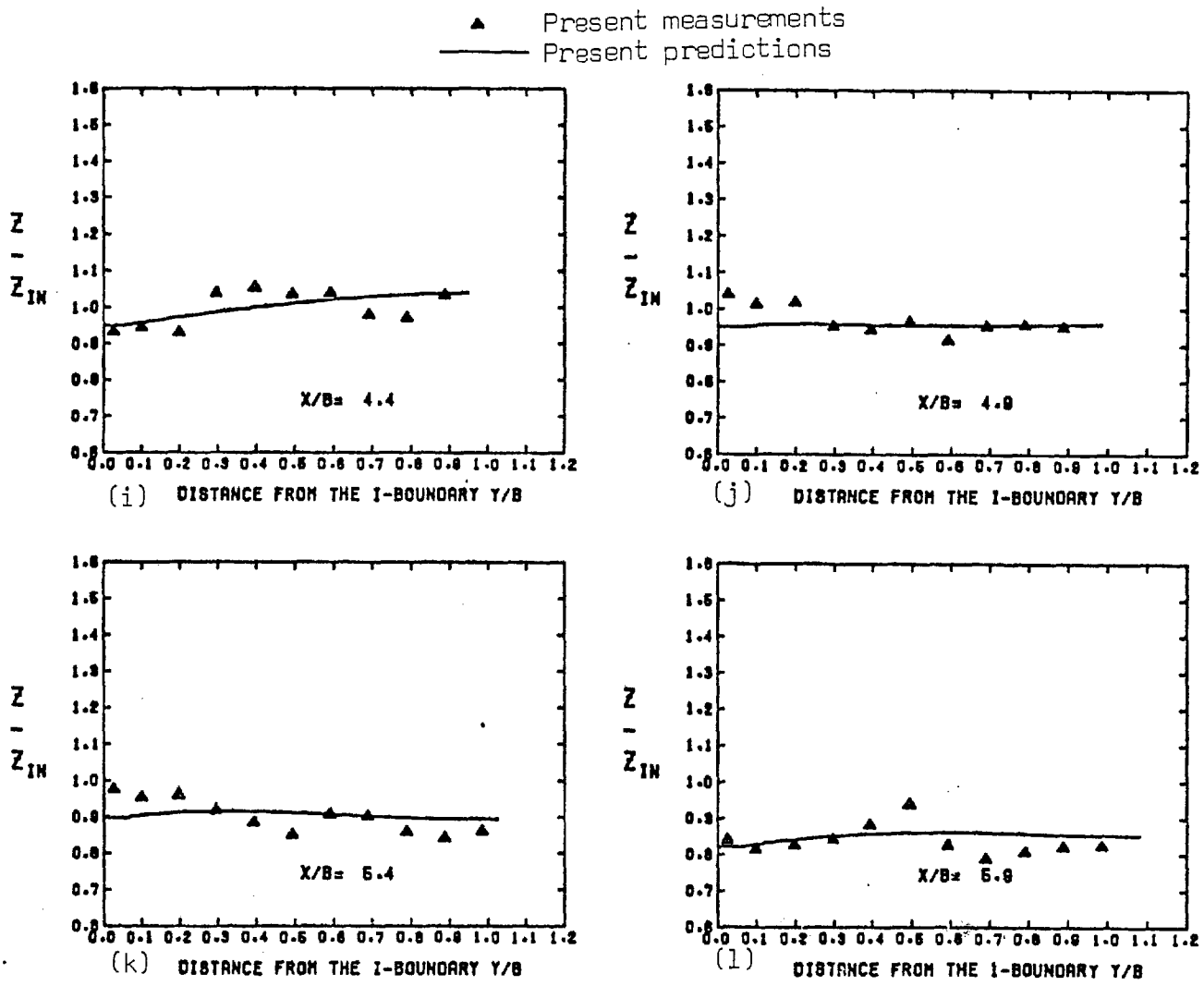


FIG. 7.5.8: (CONTINUED)

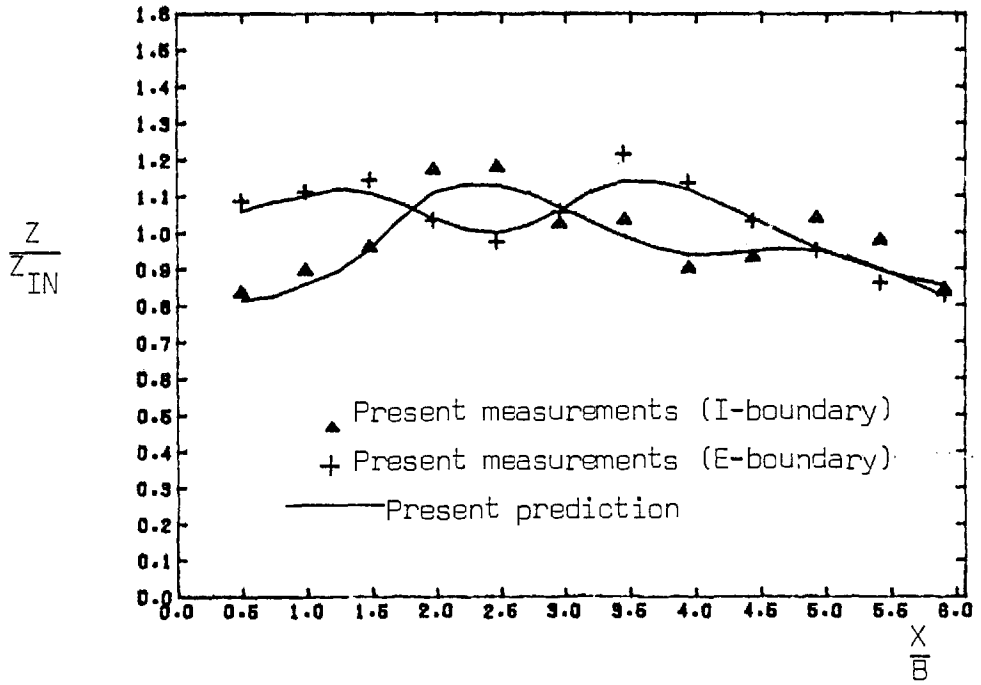


FIG. 7.5.9: PREDICTION OF LAYER DEPTHS ALONG THE WALLS; FR=1.85, R_I=6.0, θ_E=5°, A.R.=8.

both cases. The main difference between the two runs was that the maxima and the minima of the layer thickness variations reached the side walls earlier in the lower Froude number experiment. In fact, as Figures 7.5.9 and 7.5.7 show, in Run 4 there were two maxima along either wall, and Run 3 also had two maxima along the outer wall but only one along the inner wall. This observation agrees with the expectation that the angle of propagation of the cross waves should increase as the Froude number decreased, becoming 90^{o} if a hydraulic jump should occur; with the Froude number then crossing the value one.

The comparison of the predicted layer thicknesses with the experimental data of Run 5, (Figures 7.5.1(a) - (l)) was previously discussed in section 7.5.1. The outer wall made an angle of 7^{o} with the initial flow direction in this run. Figure 7.5.10 shows the longitudinal variations of the layer depths near the walls. The magnitudes of the maxima were higher and occured more frequently than in previous runs, due to the larger angle* presented to the flow. The agreement between the experimental data and the predictions is seen to be fair. The first maxima measured along the inner wall appeared to be much greater than that predicted. This may be partly due to the neglect of vertical acceleration in the mathematical model.

To estimate the level of disagreement between the predictions and the experimental data in all these runs, the root mean square deviation, σ was calculated at each cross-section, in each run.

---

*NOTE: An attempt to use an angle of 10^{o} in the experiment resulted in the inlet being submerged by a hydraulic jump.

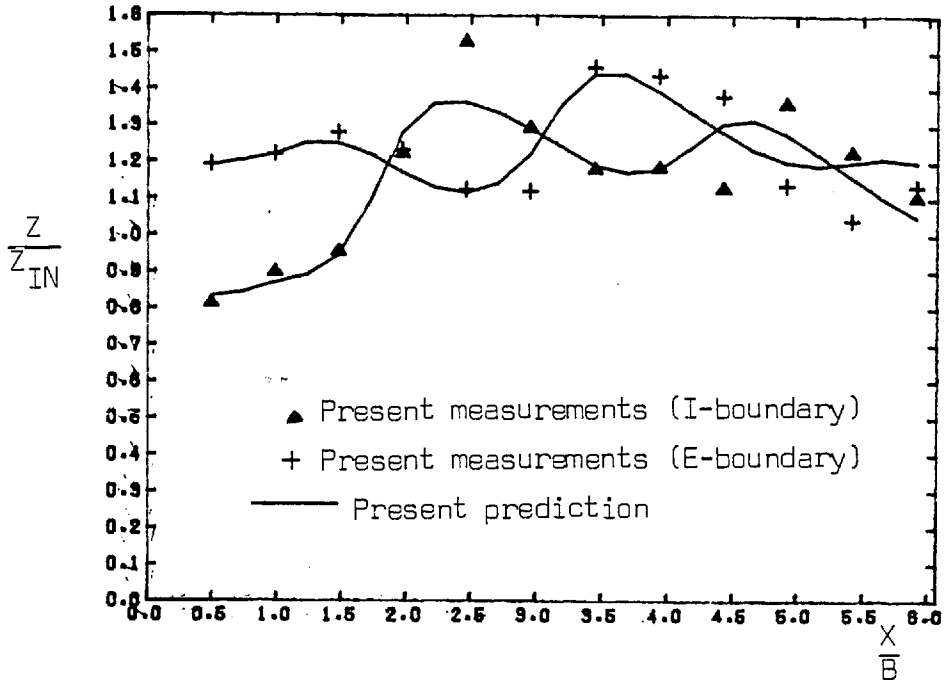


FIG. 7.5.10: PREDICTION OF LAYER DEPTHS ALONG THE WALLS; FR=2.10, R_I=6.0, θ_E=7°, A.R.=8.

These were calculated as:

$$\sigma = \left(\frac{\Sigma(z_{measured} - z_{predicted})^2}{\text{number of measured points}}\right)^{\frac{1}{2}} \qquad .(7.5.5)$$

These are plotted for the five runs in Figure 7.5.11 after they have been non-dimensionalised with the average depth, $\bar{z}$ at the respective cross-section. $\bar{z}$ is defined as:

$$\bar{z} \equiv \frac{\Sigma\, z_{measured}}{\text{number of measured points}} \qquad .(7.5.6)$$

The numbers in the figure indicate the experimental run. The number 6 stands for the prediction of experimental Run 5, with the guessed initial conditions; plotted as broken lines in Figures 7.5.1 (a) - (l). Figure 7.5.12 shows the plots of $\bar{z}$, for the 5 experimental runs, using the same notation as above.

7.6 Concluding Remarks

An experimental study of the supercritical flow of water in open channels of varying cross-section was carried out. The variations of the water layer depth were measured with a point gage. The measurements showed that the flow conditions at the inlet plane of the channel were non-uniform. Since adequate facilities for determining the exact flow conditions at the inlet plane were not available, these conditions were simulated (or guessed) when predicting the flows. The agreement of the model predictions with the experimental data was fair in all cases. This has further validated the numerical procedure developed for predicting supercritical open-channel flows.

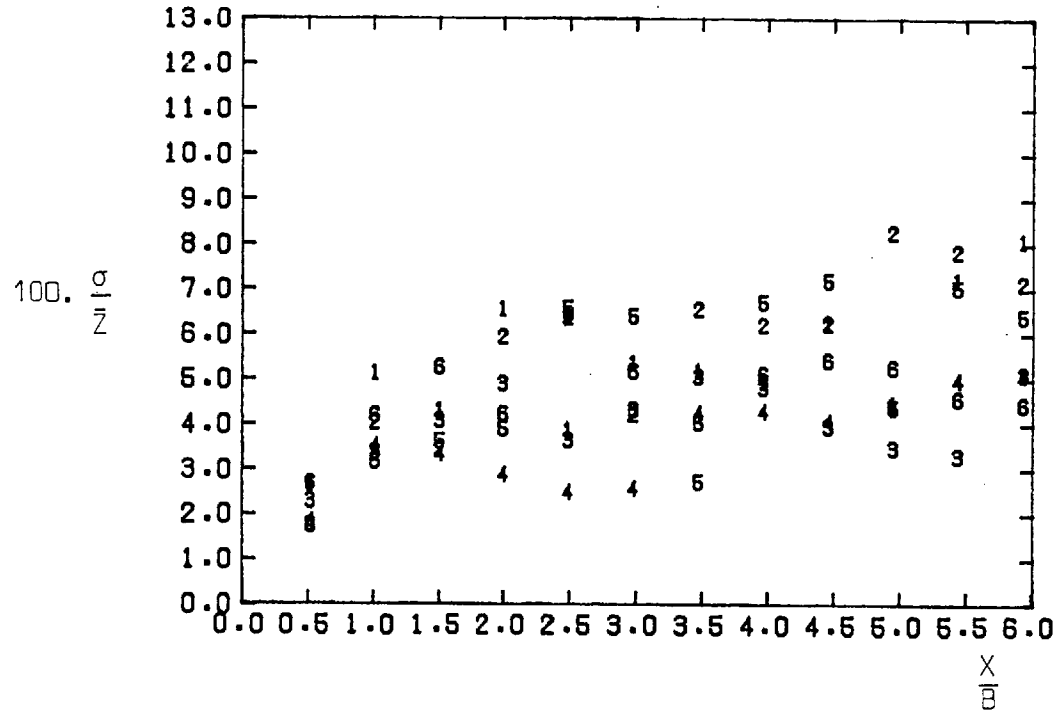


FIG. 7.5.11: PERCENTAGE R.M.S. DEVIATION OF PRESENT PREDICTIONS FORM THE MEASUREMENTS.

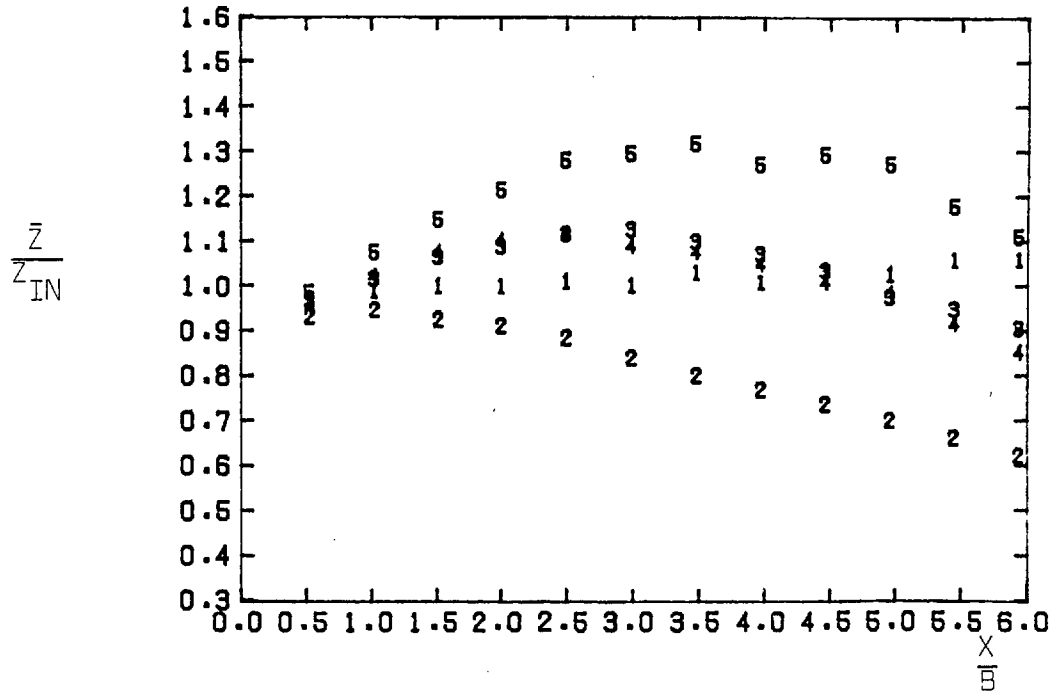


FIG. 7.5.12: AVERAGE CROSS-SECTIONAL LAYER DEPTH.

This concludes the work reported in this thesis. The main conclusions and some auxiliary material now follow.

CHAPTER 8

CONCLUSIONS

8.1 Achievements of the Present Work

The main achievements of the present study and the conclusions thereof may be summarised as:

1) Three numerical procedures have been developed for predicting surface-layer flows. Comparison of predictions with these procedures to analytical solutions to three flow problems show very good agreement. The numerical procedures can therefore be said to be mathematically accurate.

2) A rotating-grid procedure has been developed for computing flows with strong curvature effects. This was validated by predicting correctly the uniform flow of water within curved domains. Fairly high degrees of non-orthogonality were accommodated.

3) Predictions of heated surface discharges into stagnant ambient fluid showed fairly good agreement with laboratory measurements for a wide range of discharge parameters. The range of laboratory data on heated surface discharges into crossflowing ambient fluid is not so wide, and the predictions of these are mainly fair.

4) Predictions of field data on heated surface discharges into natural waters are not so good. This may be due to certain complexities surrounding these discharges, many of which are site-specific and have not been incorporated in the present mathematical model. This could be done, in future, if adequate information of these are obtained.

5) The experimental measurements of supercritical flow of water in open channels carried out in the present study showed the correct trends. The present predictions of these experimental data are mostly fair. The present predictions of other experimental data on supercritical flows in open channels are also fair.

6) In all the predictions, the present methods compared favourably with other existing methods. The computational requirements are about 25K words of storage space, and between 6~120 seconds central processor time, on the CDC 6600 computer.

8.2 Suggestions for Future Work

Some areas in which further research may be profitably undertaken are now suggested. These are:

1) It would be useful to perform more experiments on the entrainment of ambient fluid in surface-layer flows. Especially, the effects of the proximity of a wall or bottom on the rate of fluid entrainment need to be quantified. The effects of ambient turbulence, wind stress, etc. also need to be investigated. The aim should be to obtain a more sophisticated and universally applicable entrainment relation.

2) On the theoretical side, a problem that would be of interest is the solution of a mixed supercritical/subcritical flow. This may arise in both floating and full-depth layer flows. Although supercritical and subcritical flows have been solved separately in this study, a special procedure may be required for the transition from one procedure to the other.

LIST OF REFERENCES

1) ABRAMOVICH G.N. (1963)

"The Theory of Turbulent Jets".

MIT Press.

2) ANWAR H.O. (1970)

"Spread of Buoyant Jet at the Free Surface".

J. Hydraulics Div., ASCE, HY1, pp. 288-291.

3) ARUMUGAM K. (1955)

"Surface Characteristics of fast-flowing Water emerging from a Sluice".

Ph.D. Thesis, University of London.

4) BENJAMIN T.B. (1968)

"Gravity Currents and Related Phenomena".

JFM, Vol. 31, Part 2, pp. 209-248.

5) BINDER R.C. (1961)

"Flow Measurement".

Ed., V.L. Streeter: Handbook of Fluid Dynamics, McGraw Hill.

6) BRADY D. and GEYER J. (1972)

"Development of a General Computer Model for Simulating Thermal Discharges in Three Dimensions".

Rep. No. 7, Dept. of Geog. and Env. Eng., Johns Hopkins University.

7) BUSEMANN A. (1931)

"Gasdynamik",

Handbuch der Experimentalphysik, Vol. IV.

8) CARTER H.H. (1969)

"A Preliminary Report on the Characteristics of a Heated Jet Discharged Horizontally into a Transverse Current: Part 1-Constant Depth".

Tech. Rep. No. 61, CBI, Johns Hopkins University, Maryland.

9) CARTER H.H., SCHIEMER E. and REGIER R. (1973)

"The Buoyant Surface Jet Discharging Normal to an Ambient Flow at various Depths".

Tech. Rep. No. 81, CBI, Johns Hopkins University, Md.

10) CARTER H.H. and REGIER R. (1974)

"The Three-Dimensional Heated Surface Jet in a Crossflow".

Tech. Rep. No. 88, CBI, Johns Hopkins University, Md.

11) CHEN J.C. and LIST E.J. (1977)

"Spreading of Buoyant Discharges".

Eds. Spalding D.N. and Afgan N.: Heat Transfer and Turbulent Buoyant Convection, Hemisphere.

12) CHEN J.C. and SCHETZ J.A. (1975)

"Numerical Solution of the Three-Dimensional Navier-Stokes Equations with Applications to Channel Flows and a Buoyant Jet in Cross Flow".

ASME, J. Applied Mechanics, 75-ARM-21.

13) CHOUDHARY U.K. and NARASIMHAN S. (1977)

"Flow in 180^{o} Open Channel Rigid Boundary Bends".

ASCE, J. Hydraulics div., HY6, pp. 651-657.

14) CHOW VEN TEN (1959)

"Open Channel Hydraulics".

McGraw-Hill.

15) CHU V.H. and BADDDUR R.E. (1975)

"Buoyant Surface Discharge on a Step and Sloping Bottom".

Tech. Rep. No. 75-2 (FML),McGill University, Canada.

16) CHU V.H. and VANVARI M.R. (1974)

"Two-Dimensional Turbulent Surface Jets of Low Richardson Number".

Tech. Rep. No. 74-2 (BML), McGill University.

17) CHU V.H. and VANVARI M.R. (1976)

"Experimental Study of Turbulent Stratified Shearing Flow".

ASCE, J. Hydraulics Div., HY6, pp. 691-706.

18) CRDWE C.T. and RIESENBIETER H. (1967)

"An Analytical and Experimental Study of Jet Deflection in Crossflow".

Fluid Dynamics of Rotor and Fan-supported Aircraft, AGARD Preprints.

19) DINELLI G. (1975)

"Evaluation of Thermal Impact of Cooling Water Discharges into Mediteranean Coastal Waters".

ICHMT Seminar, Dubrovnik.

20) DUNN W.E., PDLICASTRD A.J. and PADDDCK R.A. (1975)

"Surface Thermal Plumes: Evaluation of Mathematical Models for the near and complete Field".

Rep. ANL/WR-75-3, Argonne National Laboratory.

21) ELLISON T.H. and TURNER J.S. (1959)

"Turbulent Entrainment in Stratified Flows".

JFM, Vol. 6, pp. 423-448.

22) ENGLAND W. and TAFT J. (1973)

"A Three-Dimensional Computer Simulation Model for Tracing and Defining Thermal Pollution".

System, Science and Software Report SSS-IR-73-1680, La Jolla, California.

23) FANG F., PARKER G.C., SHEARLS E.A. and HARGIS W.J. (1975)

"An Estuarine Thermal Monitoring Program".

Proceedings of the Conference on Thermal Pollution Analysis, Virginia Polytechnic Institute (May, 1975).

24) FAY J.A. (1969)

"The Spread of Oil Slicks on a Calm Sea".

Ed., D.P. Hoult: Oil on the sea, Plenum, pp. 53-63.

25) FRIGO A.A. and FRYE D.E. (1972)

"Physical Measurements of Thermal Plumes into Lake Michigan".

ANL/ES-16, Argonne National Laboratory.

26) HANSEN N.E.O. (1975)

"Entrainment in Two-Layered Flows".

Ph.D. Thesis, Technical University of Oenmark.

27) HARLEMAN O.R.F. (1961)

"Stratified-flow".

Ed. Streeter V.L.: Handbook of Fluid Dynamics, McGraw-Hill.

28) HARLEMAN D.R.F. (1972)

"Longitudinal Temperature Distribution in Rivers and Estuaries - One-Dimensional Mathematical Models".

MIT Summer Session.

29) HAYASHI T. and SHUTO N. (1967)

"Diffusion of Warm Water Jets Discharged Horizontally at the Water Surface".

12th Congress IAHR, Colorado, pp. 47-59.

30) HILL M.N. (Ed.) (1962)

"The Sea".

Vol. 1, Interscience.

31) HOSSAIN M.S. and RODI W. (1977)

"Influence of Buoyancy on the Turbulence Intensities in Horizontal and Vertical Jets".

Eds. D.B. Spalding and N. Afgan: Heat Transfer and Turbulent Buoyant Convection, Hemisphere.

32) HOULT D.P. (1972)

"Oil Spreading on the Sea".

Annual Review of Fluid Mechanics, pp. 340-368.

33) IPPEN A.T. (1949)

"Mechanics of Supercritical Flow".

High-Velocity Flow in Open Channels: A symposium, Trans. ASCE, 116, pp. 263-295.

34) IPPEN A.T. and DAWSON J.H. (1949)

"Design of Channel Contractions".

High-Velocity Flow in Open Channels: A symposium, Trans. ASCE, 116, pp. 326-346.

35) JEN Y., WIEGEL R.L. and MOBAREK I. (1966)

"Surface Discharge of Horizontal Warm-Water Jet".

ASCE, J. Power Div., PO4, pp. 1-28.

36) JIRKA G.H., ABRAHAM G. and HARLEMAN D.R.F. (1975)
"An Assessment of Techniques for Hydrothermal Prediction".
R.M. Parsons Lab., MIT Rept. No. 203.

37) KAO T.W. (1977)
"Density Currents and their Applications".
ASCE, J. Hydraulics Div., HY5, pp. 543-555.

38) KNAPP R.T. (1949)
"Design of Channel Curves for Supercritical Flow".
High-Velocity Flow in Open Channels: A Symposium, Trans. ASCE, 116, pp. 296-325.

39) KOESTER G. (1974)
"Experimental Study of Submerged Single-port Thermal Discharges".
Battelle Pacific Northwest Laboratories, Rep. No. BN-SA-398, Richland, Washington.

40) KOY R.C.Y. (1971)
"Two-Dimensional Surface Warm Jets".
ASCE, J. Hydraulics Div., HY6, pp. 819-836.

41) KUHLMAN J.M. and PRAHL J.M. (1974)
"Laboratory Modelling of Surface Thermal Plumes".
Rep. No. FTAS/TR-74-102, Case Western Reserve University, Ohio.

42) LAUNDER B.E. and SPALDING D.B. (1972)
"Mathematical Modelling of Turbulence",
Academic Press.

43) McGUIRK J.J. and RODI W. (1977)

"Calculation of Three-Dimensional Heated Surface Jets".

Eds., D.B. Spalding and N. Afgan: Heat Transfer and Turbulent Buoyant Convection, Hemisphere.

44) McGUIRK J.J. and RODI W. (1978a)

"A Depth-averaged Mathematical Model for the near-field of side Discharges into Open Channel Flow".

JFM, Vol. 86, pp. 761-782.

45) McGUIRK J.J. and RODI W. (1978b)

"Mathematical Modelling of Three-Dimensional Heated Surface Jets".

SFB Rep. No. SFB80/T/135, University of Karlsruhe.

46) McGUIRK J.J. and SPALDING D.B. (1975)

"Mathematical Modelling of Thermal Pollution in Rivers".

Imperial College, Dept. of Mech. Eng. Rep. No. HTS/75/18.

47) MOCKMORE C.A. (1943)

"Flow around Bends in Stable Channels".

Trans. ASCE, 109, pp. 593-619.

48) MOTZ L. and BENEDICT B. (1970)

"Heated Surface Jet Discharged into a Flowing Ambient Stream".

Rep. No. 4, Vanderbilt University, Tennessee.

49) NIKURADSE J. (1926)

"Untersuchungen über die Geschwindigkeitsverteilung in turbulenten Strömungen",

VDI-Forschungsheft 281.

50) PAILY P.P., MACAGNO E.O. and KENNEDY J.F. (1974)
"Winter-regime Thermal Response of Heated Streams".
ASCE, J. Hydraulics Div., HY4, pp. 531-551.

51) PANDE B.B.L. and RAJARATNAM N. (1975a)
"Similarity analysis of Buoyant Surface Jets into Quiescent Ambients".
16th Congress IAHR, Sao Paulo, Brazil, pp. 62-70.

52) PANDE B.B.L. and RAJARATNAM N. (1975b)
"An Experimental Study of Heated Surface Discharges into Quiescent Ambients".
Tech. Rep. Civ. Eng. Dept., University of Alberta, Canada.

53) PANDE B.B.L. and RAJARATNAM N. (1977)
"An Experimental Study of Bluff Buoyant Turbulent Surface Jets".
J. Hydraulic Research, pp. 261-275.

54) PARKER F.L. and KRENKEL P.A. (1970)
"Physical and Engineering Aspects of Thermal Pollution".
Butterworths.

55) PATANKAR S.V. and SPALDING D.B. (1972)
"A Calculation Procedure for Heat, Mass and Momentum Transfer in Three-Dimensional Parabolic Flows".
IJHMT, Vol. 15, pp. 1787-1806.

56) PAUL J.F. and LICK W.J. (1974)
"A Numerical Model for Three-Dimensional Variable-Density Jet". Proc. 16th Conference on Great Lakes Research, Ohio,

57) PLATTEN J.L. and KEFFER J.F. (1968)

"Entrainment in Deflected axi-symmetric Jets at Various Angles to the Stream".

Tech. Rep. No. 6808, Dept. of Mech. Eng., University of Toronto.

58) PRANDTL L. (1931)

"Abriss der Strömungslehre".

Braunschweig, Vieweg.

59) PRATAP V.S. (1975)

"Flow and Heat Transfer in Curved Ducts".

Ph.D. Thesis, University of London.

60) PREISWERK E. (1940)

"Application of the Methods of Gas Dynamics to Water Flows with Free Surface".

NACA Tech. Memo. Nos. 934 and 935.

61) PRITCHARD D. (1971)

"Design and Siting Criteria for once-through Cooling Systems".

68th Annual Meeting, AICHE, Texas.

62) PRITCHARD D. (1973)

"The Fate of and Effect of Excess Heat Discharged into Lake Michigan with Specific Application to the Condenser Cooling Water Discharge from Zion Nuclear Power Station".

Testimony for AEC Operating Permit, Chicago.

63) PRYCH E. (1972)

"A Warm Water Effluent Analyzed as a Buoyant Surface Jet".

Sveriges Meterologiska Och Hydrologiska Institut, Serie Hydrologi, No. 21, Stockholm.

64) PUN W.M. and SPALDING D.B. (1976)

"A General Computer Program for Two-Dimensional Elliptic Flows".

Imperial College, Mech. Eng. Dept., Rep. No. HTS/76/2.

65) RAMACHANDRA V. and SPALDING D.B. (1976)

"Fluid Flow and Heat Transfer in Rectangular-Sectioned Ducts".

Imperial College, Mech. Eng. Dept. Rep. No. HTS/76/21.

66) RASTOGI A.K. and RODI W. (1978)

"Two- and Three-Dimensional Calculations of Heat and Mass Transfer in Open Channel Flows".

ASCE, J. Hydraulics Div., HY3, pp. 397-420.

67) RIABOUCHINSKY D. (1932)

"Sur l'Analogie Hydraulique des Mouvements d'un Fluide Compressible".

Compte Rendus de l'Académic des Sciences, Vol. 195, pp.998-999.

68) ROTA A. and ZAVATERELLI R. (1973)

"Systematic Measurements of Temperature and Velocity of the Po River in the Vicinity of the Heated Condenser Water Discharged from ENEL Thermo-electric Power Plant at Piacenza".

Centre for Computational and Experimental Studies, Tech. Rep., MISTER No. 5A/B.

69) ROUSE H., BHOOTA B.V. and HSU EN-YEN (1949)

"Design of Channel Expansions",

High-velocity Flow in Open Channels: A symposium, Trans. ASCE, 116, pp. 347-400.

70) SCHLICHTING H. (1968)

"Boundary-Layer Theory".

McGraw-Hill.

71) SHARP J.J. (1969)

"Spread of Buoyant Jets at the Free Surface".

ASCE, J. Hydraulics Div., HY3, pp. 811-825.

72) SHIRAZI M. (1973)

"A Critical Review of Laboratory and Some Field Experimental Data on Surface Jet Discharge of Heated Water."

U.S., EPA Working Paper No. 4.

73) SHIRAZI M. and DAVIS L. (1974)

"Workbook of Thermal Plume Prediction, Volume 2, Surface Discharge".

U.S., EPA, Rep. No. EPA-R2-72-005b.

74) SHURKY A. (1949)

"Flow Around Bends in an Open Flame".

Trans. ASCE, 115, pp. 751-779.

75) SINGHAL A.K. (1977)

"Flow in Axial Turbomachinery Cascades".

Ph.D. Thesis, University of London.

76) SPALDING D.B. (1975)

"THIRBLE; Transfer of Heat in Rivers, Bays, Lakes and Estuaries".

Imperial College, Dept. of Mech. Eng., Rep. No. HTS/75/4.

77) SPALDING D.B. (1977)

"Heat and Mass Transfer in Rivers, Bays, Lakes and Estuaries".

Advances in Heat Transfer, Vol. 13, pp. 61-117.

78) SPALDING D.B. (1978)

"GENMIX: A General Computer Program for Two-Dimensional Parabolic Phenomena".

HMT Series, Vol. 1, Pergamon Press.

79) STEFAN H., BERGSTEDT L. and MROSLA E. (1975)

"Flow Establishment and Initial Entrainment of Heated Water Surface Jets".

St. Anthony Falls Hydraulic Lab., Rep. No. EPA-660/3-75-014, University of Minnesota.

80) STEFAN H. (1972)

"Analytical Jet-Type Model of Heated Water Surface Plumes".

Proceedings 15th Conference on Great Lakes Research.

81) STOLZENBACH K.D. (1976)

"Heat Exchange at the Water Surface".

Lecture notes for the International Advanced Course: Heat Disposal from Power Generation, Dubrovnik, Yugoslavia.

82) STOLZENBACH K.D. and HARLEMAN D.R.F. (1971)

"An Analytical and Experimental Investigation of Surface Discharges of Heated Water".

R.M. Parsons Lab., MIT, Tech. Rep. No. 135.

83) SUNDARAM T.R. and WU J. (1973)

"Wind Effects on Thermal Plumes in Waterbodies".

Flow Studies in Air and Water Pollution, ASME, pp. 25-37.

84) TAMAI N., WIEGEL R.L. and TORNBERG G.F. (1969)

"Horizontal Surface Discharge of Warm Water Jets".

ASCE, J. Power Div., PO2, pp. 253-276.

85) TATCHEL D.G. (1975)

"Convective Processes in Confined, Three-Dimensional Boundary Layers".

Ph.D. Thesis, University of London.

86) THOMPSON J. (1876)

"On the Origin and Winding of Rivers in Alluvial Plains, with Remarks on Flow Around Bends in Pipes".

Proc., Royal Soc., pp. 5-8.

87) TILL H. (1974)

"A Computer Model for Three-Dimensional Simulation of Thermal Discharges into Rivers".

Doctoral Dissertation, University of Missouri.

88) VIZEL Y.M. and MOSTINSKII I.L. (1965)

"Deflection of a Jet Injected into a Stream".

Fluid Dynamics, Vol. 8. (English translation of Inzhenerno-Fizicheskii).

89) VON KARMAN T. (1938)

"Eine Praktische Anwendung der Analogie Zwischen Überschallstromung in Gasen und über Kritische Stromung in Offenen Gerinnen".

ZAMM, pp. 49-56.

90) WALDROP W. and FARMER R. (1974)

"Three-Dimensional Computation of Buoyant Plumes".

J. Of Geophysics Research 79(9), pp. 1269-1276.

91) WEIL J, (1974)

"Verification of Heated Water Jet Numerical Model".

Swedish Meteorological and Hydrological Institute, Rep. No. RH01.

92) WILKINSON D.L. and WOOD I.R. (1971)
"A Rapidly Varied Flow Phenomenon in a Two-Layer Flow".
JFM, Vol. 47, Part 2, pp. 241-256.

93) WIUFF R. (1977)
"Experiments on the Surface Buoyant Jet".
Technical University of Denmark, Series Paper No. 16.

94) WIUFF R. (1978)
"Experiments on Surface Buoyant Jet".
ASCE, J. Hydraulics Div., HY5, pp. 667-679.

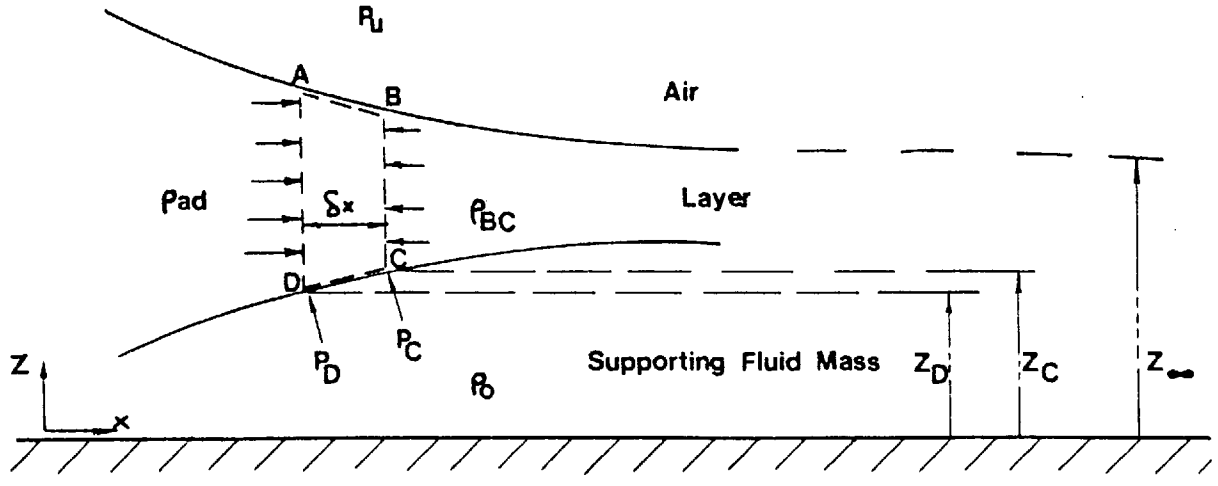
APPENDICES

APPENDIX A

DERIVATION OF THE PRESSURE-GRADIENT TERMS FOR THE MOMENTUM EQUATIONS

In surface-layer flows, the driving force per unit volume is the pressure gradient. It is generated by the gravitational or buoyancy force which depends on the variations in the layer density and the layer depth. In full-depth flows, it also depends on the slope of the supporting solid mass. The relationship between the pressure gradients and the layer density and layer depth variations are derived here from first principles.

First considered are floating-layer flows, the flow situation is illustrated below.



The following assumptions are made to facilitate the derivation:

(i) The density within the layer is constant across the depth, but may vary longitudinally and is different from the density of the supporting mass, ρ_o, which is constant everywhere.

(ii) Only normal forces are considered.

(iii) Vertical motion is negligible, so hydrostatic equilibrium exists.

(iv) x represents any horizontal distance coordinate and z represents the vertical distance coordinate.

The net force acting on the control volume ABCD of unit width, in the x-direction is given by:

$$F = \int_{ABCD} P\,dz = \int_{AB} P\,dz + \int_{BC} P\,dz + \int_{CD} P\,dz + \int_{DA} P\,dz .$$

Therefore,

$$F = P_U(z_B - z_A) + \tfrac{1}{2}(P_U+P_C)(z_C-z_B) + \tfrac{1}{2}(P_C+P_D)(z_D-z_C) + \tfrac{1}{2}(P_U+P_D)(z_A-z_D) \quad .(A.1)$$

The pressure difference between A and D is given:

directly by: $P_D - P_U = \rho_{ad} g(z_A - z_D)$;(A.2)

and through the supporting mass by:

$$P_D - P_U = \rho_o g(z_\infty - z_D) \quad .(A.3)$$

Similarly, the pressure difference between B and C is:

$$P_C - P_U = \rho_{BC} g (z_B - z_C) \qquad ,(A.4)$$

and,

$$P_C - P_U = \rho_o g (z_\infty - z_C) \qquad .(A.5)$$

Define:

$$h \equiv z_A - z_D \ ;$$

and,

$$\rho \equiv \rho_{AD} \ ; \qquad (A.6)$$

then,

$$h + \delta h \equiv z_B - z_C \ ;$$

and

$$\rho + \delta\rho \equiv \rho_{BC}.$$

If equations (A.2), (A.3), (A.4) and (A.5), and the definition set (A.6) are substituted in equation (A.1), the driving force becomes (on neglecting higher order terms):

$$F = -\tfrac{1}{2} g \{ (1 - \frac{2\rho}{\rho_o}) \, h^2 \delta\rho + (1 - \frac{\rho}{\rho_o}) \, 2\rho h \delta h \} \qquad .(A.7)$$

Hence, the net driving force per unit volume, F''' is given by:

$$F''' = - g \{ \frac{(\rho_o - 2\rho)}{2\rho_o} \, h \, \frac{\delta\rho}{\delta x} + \frac{(\rho_o - \rho)}{\rho_o} \, \rho \, \frac{\delta h}{\delta x} \} \qquad .(A.8)$$

Define:

$$\Delta\rho \equiv \rho_o - \rho ;$$

then, (A.9)

$$d\Delta\rho = d(\rho_o - \rho) = - d\rho \ .$$

If δx is sufficiently small, then

$$\frac{\delta \rho}{\delta x} = \frac{d\rho}{dx} \; ;$$

and, (A.10)

$$\frac{\delta h}{\delta x} = \frac{dh}{dx} \; .$$

Therefore,

$$F''' = - g \left\{ \left(\frac{\rho}{2\rho_o} - \frac{\Delta\rho}{2\rho_o} \right) h \frac{d\Delta\rho}{dx} + \frac{\Delta\rho}{\rho_o} \rho \frac{dh}{dx} \right\} \quad .(A.11)$$

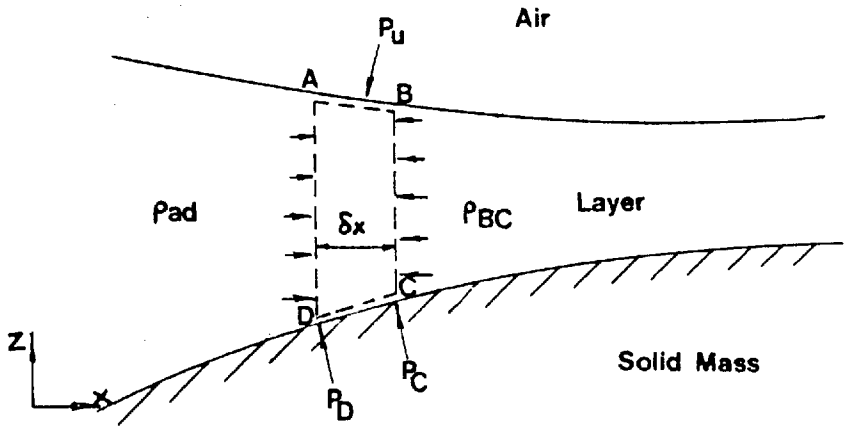
But,

$$\frac{d\bar{p}}{dx} \quad -F''' \quad ;(A.12)$$

hence,

$$\frac{d\bar{p}}{dx} = g \left\{ \left(\frac{\rho}{2\rho_o} - \frac{\Delta\rho}{\rho_o} \right) h \frac{d\Delta\rho}{dx} + \frac{\Delta\rho}{\rho_o} \rho \frac{dh}{dx} \right\} \quad .(A.13)$$

In full-depth flows, the derivation is slightly different. The flow situation is illustrated below.



The assumptions are the same as those for floating-layer flows, and similarly, the net force per unit volume acting on the control volume ABCD is given by:

$$F = P_U(z_B-z_A) + \tfrac{1}{2}(P_U+P_C)(z_C-z_B) + \tfrac{1}{2}(P_C+P_D)(z_D-z_C) + \tfrac{1}{2}(P_U+P_D)(z_A-z_D) \quad .(A.14)$$

The pressure difference between A and D is:

$$P_D-P_U = \rho_{AD}g(z_A-z_D) \quad ,(A.15)$$

at the pressure difference between B and C is:

$$P_C-P_U = \rho_{BC}g(z_B-z_D) \quad .(A.16)$$

Define:

$$\delta Z_o \equiv z_C-z_D \quad ;$$

$$h \equiv z_A-z_D \quad ;$$

and, (A.17)

$$\rho \equiv \rho_{AD} \quad ;$$

then,

$$h + \delta h \equiv z_B-z_C \quad ;$$

and,

$$\rho + \delta\rho \equiv \rho_{BC} \quad .$$

If equations (A.15), (A.16), and the definition set (A.17) are substituted in equation (A.14), the net driving force becomes (on neglecting higher order terms):

$$F = \tfrac{1}{2}g\{(2\rho h\delta h + h^2\delta\rho) + 2\rho h\delta z_o\} \quad .(A.18)$$

The net driving force per unit volume, F''' is given by:

$$F''' = -g \{\rho(\frac{\delta h}{\delta x} + \frac{\delta z_o}{\delta x}) + \frac{h}{2} \frac{\delta \rho}{\delta x}\} \qquad .(A.19)$$

If δx is sufficiently small,

$$\frac{\delta h}{\delta x} = \frac{dh}{dx} \; ,$$

$$\frac{\delta z_o}{\delta x} = \frac{dz_o}{dx} \; ; \qquad (A.20)$$

and $$\frac{\delta \rho}{\delta x} = \frac{d\rho}{dx} \; .$$

Therefore,

$$\frac{d\overline{P}}{dx} \equiv - F''' = g \{\rho(\frac{dh}{dx} + \frac{dz_o}{dx}) + \frac{h}{2} \frac{d\rho}{dx}\} \qquad .(A.21)$$

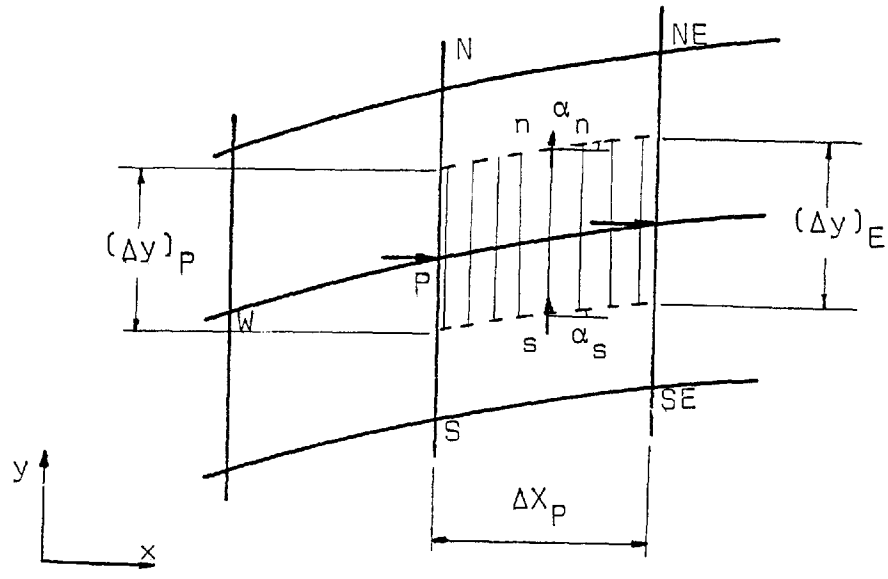
Equations (A.13) and (A.21) are the desired pressure-gradient terms for the floating-layer and full-depth flows, respectively.

APPENDIX B

DERIVATION OF THE EQUATIONS FOR THE LOCAL CORRECTION OF PRESSURE OR LAYER DEPTH

In surface-layer flows, the variable that is of direct physical significance is the layer depth. It is related to the pressure in the way described in Appendix A. The "pressure-correction" equations are therefore derived as layer-depth correction equations. For simplicity, the equations are derived here for layer flows without lateral entrainment.

Consider the following grid domain:



The basis of the layer-depth correction equation is the requirement of kinematic compatibility of the flow. This may be expressed for the above control volume as:

$$(\Delta y)_E - (\Delta y)_P = \Delta x_P \, (\tan \alpha_n - \tan \alpha_s) \qquad .(B.1)$$

This condition would be satisfied if the pressure field were correct, since the terms in equation (B.1) depend on the continuity and momentum equations which are in turn influenced

by the pressures or layer depths. Since the pressure field is not known beforehand, the terms of equation (B.1) are calculated from guessed values, resulting in:

$$(\Delta y)^{*}_{E} - (\Delta y)^{*}_{P} = \Delta x_P \, (\tan\alpha^{*}_{n} - \tan\alpha^{*}_{s}) + \varepsilon_P \qquad ,(B.2)$$

where,

ε_P represents the kinematic-compatibility error, arising from the use of guessed quantities.

The correct layer depth and velocities may be expressed as:

$$z = z^{*} + z' \; ;$$
$$U = U^{*} + U' \; ; \qquad (B.3)$$

and $$V = V^{*} + V' \; ;$$

where,

the primed quantities represent the appropriate corrections to the guessed (starred) values.

Subtracting equation (B.2) from equation (B.1), gives:

$$(\Delta y)'_{E} - (\Delta y)'_{P} = \Delta x_P \, (\tan\alpha'_{n} - \tan\alpha'_{s}) - \varepsilon_P \qquad .(B.4)$$

By expression of the correction terms in this equation in terms of the layer-depth corrections, the required layer-depth correction equation(or "pressure-correction equation, as it is more usually known) is obtained. The necessary algebra is now described.

Expressions for $(\Delta y)'_E$ and $(\Delta y)'_P$

The continuity equation gives:

$$(\Delta y)_E = \left(\frac{\Delta\psi}{\rho U z}\right)_E \qquad ,(B.5)$$

where,

$\Delta\psi$ is the mass flow rate through the control volume at E.

By taking, first, logarithm of both sides and, then, the total derivative of each term, one gets:

$$\frac{d(\Delta y)_E}{(\Delta y)_E} = - \frac{dz_E}{z_E} + \frac{dU_E}{U_E} \qquad ,(B.6)$$

or,

$$\frac{(\Delta y)'_E}{(\Delta y)_E} = - \frac{z'_E}{z_E} + \frac{U'_E}{U_E} \qquad .(B.7)$$

Similarly,

$$\frac{(\Delta y')_P}{(\Delta y)_P} = - \frac{z'_P}{z_P} + \frac{U'_P}{U_P} \qquad .(B.9)$$

Expressions for $(\tan\alpha_n)'$ and $(\tan\alpha_s)'$

$\tan\alpha_n$ and $\tan\alpha_s$ may be expressed as:

$$\tan\alpha_n = \frac{V_n}{U_n} \qquad ,(B.10)$$

and,

$$\tan\alpha_s = \frac{V_s}{U_s} \qquad ,(B.11)$$

where,

U_n and U_s are each interpolated from the four neighbouring values.

Differentiating equations (B.10) and (B.11) give:

$$(\tan\alpha_n)' = \frac{V_n'}{U_n} - \frac{V_n}{U_n^2} \cdot U_n' \qquad ,(B.12)$$

and,

$$(\tan\alpha_s)' = \frac{V_s'}{U_s} - \frac{V_s}{U_s^2} \cdot U_s' \qquad .(B.13)$$

In equations (B.12) and (B.13), the terms containing U_n' and U_s' may be neglected on the grounds that, though the U''s and V''s may be of the same order, the V''s are usually much less than the U's.

Expressions for U''s and V''s

It now remains to express the velocity corrections in terms of the layer-depth corrections. These may be done as:

$$U_E' = \frac{\partial U_E}{\partial z_P} z_P' + \frac{\partial U_E}{\partial z_E} z_E' \qquad ;(B.14)$$

$$U_P' = \frac{\partial U_P}{\partial z_P} z_P' + \frac{\partial U_P}{\partial z_E} z_E' \qquad ;(B.15)$$

$$V_n' = \frac{\partial V_n}{\partial z_{NNE}} z_{NNE}' + \frac{\partial V_n}{\partial z_{PE}} z_{PE}' \qquad ;(B.16)$$

and,

$$V_s' = \frac{\partial V_s}{\partial z_{SSE}} z_{SSE}' + \frac{\partial V_s}{\partial z_{PE}} z_{PE}' \qquad ;(B.17)$$

where,

$$z_{NNE} \equiv \tfrac{1}{2}(z_N + z_{NE}),$$

$$z_{SSE} \equiv \tfrac{1}{2}(z_S + z_{SE}),$$

and $$z_{PE} \equiv \tfrac{1}{2}(z_P + z_E) .$$

The effect of z_P on U_E may be neglected, because any direct effect on U_E is counteracted by an indirect effect on U_P.

Similarly, the effect of z_E on U_P may be neglected. Hence, equations (B.14) and (B.15) become:

$$U_E' = \frac{\partial U_E}{\partial z_E} z_E' \qquad ;(B.18)$$

and,

$$U_P' = \frac{\partial U_P}{\partial z_P} z_P' \qquad .(B.19)$$

The differential coefficients in equations (B.16) - (B.19) are obtained by differentiating the momentum versions of equation (3.3.12). When only the main influences are considered, differentiation of equation (3.3.12), for V_n leads to:

$$\frac{\partial V_n}{\partial z_{PE}} = \frac{\rho g \left(\frac{\Delta\rho}{\rho_o}\right)_n}{\frac{(\Delta y)_n}{\Delta x_P}\left(\rho U + \frac{\dot{m}_V'' \Delta X_P}{z}\right)_n} \qquad ;(B.20)$$

and,

$$\frac{\partial V_n}{\partial z_{NNE}} = -\frac{\partial V_n}{\partial z_{PE}} \qquad .(B.21)$$

Similarly,

$$\frac{\partial V_s}{\partial z_{PE}} = \frac{\rho g \left(\frac{\Delta\rho}{\rho_o}\right)_s}{\frac{(\Delta y)_s}{\Delta X_P}\left(\rho U + \frac{\dot{m}_V'' \Delta X_P}{z}\right)_s} \qquad ;(B.22)$$

$$\frac{\partial V_s}{\partial z_{SSE}} = -\frac{\partial V_s}{\partial z_{PE}} \qquad :(B.23)$$

$$\frac{\partial U_P}{\partial z_P} = -\frac{\rho g \left(\frac{\Delta\rho}{\rho_o}\right)_E}{\left(\rho U + \frac{\dot{m}_V'' \Delta X_P}{z}\right)_E} \qquad ;(B.24)$$

and,

$$\frac{\partial U_E}{\partial z_E} = -\frac{\rho g \left(\frac{\Delta\rho}{\rho_o}\right)_E}{\left(\rho U + \frac{\dot{m}_V'' \Delta X_P}{z}\right)_E} \qquad .(B.25)$$

The correction equation

The correction equation now has the final form:

$$(A_N + A_S + A_P)\, z_P' + (A_N + A_S + A_E)\, z_E'$$

$$= A_N z_N' + A_S z_S' + A_N z_{NE}' + A_S z_{SE}' + C \qquad ;(B.26)$$

where,

$$A_N \equiv \frac{\rho g \left(\frac{\Delta\rho}{\rho_o}\right)_n \Delta X_P^2}{2U_n (\Delta y)_n \sigma_n} \quad ;$$

$$A_S \equiv \frac{\rho g \left(\frac{\Delta\rho}{\rho_o}\right)_s \Delta X_P^2}{2U_s (\Delta y)_s \sigma_s} \quad ;$$

$$A_P \equiv -\frac{(\Delta y)_P}{z_P} - \frac{\rho g \left(\frac{\Delta\rho}{\rho_o}\right)_P (\Delta y)_P}{U_P \sigma_P} \quad ; \qquad (B.27)$$

$$A_E \equiv \frac{(\Delta y)_E}{z_E} - \frac{\rho g \left(\frac{\Delta\rho}{\rho_o}\right)_E (\Delta y)_E}{U_E \sigma_E} \quad ;$$

$$\sigma \equiv \left(\rho U + \frac{\dot{m}_V'' \Delta X_P}{z}\right) \quad ;$$

and,

$$C \equiv \varepsilon_P \equiv (\Delta y^*)_E - \Delta y_P^* - \Delta X_P \,(\tan\alpha_n^* - \tan\alpha_s^*).$$

Equations such as (B.26) are derived for each of the grid cells at any cross-section. There would then be twice as many unknowns as there are equations. Physical reasoning is now used to reduce the number of unknowns so that the set of simultaneous equations can be solved. If the flow is super-critical, pressure influences may not travel upstream, so the downstream layer depths, Z_E's are corrected; Z_P', Z_N' and Z_S'

being set to zero. If the flow is subcritical, pressure influences may travel in either direction. To enable the pressure influences to travel upstream, the upstream layer depths are corrected; Z'_E, Z'_{NE} and Z'_{SE} being set to zero. The corrections to the downstream depths would take place during the next integration step. Inspection of coefficients A_P and A_E shows that this practice would keep them positive and hence enhance convergence.

The two terms in A_P and A_E have opposing signs, and the second term in each case may be expressed as an inverse square of a "Froude number", F_o^*, say. Thus:

$$A_P \equiv - \left(\frac{\Delta y}{z}\right)_P \left(1 - \frac{1}{F_o^{*2}}\right) \qquad ;(B.28)$$

and,

$$A_E \equiv \left(\frac{\Delta y}{z}\right)_P \left(1 - \frac{1}{F_o^{*2}}\right) \qquad .(B.29)$$

In supercritical flows,

$F_o^* > 1$; A_P is negative; and A_E is positive.

In subcritical flows,

$F_o^* < 1$; A_P is positive; and A_E is negative.

In differentiating the momentum equations, a floating-layer flow was assumed, for generality. The correction equations for full-depth flows may be obtained by setting:

$$\frac{\Delta\rho}{\rho_o} = 1, \text{ and } \dot{m}''_V = 0.$$

Finally, when considering flows with lateral entrainment, only the expressions for calculating $\tan\alpha^*$ need be changed. This change would only have a secondary effect on $\tan\alpha'$, so the same correction equation applies.

APPENDIX C

DERIVATION OF THE EQUATIONS FOR THE BLOCK CORRECTION OF PRESSURE OR LAYER DEPTH

This correction is applied to the pressure or layer depth, when solving confined subcritical flows, to ensure that the total sum of the calculated cell widths, at any cross-section, match the width of the confining duct.

Suppose the width of the confining duct is B_1, and the total sum of calculated cell widths, $\Sigma\Delta y$ is given by:

$$\Sigma\Delta y = \int_I^E \frac{d\psi}{(\rho U z)} \qquad .(C.1)$$

The error in calculating the total cell width, $\delta\Sigma\Delta y$ is equal to:

$$\delta\Sigma\Delta y = B_1 - \Sigma\Delta y \qquad .(C.2)$$

It is required to find what pressure or layer-depth correction, δP or δZ should be applied in block to the whole flow at the cross-section to make $\delta\Sigma\Delta y = 0$. These may be obtained from the relations:

$$\delta P = \frac{dP}{d\Sigma\Delta y}\,\delta\Sigma\Delta y \qquad ,(C.3)$$

or,

$$\delta z = \frac{dz}{d\Sigma\Delta y}\,\delta\Sigma\Delta y \qquad .(C.4)$$

First, differentiating equation (C.1) with respect to P:

$$\frac{d\Sigma\Delta y}{dP} = \int_I^E -\frac{1}{(\rho U z)^2}\left(\rho U \frac{dz}{dP} + \rho z \frac{dU}{dP} + U z \frac{d\rho}{dP}\right) d\psi \qquad .(C.5)$$

The 'Hydrostatic approximation' gives:

$$\frac{dz}{d\bar{P}} = \frac{1}{\Delta\rho g} \qquad .(C.6)$$

The U-momentum equation gives:

$$\frac{dU}{d\bar{P}} = -\frac{1}{\rho U} \qquad .(C.7)$$

Since the flow is incompressible, $\frac{d\rho}{d\bar{P}} = 0$.

Hence, equation (C.5) may be expressed as:

$$\frac{d\varepsilon\Delta y}{d\bar{P}} = \int_I^E \frac{1}{\rho^2 U^3 z}\,(1 - Fr^2)\,d\psi \qquad ,(C.8)$$

where,

$$Fr \equiv \frac{U}{(\frac{\Delta\rho}{\rho} g z)^{\frac{1}{2}}}; \quad \text{the densimetric Froude number.}$$

Hence, $\bar{P}'$ is calculated from:

$$\bar{P}' = \delta P = \frac{\delta \Sigma \Delta y}{\int_I^E \frac{1}{I\rho^2 U^3 z}(1-Fr^2)\,d\psi} \qquad .(C.9)$$

Similarly,

$$\bar{z}' = \delta z = \frac{\delta \Sigma \Delta y}{\int_I^E \frac{1}{I\rho U z^2}(\frac{1}{F_r^2} - 1)\,d\psi} \qquad .(C.10)$$

Finally, the U-velocities are corrected with

$$\bar{U}' = -\frac{1}{\rho U}\,\bar{P}' \qquad ,(C.11)$$

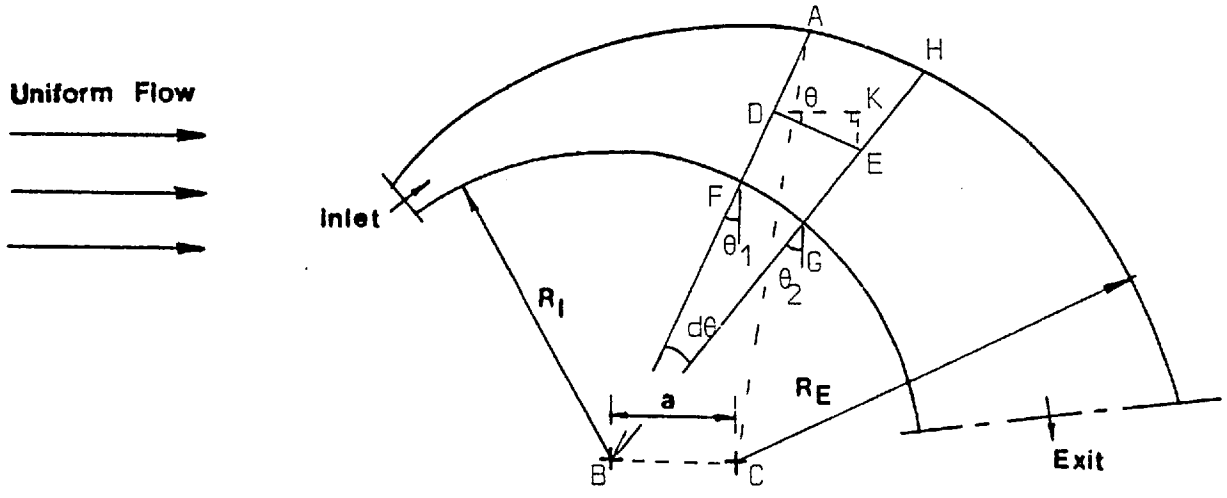
or,

$$\bar{U}' = -\frac{\Delta\rho g}{\rho U}\,\bar{z}' \qquad .(C.12)$$

APPENDIX D

EXACT SOLUTION OF THE ANGLES OF INCLINATION IN THE COMPUTATIONS OF UNIFORM FLOW IN CURVED DOMAINS

The prediction of the flows within curved domains, superposed on to a uniform flow, was used in Section 4.2 as a test case for the parabolic solution procedure and the rotating-grid procedure. The flow domain is illustrated below:



Define:

$$h_1 = AF,$$
$$h_2 = HG,$$
$$R_1 = DB,$$
and, $$R_2 = EB,$$

(D.1)

Suppose:

DE is a typical ω-grid line with a value of $\omega = \omega_i$.

The I-boundary is the reference grid line, so:

$$\theta_{I_{C_L},u} = \theta_1,$$

and, (D.2)

$$\theta_{I_{C_L},d} = \theta_2 = \theta_1 + d\theta \quad .$$

The total widths of the flow domain at the upstream and downstream stations may be obtained from the properties of triangles ABC and HBC, respectively, as:

$$h_1 = (R_E^2 - a^2\cos^2\theta_1)^{\frac{1}{2}} - a\sin\theta_1 - R_I \quad ;(D.3)$$

and,

$$h_2 = (R_E^2 - a^2\cos^2\theta_2)^{\frac{1}{2}} - a\sin\theta_2 - R_I \quad .(D.4)$$

Since the flow is uniform, R_1 and R_2 are given by:

$$R_1 \equiv BD \equiv BF+FD = R_I + \omega_i h_1 \quad ;(D.5)$$

and,

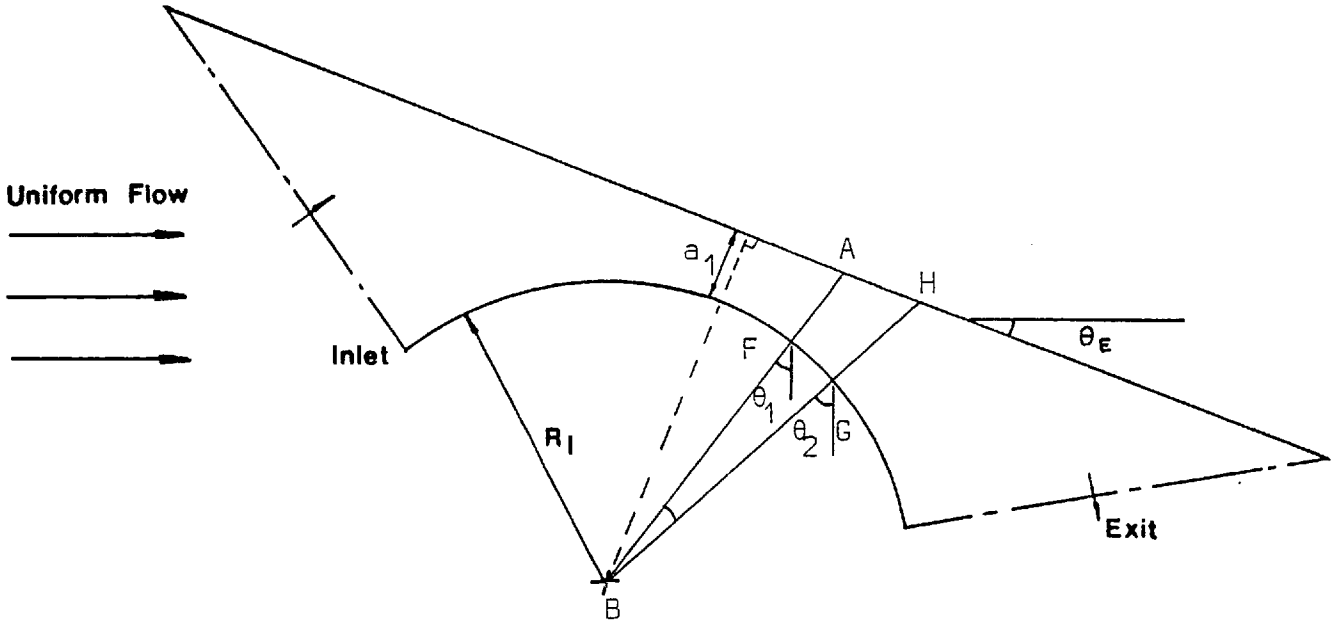
$$R_2 \equiv BE \equiv BG+GE = R_I + \omega_i h_2 \quad .(D.6)$$

Finally, angle θ may be calculated from:

$$\theta = \tan^{-1}\frac{EK}{DK} = \tan^{-1}\left(\frac{R_2\cos\theta_2 - R_1\cos\theta_1}{R_2\sin\theta_2 - R_1\sin\theta_1}\right) \quad .(D.7)$$

If the flow domain is of the second type, as illustrated below, the analysis is identical, except for the equations for calculating the total widths of the flow domain, h_1 and h_2.

Illustration of the flow domain:



The length, a_1 is the specified spacing of the flow domain, along the normal to the ε-boundary. h_1 and h_2 are simply obtained by resolving AB and HB, respectively, in the direction of the normal. Thus,

$$h_1 = \frac{a_1 + R_I}{\cos(\theta_1 - \theta_E)} - R_I \qquad ;(D.8)$$

and

$$h_2 = \frac{a_1 + R_I}{\cos(\theta_2 - \theta_E)} - R_I \qquad .(D.9)$$

The analysis then continues as for the previous case.

APPENDIX E

ANALYTICAL SOLUTION FOR THE STEADY FLOW OF A RADIAL POOL OF WARM WATER ABOVE A COLD WATER MASS

The prediction of the radial pool problem was used in Section 4.3 as a test case for the hyperbolic solution procedure. Figure 4.8 shows the flow configuration of the radial pool being considered. Two assumptions are made for simplicity, namely:-

(i) there is no heat transfer to and from the pool;

(ii) there is no entrainment of cold fluid into the radial pool.

Consider a segment of the pool which subtends an angle of 1 radian: the differential equations governing the flow are then:

continuity,

$$\frac{d}{dx}\,(z \times U) = 0 \qquad ;(E.1)$$

and,

momentum,

$$\frac{d}{dx}\,(z \times U^2) = -\,g\frac{\Delta\rho}{\rho_o}\,z \times \frac{dz}{dx} \qquad ,(E.2)$$

(where, x is the radial distance from the origin of the flow).

Let,

$$\lambda \equiv \frac{\Delta\rho}{\rho_o}\,g.$$

Equation (E.1) is differentiated to give:

$$zU + Ux \frac{dz}{dx} + zx \frac{dU}{dx} = 0 \qquad ,(E.3)$$

and equation (E.2) is differentiated to give:

$$zU^2 + 2Uzx \frac{dU}{dx} + U^2 \times \frac{dz}{dx} = - \lambda zx \frac{dz}{dx} \qquad .(E.4)$$

(E.4) - U times (E.3), gives:

$$Uzx \frac{dU}{dx} = - \lambda zx \frac{dz}{dx} \qquad .(E.5)$$

If neither z, nor x is zero, equation (E.5) may be integrated, giving as result:

$$U^2 = - 2\lambda z + C_1 \qquad ,(E.6)$$

where,

C_1 = constant.

If equation (E.6) is now substituted in equation (E.2), one gets:

$$\frac{d}{dx} (- 2\lambda z^2 x + C_1 xz) = - \lambda zx \frac{dz}{dx} \qquad .(E.7)$$

Let,

$A \equiv zx.$

Equation (E.7) can now be expressed as:

$$\frac{d}{dx} \left(-2\lambda \frac{A^2}{x} + C_1 A\right) = - \lambda A \frac{d}{dx} \left(\frac{A}{x}\right) \qquad ,(E.8)$$

which gives on differentiating:

$$3\lambda A \frac{dA}{dx} - C_1 \times \frac{dA}{dx} - \frac{A^2}{x} = 0 \qquad .(E.9)$$

Equation (E.9) may be converted to one of the "exact" form by multiplying with the integrating factor:-

$$\mu = \frac{A}{x} .$$

It then becomes:

$$(\frac{3\lambda A^2}{x} - C_1 A)\, dA - \frac{\lambda A^3}{x^2}\, dx = 0 \qquad .(E.10)$$

The general solution of equation (E.10) is:

$$\frac{\lambda A^3}{x} - \frac{C_1 A^2}{2} = \text{constant, } C_2 \qquad .(E.11)$$

The boundary conditions are:-

At inlet,

$$\begin{aligned} z &= z_{In} \quad ; \\ A &= A_{IN} = z_{IN}\, x_{IN} \quad ; \\ U &= U_{IN} \quad ; \\ x &= x_{IN} \quad . \end{aligned} \qquad (E.12)$$

These are substituted in equations (E.6) and (E.12), to give the constants C_1 and C_2 as:

$$C_1 = U_{IN}^2 + 2\lambda z_{IN} \qquad :(E.13)$$

and,

$$C_2 = \frac{\lambda A_{IN}^3}{x_{IN}} - \frac{C_1 A_{IN}^2}{2} = \frac{U_{IN}^2 A_{IN}^2}{2} \qquad .(E.14)$$

Equation (E.11) may be expressed as:

$$x = \frac{\lambda A^3}{\frac{C_1}{2}A^2 - C_2} \equiv \frac{\lambda x^3 z^3}{\frac{C_1}{2} z^3 x^2 - C_2} \qquad .(E.15)$$

By rearranging equation (E.15) one gets:

$$x = \frac{(2\,C_2)^{\frac{1}{2}}}{z(C_1-2\lambda z)^{\frac{1}{2}}} = \frac{U_{IN}\,A_{IN}}{z(C_1-2\lambda z)^{\frac{1}{2}}} \qquad .(E.16)$$

There is no simple way of expressing z as an explicit function of x, so the relationships between U,z, and x are obtained, numerically, from the following sequence:

(1) Guess a value of z;

(2) Calculate U from, $U = \sqrt{(C_1 - 2\lambda z)}$;

(3) Calculate x from, $x = \frac{U_{IN}\,A_{IN}}{Uz}$;

(4) Return to (1), and repeat the sequence with a new value of z.

APPENDIX F

TABULATED EXPERIMENTAL DATA

This appendix contains the data obtained in the experimental investigation reported in Chapter 7. The tabulated values are the measured layer thickness at the specified cross-sections, and at various lateral distances from the I-boundary. All the distances are in centimeters. The discharge is, in each case, through a fixed rectangular orifice, 2.54 cms. deep and 20.32 cms. wide. The I-boundary is a circular wall of radius 6m., tangential to the flow at the orifice. Its coordinate relative to the point of taught at the orifice was measured as:

x	0	10	20	30	40	50	60
y_I	0.0	-0.2	-0.5	-0.9	-1.5	-2.2	-3.1

x	70	80	90	100	110	120
y_I	-4.4	-5.4	-6.8	-8.4	-10.1	-12.1

These experimental results have been plotted in Figures 7.4.1 - 7.4.5. The relevant discharge parameters are given at the top of each table.

Table F.1: Run 1; FR=2.20, A.R.=8, R_E=6.2m.

Distance from the I-boundary	x=10 Z	x=20 Z	x=30 Z	x=40 Z	x=50 Z	x=60 Z
.50	2.19	2.44	2.44	2.41	2.18	2.00
2.00	2.16	2.45	2.40	2.32	2.17	2.04
4.00	2.60	2.20	2.53	2.27	2.24	2.26
6.00	2.66	2.45	2.20	2.33	2.29	2.59
8.00	2.68	2.59	2.23	2.22	2.43	2.62
10.00	2.65	2.61	2.29	2.14	2.69	2.60
12.00	2.59	2.58	2.36	2.30	2.69	2.68
14.00	2.51	2.47	2.41	2.72	2.66	2.86
16.00	2.42	2.25	2.86	2.80	2.75	2.70
18.00	2.04	2.59	2.88	2.95	2.83	2.65
20.00	2.33	2.66	2.97	3.13	2.95	2.65

Distance from the I-boundary	x=70 Z	x=80 Z	x=90 Z	x=100 Z	x=110 Z	x=120 Z
.50	2.40	2.75	2.50	2.51	2.56	2.59
2.00	2.37	2.69	2.45	2.47	2.47	2.50
4.00	2.50	2.46	2.71	2.40	2.55	2.55
6.00	2.48	2.40	2.80	2.49	2.54	2.60
8.00	2.45	2.36	2.54	2.71	2.52	2.49
10.00	2.69	2.35	2.45	2.72	2.72	2.36
12.00	2.54	2.48	2.47	2.56	2.82	2.49
14.00	2.67	2.51	2.62	2.52	2.89	2.76
16.00	2.75	2.64	2.71	2.56	2.76	2.97
18.00	2.72	2.67	2.62	2.67	2.62	3.09
20.00	2.87	2.54	2.77	2.74	2.80	2.85

NOTE: All distances are in centimeters.

Table F.2: Run 2; FR=2.20, A.R.=8, $\theta_E=0^o$.

Distance from the I-boundary	x=10 Z	x=20 Z	x=30 Z	x=40 Z	x=50 Z	x=60 Z
.50	1.98	2.29	2.24	2.36	2.14	1.86
2.00	2.04	2.37	2.25	2.25	2.18	1.88
4.00	2.38	2.10	2.44	2.17	2.18	1.94
6.00	2.47	2.33	2.20	2.30	2.07	2.10
8.00	2.51	2.45	2.21	2.22	2.03	2.13
10.00	2.51	2.52	2.27	2.05	2.23	2.06
12.00	2.49	2.52	2.29	2.06	2.16	2.29
14.00	2.47	2.46	2.29	2.14	2.17	2.30
16.00	2.42	2.30	2.42	2.31	2.19	2.31
18.00	2.21	2.34	2.44	2.35	2.37	2.21
20.00	2.19	2.39	2.42	2.52	2.43	2.13
22.00				2.66	2.44	2.06

Distance from the I-boundary	x=70 Z	x=80 Z	x=90 Z	x=100 Z	x=110 Z	x=120 Z
.50	1.69	1.71	1.70	1.80	1.59	1.42
2.00	1.64	1.75	1.72	1.70	1.52	1.37
4.00	1.74	1.71	1.82	1.63	1.64	1.38
6.00	1.84	1.81	1.79	1.64	1.55	1.49
8.00	2.04	1.86	1.73	1.72	1.52	1.44
10.00	2.25	1.89	1.79	1.66	1.57	1.40
12.00	2.18	2.05	1.74	1.58	1.54	1.48
14.00	2.14	2.16	1.70	1.60	1.60	1.58
16.00	2.25	1.91	1.80	1.64	1.64	1.62
18.00	2.15	1.93	1.99	1.72	1.64	1.60
20.00	2.04	2.02	1.94	1.86	1.64	1.57
22.00	1.99	2.12	1.99	1.95	1.62	1.59
24.00	2.12	2.10	1.98	1.84	1.82	1.66
26.00			2.07	1.91	1.90	1.59
28.00				2.02	1.81	1.62
30.00					1.78	1.69
32.00						1.77

Table F.3: Run 3; FR=2.20, A.R.=8, $\theta_E=5^o$.

Distance from the I-boundary	x=10 Z	x=20 Z	x=30 Z	x=40 Z	x=50 Z	x=60 Z
.50	2.05	2.22	2.26	2.60	2.99	3.11
2.00	2.18	2.24	2.32	2.53	3.02	3.10
4.00	2.33	2.09	2.48	2.65	2.93	2.92
6.00	2.42	2.27	2.33	2.97	2.67	3.04
8.00	2.44	2.48	2.50	2.82	2.83	2.77
10.00	2.45	2.60	2.83	2.57	2.87	2.76
12.00	2.46	2.75	2.99	2.68	2.66	2.75
14.00	2.50	3.02	2.89	2.87	2.63	2.55
16.00	2.59	2.93	3.02	2.90	2.62	2.45
18.00	2.83	2.87	3.09			

Distance from the I-boundary	x=70 Z	x=80 Z	x=90 Z	x=100 Z	x=110 Z	x=120 Z
.50	2.63	2.59	2.39	2.10	2.24	2.28
2.00	2.60	2.70	2.35	2.07	2.14	2.23
4.00	2.93	2.42	2.37	2.31	2.14	2.25
6.00	2.87	2.42	2.45	2.35	2.29	2.19
8.00	2.87	2.61	2.37	2.59	2.38	2.13
10.00	3.04	2.69	2.59	2.55	2.48	2.18
12.00	2.60	2.89	2.68	2.62	2.46	2.30
14.00	2.65	2.77	2.96	2.53	2.51	2.50
16.00	2.64	2.88	2.96	2.63	2.58	2.32
18.00	2.75	2.92	2.83	2.69	2.47	2.26
20.00					2.40	2.21

Table F.4: Run 4; FR=1.85, A.R.=8, $\theta_E=5^o$.

Distance from the I-boundary	x=10 Z	x=20 Z	x=30 Z	x=40 Z	x=50 Z	x=60 Z
.50	2.12	2.28	2.44	2.98	2.99	2.60
2.00	2.05	2.34	2.48	2.88	2.93	2.74
4.00	2.24	2.21	2.63	2.89	2.94	2.86
6.00	2.38	2.28	2.72	2.76	2.91	1.83
8.00	2.40	2.44	2.70	2.70	2.80	2.81
10.00	2.42	2.63	2.71	2.70	2.81	2.77
12.00	2.42	2.84	2.65	2.68	2.70	2.66
14.00	2.50	2.94	2.78	2.63	2.63	2.67
16.00	2.60	2.80	2.90	2.63	2.48	2.70
18.00	2.76	2.83	2.91			2.69

Distance from the I-boundary	x=70 Z	x=80 Z	x=90 Z	x=100 Z	x=110 Z	x=120 Z
.50	2.63	2.29	2.37	2.64	2.48	2.14
2.00	2.47	2.33	2.40	2.57	2.42	2.07
4.00	2.39	2.45	2.36	2.59	2.44	2.10
6.00	2.51	2.41	2.63	2.42	2.34	2.14
8.00	2.56	2.53	2.68	2.40	2.25	2.24
10.00	2.71	2.65	2.63	2.45	2.17	2.39
12.00	2.82	2.82	2.64	2.32	2.31	2.10
14.00	2.88	2.96	2.49	2.42	2.29	2.00
16.00	2.93	2.99	2.47	2.43	2.18	2.05
18.00	3.09	2.89	2.62	2.41	2.14	2.09
20.00					2.19	2.10

Table F.5: Run 5; FR=2.10, A.R.=8, $\theta_E=7^o$

Distance from the I-boundary	x=10 Z	x=20 Z	x=30 Z	x=40 Z	x=50 Z	x=60 Z
.50	2.07	2.28	2.43	3.10	3.88	3.28
2.00	2.13	2.31	2.47	3.03	3.81	3.31
4.00	2.34	2.18	2.71	3.16	3.27	3.62
6.00	2.42	2.37	2.65	3.08	3.10	3.70
8.00	2.44	2.56	2.98	2.86	3.21	3.25
10.00	2.45	2.74	3.19	2.89	3.07	3.28
12.00	2.50	3.03	3.09	3.05	2.92	3.11
14.00	2.56	3.27	3.15	3.07	2.83	2.90
16.00	2.72	3.10	3.25	3.13	2.85	2.84
18.00	3.08	3.10				

Distance from the I-boundary	x=70 Z	x=80 Z	x=90 Z	x=100 Z	x=110 Z	x=120 Z
.50	3.00	3.01	2.86	3.45	3.11	2.80
2.00	2.99	3.03	2.97	3.46	3.13	2.74
4.00	3.04	2.86	3.23	3.33	3.15	2.73
6.00	3.12	2.90	3.43	3.30	2.97	2.89
8.00	3.38	3.08	3.38	3.33	2.80	2.87
10.00	3.54	3.35	3.39	3.06	3.03	2.80
12.00	3.40	3.67	3.19	3.04	2.99	2.61
14.00	3.61	3.65	3.32	2.94	2.80	2.72
16.00	3.71		3.50	2.89	2.65	2.88

NOTE: All distances are in cms.